Phthalocyanine-Based Bio-Functional Conjugates: Photodynamic Therapy and Photoantimicrobial Chemotherapeutic Efficacy Evaluation *in-Vitro*

A thesis submitted in fulfilment of the requirements for the degree of

DOCTOR OF PHILOSOPHY
Of
RHODES UNIVERSITY

By

Aviwe Magadla

December 2023

ACKNOWDGEMENTS

My heartfelt gratitude goes to Distinguished Professor Tebello Nyokong for her unwavering leadership, support, mentorship, and encouragement throughout the program, as well as the numerous chances she provided me. I'd want to express my gratitude to Dr. Mack, Dr. Britton, Ms. Gail, and Papa Francis for their aid throughout my studies. To my family, thank you for your prayers and presence; you've been a constant source of joy and support for me. Special thanks to Dr. D. van Niekerk and Mr. M. Randall from the E.M.U. for training, determining experimental parameters, and assisting with sample preparation, training, and data collection.

I'd like to thank the former and present members of the S22 research group, especially Dr. Balaji, Mpeta, and Openda, for their help and support in running my experiments. I would also want to thank the National Research Foundation (NRF), the Chemistry Department at Rhodes University, all staff members, for their financial support.

ABSTRACT

This thesis reports on the syntheses and characterisation of symmetrical and asymmetrical phthalocyanines (Pcs) with different ring substituents derived to form either cationic styryl pyridine, cationic styryl pyridine triphenylphosphonium (TPP+)-based, benzothiazole, cationic pyridyl-dihydrothiazole and other closely related groups. The starting Pc complex of the synthesised Pc derivatives was typically obtained through the cyclotetramerisation of a substituted phthalonitrile. Then, depending on the desired final complex, the desired complexes were synthesised through the Knoevenagel condensation, alkylation reaction, and Schiff base reaction.

Furthermore, silica nanoparticles (SiNPs) were also used to encapsulate Pcs. Following aminopropyl triethoxysilane amino (APTES) functionalisation of the surface of the Pc@SiNPs-APTES, biomolecules such as gallic acid, folic acid, and ampicillin were covalently attached to the surface. Additionally, Pc@SiNPs-APTES is protonated with 1,3-propanesultone. The pair of synthesised asymmetric Pcs is attached to ciprofloxacin (CIP) via an amide bond. Different analytical methods were used to characterise the Pcs and their conjugates.

The photophysics and photochemistry of the Pcs both by themselves and in their conjugate form when doped with SiNPs. The cationic Pcs were able to produce sufficient singlet oxygen on their own in most cases. This is explained by the Pcs greater solubility in water. Since singlet oxygen is produced from the triplet state, singlet oxygen quantum yield (Φ_Δ) values complement triplet quantum yield (Φ_T) values. Low Φ_Δ values could be attributed to ineffective energy transfer; screening effects may have prevented the excited triplet state of the Pcs from interacting with the ground state molecular oxygen, lowering the Φ_Δ values. In other instances, the Pcs' protection by the SiNPs could be credited with extending the triplet lifetime. The direct connection of Pcs with CIP increased the formation of Φ_T and Φ_Δ in

comparison to Pcs alone. Both in planktonic and biofilm form, the cationic Pcs and conjugates showed enhanced bacterial elimination. The Pcs and conjugates demonstrated significant activity in photodynamic therapy treatment (PDT) experiments at the tested doses. In both PDT and photodynamic antimicrobial chemotherapy (PACT) treatment, the cationic Pcs outperformed the neutral Pc in terms of biological activity.

TABLE OF CONTENTS

ADMA	=	tetrasodium α, α–(anthracene–9,10–diyl) dimethylmalonate
AlPc-Smix	=	Aluminium sulfonated phthalocyanine
APTES	=	3–Aminopropyltriethoxysilane
BET	=	Brunauer–Emmet–Teller
$CDCl_3$	=	Deuterated Chloroform
DBU	=	1,8–Diazabicyclo–[5.4.0]–undec–7–ene
DCC	=	Dicyclohexylcarbodiimide
DCM	=	Dichloromethane
DLS	=	Dynamic light scattering
DMAP	=	Dimethylaminopyridine
DMF	=	Dimethylformamide
DMSO	=	Dimethyl Sulfoxide
DMSO-d_6	=	Deuterated Dimethylsulfoxide
DPBF	=	1,3–Diphenylisobenzofuran
EDC	=	N–(3–Dimethylaminopropyl)–N'–ethylcarbodiimide
EIS	=	Electrochemical impedance spectroscopy
EPS	=	Exopolymeric substance
Flu	=	Fluorescence
FT–IR	=	Fourier Transform Infrared
HOMO	=	Highest Occupied Molecular Orbital
IC	=	Internal Conversion
ISC	=	Intersystem Crossing
LUMO	=	Lowest Unoccupied Molecular Orbital
MALDI	=	Matrix–Assisted Laser Desorption/Ionization
MPcs	=	Metallophthalocyanines
H_2Pc	=	Metal Free Phthalocyanine
MS	=	Mass Spectrometer
Nd–YAG	=	Neodymium–doped Yttrium Aluminum Garnet
NHS	=	N–Hydroxy succinimide

NIR	=	Near Infrared
NPs	=	Nanoparticles
^{1}H NMR	=	Proton Nuclear Magnetic Resonance
Pcs	=	Phthalocyanines
PDT	=	Photodynamic Therapy
PACT	=	Photodynamic antimicrobial chemotherapy
Ph	=	Phosphorescence
ROS	=	Reactive Oxygen Species
SiNPs	=	Silica Nanoparticles
SEM	=	Scanning electron microscopy
TCSPC	=	Time Correlated Single Photon Counting
TEM	=	Transmission Electron Microscope
TEOS	=	Tetraethyl orthosilicate
UV–vis	=	Ultraviolet–Visible
XPS	=	X–ray Photoelectron Spectroscopy

R_{ct}	=	Charge transfer resistance
Φ_F	=	Fluorescence Quantum Yield
τ_F	=	Fluorescence Lifetime
Z''	=	Imaginary impedance
$^3O_2$	=	Molecular Oxygen
α	=	Non–peripheral Position
β	=	Peripheral Position
ΔE	=	Peak potential separation
Z'	=	Real impedance
$^1O_2$	=	Singlet Oxygen
S_0	=	Singlet ground state
S_1	=	Singlet excited state
Φ_Δ	=	Singlet Oxygen Quantum Yield
Φ_T	=	Triplet Quantum Yield
t	=	Time
T_1	=	Triplet excited state
τ_T	=	Triplet Lifetime

Preamble to thesis

This thesis introduces the concepts of photodynamic antimicrobial chemotherapy (PACT), photodynamic therapy (PDT), and metallophthalocyanines (MPc), and discusses the role of silica nanoparticles (SiNPs) as PACT/PDT agents when combined with MPcs. The spectrochemical behaviour, delivery techniques, and applications of MPcs, as well as their structural features, will be discussed.

CHAPTER ONE
INTRODUCTION

1.1 Preamble to Photodynamic therapy (PDT) and photodynamic antimicrobial chemotherapy (PACT)

Microbial infections constitute one of the major global health burdens with an alarming rate of antimicrobial resistance [1]. The presence of biofilms reduces the efficacy of antibiotics causing multidrug resistance. Biofilms are known to influence the behaviour of bacteria through their extracellular polysaccharide matrix (EPS) causing them to be recalcitrant against the host immunity and antibiotics [2–5].

There are excellent reviews which reflect on the fact that the global burden of cancer is increasing, especially in the most vulnerable sociodemographic populations, and that a substantial global effort is required not only to reduce the incidence of cancer but also to provide more evenly distributed cancer control [6–8].

It has been suggested that bacterial infections may contribute to cancer development and spread [9]. Some cancer-causing pathogens are able to evade the immune system, cause chronic inflammation that promotes unchecked cell proliferation, and even enhance the chance of oncogenic transformation in otherwise healthy people [10].

To combat antimicrobial resistance (AMR) and tumourigenic cells, a new category of antimicrobial and anti-cancer agents with superior drug delivery must be developed. Several studies have demonstrated the effectiveness of photoantimicrobial agents (photosensitisers, PS) in destroying various bacterial infections/cancerous cells without resistance due to their rapid mechanism of action [11–15]. The same PS used for PACT can also be used cancer in PDT. Hence, PACT and PDT are combined in this work.

1.2 Photosensitisation for PACT and PDT

PACT and PDT are conceptually similar since they both employ PS and light to selectively kill unhealthy human cells or bacterial cells [16,17]. Applications and targets for bacterial and human cells are different due to the presence of a cell wall. The Jablonski diagram is a graphical representation of the energy levels and transitions that occur in a PS when it is excited by light, **Figure 1.1**. It is an ideal tool for understanding the energy transfer processes involved in PACT and PDT.

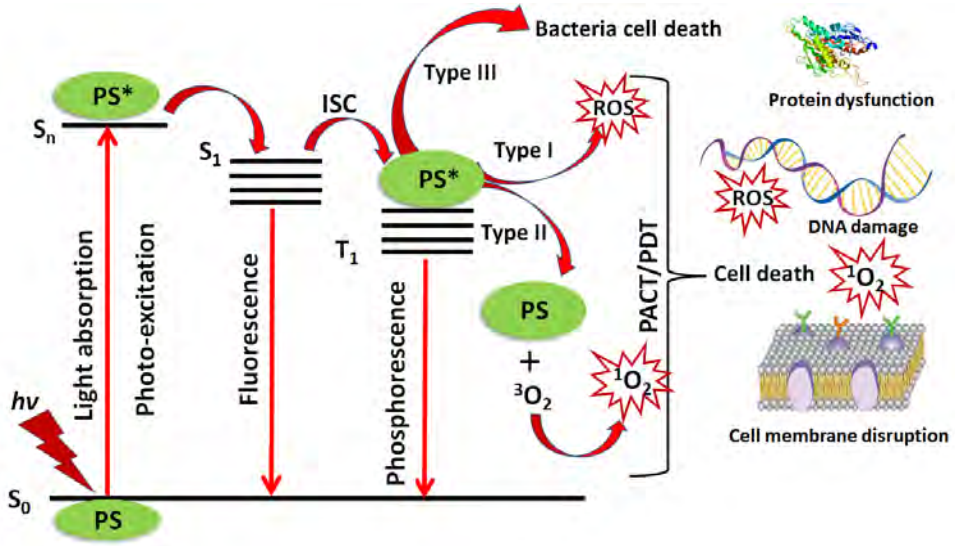

Figure 1.1: Jablonski diagram demonstrating how a photosensitizer (PS) can transition from its ground state (S_0) to a singlet excited state (S_n) by absorbing light (*hv*) of a certain wavelength and undergo intersystem crossing (ISC) to generate reactive oxygen species (ROS).

Once excited to the triplet state (T_1) the PS can generate reactive oxygen species (ROS) via two competing pathways—Type I and Type II. In the Type I reaction, electron transfer with substrate occurs to form superoxide anion radical ($O_2^{\bullet-}$) and, hydrogen peroxide (H_2O_2) and hydroxyl radical ($OH^{\bullet-}$). In the Type II process, energy goes directly from the PS* to the ground state molecular oxygen ($^3O_2$), which is then converted into singlet oxygen ($^1O_2$) [18]. ROS are

non-specific, and they can cause irreversible destruction of cell membrane function, proteins and DNA [19–22]. Recent research has revealed a Type III mechanism that can also cause bacterial mortality through oxygen-independent photoinactivation [23].

The properties of an ideal PS for PDT include high extinction coefficients; tuneable photophysical properties; selectivity towards malignant cells; good photostability; biocompatibility; and light absorption in the therapeutic window (650—800 nm) for deep seated tumour cells. The overarching objective of this effort is to develop PSs with strong bacterial and cancer cell affinity.

1.2.1 Photodynamic antimicrobial chemotherapy (PACT)

In healthcare settings, gram (+) and gram (-) bacteria are responsible for various illnesses including meningitis, wound or surgical infections, intestinal and extraintestinal disease, and pneumococcal infections [24–26]. Gram (-) bacteria have a single, thin layer of peptidoglycan (**Figure 1.2**). Lipopolysaccharide coating (LPS) indicators are found in gram (-) bacteria [27,28], but not in gram (+). In this work phthalocyanine (Pc) derived PS are used alone and in the presence of nanoparticles (NPs) against gram-positive (gram (+)) and gram-negative (gram (-)) bacteria.

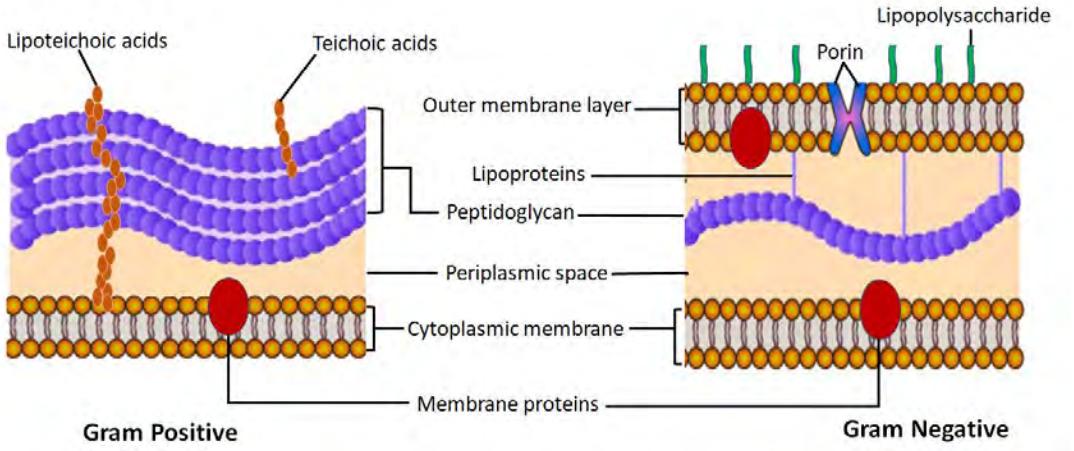

Figure 1.2: Structural cross-section of gram-positive and gram-negative cell composition

Since its main purpose is to maintain structural integrity, LPS is exposed to the surface of the cell. As a result, most gram (-) bacteria exhibit intrinsic resistance to many antimicrobial treatments because LPS creates a permeability barrier at the cell surface [28,29]. LPS on the surface of gram (-) bacteria reduces the ability of neutral or anionic-charged molecules to penetrate the vital components of the cell, which results in ineffective PACT activity [14,30]. To improve the electrostatic interactions between gram (-) bacteria and the antimicrobial agents, this thesis will employ cationic functionalised photoantimicrobial agents towards treatment of *Escherichia coli* (*E. coli*) as an example [31,32].

Gram (+) strains have teichoic acids, lipoteichoic acids, and thick-layer peptidoglycan on their surfaces [33,34], but lack LPS (**Figure 1.2**). Consequently, they are sensitive to neutral, anionic, and cationic charged compounds [35,36]. In this thesis gram (+) pathogens; *Streptococcus pneumoniae* (*S. pneumoniae*) and *Staphylococcus aureus* (*S. aureus*), which coexist in polymicrobial form [37,38] will be treated using cationic and anionic PS in planktonic and

biofilm form. A microbiological biofilm is a tiny community of microorganisms that is three-dimensional and adheres to a surface (**Figure 1.3**). Biofilms may form on a wide variety of surfaces, including but not limited to pipes, metallic surfaces, glass surfaces, medical equipment, aquatic systems, and living tissue, to name just a few examples [39–41]. The thickness of the biofilm is affected not only by the type of bacterium that is present but also by the age of the biofilm, the quantity of nutrients, and a variety of other environmental conditions.

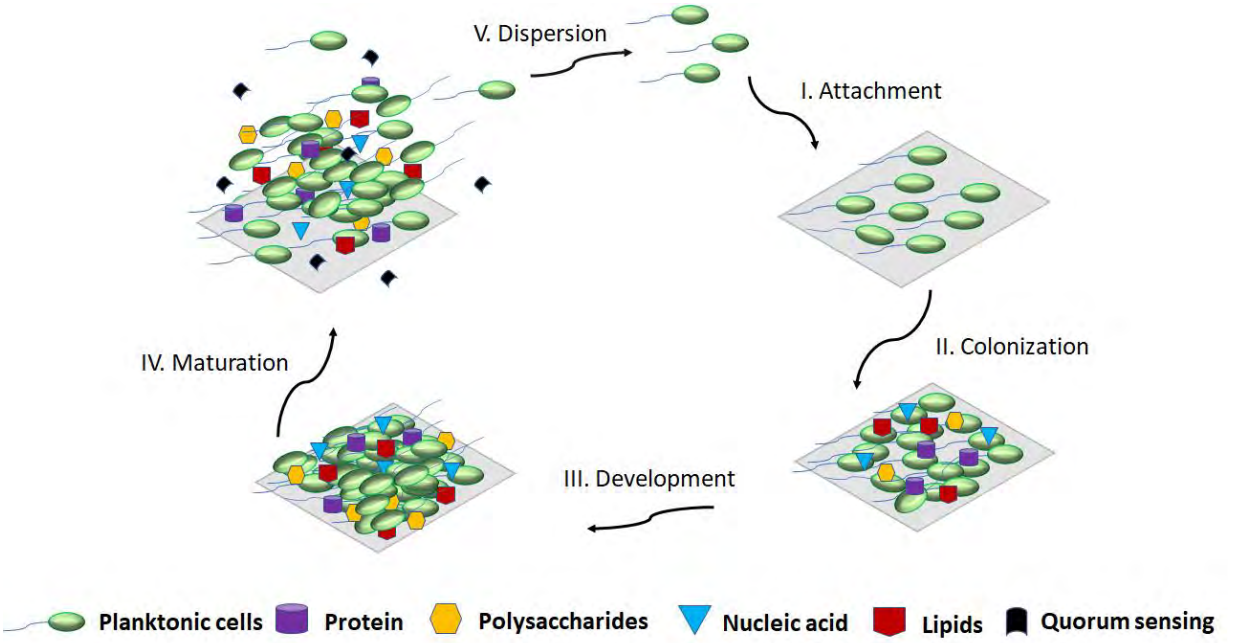

Figure 1.3: Biofilm life cycle: (I) free-floating planktonic cells reversible attachment to a surface, (II) irreversible attachment mediated by the formation of exopolymeric material, (III) formation of microcolonies and the beginning of biofilm maturation, (IV) Formation of a mature biofilm with a 3-dimensional structure containing cells packed in clusters with channels between the clusters that allow transport of water and nutrients and waste removal, and (V) detachment and dispersion of cells from the biofilm and initiation of new biofilm formation; dispersed cells are more similar to planktonic (that is, nonadherent) than to mature biofilm cells, cell–cell interaction, and signalling (quorum sensing) occurs before they disperse and colonize new surfaces [42]**.**

In this study, biofilm cells are cultured on the extracellular surface of indium tin oxide (ITO) semiconductors, and an investigation on how the uptake of PS-antimicrobials is affected by the cellular charge transfer of EPS molecules is undertaken. ITO-glass offers a practical approach to identifying the first stages of biofilm accumulation on surfaces.

The structural and metabolic changes in a biofilm following PACT treatment are examined in this work using scanning electron microscopy (SEM) and Raman spectroscopy. The chemical makeup of distinct bacterial strains may be examined after PS-antimicrobial activity using Raman spectroscopy.

1.2.2 Photodynamic therapy (PDT)

PDT has been demonstrated as a dependable treatment option for the elimination of tumourigenic cells due to its reliable selectivity and specificity. As stated above, the treatment involves the intravenous administration of a PS that accumulates in malignant tissue which is then activated by a laser light of appropriate wavelength resulting in the production of ROS that are poisonous to cancer cells and ultimately cause their death [15,43,44]. Clinical trials using MPc-based PS (**Figure 1.4**) for PDT have been reported [45–52].

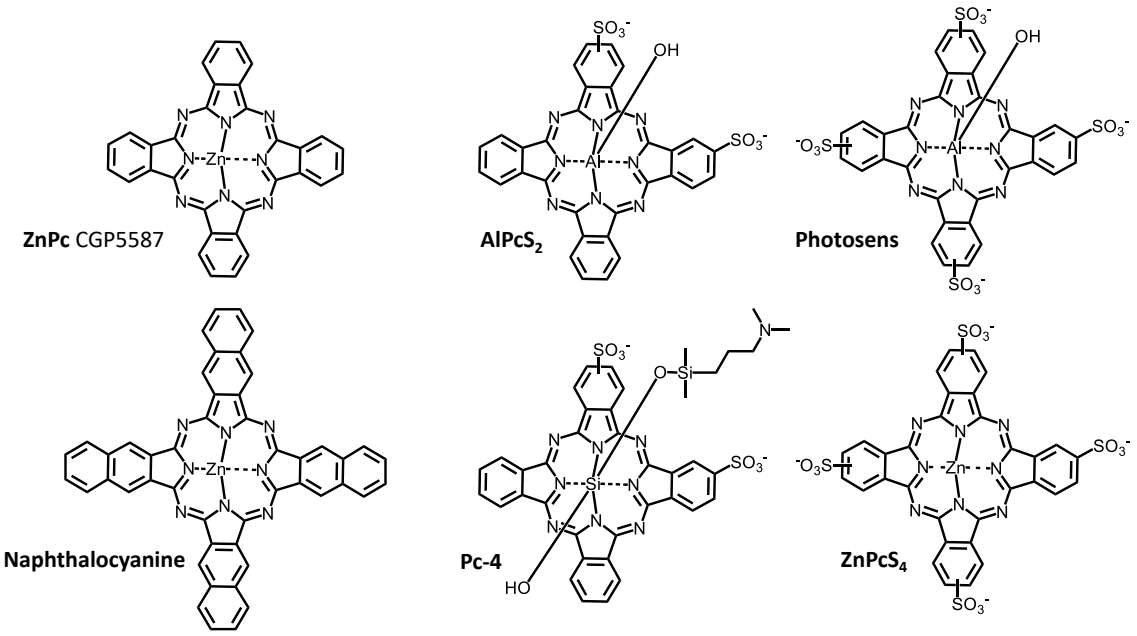

Figure 1.4: Molecular structure of some MPcs in clinical trials.

Despite PDT's demonstrated efficacy, studies are ongoing to identify even more potent PSs, and effective delivery systems. PS offer several promising features, but their lack of selectivity and specificity is still a major drawback. The most studied PS are hydrophobic, presenting a significant difficulty in their broad application in biological environment. These hydrophobic compounds tend to be poorly soluble in water, affecting their dosing and enhancing aggregation, both of which have a negative impact on the PS's photosensitisation [16,53,54].

To increase the PS concentration in tumours, scientists are investigating several PDT delivery techniques including their incorporation with suitable carriers. Various carrier systems including biodegradable nanoparticles, micelles, and polymer-drug conjugates or liposomes have been explored [16,54,55]. The applicability of carrier systems for PS in PDT can be attributed to their versatility in penetrating the leaky vasculature of tumours thereby accumulating in them passively via a process known as enhanced permeability and retention

(EPR) effect. The EPR effect describes the preferred accumulation of a PS in tumour tissues [56,57]. This occurs due to defects of the neo vasculature, which include vascular walls that are aberrant, oversized, leaky, and irregular blood vessels. This morphological flaw in tumour tissues allows plasma components of the blood to enter a tumour [16,56,57]. Poor lymphatic drainage and a sluggish venous return in tumour tissue both impede macromolecules from escaping a lesion.

The combination of various carrier systems with drug molecules have been proven to increase their selectivity and specificity. Developments, such as the integration of appropriate drug-carriers including nanoparticles, folic acid receptors, and 4-bromo-butyl-triphenylphosphonium derived mitochondria-targeting moieties [58,59], have been implemented in this research to improve the accumulation of metallophthalocyanines (MPcs) based PS for PDT of human breast adenocarcinoma (MCF7).

1.3. Metallophthalocyanines (MPcs)

1.3.1 Properties and structure of MPc

Metallophthalocyanines (MPcs) are cyclic organic complexes composed of 4-isoindoline units linked by nitrogen atoms to form a macrocyclic ring structure (**Figure 1.5**), with central metals located within the cavity of the rings for metalated derivatives [60,61]. The central cavity of Pcs can accommodate over seventy metals and metalloids. In their metalated state, Pcs exhibit D_{4h} geometry, whereas their unmetalised counterparts (H_2Pc) exhibit D_{2h} symmetry. Substituents may be attached to the peripheral (β-positions) or non-peripheral (α-positions) of Pcs **Figure 1.5**. It has been established that the substitution design of the Pc has a substantial effect on the intermolecular – stacking and electronic coupling of the complex [62–65].

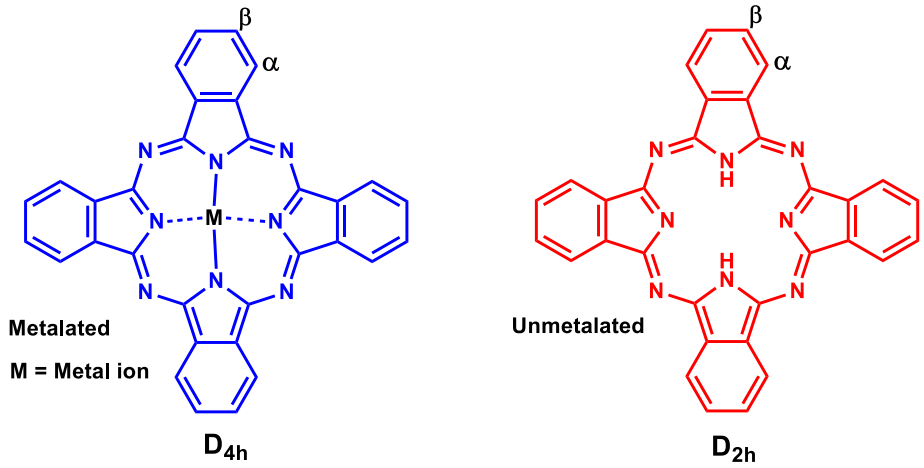

Figure 1.5: Molecular structures of Pc showing α- and β- positions with their geometrical confirmation: Metalated (D_{4h}) and Unmetalated (D_{2h}) symmetry.

The combination of the 18-π electron cloud system and the central metal in the Pcs cavity produces a strong absorption in the red region of the visible spectrum with a normally narrow Q-band (Q_{00} (D_{4h}); Q_1 and Q_2 (D_{2h})) accompanied by a weak vibronic bands Q_V **Figure 1.6**. Typically, an additional broad B-band around 300–350 nm is observed (**Figure 1.6**). Due to their exceptional stability, Pcs have found use in a variety of applications, including solar cells [66], electrocatalysis [67], nonlinear optics [68], and medicinal chemistry as PS agents in PDT for cancer treatment and PACT as antimicrobials [21,32,50,63,69,70]. Therefore, Pcs when alone and in combination with nanocarriers were employed as PSs for PACT or PDT in this thesis.

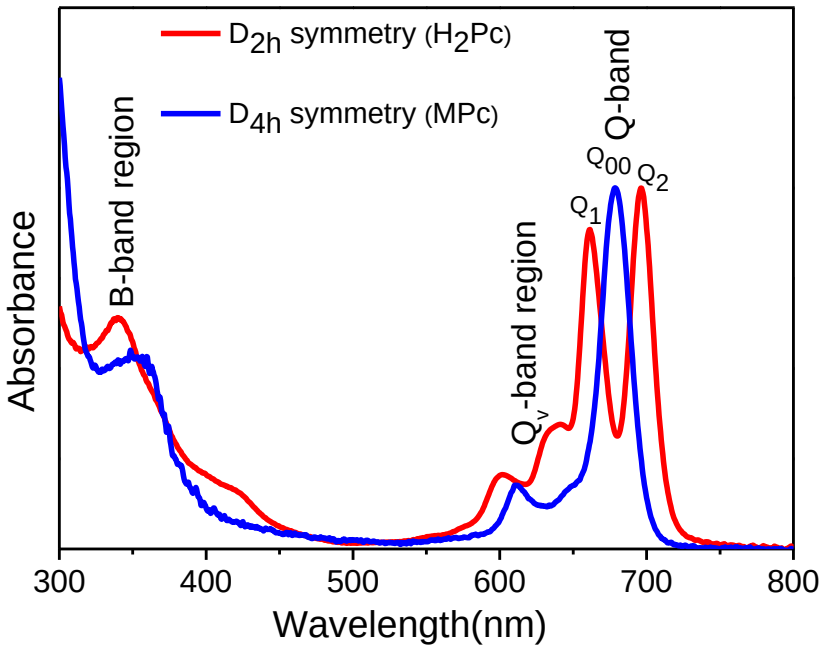

Figure 1.6: Typical absorption spectra of a free base H2Pc (red) and metalated Pc (blue).

1.3.2 Synthesis

Depending on their strategic formation, Pcs are either symmetrically or asymmetrically substituted. For a successful synthesis, it is necessary to take into account the nature of substituents on their precursor, the metal salt, the solvent, the temperature, and the catalyst [71–73]. In this work, both symmetric and asymmetric Pcs are employed.

1.3.2.1 Synthesis of symmetrical Pcs

There are several synthetic pathways using diverse precursors as starting materials that have been established for the synthesis of symmetrical Pcs, **Scheme 1.1**. This is typically accomplished using the cyclotetramerization reaction of (a) phthalonitriles, (b) o-cyanobenzamide, (c) phthalic acids, d) phthalamides, e) phthalimides (f) 1,3-diiminoisoindolines, and (g) phthalic anhydrides derivatives in the presence of a strong base such as 1,8-

diazabicyclo[5.4.0]undec-7-ene (DBU) [74,75]. Substituted phthalonitriles were explored in this study to improve the photo-physicochemical behaviour of the formed Pcs.

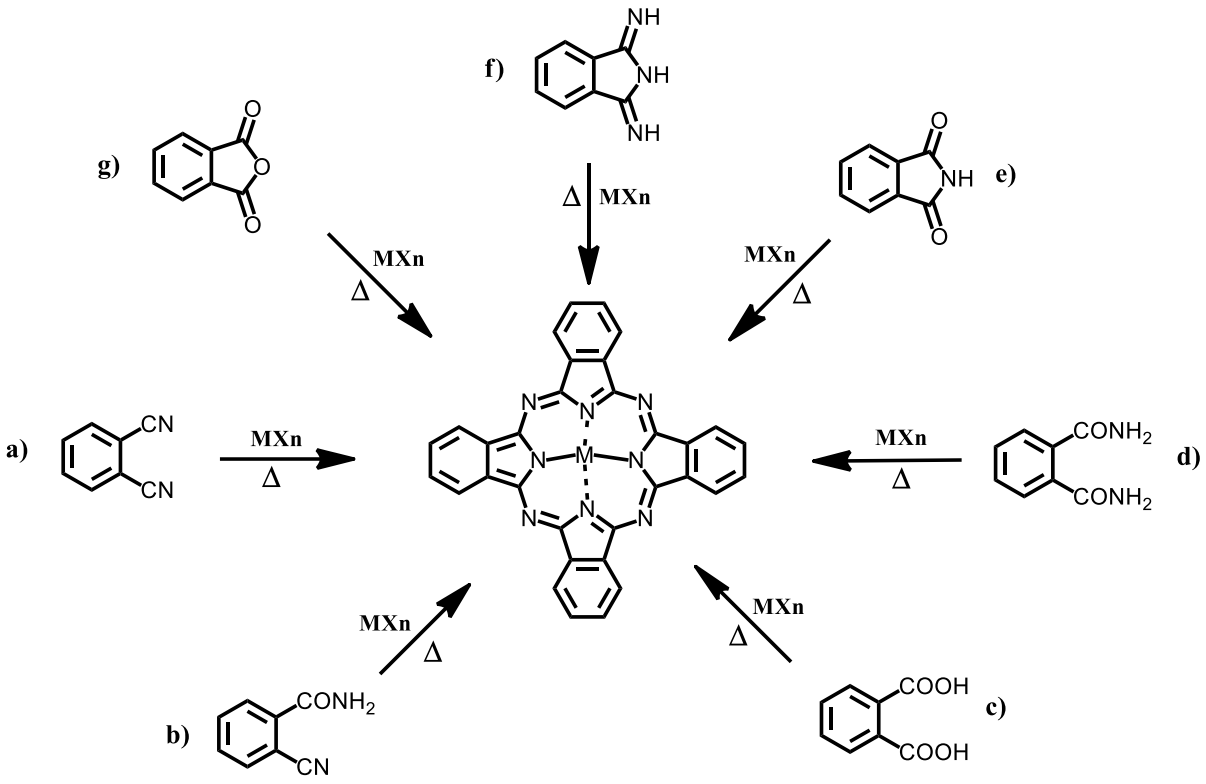

Scheme 1.1. Synthesis of Phthalocyanines from different precursors including, a) phthalonitriles, b) o-cyanobenzamide, c) phthalic acids, d) phthalamides, e) phthalimides, f) 1,3-diiminoisoindolines, and g) phthalic anhydrides derivatives.

1.3.2.2 Synthesis of asymmetrical Pcs

Asymmetrically substituted Pcs show distinct electrical and photophysical properties, enhanced solubility, and a reduced propensity to agglomerate compared to their symmetrically substituted counterparts. The intrinsic biological application potential of a Pc complex is enhanced by the coexistence of multiple functional groups while maintaining the

photophysical-chemical characteristics of symmetric Pcs. Asymmetric Pcs with donor-acceptor, hydrophilic, and hydrophobic moieties are synthesised in this work.

This study will investigate the structural conformation and physicochemical properties of A_3B-type asymmetric Pc derivatives. To synthesize A_3B-type compounds, one uses a non-selective method: cyclotetramerizing a mixture of two phthalonitriles with different substituents [76,77]. **Scheme 1.2** shows that this method yields a mixture of the six possible isomers of the Pc complex: AAAA, AAAB, AABB, ABAB, ABBB, and BBBB. Significant chromatographic procedures are required to isolate the target A_3B-complex from the statistical mixture of Pcs. The mole ratios of 3:1 or 9:1 (A: B) are common for asymmetrical Pcs. Higher mole ratios may also be used [77–79] depending on the reactivity of the different phthalonitrile precursors.

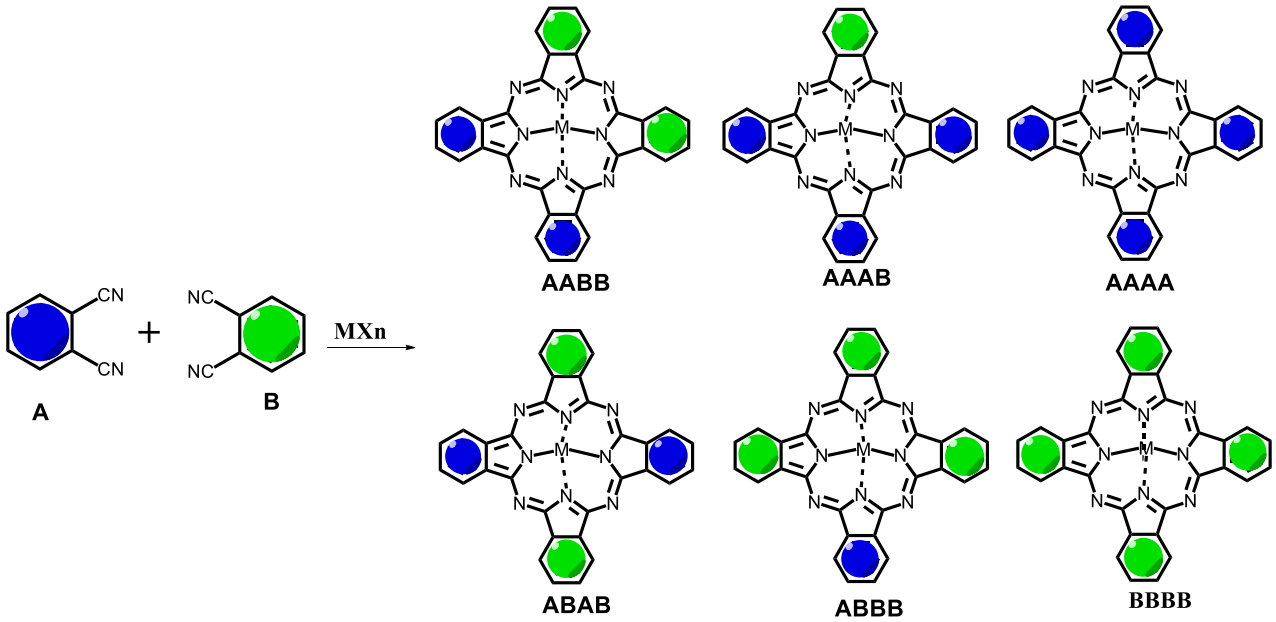

Scheme 1.2: Mixed synthesis of asymmetrical MPcs by the statistical condensation method.

1.3.3 Phthalocyanine aggregation

Pc complexes self-assemble into Pc aggregates, known as *H*-aggregates or *J*-aggregates [80–82], **Figure 1.7**. Van der Waals forces, hydrogen bonds, and π-stacking interactions, among others, hold the molecules together [83–86]. When compared to individual molecules (monomer), the resulting aggregates can exhibit special optical and electrical characteristics, making them desirable building blocks for a variety of applications [83,87,88]. The *J*-aggregate is created by a linear arrangement of Pc molecules via π-stacking interactions.

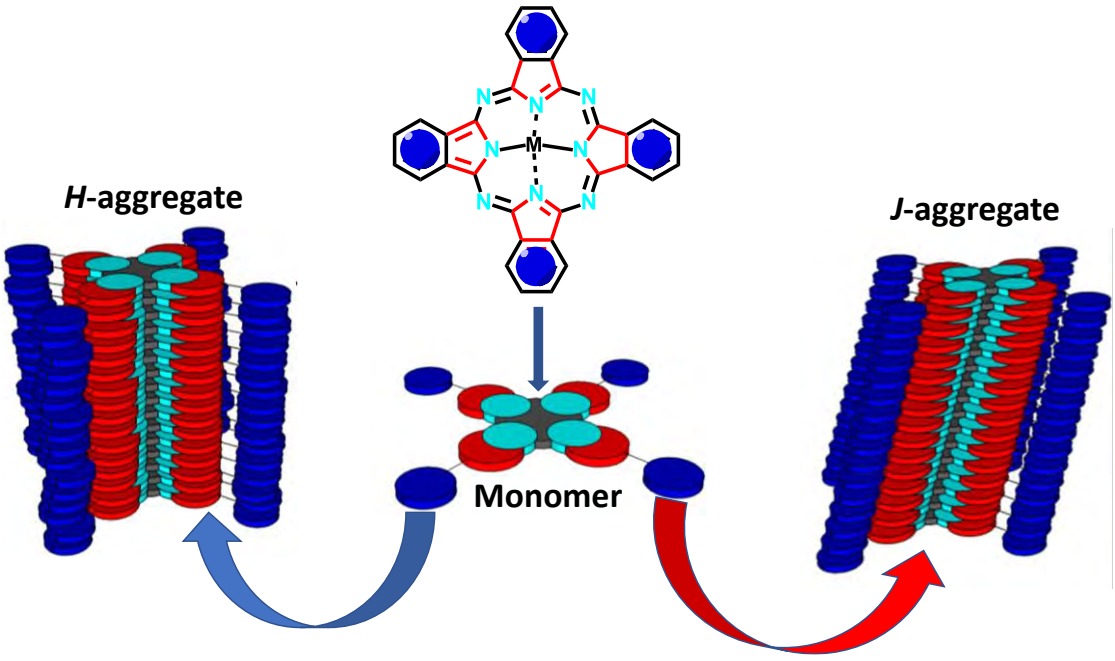

Figure 1.7: Self-assembly of Pc monomer into its Dipole stacking modes of *H*-aggregate and *J*-aggregate states.

The more common *H*-aggregates, on the other hand, are made of a more intricate arrangement of Pc molecules that involves hydrogen-bonding interactions, and π-stacking. *J*-aggregates are known to be photoactive, whereas *H*-aggregates are thought to be photoinactive in literature [80,81,89,90]. Because Pc aggregates are less soluble and have

poor localization and distribution, they are less effective as therapy agents, making them unattractive for PACT/PDT studies. The biological value of a Pc can be diminished if it aggregates. When Pcs get aggregated, their photoactivity and selectivity for particular target tissues or cells are both diminished. Pcs' aggregation status must be managed for optimal utilization in biological settings.

Factors that may affect the aggregation of Pcs include the type of central metal and its axial ligands and positions of the substituents on the perimeter of the Pc macrocycle, and the solvents used [91–94]. In this investigation, Pc complexes were synthesised, and structural modifications that reduce the influence of aggregation on PACT/PDT activity were considered, as described in the following sections.

1.3.4 Pcs used in this thesis.

One of the research interests in this work is characterising structural variables that optimise the photophysical-chemical properties and biological activity of Pcs as PDT/PACT agents. A number of strategies, such as the use of water-solubilising groups that promote improved optical properties through improved solubility, antibacterial/anticancer active targeting units to ensure effective Pc-drug localisation, and distribution in bacterial/cancer cells, were implemented to address some of the issues frequently encountered when using Pcs in PACT/PDT.

Bulky substituents can also inhibit Pcs from forming aggregates. This is because the Pc macrocyclic rings are unable to assemble due to the big substituents, which in turn increases the steric hindrance surrounding the rings. Hence, in this research, the use bulky cationic-based substituents to inhibit aggregation is reported. In order to connect to the negatively charged bacterial cell walls, the ideal PS (particularly for PACT) should be hydrophilic and have positive charges [69,95]. In this investigation, the addition of positively charged substituents to the already-formed Pc derivative is performed.

The Pc derivatives synthesised in this study are listed in **Table 1.1** with complex numbers ranging from ***1*** to ***13***. In this effort, symmetrical and asymmetrical Pcs were synthesised. Complexes ***4***, ***9***, ***10***, and ***11*** were synthesised in accordance with published reports [96–99], whereas complexes ***1***, ***1Q***, ***2***–***8***, ***8Q***–***11Q***, as well as ***12*** and ***13***, are first reported in this study.

Table 1.1 A: Synthesised Pcs for photophysicochemical properties and PACT or PDT applications

Symmetrical Pcs synthesised	
M = Zn(II) 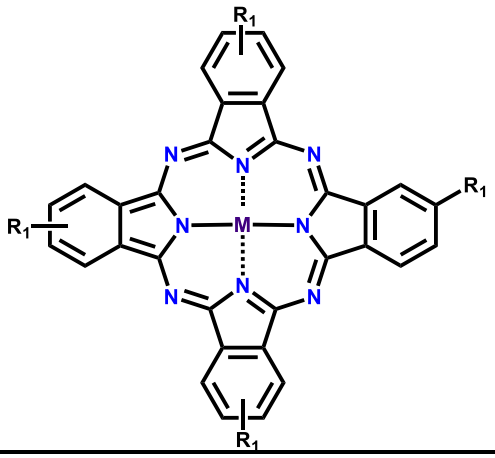	
Name of Pc complex and R_1 groups	
2, 9,16, 23-*Tetrakis*(2-(piperidin-1-yl) ethoxy) phthalocyanine ***1***, ***New*** 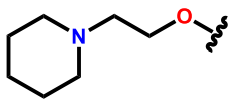	*Tetrakis* (ethane-2,1-diyl)) tetrakis(1-methylpiperidin-1-ium) phthalocyanine ***1Q***, ***New*** 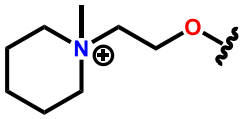
Tetra-phenoxy N, N-dimethyl-4-((methylimino) phthalocyanine ***2***, ***New*** 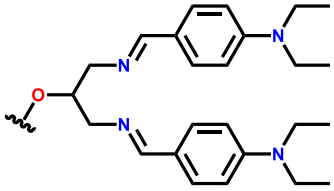	*Tetrakis N, N'*–Bis (4-(diethylamino) benzylidene) amino) propan-2-yl) oxy) phthalocyanine ***3***, ***New*** 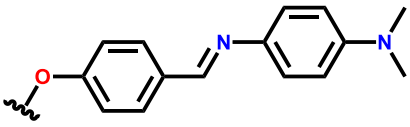
Tetrakis (2-formylphenoxy) phthalocyanine ***4*** [96] 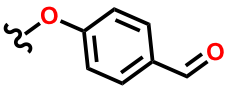	*Tetrakis*(1-butyl-4-(4(tetraphenoxy)styryl) pyridin-1-ium) phthalocyanine ***5***, ***New*** 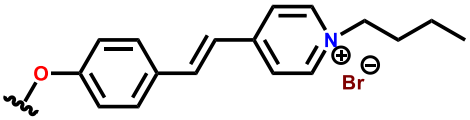

Tetrakis(4-(4-(tetraphenoxy)styryl)-1-(4-(triphenyl-phosphonio)butyl)pyridin-1-ium) phthalocyanine ***6***, ***New*** 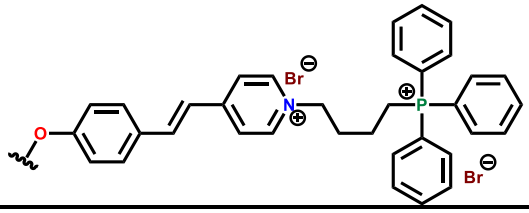	*Tetrakis* 4-(5-formylpyridin-2-yl)oxy) phthalocyanine ***7***, ***New*** 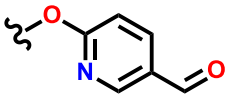
Tetrakis-1-butyl-4-(2-(6- (*tetra*phenoxy)pyridin-3-yl) vinyl)pyridin-1-ium phthalocyanine ***8***, ***New*** 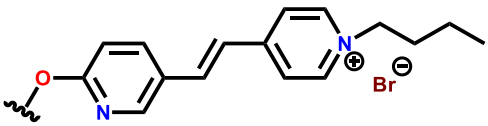	*Tetrakis* 1-butyl-5-(2-(1-butylpyridin-1-ium-4-yl)vinyl)-2-(*tetra*-phenoxy)pyridin-1-ium phthalocyanine ***8Q***, ***New*** 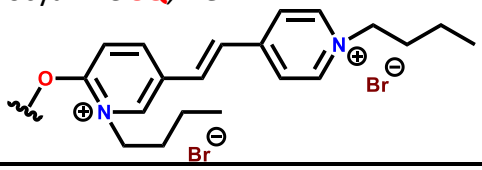
Tetra{4-(pyridin-4-yloxy) phthalocyanine ***9***, [97] 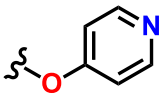	Tetra{4-(pyridin-3-yloxy) phthalocyanine ***10***, [99] 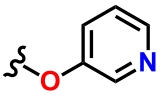
Tetra{4-(pyridin-2-yloxy) phthalocyanine ***11***, [98] 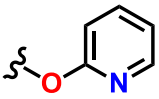	*Tetrakis* 3-(4-(4-pyridin-1-ium-1-yl) butyl)-2 mercapto-4,5-dihydrothiazol-3-ium phthalocyanine ***9Q***, ***New*** 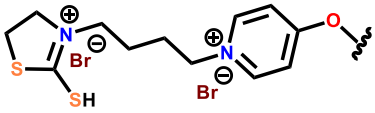
Tetrakis 3-(4-(3-pyridin-1-ium-1-yl) butyl)-2-mercapto-4,5-dihydrothiazol-3-ium phthalocyanine ***10Q***, ***New*** 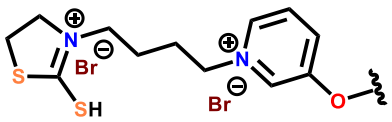	*Tetrakis* 3-(4-(2-pyridin-1-ium-1-yl) butyl)-2-mercapto-4,5-dihydrothiazol-3-ium phthalocyanine ***11Q***, ***New*** 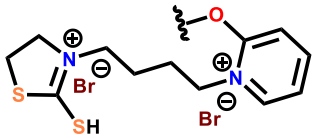

Table 1.1 A: Continued

Asymmetrical Pcs synthesised	
M = Zn(II) 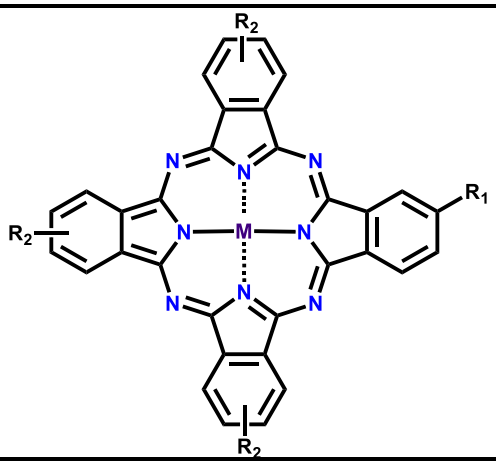	
Name of Pc complex, R_1 and R_2 groups	
3-(4-((3,17,23-tris(4-(Benzo(d)thiazol-2-yl] thiol) phthalocyanine-9-yl) oxy) phenyl) propanoic acid ***12***, ***New***	
R_1 = 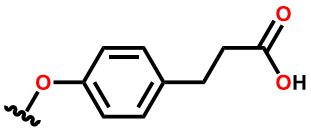	R_2 = 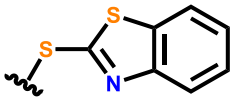
3-(4-(3,17,23-tris(3-(4-(triphenylphosphine) butyl) benzo[d]thiazol-3-ium bromide phthalocyanine-9-yl) oxy) phenyl) propanoic acid ***13***, ***New***	
R_1 = 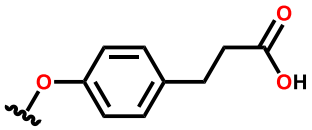	R_2 = 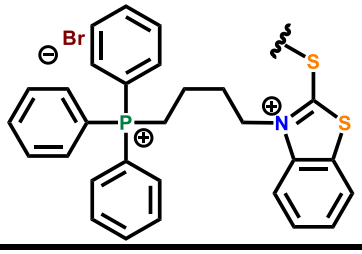

Table 1.1 B provides an overview of the categorisation of the synthesised Pcs into groups based on the applications to which they are put and the supporting materials they are linked with where applicable

Table 1.1 B

Complex	Nanoparticles	Biological molecule	Bacteria for PACT	PDT
1	SiNPs (Pc encapsulated)	Ampicillin and 1,3-propane sultone linked to SiNPs	*S. aureus* (planktonic)	No
1Q	SiNPs (Pc encapsulated)	Ampicillin and 1,3-propane sultone linked to SiNPs	*S. aureus* (planktonic)	No
2	SiNPs (Pc encapsulated)	Folic acid, linked to SiNPs	none	PDT
3	SiNPs (Pc encapsulated)	Folic acid, linked to SiNPs	none	PDT
4	none	none	*E. coli* planktonic	PDT
5	none	none	*E. coli planktonic*	PDT
6	none	none	*E. coli* planktonic	PDT
7	SiNPs (Pc encapsulated)	Gallic acid linked to SiNPs	*E. coli and S. aureus,* planktonic and biofilms	none
8	SiNPs (Pc encapsulated)	Gallic acid linked to SiNPs	*E. coli and S. aureus,* planktonic and biofilms	none
8Q	SiNPs (Pc encapsulated)	Gallic acid linked to SiNPs	*E. coli and S. aureus,* planktonic and biofilms	none
9	none	none	*E. coli and S. aureus,* planktonic and biofilms	none
9Q	none	none	*E. coli and S. aureus,* planktonic and biofilms	none
10	none	none	*E. coli and S. aureus,* planktonic and biofilms	none
10Q	none	none	*E. coli and S. aureus,* planktonic and biofilms	none
11	none	none	*E. coli and S. aureus,* planktonic and biofilms	none
11Q	none	none	*E. coli and S. aureus,* planktonic and biofilms	none
12	none	Pc linked to Ciprofloxacin	*S. pneumoniae and E. coli* Planktonic and biofilm	none
13	none	Pc linked to Ciprofloxacin	*S. pneumoniae and E. coli* Planktonic and biofilm	none

Based on the molecular design technique and component investigated, **Table 1.2** offers a logical grouping of the synthesised Pcs and nanomaterial.

Table 3.2: Synthesised particles and, when appropriate, their doped conjugates with SiNPs, as well as their functional suitability for PDT or PACT applications.

Pc complex grouped according to functionality.	**Pc complex**	**Other molecules**	**Supporting material(s)/compound**
Pcs loaded on Silica nanoparticles (SiNPs).	***1***, ***1Q, 2, 3 7***, ***8, 8Q***	—	SiNPs for transport- since ***1***,***2***,***3***,***7***,***8*** are not water soluble, ***1Q*** and ***8Q*** for comparison
Pcs used for both PACT (planktonic) and PDT.	***4***, ***5***, ***6***	none	Comparing PACT & PDT
Pc complexes linking to SiNPs containing cancer targeting molecules	***2, 3***	Folic acid	Transportation and targeting
Pc linking to SiNPs containing antimicrobial molecules	***1, 1Q***	Ampicillin & 1,3-propanesultone	Zwitter ionic (sultone) vs neutral ampicillin
	7, ***8*** &, ***8Q***	Gallic acid	Synergistic antibacterial effects of Pc@SiNPs**–GA**
Pcs linked directly linked with antimicrobial molecules	***12*** ,***13***	Ciprofloxacin	Synergistic antibacterial effects of Pc-antibiotic molecule
Effect of the number of cationic charges	***5*** with ***6***	none	Effect of the number of charges
	8 with ***8Q***	Gallic acid (GA)	Effect of the number of charges
Effect of the position number of the nitrogen group	***9***, ***10***, ***11***	none	Position of the group & effect of charge
	9Q, ***10Q***, ***11Q***	none	Position of the group & effect of charge
Effect of the type of bacteria	***7***, ***8***, ***8Q***	Gallic acid	*E. coli* vs *S. aureus*
	9, ***9Q***, ***10***, ***10Q***, ***11***, ***11Q***	none	*E. coli* vs *S. aureus*
	12 ,***13***	Ciprofloxacin	*S. pneumoniae* vs *E. coli*

Biofilms vs planktonic	***7***, ***8***, ***8Q***	Gallic acid	*E. coli* vs *S. aureus*
	9, ***9Q***, ***10***, ***10Q***, ***11***, ***11Q***	none	*E. coli* vs *S. aureus*
	12 ,***13***	Ciprofloxacin	*S. pneumoniae* vs *E. coli*

1.3.5 Pcs incorporated in nanomaterial

The presence of functional groups and nano delivery platforms offers efficient new options for the administration and specificity of Pcs, which could increase Pcs' effectiveness as antimicrobial and cancer treatment agents. Therefore, Pcs are loaded onto nanocarriers to improve their contact with bacterial (planktonic or biofilm) cells and cancer cells. SiNPs are used in this work and their importance will be discussed below. **Table 1.3** illustrates some of the Pcs that have been associated with different types of silica-based NPs. It has thus been reported in the literature [100–107] that SiNPs can be linked to bare/COOH/NH_2 substituted Pc derivatives, and that Pcs can be doped into SiNPs.

Table 1.3. Examples of Pcs linked with silica nanoparticles in literature.

Pc complex	Nanoparticle carrier	Surface modifications	Application & REF
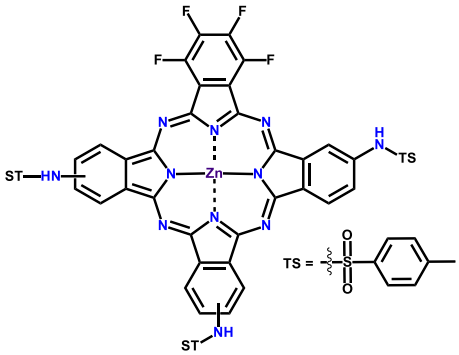 Tetrafluoro-9(10),16(17),23(24)-tri(tosylamino) phthalocyaninato zinc (II)	Fe_3O_4@SiNPs-NH_2-Pc (amide)	**Fe_3O_4@SiNPs-NH_2**	Water purification [100]
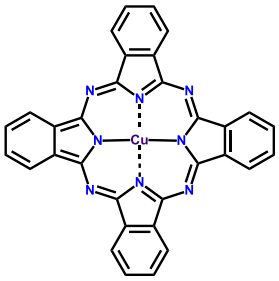 Cu (II) Phthalocyanine	CuPc/SiNPs dispersion	**Bare-SiNPs**	[106]
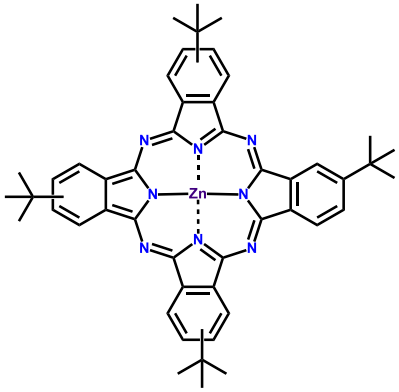 Tetra-tert-butyl zinc (II)	Pc@SiNPs	**APTES**	Photophysics [107]

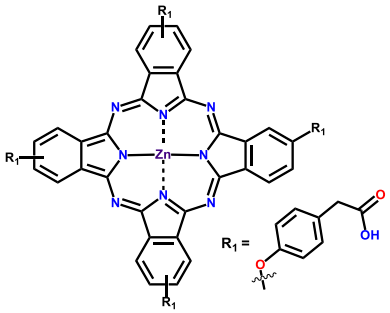 Phenoxy propanoic acid zinc phthalocyanine	Pc—SiNPs(amide)	**APTES**	PACT (planktonic) [103]
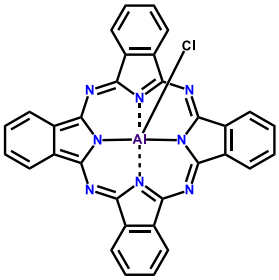 Aluminum chloride phthalocyanine	Pc@MSiNPs & Pc/Cisplatin@MSiNPs	**Bare-MSiNPs**	PDT & Chemotherapy [105]
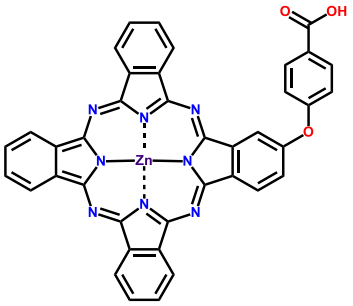 Zinc (II) phthalocyanine 1-phenoxy) benzoic acid	Pc-Doxorubicin@MSiNPs	**Bare-MSiNPs**	PDT & Chemotherapy [102]
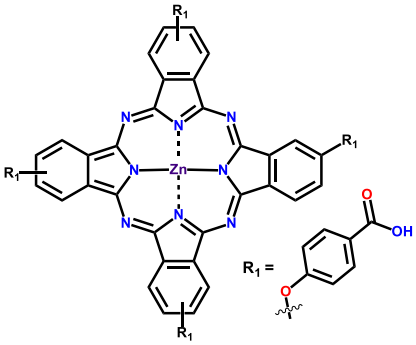 Tetra-substituted 4-carboxyphenoxyl and 3-carboxyphenoxyl Zn (II) phthalocyanine	Pc-SiNPs-NH_2(amide)	**APTES**	Photophysics [101]

MSiNPs = mesoporous SiNPs, APTES = (3-Aminopropyl) triethoxysilane, NP = nanoparticle

The table demonstrates that there are no Pcs encapsulated in SiNPs and used for PACT; this is the first time this has been documented for complexes ***1***, ***1Q***, ***7***, ***8***, and ***8Q*****.** Furthermore, no Pc has been encapsulated into SiNPs, linked to folic acid (FA) and applied as a cancer agent for PDT. This is done in this work with complexes ***2*** and ***3***. Finally, in this work, an asymmetrical Pc complex is directly coupled to the antibiotic ciprofloxacin (CIP) via the secondary amine of the latter's piperazine ring via an amide linkage for the first time.

1.4 Biomolecules used

Attachment of ampicillin (AMP) to penicillin-binding proteins (PBPs) inhibits cell wall peptidoglycan synthesis, thereby interfering with cell wall synthesis, hence enhances antimicrobial activity [108]. According to reports, gallic acid (GA) has a potent antibacterial effect that induces cell death by disrupting the membrane integrity of some gram-negative and gram-positive bacteria [109–111]. GA has been incorporated into SiNPs for bioactivity research [112,113]. Folic acid (FA) has a high affinity for folic receptors, which are recognised biomarkers for cancer cells due to their overexpression on a variety of cancer cells [114,115]. FA enhances PDT activity and photophysical behaviour of Pcs [116–118]. A combination of an anticancer prodrug encapsulated into SiNPs-FA has also been reported in the literature [119].

The antimicrobial activity of Pc@SiNPs-APTES after protonation of the NH_2 group in (3-aminopropyl) triethoxysilane (APTES) with 1,3-propanesultone (PSn) is investigated. PSn is a chemical compound with antimicrobial properties [120,121]. It is a sulfonate ester that can bind to nucleophiles such protein amino groups and DNA [122]. By changing cell membranes and metabolic processes, this procedure can render bacteria inert. PSn-protonated surfaces eliminate zwitterionic charges, thereby decreasing microbial adhesion.

This research includes the combination GA/PSn/AMP/FA, with SiNPs and Pc to enable passive targeting in PDT dependent on the surface moiety employed. There are no reports of Pc embedded in SiNPs followed by linking to PSn, AMP, and GA for PACT, and this is reported for the first time in this thesis. Furthermore, the exploration of a multidrug approach where Pcs and an antibiotic, ciprofloxacin (CIP), are directly linked and employed for PACT (towards biofilms and planktonic cells) is investigated.

1.5 Nanoparticles (NPs)

Nanoparticles (NPs) are particulates with one or more nanoscale dimensions (1–100 nm). Their superior physicochemical, optical, and thermal properties make them valuable functional materials for various technologies [123–125]. There are numerous varieties of NPs, including metallic and non-metallic NPs [126]. Mesoporous silica nanoparticles (MSiNPs) are a subject of this work and this is due to their interesting properties which will be highlighted below [127–129].

SiNPs are distinguished by their large specific surface area, simple synthesis and amplification, facile surface modification, and robust delivery [130,131]. MSiNPs are advantageous for biological applications due to their superior physicochemical properties, controlled distribution of drugs, biocompatibility, minimal toxicity, thermal stability, and adjustable pore sizes [132,133]. Mesoporous refers to particles with pore sizes ranging from 2 to 100 nm diameters. MSiNPs contain a complex 'worm-like' network of channels throughout their interior, resulting in a large surface area and an exceptionally high drug-loading capacity. MSiNPs are used as reservoirs for encapsulating Pcs because of their porous interior and large surface area.

By adjusting parameters such as NPs nucleation, growth, the pH of the reaction mixture, the characteristics of surfactants or copolymers, the concentrations, and sources of silica, SiNPs can be synthesised to have functional properties suitable for various applications including antimicrobials cargo carrier. Applications for dye-doped SiNPs in nonlinear optical materials, photonics materials, bioimaging applications, and biochemical analysis are documented [134–137]. In this work, many Pc derivatives were synthesised and packaged into SiNPs. Pcs that have been inserted into SiNPs can be protected against degradation by being enclosed [107,127]. To effectively fight infection, a Pc-based medication nanocarrier must successfully carry the antimicrobial agent to the targeted cell or tissue while also protecting its antimicrobial cargo.

To create Pc/dye-infused SiNPs, three basic synthetic methods could be used: direct micelle-assisted, Stober, and reverse microemulsion. In this work, the reverse micro-emulsion synthetic method was used to encapsulate the Pc complexes. Due to the abundance of accessible pores, MSiNPs may encapsulate both hydrophilic and hydrophobic molecules with comparable loading efficiency [138,139]. A solution of a Pc molecule, water, and aqueous ammonia are commonly combined with sufficient amounts of surfactant, cosurfactant, organic solvent, to form a micro-emulsion solution [140].

Pc-doped SiNPs are modified with amino groups (Pc@SiNPs-NH_2) through the self-assembly of (3-aminopropyl) triethoxysilane (APTES) onto the surfaces of Pc@SiNPs particles. In this study, the effects of surface modification of Pc@SiNPs-APTES is investigated.

1.6. Photophysics and Photochemistry

The photophysicochemical properties of Pcs are depicted in **Figure 1.1** using the Jablonski diagram. The electronic transitions of Pcs depend on the symmetry of the molecule, the

nature of the substituents, and the intermolecular interactions. In this work, the photophysical and photochemical properties of the PS were conducted including fluorescence (Φ_F), triplet (Φ_T) and singlet oxygen (Φ_Δ) quantum yields along with fluorescence (τ_F) and triplet (τ_T) lifetimes.

1.6.1 Fluorescence quantum yield (Φ_F) and fluorescence (τ_F) lifetimes

Fluorescence quantum yield (Φ_F) quantifies the number of photons emitted per photon of excitation absorbed [141]. Moreover, the fluorescence lifetime (τ_F) measures the average time fluorophores spend in the excited singlet state. Several factors have been reported to affect the Φ_F of Pcs, including the nature of the solvent, the pH, the aggregation, the temperature, and the nature of the central metal. In this study, a comparative method based on equation **1.1** [142] was used to determine the Φ_F of Pcs and its doped SiNPs conjugates, with unsubstituted ZnPc serving as the standard for Pcs in dimethyl sulfoxide (DMSO) (Φ_F = 0.2 [143]).

$$\Phi_F = \Phi_F^{std} \frac{F\ A^{std} n^2}{F^{std} A\ n^{2\ std}} \qquad (\mathbf{1.1})$$

where Φ_F and Φ_F^{std} stand for the sample's and the standard's fluorescence quantum yields, respectively. The fluorescence area under emission curves for the sample and the standard, referred to as F and F^{std}, respectively. The sample's and the standard's absorbances at the excitation wavelength are A and A^{std}, respectively. The refractive indices of the solvents used to prepare the sample and the standard preparation are n and n^{std}, respectively. Because there is no spin change involved in the transition from S_1 to S_0, fluorescence is a the short lived process, with a half-life of 10^{-8} seconds [144]. Φ_F are further reduced in the presence of

paramagnetic metals and typically metals with a high atomic number; this phenomenon is attributed to the heavy atom effect [145]. Using the time–correlated single–photon counting (TCSPC) system [146], the fluorescence lifetime of all Pcs and their conjugates can be determined.

1.6.2 Triplet quantum yield (Φ_T) and triplet lifetime (τ_T)

The triplet quantum yields (Φ_T) quantify the fraction of absorbing Pcs that undergo intersystem crossing (ISC) to populate the triplet state. The lifetime of the triplet state (τ_T) is the average duration Pcs spend in the excited triplet state (T_1). Using laser flash photolysis, triplet state properties, τ_T and Φ_T, of the Pcs are typically determined. Laser flash photolysis entails rapidly introducing an intense light pulse into a Pc solution using a laser source. The instrument monitors the change in Pc absorption from excited triplet state (T_1), **Figure 1.1**, as a function of time in order to calculate the τ_T [147]. The Φ_T values of the Pcs alone and in conjugates were calculated using a comparative method as described in the scientific literature, equation **1.2** [148,149]:

$$\Phi_T = \Phi_T^{std} \frac{\Delta A_T \varepsilon_T^{std}}{\Delta A_T^{std} \varepsilon_T} \qquad (\mathbf{1.2})$$

where Φ_T^{std} is the triplet quantum yield of the ZnPc standard (Φ_T^{std}= 0.65 in DMSO [149]), ΔA_T and ΔA_T^{std} are the changes in the triplet state absorption of the sample and standard, and ε_T and ε_T^{std} are the triplet state molar extinction coefficients of the sample and standard, respectively. ε_T and ε_T^{std} were determined utilizing Equation **1.3a** and **1.3b**.

$$\varepsilon_T = \varepsilon_S \frac{\Delta A_T}{\Delta A_S} \qquad (\mathbf{1.3a})$$

$$\varepsilon_T^{std} = \varepsilon_S^{std} \frac{\Delta A_T^{std}}{\Delta A_S^{std}} \qquad (\mathbf{1.3b})$$

where ε_S and ε_S^{std} is the sample's or the standard's singlet state molar extinction coefficient, respectively. ΔA_s and ΔA_S^{std} are the changes in singlet state absorbances of the sample and standard, respectively. The variations in the singlet state absorbances of the standard and the measured sample are obtained by fitting the triplet state absorption data (**Figure 1.8**).

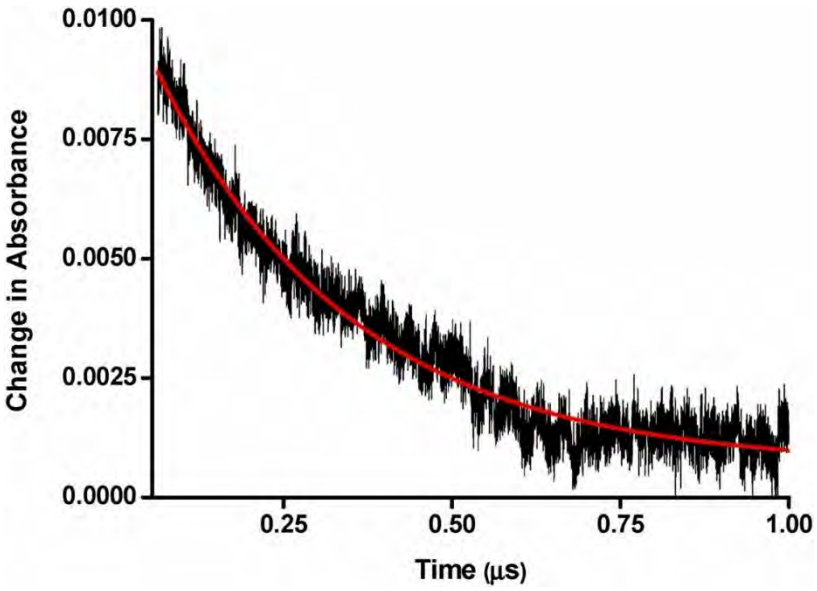

Figure 1.8 : Fitted excited triplet state absorption decay curve [103].

1.6.3 Singlet oxygen (Φ_Δ) quantum yield

The amount of singlet oxygen a PS can produce, also referred to as the singlet oxygen quantum yield (Φ_Δ), serves as a measure of its efficacy. Singlet oxygen, a reactive form of oxygen, is produced during numerous photochemical processes. A unitless number between 0 and 1 is used to express Φ_Δ, with larger values signifying greater efficiency. Φ_Δ is a crucial element in figuring out how well photosensitizers function in PACT/PDT.

Spectroscopic methods, such as time-resolved absorption, fluorescence, or phosphorescence studies, are generally used to measure Φ_Δ [150]. In this thesis, the chemical approach was used. This procedure uses singlet oxygen scavengers that such as 1,3 diphenylisobenzofuran (DPBF) in organic media or anthracene-9,10-bismethylmalonate (ADMA) in aqueous media. Spectroscopic techniques are used to track the singlet oxygen scavenger's deterioration [151,152].

With the aid of equation (**1.4**), the singlet oxygen quantum yield was quantified.

$$\Phi_\Delta = \Phi_\Delta^{std} \frac{R \,.\, I_{Abs}^{std}}{R^{std} . I_{Abs}} \qquad (\mathbf{1.4})$$

where Φ_Δ^{std} is the standard's singlet oxygen quantum yield (ZnPc, Φ_Δ^{std}= 0.67 in DMSO [153]). R^{std} and R are the photobleaching rates of ADMA or DPBF in the presence of a standard and a measured sample, respectively. I_{Abs} and I_{Abs}^{std} are the rates of light absorption by the Pcs and the standard, respectively. I_{Abs} and I_{Abs}^{std} are calculated using equations (1.5a) and (1.5b), respectively.

$$I_{Abs} = \frac{\alpha.A.I}{N_A} \qquad (\mathbf{1.5a})$$

$$I_{Abs}^{Std} = \frac{\alpha^{Std}.A.\ I}{N_A} \qquad (\mathbf{1.5b})$$

where $\alpha = 1 - 10^{-A(\lambda)}$, $A(\lambda)$ is the absorbance of PS at the excitation wavelength, *A* is the illuminated cell area (expressed in cm^2), *I* is the intensity of light (expressed in photons cm^{-2} s^{-1}) and N_A is the Avogadro's constant.

1.7 Summary of aims of thesis

1. First, symmetrical, and asymmetrical phthalocyanines were synthesised and characterised.
2. Doping of phthalocyanines into silica nanoparticles using reverse microemulsion and their surface functionalisation with APTES, FA, GA, PSn and AMP.
3. Study of in-solution photophysical and photochemical studies of phthalocyanine complexes and their conjugates.
4. Study of *In vitro* cytotoxicity, photodynamic therapy, and photoantimicrobial chemotherapy activities of phthalocyanines and their silica nanoparticle analogues.

CHAPTER TWO
EXPERIMENTAL

2.1 Materials

2.1.1 General reagents

Absolute ethanol (EtOH), cyclohexane, chloroform, dichloromethane (DCM), dimethylformamide (DMF), tetrahydrofuran (THF), deuterated dimethyl sulfoxide (DMSO-d_6), deuterated methanol (MeOH-d_4), spectroscopic dimethyl sulfoxide (DMSO), methanol (MeOH), ethyl acetate (EtOAc), tetrahydrofuran (THF), 1-octanol, toluene, pentanol, and piperidine were purchased from Sigma Aldrich. Highly purified water was obtained through installed water purifying system from ELGA, Veolia water PURELAB, flex system (Marlow, UK). Nitric acid, sulfuric acid, diethyl ether (Et_2O), acetone and 25% ammonium hydroxide, diethyl ether were obtained from SAARCHEM®.

2.1.2 Chemicals and reagents used for PDT and PACT cell studies

E. coli (ATCC 25922), *S. aureus* (ATCC 25923) and *S. pneumoniae* (ATCC 13883) were purchased from Microbiologic USA. Agar bacteriological BBL Muller Hinton broth and nutrient agar were obtained from Merck. Phosphate buffer saline (PBS; 10 Mm; pH 7.4) was prepared using appropriate amounts of Na_2HPO_4, KH_2PO_4 and chloride salts. Glutaraldehyde, iron ferricyanide, iron ferrocyanide and potassium chloride, crystal violet, and tryptic soy were purchased from Sigma Aldrich. MCF-7 breast cancer cells were acquired from Cellonex. Dulbecco's phosphate-buffered saline (DPBS) and Dulbecco's modified Eagle's medium (DMEM) were obtained from Lonza, 10% (v/v) heat-inactivated fetal calf serum (FCS), 100 mg per mL-penicillin-100 unit per mL-streptomycin-amphotericin B mixture were obtained from Biowest®.

2.1.3 Chemicals reagents for phthalonitrile precursors, phthalocyanine syntheses and doping to SiNPs and their surface functionalisation

3-Aminopropyl-triethoxysilane (APTES), ampicillin (AMP), ciprofloxacin (CIP), 1.3-propane sultone (PSn), folic acid (FA), gallic acid (GA), tetraethyl orthosilicate (TEOS), 1,8-diazabicyclo [5.4.0] undec-7-ene (DBU), dicyclohexylcarbodiimide (DCC), 2-(piperidin-1-yl)ethan-1-ol, methyl iodide, N-ethyl-N'-(3-dimethylaminopropyl) carbodiimide hydrochloride (EDC), zinc acetate ($Zn(OAc)_2$), N-hydroxysuccinimide (NHS), 4-dimethylaminopyridine (DMAP), 2-hydroxy-5-formylpyridine, Triton X-100, n–pentanol, n–hexanol, sodium hydride, toluene, 4-nitrophthalonitrile, 2-thiazoline-2-thiol, 4-methyl pyridine, potassium carbonate, 1-bromobutane, 1,3-diamino-2-propanol, and 4-(diethylamino)benzaldehyde were obtained from Sigma Aldrich®. 1-butyl-4-methylpyridin-1-ium bromide (**PyB**), 4-methyl-1-(4-(triphenylphosphonio) butyl) pyridin-1-ium bromide (**PyBP**), and 3-(4-bromobutyl)-2-mercapto-4,5-dihydrothiazol-3-ium bromide (**BMDBr**) were synthesised using literature [154,155] with slight modifications.

2.1.4 Chemicals and reagents for photophysicochemical studies

Unsubstituted zinc phthalocyanine (ZnPc), 1,3-diphenylisobenzofuran (DPBF), and anthracene–9,10–bis–methylmalonate (ADMA) were obtained from Sigma Aldrich®. Aluminium sulfonated phthalocyanine, a mixture of sulfonated derivatives (AlPc-Smix) was synthesised as reported in the literature [156].

2.2 Instrumentation

1. Electronic absorption spectra in the ground state were acquired using either a Shimadzu® UV–2550 spectrometer (solution sample measurements) or a Perkin–

Elmer® UV/Vis/NIR spectrometer over the wavelength range of 250 nm–2500 nm (solid sample measurements).

2. Magnetic circular dichroism (MCD) spectra were measured with a Chirascan plus spectrodichrometer equipped with a 1 T (tesla) permanent magnet by using both the parallel and antiparallel fields.
3. Mass spectra data of Pcs were acquired on a Bruker® Auto FLEX III Smart-beam TOF/TOF mass spectrometer using α-cyano-4-hydrocinnamic acid or dithranol as MALDI matrix.
4. FT–IR spectra were acquired on a Bruker® ALPHA FT–IR spectrometer with universal attenuated total reflectance (ATR) sampling accessory.
5. The proton nuclear magnetic resonance (^{1}H NMR) spectra of phthalonitriles and Pcs were acquired on a Bruker® AMX 80 MHz, 400 MHz, or 600 MHz spectrometer.
6. The Vario-Elementar® Microcube ELIII Series elemental analyser (CHNS) was used to collect data on Pcs's elemental composition (carbon, hydrogen, nitrogen, and sulfur).
7. A Varian Eclipse® spectrofluorometer with a 360–1100 nm filter was used to detect the fluorescence excitation and emission spectra. At the wavelength where the emission maximum occurred, excitation spectra were obtained.
8. Using a time-correlated single-photon counting setup (TCSPC) (FluoTime 300, Picoquant GmbH) and a diode laser (LDHP-670, Picoquant GmbH, 20 MHz repetition rate, 44 ps pulse width), the fluorescence lifetimes were determined. Under the magic angle, fluorescence was found with the help of a peltier-cooled photomultiplier tube (PMA-C 192-N-M, Picoquant®) and integrated electronics (PicoHarp® 300E, Picoquant GmbH). An 8 nm monochromator was used to choose the frequency of the emission.

The system's reaction function was measured with a scattering Ludox solution (DuPont®), and it had a full width at half maximum (FWHM) of about 300 ps. The stop-to-start pulse ratio was kept low (0.05) for good data. All decay curves of luminescence were recorded at the wavelength of maximum emission. The results were looked at by FluoFit (Picoquant®). The support plane method calculated errors in the decay time [141].

9. To determine triplet quantum yields and lifetime, we utilised a laser flash photolysis system that included an Andor DH320T-25F03 ICCD camera and an LP980 spectrometer with a PMT-LP detector. A Tektronix TDS3012C digital storage oscilloscope was used to capture the signal from a PMT detector. The excitation pulses came from a tunable laser system that used a Nd: YAG laser (355 nm, 135 mJ/46 ns) to pump a 420-2300 nm (NT-342B, Ekspla) optical parametric oscillator (OPO, 30 mJ/35 ns).

10. Analysis of the singlet oxygen quantum yield was carried out with a tunable laser system that consisted of a Nd: YAG laser (355 nm, 135 mJ/4–6 ns) pumping an optical parametric oscillator (OPO, 30 mJ/3–5 ns) with a wavelength range of 420–2300 nm (NT-342B, Ekspla), with the excitation wavelength set to 670-675 nm.

11. The synthesised Pc complexes and nanomaterial were extracted from solvent system following purification of unreacted material using an Eppendorf Centrifuge 5810, equipped with medium to high-throughput applications reaching speeds of up to 14,000 rpm and includes a A-4-62 swing out rotor with a max. speed of 4000 Rpm. The Pc@SiNPs material were washed at 3500 Rpm for five mines per interval and followed by filtration using standard glass filters.

12. Transmission electron microscope (TEM) ZEISS® LIBRA model 120 operating at 90 kV and iTEM® software were used to investigate the size distribution of the Pc-doped SiNPs.

13. Experiments involving dynamic light scattering (DLS) and zeta potential were carried out with a Malvern Zetasizer Nano Series, Nano-ZS90.

14. For the purpose of determining the surface area and porosity of the doped SiNPs, the Brunauer–Emmett–Teller (BET) approach was applied. The surface areas and pore sizes of the Pc@SiNPs analogues were obtained from the nitrogen adsorption/desorption isotherms using a surface and porosity analyser operated at 77K (Micrometrics ASAP® 2020).

15. The illumination for the PACT/PDT study was obtained using a Modulight ML7710-680-RHO laser system with a probe with a wavelength of 680 nm and a power output of 524 mW/cm^{-2}. The system is equipped with a cylindrical output channel, aiming beam, integrated calibration module, foot/hand switch pedal, fibre sensors (subminiature version A) connectors and safety interlocks.

16. Sterilization of PDT disposables and autoclaving of nutrient broth, nutrient agar and phosphate buffer and other various apparatus for PACT studies were done using an Autoclave RAU®–530D.

17. The culturing and incubation processes for bacterial cell for PACT studies were performed using the thermostatic oven.

18. Scan® 500 automatic colour colony counter was utilised to determine the colony forming units (CFU)/mL of the bacteria.

19. The homogenization of the bacteria suspension was done using PRO VSM-3 Lab plus Vortex mixer.

20. The cells for PDT were cultured in humidified atmosphere incubator with ~5% CO_2 and physiological temperature at 37 °C (HealForce®).

21. The cell viability for PDT studies was measured using a WST–1 cell proliferation neutral red reagent (Roche®) with a Synergy 2 multi-mode microplate reader (BioTek®).

22. A Bruker Vertex 70 Ram II Raman spectrometer (equipped with a 1064 nm Nd: YAG laser and liquid nitrogen cooled germanium detector) was used to measure the antimicrobial activity and the successful formation of biofilm cells on the ITO-glass slide surface. Signals from 50–60 mW of 1064 nm laser were recorded in the spectral range 600–1800 cm^{-1} collected.

23. Scanning electron microscopy (SEM) was used to study the distribution of *E. coli*, *S. pneumoniae* and *S. aureus* biofilms. The samples for SEM analysis were prepared by rinsing the biofilm attached ITO-glass slide samples gently with PBS (pH 7.2) several times and then fixed using 2.5% glutaraldehyde in 0.1 M PBS (pH 7.2) for 4 h at 4 °C. The fixed samples were dehydrated in increasing concentrations of ethanol (30%, 50%, 70%, 80%, 90%, 95%, and 100%) for 5 min (30-95%) and (100%) 10 min. Subsequently, the biofilms were preserved using evaporated carbon by critical point freezing, this was done as follows liquid CO_2 was used for dehydrating the wet samples, since it possesses lower critical point (73.8 bar, 31 °C). As far as the water and ethanol are concerned, critical point is around 228.5 bar, 374 °C and 60.8 bar, 241 °C, respectively. Following this, the samples were coated with sputtered gold and analysed under secondary

electron images in a high vacuum on a Tescan Vega 2 Scanning Electron Microscope with a W-filament. Secondary electron images (SE) were collected in high vacuum on a Tescan Vega 2 Scanning Electron Microscope with a W-filament at 5 kV.

24. The Electrochemical impedance spectroscopy (EIS) experiments were performed between 0.1 and 100000 Hz, using 0.01 VRMS sinusoidal modulation. A non-linear least squares (NLLS) method based on the EQUIVCRT program was used for automatic fitting of the obtained EIS data. A three-electrode electrochemical cell made up of indium doped tin oxide (ITO) as the working electrode, %1-DMSO/PBS was used as electrolyte for Pc complexes, platinum wire (Pt) as the counter electrode and silver|silver chloride (in 3.0 M KCl) |(Ag|AgCl) as reference electrode was used. Cyclic Voltammetry (CV) studies were performed on a potential window of -0.35 to 0.60 V vs Ag/AgCl in ferro-ferricyanide using an Autolab Potentiostat PGSTAT30 equipped with Nova software version 2.1.

25. Time-of-Flight-Secondary Ion Mass Spectrometer (TOF-SIMS) data was recorded with ION TOF GmbH TOF SIMS 5 – 100 runs in micro-raster mode. The raster area was 3000 µm x 3000 µm, and the sample was run in both positive and negative ion modes. The analyser was set to a standard operating mode with a cycle time of 100 µs, whilst the primary beam was a Bi_3 ion cluster gun with a current of 0.40 pA and an energy of 3000 eV (termed as spectrometry mode). The Bi_3 cluster and electron flood gun was used to get a better ion signal from the sample. Charge compensation was used to account for the electron flood gun. The raw data was processed using the Surface Lab 6.5 software provided by ION TOF.

2.3 Syntheses of phthalonitriles and phthalocyanines

The synthetic pathways for the phthalonitriles, precursor—substituents and phthalocyanines are shown in **Schemes 3.1–3.6**.

2.3.1 Phthalonitriles and other precursors

2.3.1.1 4-(3-(Piperidin-1-yl) ethanoxy) phthalonitrile (*A*) (Scheme 3.1).

4-Nitrophthalonitrile (2.5 g, 14.45 mmol) and 2-(piperidin-1-yl) ethan-1-ol (1.9 g, 9.16 mmol) were dissolved in DMF (15 mL) under nitrogen atmosphere and the mixture was stirred at ambient temperature for 15 min. Potassium carbonate (4.4 g. 31.84 mmol) was added thereafter, and the mixture was left to stir further at ambient temperature for 48 h. The mixture was then added to ice water (200 mL). The resulting precipitate was filtered off, washed with water, air dried and recrystallised from methanol to give 4-(3-(piperidin-1-yl) ethanoxy) phthalonitrile (***A***). Yield = 43 %: IR (cm^{-1}): 2931(C-N 2° amine), 2841(C–H aromatic), 2779 (aliphatic C—H), 2225 (nitrile C≡N), 1621, 1523 (C=C), 1265, 1253, 1093 (C–O–C), 919−732 (C—C). ^{1}H NMR (400 MHz, DMSO-d_6): δ (ppm) 8.24 (d, *J* = 8.64 Hz, 1H, aromatic–H), 7.46 (dd, *J* = 8.8, 2.0 Hz, 1H, aromatic–H), 7.29 (s, 1H, aromatic–H), 4.23 (t, *J* = 5.6 Hz 2H, CH_2), 2.68 (t, *J* = 5.6 Hz, 2H, CH_2), 2.50 (s, 4H, piperidine−CH_2), 1.47 (m, 4H, piperidine−CH_2), 1.36 (s, 2H, piperidine−CH_2). MALDI TOF MS m/z: Calculated: 255.14, found 256.38 $[M+H]^+$. Calcd for $C_{15}H_{17}N_3O$: C (70.56), H (6.71), N (16.46), found C (69.03), H (5.74), N (15.98).

2.3.1.2 *N, N'*–bis (4-(diethylamino) benzylidene) amino) propan-2-ol (*B*), (Scheme 3.2).

4-(Diethylamino) benzaldehyde (0.5 g, 2.82 mmol) was dissolved in 20 mL ethanol, 1,3-diamino-2-propanol (0.13 g, 1.45 mmol) was then added to the solution in presence of catalytic amount of acetic acid. The reaction mixture was purged with argon and left to stir

under reflux for 8 h. The progress of the reaction was monitored by thin layer chromatography (TLC) ($CHCl_3$/EtOH 10/0.1). After the reaction completed, the solution was evaporated to 1/3 vol. The formed precipitate was filtered off, washed with ethanol and dried in vacuum desiccators. Yield: 75% (0.43 g). IR (cm^{-1}): 3440 (O–H), 3103 (aromatic C—H), 2973–2810 (aliphatic C—H), 1635 (C=N), 1591 (aromatic C=C), 1268 (C–OH). ^{1}H NMR (400 MHz, DMSO-d_6): δ (ppm) 8.09 (s, 2H, alkene), 7.52 (d, 4H, aromatic–H), 6.67 (d, 4H, aromatic–H), 4.60 (s, H, OH), 3.89 (s, 1H, CH), 3.65 (t, 2H, CH_2), 3.42 (t, 2H, CH_2), 3.36 (q, 8H, CH_2), 1.10 (m, 12H, CH_3).

2.3.1.3 *N, N'*–bis (4-(diethylamino) benzylidene) amino) propan-2-yl) oxy) phthalonitrile (*C*), (Scheme 3.2).

N, N'–bis (4-(diethylamino) benzylidene) amino) propan-2-ol ***B***, (0.4 g, 0.98 mmoL) was dissolved in DMF (30 mL). NaH (0.047 g, 1.95 mmol) and 4-nitrophthalonitrile (0.17 g, 0.98 mmol) were added to the reaction mixture. The temperature was brought up to 60 °C and kept at this value for 24 h under nitrogen atmosphere. The progress of the reaction was monitored by thin layer chromatography (TLC) ($CHCl_3$/EtOH 10/0.1). The product was precipitated out by pouring into ice-water mixture. The formed precipitate was filtered off. The crude product was washed with hot water, ethanol, and dried in vacuum desiccator. Yield: 42% (0.25 g). IR (cm^{-1}): 3071 (aromatic C—H), 2969–2918 (aliphatic C—H), 2224 (nitrile C≡N), 1666 (imine), 1596, 1517 (aromatic C=C 1254, 1158 (aromatic–O–aromatic).^{1}H NMR (400 MHz, DMSO-d_6): δ (ppm) 9.62 (s, 2H, imine), 8.11 (s, 1H, aromatic–H), 7.91 (d, 1H, aromatic–H), 7.79 (d, 1H, aromatic–H), 7.65 (d, 2H, aromatic–H), 7.46 (d, 2H, aromatic–H), 6.76 (d, 2H, aromatic–H), 6.64 (d, 2H, aromatic–H), 5.14 (s, H, CH), 3.96 (t, 2H, CH_2), 3.76 (t, 2H, CH_2), 3.45 (q, 8H, CH_2), 1.08–1.13 (m, 12H, CH_3). MALDI TOF MS m/z: Calculated: 534.31, found 534.68

$[M + H]^+$. Calcd for $C_{33}H_{38}N_6O$: C (74.13), H (7.16), N (15.72), found C (73.68), H (7.74), N (15.18).

2.3.1.4 Synthesis of 4-((5-formylpyridin-2-yl) oxy) phthalonitrile (*D*), (Scheme 3.4).

4-Nitrophthalonitrile (2.5 g, 14.45 mmol) and 2-hydroxy-5-formylpyridine (1.9 g, 15.43 mmol) were dissolved in DMF (15 mL) under nitrogen atmosphere and the mixture was stirred at ambient temperature for 15 min. Potassium carbonate (4.4 g. 31.84 mmol) was added thereafter, and the mixture was left to stir further at 70 °C for 48 h. The mixture was then added to ice water (200 mL). The resulting precipitate was filtered off, washed with water, air dried and recrystallised from methanol to give 4-((5-formylpyridin-2-yl) oxy) phthalonitrile. Yield = 53%: IR (cm^{-1}) at 3126-3003 (aromatic C—H), 2212 (nitrile C≡N), 1596 (aromatic C=C), 1231 cm^{-1} (C–O–C): ^{1}H NMR (400 MHz, DMSO-d_6): δ (ppm), 8.25 (s, 1H, COH), 7.90-7.79 (1H, aromatic—H), 7.63–7.60 (d, *J* = 7.61 Hz, 1H, aromatic—H), 7.50–7.31 (m, 2H, aromatic—H), 7.27–7.21 (d, *J* = 7.25 Hz, 1H, aromatic —H), 7.13 (d, 1H, aromatic—H).

2.3.1.5 Synthesis 1-butyl-4-methylpyridin-1-ium bromide (PyB) 4-methyl-1-(4-(triphenylphosphonio) butyl) pyridin-1-ium bromide (PyBP), Scheme 3.3 and 3-(4-bromobutyl)-2-mercapto-4,5-dihydrothiazol-3-ium bromide (BMDBr) Scheme 3.5.

The precursor **BMDBr**, **PyB** and **PyBP** were synthesised using literature [154,155] with slight modifications. The refluxing of 2-thiazoline-2-thiol (0.1 mol) or 4-methyl pyridine (0.1 mol) with the corresponding alkyl halide (0.12 mol) in toluene containing 1%DMF or toluene alone for 6 to 24 h **Scheme 3.3 and 3.5**. The reaction mixtures were cooled, and the solidified products were washed with excess toluene followed by MeOH to form **BMDBr** as white solid, **PyB** and **PyBP** are washed with diethyl ether to give as pink solid.

PyB: (Yield: 79%);^{1}H NMR (400 MHz, DMSO-d_6): δ (ppm), (d, J = 6.0 Hz, 2H), 7.99 (d, *J* = 6.4 Hz, 2H), 4.63 (t, *J* = 8.0 Hz, 2H), 3.53 (s, 3H), 1.79 (t, *J* = 7.5 Hz, 2H), 1.17 (m, 2H), (d, *J* = 5.8 Hz, 3H).

PyBP: (Yield: 84%); ^{1}H NMR (400 MHz, DMSO-d_6): δ (ppm), 9.02 (d, 2H), 8.03 (d, *J* = 6.4 Hz, 2H), 7.81 (m, 15H), 4.68 (t, *J* = 6.5 Hz, 2H), 3.83 (t, *J* = 12.7 Hz, 2H), 2.56 (m, 3H), 2.19 (m, 2H), 1.59 (m, 2H)

BMDBr: (Yield: 89%);^{1}H NMR (80 MHz, MeOH-d_4): δ (ppm), 4.41-4.31 (d, 2H), 3.97-3.87 (d, 2H), 3.35 (d, 2H), 3.02 (s, 2H), 2.72 (s, 2H), 2.34 (s, 1H), 2.02 (m, 2H)

2.3.2 Synthesis of Pcs

2.3.2.1 Synthesis of 2,9,16, 23-Tetrakis(2-(piperidin-1-yl) ethoxy) phthalocyanine zinc (II) (*1*) (Scheme 3.1).

Complex *1* was synthesised as follows, 4-(3-(piperidin-1-yl) ethanoxy) phthalonitrile (***A***) (1.5 g, 5.87 mmol), zinc (II) acetate dihydrate (0.25 g, 1.1 mmol), dry 1–pentanol (3 mL) and DBU (0.5 mL) were transferred into a 100 mL round bottom flask. The mixture was then refluxed at 220 °C for 24 h with constant stirring under deaerated conditions using nitrogen gas. The reaction mixture was cooled to room temperature and transferred to a centrifuge tube. Methanol was added to precipitate the product. The mixture was centrifuged several times with methanol. Purification of complex *1* was completed using silica packed column and a solvent mixture of THF and EtOAc (8:2) as eluent. Yield = 67 %: IR (cm^{-1}): 2924 (C—N 2° amine), 2786 (aromatic C–H), 2786 (aliphatic C—H), 1696, 1607 (C=C), 1438, 1370, 1238 (C–O–C), 960−628 (C—C). ^{1}H NMR (600 MHz, DMSO-d_6): δ (ppm) 9.27 (m, 2H, aromatic—H), 8.99 (s, 4H, aromatic—H), 8.61

(m, 2H, aromatic—H), 7.65 (m, 4H, aromatic —H), 4.61 (s, 8H, CH_2), 2.99 (s, 8H, CH_2), 2.68 (s, 14H, piperidine−CH_2), 1.67 (m, 16H, piperidine−CH_2), 1.48 (s, 10H, piperidine−CH_2). UV–vis (DMSO): λ_{max} (nm), (log ε): 678 (5.6), 613 (4.3), 345 (4.8). MALDI TOF MS *m/z*: Calculated: 1084.64, found 1085.56 $[M+H]^+$. Calcd for $C_{60}H_{68}N_{12}O_4Zn$: C (66.32) H (6.31) N (15.47), found C (65.12), H (6.27), N (16.67).

2.3.2.2 *Tetrakis* (ethane-2,1-diyl)) tetrakis(1-methylpiperidin-1-ium) phthalocyanine zinc (II) (*1Q*), (Scheme 3.1).

The protonation of complex ***1*** was completed using the procedure reported in literature [157], Briefly, a mixture of complex ***1*** (60 mg, 0.046 mmol), methyl iodide (2.5 mL), and chloroform (4 mL) was stirred at ambient temperature for 2 days. The obtained green precipitate was filtered off, washed with chloroform, acetone and diethyl ether, respectively. Finally, water soluble quaternised Pc derivative was air dried in vacuo. The resultant product was represented as complex ***1Q***. 3370−3091 (aromatic C–H), 2924 (N−CH), 2786 (C–H aromatic), 2862 (CH_2), 1752, 1606 (C=C), 1481, 1391, 1099 (C–O–C), 1037−614 (C—C). ^{1}H NMR (600 MHz, DMSO-d_6): δ (ppm) 9.39 (m, 4H, aromatic–H), 9.04 (s, 2H, aromatic–H), 8.31 (m, 2H, aromatic–H), 7.91 (m, 4H, aromatic–H), 4.15 (s, 8H, piperidine CH_2), 3.65–3.71 (d, 16H, CH_2), 3.15 (s, 12H, N−CH_3), 2.01 (m, 16H, piperidine−CH_2), 1.84 (s, 8H, piperidine−CH_2), 1.69 (s, 8H, piperidine−CH_2). UV–vis (DMSO): λ_{max} (nm), (log ε): 684 (5.9), 616 (3.9), 347 (4.1). MALDI TOF MS *m/z*: Calculated: 289.90, found 1144.17 $[M+H]^+$. Calcd for $C_{64}H_{80}N_{12}O_4Zn$: C (67.20), H (7.20), N (14.47), found C (68.53), H (6.27), N (13.14).

2.3.2.3 Tetra-phenoxy *N, N*-dimethyl-4-((methylimino) phthalocyanine zinc (II) (*2*), (Scheme 3.2).

N, N'–bis (4-(diethylamino) benzylidene) amino) propan-2-yl) oxy) phthalonitrile (***C***; 0.2 g, 0.37 mmol) was mixed anhydrous $Zn(OAc)_2$ (0.017 g, 0.092 mmol) and catalytic amount of DBU in n-hexanol (4 mL). The mixture was degassed using nitrogen and stirred at 150 °C for 18 h. After cooling to ambient temperature, the product was allowed to precipitate with the addition of water/methanol (1/1) and subsequently collected by centrifugation. The collected compound was washed several times with ethanol, acetone and water remove the soluble by-products and any un-reacted metal salt. Pure ZnPc ***2*** was obtained as a green solid by dissolving in DMF and precipitating in hot acetone (3 times). Yield: 20% (0.04 g): IR (cm^{-1}): 3002 (aromatic C–H), 2918,2855 (aliphatic C–H), 1647 (C=N imine), 1600,1529 (aromatic C=C), 1235, 1007 (aromatic−O−aromatic).^{1}H NMR (DMSO-d_6): δ (ppm) 9.56 (s, 8H, imine), 8.64 (s, 8H, Pc-aromatic), 8.28 (s, 4H, Pc-aromatic), 7.61 (d, 8H, aromatic), 7.35 (t, 8H, aromatic), 6.93 (d, 8H, aromatic), 6.70 (d, 8H, aromatic), 3.36–3.38 (m, 32H, CH_2), 3.07 (s, 4H, CH), 2.97 (s, 16H, CH_2), 1.04–1.06 (m, 24H, CH_3), 0.97–1.00 (m, 24H, CH_3). UV–vis (DMSO): λ_{max} (nm), (log ε): 690 (5.3), 634 (4.7), 347 (4.1). MALDI TOF MS m/z: Calculated: 2201.17, found 2202.13 $[M+H]^+$. Calcd for $C_{132}H_{152}N_{24}O_4$: C (71.93), H (6.95), N (15.25), found C (70.68), H (6.54), N (15.94).

2.3.2.4 *Tetrakis N, N'*–Bis (4-(diethylamino) benzylidene) amino) propan-2-yl) oxy) phthalocyanine zinc (II) (*3*), (Scheme 3.2).

Prior to the synthesis of ***3***, complex ***4*** was synthesised according to procedures reported in the literature [96], **Table 1.1**. Complex ***3*** was obtained as follows: zinc (II) (2-formylphenoxy) Pc, ***4*** (0.157 g, 0.153 mmol) in 10 mL dry THF was added dropwise to a solution of 4-

(dimethylamino) benzaldehyde (0.091 g, 0.611 mmol) in 15 mL dry THF. The mixture was refluxed under argon for 24 h. The crude product was separated by filtration as a dark green solid, this was dissolved in chloroform (5 mL) and complex ***3*** was precipitated by the dropwise addition of methanol. The precipitate was filtered, successively washed with cold water, methanol and ethanol and air dried. Yield: 64%: IR (cm^{-1}): 3092 (aromatic C–H), 2956 (aliphatic C–H), 1605 (C=N imine), 1594 (aromatic C=C), 1248, 1152 (aromatic–O–aromatic). ^{1}H NMR (600 MHz, DMSO-d_6): δ (ppm) 9.37 (s, 4H, CH=N), 8.37 (s, 4H, Pc–aromatic), 7.68 (s, 4H, aromatic–H), 7.41 (d, 4H, aromatic–H), 7.26 (s, 8H, aromatic–H), 7.08 (s, 8H, aromatic–H), 6.56 (s, 8H, aromatic–H), 6.41 (s, 8H, aromatic–H), 1.64–1.78 (m, 24H, CH_3). UV–vis (DMSO): λ_{max} (nm), (log ε): 684 (5.4), 614(4.3), 372 (3.9). MALDI TOF MS m/z: Calculated: 1528.52, found 1529.50 $[M+H]^+$. Calcd for $C_{92}H_{72}N_{16}O_4$: C (72.17), H (4.74), N (14.64), found C (71.04), H (4.27), N (13.14).

2.3.2.5 *Tetrakis* (1-butyl-4-(4-(tetra phenoxy) styryl) pyridin-1-ium) phthalocyanine zinc (II) (*5*), (Scheme 3.3).

Complex ***5*** was synthesised as follows: a solution of 1-butyl-4-methylpyridin-1-ium bromide (**PyB**) (50.6 mg, 0.220 mmol) in dry THF (10 mL) was added to a solution of ***4*** (50 mg, 0.044 mmol) in THF (10 mL). Then a few drops of piperidine (as a catalyst) were added and the mixture was heated at 70 °C for 24 h. The solvent was evaporated, and reaction mixture was re-dissolved in minimum amount of DMF. The product was precipitated out by adding excess of diethyl ether (Et_2O), followed by filtering. The crude product was washed successively with cold MeOH and EtOH to remove unreacted starting materials. After drying in vacuum, the product was obtained as a green solid after purifying by chromatography over silica gel using MeOH: THF (1:1). Yield = 63%: IR (cm^{-1}): 3383–3138 (aromatic C–H), 2996 (aliphatic-CH), 1680

(C=C), 1486 (aromatic C=C), 1186 (C–O–C): (600 MHz, DMSO-d_6): δ (ppm), 8.70 (s, 12H, Pc–aromatic), 8.06 (s, 16H, aromatic–H), 7.10 (s, 16H, aromatic–H), 3.65 (s, 8H, CH), 1.72 (s, 8H, CH_2), 0.98 (s, 8H, CH_2), 0.38 (s, 8H, CH_2), 0.02 (s, 12H, CH_3). UV–vis (DMSO): λ_{max} (nm), (log ε): 354 (5.61), 616 (4.87), 683 (5.86). MALDI-TOF-MS: Calcd 1584.63, found m/z: 395.62 $[M-H]^{4+}$. Anal. cal. for $C_{100}H_{88}N_{12}O_4Zn^{4+}$: C (75.67), H (5.59), N (10.59), found C (75.15), H (5.74), N (9.84).

2.3.2.6 *Tetrakis*(4-(4-(tetraphenoxy) styryl)-1-(4-(triphenyl-phosphonio) butyl) pyridin-1-ium) phthalocyanine zinc (II) (*6*), (Scheme 3.3).

Synthesis of ***6*** was as described for ***5*** but using 4-methyl-1-(4-(triphenylphosphonio) butyl) pyridin-1-ium bromide (**PyBP**) (125.7 mg, 0.220 mmol). The amounts of the other reagents and solvents as well as reaction conditions and purification methods were as outlined for ***5*** above to give ***6***. Yield = 79%. IR (cm^{-1}): 3357–3167 (C–H aromatic), 2996 (aliphatic C—H), 1680 (C=C), 1431 (aromatic C=C), 1244 (C–O–C). ^{1}H NMR (400MHz, DMSO-d_6): δ (ppm), 8.73 (s, 12H, Pc–aromatic), 8.07 (s, 16H, aromatic–H), 7.12 (s, 16H, aromatic–H), 7.01–6.91 (m, 60H, aromatic–H), 3.67 (s, 8H, CH), 1.76 (d, 8H, CH_2), 1.01 (d, 8H, CH_2), 0.69 (s, 16H, CH_2). UV–vis (DMSO): λ_{max} (nm), (log ε): 354 (5.64), 616 (5.15), 684 (5.80). MALDITOF-MS: calcd 2628.96, found *m/z*: 328.49 $[M-H]^{8+}$. Anal. Cal. for $C_{172}H_{144}N_{12}O_4P_4Zn^{8+}$: C (78.48), H (5.51), N (6.39), found C (77.35), H (5.24), N (5.82).

2.3.2.7 *Tetrakis* 4-(5-formylpyridin-2-yl) oxy) phthalocyanine zinc (II) (*7*), (Scheme 3.4).

The 4-((5-formylpyridin-2-yl) oxy) phthalonitrile, ***D*** (0.5 g, 2.01 mmol) was mixed with Zn $(OAc)_2$ (0.223 mg, 1.2 mmol) and catalytic amount of DBU in 1-pentanol (5 mL). The mixture was degassed using nitrogen and stirred at reflux temperature for 24 h. The reaction mixture was cooled to room temperature and allowed to precipitate with the addition of H_2O: MeOH

(1/1) and subsequently collected by centrifugation. The collected complex was washed several times with ethanol, acetone, and water. Yield = 79%: IR (cm^{-1}): 3003 (aromatic C—H), 2819 (Aldehyde C—H), 1488 (aromatic C═C), 1231 cm^{-1} (C–O–C): ^{1}H NMR (400MHz, DMSO-d_6): δ (ppm), 9.66 (s, 4H, COH), 9.06 (s, 12H, Pc–aromatic), 8.12–7.77 (m, 12H, aromatic–H). UV–vis (DMSO): λ_{max} (nm), (log ε): 339 (5.61), 619 (4.82), 680 (5.76). MALDI-TOF-MS: Calcd 1060.14, found *m/z*: 1062.55 $[M + 3H]^+$. Anal. Cal. for $C_{56}H_{28}N_{12}O_8Zn$: C (63.32), N (15.82), found C (62.52), N (14.88).

2.3.2.8 *Tetrakis*-1-butyl-4-(2-(6-(tetra-phenoxy) pyridin-3-yl) vinyl) pyridin-1-ium phthalocyanine zinc (II) (*8*), (Scheme 3.4).

The synthesis of ***8*** was as described for complexes ***5*** and ***6***. In brief, a solution of 1-butyl-4-methylpyridin-1-ium bromide, **PyB** (50.6 mg, 0.220 mmol) in dry THF (10 mL) was added to a solution of ***7*** (50 mg, 0.047 mmol) in THF (10 mL). Then a few drops of piperidine (as a catalyst) were added and the mixture was heated at 70 °C for 24 h. The solvent was evaporated, and reaction mixture was re-dissolved in minimum amount of DMF. The product is precipitated out by adding excess of Et_2O, followed by filtration. The crude product was washed successively with cold methanol and ethanol to remove unreacted starting materials. After drying in vacuum, a product was obtained as a green solid after purifying by chromatography over silica gel using MeOH: THF (1:1). Yield: 73%: IR (cm^{-1}): 3383–3003 (aromatic C—H), 2940–2861 (aliphatic C—H), 1646 (C═C), 1439 (aromatic C═C), 1230 cm^{-1} (C–O–C). ^{1}H NMR (400 MHz, DMSO-d_6): δ (ppm), 8.87–8.55 (m, 20H), 7.91–7.50 (m, 28H), 4.25 (t, 8H), 1.62–1.54 (m, 8H, CH_2), 0.95 (s, 8H), 0.71–0.60 (m, 12H). UV–vis (DMSO): λ_{max} (nm), (log ε): 343 (5.11), 622 (4.36), 684 (5.55). MALDI-TOF-MS (m/z): Calcd 397.8, found m/z: 396.8 [M - H]. Anal. Cal. for $C_{96}H_{84}N_{16}O_4Zn^{4+}$: C (72.46), N (14.08), found C (72.23), N (14.59).

2.3.2.9 *Tetrakis* 1-butyl-5-(2-(1-butylpyridin-1-ium-4-yl) vinyl)-2-(*tetra*-phenoxy) pyridin-1-ium phthalocyanine zinc (II) (*8Q*), (Scheme 3.4).

Complexes ***8Q*** was synthesised by a revised alkylation method in literature [154,155] as follows: Complex ***8*** (0.1 mol) was dissolved in toluene (5 mL, 1% DMF), this was then followed by the addition of 1-bromobutane (0.12 mol) the mixture was then refluxed for 24 h. The reaction mixture was cooled and precipitated out of solution by centrifuge with excess Et_2O. The solidified product is washed with diethyl ether. The green solid is filtered and the crude product was washed successively with cold methanol and ethanol to remove unreacted starting materials. After drying in vacuum, a product was obtained as a green solid after purifying by chromatography over silica gel using MeOH: THF (1:1). Yield: 51%: IR (cm^{-1}): at 3383-3003 (aromatic C—H), 2940-2853 (aliphatic C—H), 1646 (C=C), 1473 (aromatic C=C), 1165 (C–O–C): ^{1}H NMR (400 MHz, DMSO-d_6): δ (ppm), 9.03–8.62 (m, 20H), 8.25–7.02 (m, 28H), 4.24 (t, 16H), 1.65–1.41 (m, 16H), 1.10–0.84 (m, 16H), 0.67–0.52 (m, 24H). UV–vis (DMSO): λ_{max} (nm), (log ε): 345 (4.95), 621 (4.61), 684 (5.64). MALDI-TOF-MS (m/z): Calcd 227.45, found 226.38 [M-H]. Anal. Cal. for $C_{112}H_{120}N_{16}O_4Zn^{8+}$: C (73.93), N (12.32), found C (72.02), N (11.95).

2.3.2.10 Synthesis of phthalocyanine complexes (*9Q*, *10Q*, and *11Q*), (Scheme 3.5).

Before the synthesis of ***9Q***, ***10Q***, and ***11Q*** was performed, tetra{4-(pyridin-4-yloxy) phthalocyanine zinc(II) (***9***) [97], tetra{4-(pyridin-3-yloxy) phthalocyanine zinc(II) (***10***) [99], tetra{4-(pyridin-2-yloxy) phthalocyanine zinc(II) (***11***) [98] were synthesised in accordance with the respective literature. The Pc complexes ***9Q***, ***10Q***, *and* ***11Q*** were synthesised by revised alkylation method described above [154,155] as follows: 3-(4-bromobutyl)-2-mercapto-4,5-dihydrothiazol-3-ium bromide (**BMDBr**) (203 mg, 0.61 mmol) was dissolved in acetone (10

mL, 1% MeOH) and added to solutions of ***9***, ***10*** or ***11*** (144 mg, 0.151 mmol) in acetone (5 mL, 1% DMF) and the mixtures were refluxed for 24 h. The resulting products were precipitated out of solution by centrifuge using toluene. The dark green products were re-dissolved in minimum amount of DMF and precipitated out by adding excess of Et_2O. Following filtration, the crude products were washed successively with cold MeOH and EtOH to remove unreacted starting materials. The respective Pc complexes were obtained as green solids after purifying by chromatography over silica gel using MeOH: THF (3:1) and drying in vacuum. The Pcs are denoted ***9Q***, ***10Q***, *and* ***11Q*** for the para, meta, and ortho position of nitrogen on the pyridine substituents on the Pcs, respectively.

Tetrakis 3-(4-(4-pyridin-1-ium-1-yl) butyl)-2-mercapto-4,5-dihydrothiazol-3-ium phthalocyanine zinc (II) (*9Q*), (Scheme 3.5).

IR (cm^{-1}):3390-3186 (aromatic C—H), 2920 (aliphatic C—H), 2560 (S—H), 1629 (C=C), 1484 (aromatic C=C), 1246 (C–O), 1015 (C–O–C), 738, 848 cm^{-1} (C—H). ^1H NMR (80 MHz, DMSO-d_6): δ (ppm), 8.76-8.64 (m, 8H, Pc–aromatic), 8.35-8.29 (s, 4H, Pc–aromatic), 6.37 (s, 16H, aromatic–H), 3.19 (m, 16H, aliphatic—CH_2), 3.10 (m, 8H, Cy-CH_2), 2.66 (s, 8H, Cy-CH_2), 1.60 (m, 16H, CH_2), 1.41 (s, 4H, SH). UV–vis (DMSO): λ_{max} (nm), (log ε):364 (5.31), 619 (4.93), 683 (5.71). MALDITOF-MS: Calcd 1651.9, found m/z: 205.936 $[M]^{8+/z}$. Anal. Cal. for $C_{80}H_{80}N_{16}O_4S_8Zn^{8+}$: C (58.18), H (4.88), N (13.57), S (15.53), found C (59.09), H (4.63), N (13.50), S (14.79).

Tetrakis **3-(4-(3-pyridin-1-ium-1-yl) butyl)-2-mercapto-4,5-dihydrothiazol- 3-ium phthalocyanine zinc (II) (*10Q*), (Scheme 3.5).**

IR (cm^{-1}): 3328-3122 (aromatic C—H), 2926 (aliphatic C—H), 2598 (S—H), 1645 (C=C), 1470 (aromatic C=C), 1246 (C–O), 1021 (C–O–C), 746, 830 cm^{-1} (C—H). ^1H NMR (80 MHz, DMSO-

d_6): δ (ppm), 8.68-8.65 (m, 4H, Pc–aromatic), 8.36 (s, 4H, Pc–aromatic), 8.15-8.08 (m, 4H, Pc–aromatic), 7.76-7.66 (m, 16H, aromatic–H), 3.16 (m, 8H, CH_2), 3.08 (m, 8H, CH_2), 2.85 (m, 8H, Cy-CH_2), 2.66 (s, 8H, Cy-CH_2), 1.40 (m, 16H, CH_2), 0.96 (s, 4H, S—H). UV–vis (DMSO): λ_{max} (nm), (log ε): 352 (4.89), 614 (4.55), 678 (5.45). MALDITOF-MS: Calcd 1651.9, found m/z: 205.338 $[M]^{8+/z}$. Anal. Cal. for $C_{80}H_{80}N_{16}O_4S_8Zn^{8+}$: C (58.18), H (4.88), N (13.57), S (15.53), found C (59.09), H (4.41), N (12.53), S (14.79).

***Tetrakis* 3-(4-(2-pyridin-1-ium-1-yl) butyl)-2-mercapto-4,5-dihydrothiazol-3-ium phthalocyanine zinc (II) (*11Q*), (Scheme 3.5).**

IR (cm^{-1}):3330-3180 (aromatic C—H), 2923 (aliphatic C—H), 2545 (S—H), 1650 (C=C), 1445 (aromatic C=C), 1256 (C–O), 1027 (C–O–C), 756, 830 cm^{-1} (C—H): ^{1}H NMR (80 MHz, DMSO-*d_6*): δ (ppm), 8.77-8.68 (m, 4H, Pc–aromatic), 8.23 (s, 4H, Pc–aromatic), 7.72 (s, 4H, Pc–aromatic), 6.62-6.57 (s, 16H, aromatic–H), 3.90 (m, 8H, aliphatic—CH_2), 3.44 (m, 8H, aliphatic —CH_2), 3.20-3.11 (m, 8H, Cy-CH_2), 2.66 (s, 8H, Cy-CH_2), 1.44 (m, 16H, aliphatic CH_2), 0.66 (s, 4H, S—H). UV–vis (DMSO): λ_{max} (nm), (log ε): 348 (5.17), 618 (4.63), 682 (5.38). MALDITOF-MS: Calcd 1651.9, found m/z: 206.809 $[M]^{8+/z}$. Anal. Cal. for $C_{80}H_{80}N_{16}O_4S_8Zn^{8+}$: C (58.18), H (4.88), N (13.57), S (15.53), found C (58.51), H (4.56) N (13.28), S (14.82).

2.3.2.11 Zinc (II) 3-(4-((3,17,23-tris(4-(Benzo(d)thiazol-2-yl] thiol) phthalocyanine-9-yl) oxy) phenyl) propanoic acid (*12*) (Scheme 3.6).

The precursor phthalonitriles used for the synthesis of ***12***, 3((4-phenoxy)-propanoic acid) phthalonitrile (***E***) [158] and 4-{[benzo(d)thiazol-2-yl] thiol} phthalonitrile (***F***) [159] were synthesised as reported in literature. Complex ***12*** was synthesised by cyclotetramerization of as follows: a mixture containing ***E*** (0.20 g, 0.684 mmol), ***F*** (1.004 g, 3.42 mmol), anhydrous Zn $(OAc)_2$ (0.08 g, 0.39 mmol) and catalytic amount of DBU was sonicated to form a

homogeneous solution in n-hexanol (3 mL). The solution was then refluxed with efficient stirring for 24 h under nitrogen atmosphere.

After cooling, the crude product was precipitated out by adding excess methanol. The precipitate was washed several times with methanol under centrifugation, dried under vacuum. After drying, the product was purified by chromatography over silica gel using DMF: THF (2:8). Yield : 59%: IR (cm^{-1}): 3055, 2924 (aromatic C—H), 2849 (aliphatic C—H) 1715 (C=O), 1596 (C=C), 1454, 1380 (C–S–C), 1223 (C–O–C): ^{1}H NMR (400 MHz, DMSO-d_6): δ (ppm), 7.90-7.81 (m, 8H, Pc–aromatic), 7.71 (d, 4H, Pc–aromatic), 7.53-7.42 (m, 8H, aromatic–H), 7.30 (d, 4H, aromatic–H), 7.16 (d, 2H, aromatic–H), 6.87 (s, 2H, aromatic–H), 1.82 (s, 4H, aliphatic—CH_2). UV–vis (DMSO): λ_{max} (nm), (log ε): 362 (5.01), 620 (4.95), 690 (5.23). MALDI-TOF-MS: Calcd 1235.04, found m/z: 1237.550 [M+2H].

2.3.2.12 Zinc (II) 3-(4-(3,17,23-tris(3-(4-(triphenylphosphine) butyl) benzo[d]thiazol-3-ium bromide phthalocyanine-9-yl) oxy) phenyl) propanoic acid (*13*).

Complex ***13*** was synthesised as outlined for ***6***. A solution of 4-bromo-butyl-triphenylphosphonium (58.08 mg, 0.12 mmol) was added to a solution of complex ***12*** (50 mg, 0.040 mmol) in toluene (1% DMF, 10 mL). Then reaction mixture was refluxed for 24 h, **Scheme 3.6.** The solvent was evaporated, and reaction mixture was re-dissolved in minimum amount of DMF. The product was precipitated out by adding excess of Et_2O, followed by filtering. The crude product was washed successively with cold MeOH and EtOH to remove unreacted starting materials and dried in vacuum Yield: 52%: IR (cm^{-1}): 3055, 2924 (aromatic C—H), 2849 (aliphatic C—H) 1715 (C=O), 1596 (C=C), 1454, 1380 (C–S–C), 1223 (C–O–C): IR (cm^{-1}): 3357–3167 (aromatic C—H), 2996 (aliphatic C—H), 1680 (C=C), 1431 (aromatic C=C),

1244 (C–O–C). ^{1}H NMR (400 MHz, DMSO-d_6): δ (ppm), 7.10 (s, 2H, aromatic–H), 7.04 (m, 14H, aromatic–H), 7.00 (m, 12H, Pc–aromatic), 6.95-6.93 (m, 45H, aromatic–H), 2.84-2.73 (m, 12H, aliphatic CH_2), 1.65 (s, 4H, CH_2), 1.45 (s, 2H, CH_2), 1.18-1.13 (m, 2H, aliphatic—CH_2), 0.96-0.89 (m, 4H, aliphatic—CH_2), 0.76-0.70 (m, 4H, CH_2). UV–vis (DMSO): λ_{max} (nm), (log ε): 341 (4.91), 640 (4.82), 684 (5.02). MALDI-TOF-MS: Calcd 445.33, found m/z: 448.33 $[M+3H]^{6+}$.

2.3.2.13 General procedure for amide coupling complexes *12* and *13* to ciprofloxacin (CIP), Scheme 3.6.

The covalent linkage of the Pc complexes to CIP was carried out as outlined in literature using the secondary amine on ciprofloxacin [160] as follows: a solution was prepared by dissolving 0.2 mg of ***12*** or ***13*** (0.162 mmol for ***12***, 0.075 mmol for ***13***), EDC (0.019 g, 0.092 mmol), and DMAP (0.005 g, 0.042 mmol) in 15 mL DCM; the mixture was stirred for 2h in the dark. The coupling agents were added to activate the carboxylic acid group of the Pc complexes. This was followed by addition of CIP (1:1 equivalent, CIP to Pc) to the reaction mixture to allow for the formation of amide bond between the activated COOH and the secondary amine of the piperazine ring of CIP, **Scheme 3.6**. The solution was stirred for a further 22 h at ambient temperature. The conjugates were separated from the solution with ethanol under centrifugation, then washed several times with cold methanol and air-dried.

12-CIP:Yield = 91%: IR (cm^{-1}): 3055, 2924 (C–H aromatic), 2849-2922 (aliphatic C—H) 1711 (C=O), 1624 (O=C–NH), 1591 (C=C), 1454, 1380 (C–S–C), 1223 (C–O–C): ^{1}H NMR (DMSO-d_6): δ (ppm), 8.67 (s, 1H, COOH (CIP)), 8.17-5.93 (31H, aromatic–H), 3.83 (m, 1H, CH(CIP)), 3.20 (s, 4H, CH_2(CIP)), 2.59 (s, 4H, CH_2(CIP)), 1.31-1.30 (d, 2H, CH_2(CIP), 1.18-1.17 (d, 2H, CH_2(CIP)), 0.97-0.96 (s, 4H, CH_2). UV–vis (DMSO): λ_{max} (nm), (log ε): 331 (5.22), 642 (5.04), 687 (5.18). MALDI-TOF-MS: Calcd 1548.16, found m/z: 1546.4 [M-2H].

13-CIP:Yield = 82%: IR (cm^{-1}): 3055, 2924 (aromatic C—H), 2849 (aliphatic C—H) 1711 (C=O), 1636 (O=C-NH), 1596 (C=C), 1454, 1380 (C–S–C), 1223 (C–O–C): ^{1}H NMR (DMSO-d_6): δ (ppm), 8.64 (s, 1H, COOH (CIP)), 8.17-6.90 (75H, aromatic—H), 3.99 (m, 1H, CH(CIP)), 3.53 (s, 12H, CH_2), 1.89 (t, 4H, CH_2 (CIP)), 1.73-1.69 (t, 4H, CH_2 (CIP)) 1.56-1.55 (m, 4H, CH_2), 1.29-1.28 (m, 8H, CH_2), 1.15-1.14 (m, 8H, CH_2). UV–vis (DMSO): λ_{max} (nm), (log ε): 341 (5.20), 640 (4.94), 684 (5.24). MALDI-TOF-MS: Calcd 497.56, found m/z: 496.48 $[M - H]^{6+}$.

2.4 Doping of Pcs into SiNPs using reverse micro-emulsion method and APTES functionalisation of Pc@SiNPs, (Scheme 3.7).

To encapsulate Pc complexes into silica nanoparticles, the method described in the literature [161] was used. In summary, in separate 50 mL round bottom flasks mixtures containing Triton X-100 (1.80 mL), 1-hexanol (1.80 mL), and cyclohexane (7.5 mL) were prepared. The mixtures were stirred for 20 min until they reached homogeneity. Then, 1 mL of Pc complexes (***1***, ***1Q***, ***2***, ***3***, ***7***, ***8***, or ***8Q***; 0.081 mM) in DMF were added separately to each flask. After 10 min of stirring, TEOS (0.15 mL, 0.77 mmol) and H_2O (0.4 mL) were added to the reaction solutions, followed by the addition of 25% NH_4OH solution (0.06 mL). The product was collected using centrifugation with ethanol. Unreacted components were washed away from the final products using ethanol and water.

The surface of the Pc doped SiNPs (**Pc**@SiNPs) was functionalised (3-aminopropyl) triethoxysilane (APTES) as follows: Degassed toluene (40 mL) was used to disperse Pc-doped SiNPs (0.26 g). The mixtures were then refluxed in a nitrogen environment at 110 °C for 24 h after APTES (0.5 mL) was added. The products were precipitated under centrifugation using ethanol and air-dried to give **Pc**@SiNPs-APTES.

2.4.1 Amide bond formation for FA, GA and AMP with Pc@SiNPs-APTES, (Scheme 3.8).

The surface functionalisation of **Pc**@SiNPs-APTES with ampicillin (AMP)/folic acid (FA)/gallic acid (GA) was completed as reported in literature [158,162]. For AMP, a solution was prepared by dissolving the Pc = ***1*** or ***1Q*** incapsulated as Pc@SiNPs-APTES (0.5 g), and AMP (0.3 g, 8.58 mmol) in DMSO/H_2O in the presence of DCC (0.01 g, 0.049 mmol) and DMAP (0.005 g, 0.042 mmol). The mixture was stirred for 48 h. The coupling agents were added to activate the carboxylic acid group of AMP to allow for covalent linkage with **Pc**@SiNPs-APTES via amide bond formation, **Scheme 3.8**. The solution was stirred for a further 48 h at ambient temperature.

A slight difference in experimental outline was conducted for FA (using Pc = ***2*** or ***3***) and GA (using Pc = ***7***, ***8***, or ***8Q***), this was done as follows, folic acid (0.014 g, 0.031 mmol) and EDC (0.019 g, 0.092 mmol) in DMF/ethanol (2/1) 8 mL followed by stirring in the dark for 2 h. This was then followed by the addition of the appropriate **Pc**@SiNPs-APTES (0.5 g each) and NHS (7.24 g, 0.064 mol) to the reaction mixture. The reaction was further stirred in the dark at room temperature for 24 h.

Similarly, a mixture of GA (0.3 g, 1.76 mmol) and EDC (0.019 g, 0.092 mmol) in methanol/ethanol (2/1) (8 mL) followed by stirring in the dark for 2 h was prepared. This was then followed by the addition of **Pc**@SiNPs-APTES (0.5 g each) and NHS (7.24 g, 0.064 mmol) to the reaction mixture. The coupling agents were added to activate the carboxylic acid group of GA to enable amide bond linkage with the amino functionalised surface (APTES), **Scheme 3.8**. The mixtures were stirred for a further 48 h at ambient temperature. All the conjugates were separated with methanol under centrifugation and air-dried giving the respective

Pc@SiNPs-AMP (Pc = ***1*** or ***1Q***), **Pc**@SiNPs-FA (**Pc** = ***2*** or ***3***), and **Pc**@SiNPs-GA (**Pc** = ***7***, ***8***, or ***8Q***) analogues.

2.4.2 Protonation of Pc@SiNPs-APTES with 1.3-propanesultone, (Scheme 3.8).

The protonation of **Pc**@SiNPs-APTES (Pc = ***1*** or ***1Q***) was carried out as reported in literature [163] with slight modifications as follows: The appropriate analogues of **Pc**@SiNPs-APTES (0.06 g each) were dissolved in DMSO/ethanol (5 mL). 1,3-Propanesultone (PSn, 1.46 g, 12 mmol) was added to the mixtures which was then kept at 45 °C for 22 h under deaerated conditions using nitrogen gas with stirring. The green products were precipitated by the addition of CH_2Cl_2. The precipitates were filtered off under centrifugation and washed with acetone to remove unreacted 1.3-propanesultone. The final products are represented **Pc**@SiNPs-PSn (**Pc** = ***1*** or ***1Q***).

2.5 Antimicrobial studies

2.5.1 Planktonic cells

The bacteria culture was prepared according to a method previously reported in the literature [164]. This was done as follows, aliquots of the culture were aseptically transferred to 4 mL of fresh broth and incubated at 37 °C to mid logarithmic phase (absorbance ~ 0.6 at 620 nm). The bacteria culture in the logarithmic phase of growth were harvested through the removal of broth culture by centrifugation (3000 RPM for 15 min), washed once with 10 mM of PBS and re-suspended in 4 mL of PBS. Then the bacteria culture was diluted to 1/1000 in PBS (working stock solution), corresponding to ~10^8 colony forming units (CFU)/mL.

The photoantimicrobial chemotherapy studies were performed by administration of appropriate concentration Pc complexes and conjugates in PBS to a bacterial suspension 10^6 CFU/mL in PBS. The bacterial suspensions were incubated in an oven equipped with a shaker for 30 min in the dark at 37 °C. Then, half (2.5 ml) of the incubated bacterial suspension were irradiated in 24 well plates at the Q-band maximum of the photosensitizers with 680 nm light from Modulight (irradiance: 524 mV/cm^2 and dose: 472 J/cm^2), while the other half kept in the dark. After irradiation, 100 µL samples were diluted with 900 µL PBS and were spotted on agar plates using a micropipette. The plates were incubated at 37 °C for 24 h. All the studies were conducted in triplicates.

2.5.2 Biofilm formation

The formation of the single-species biofilms of *S. pneumoniae, S. aureus* and *E. coli* was done as follows: Freshly prepared inoculum of the bacterial species at 10^8 CFU/mL was suspended in nutrient broth to a final concentration of 10^9 CFU/mL. A 200 µL aliquot of the suspension was seeded in 96 well plates and incubated statically and anaerobically at 37°C for 48 h. After

every 24 h of the adhesion phase, unbound cells were removed by gentle washing with 200 µL PBS, and 200 µL fresh tryptic soy broth was added to stimulate biofilm formation. Bacterial species individually cultured in the 96-well plates served as a positive control. At the end of the incubation period, the biofilm-coated wells of the 96 well-plates were carefully washed twice with 200 µL of PBS to remove the unbound planktonic cells and left to air dry for 30 min. To quantify the biofilm biomass (OD 570 nm), 200 µL of 1 % aqueous crystal violet (CV) solution was added in each well and left to stain for 30 min, followed by gentle rinsing with PBS to remove the excess dye before air drying the plates [165,166]. The bacterial biofilm cell viability (%) is defined by Eq. (**2.1**), based on optical density (OD) and determined at λ = 570 nm:

$$\text{Percentage survival } (\%) = \frac{\text{OD}_\text{t}}{\text{OD}_\text{c}} x\ 100 \qquad (\mathbf{2.1})$$

where OD_t is the optical density of the biofilm cells treated with the drug after 15/60 min light and OD_C is the optical density of the control groups, corresponding to 100% cell survival.

96-well plates containing biofilms were inoculated with 100 µL of Pcs alone and Pc conjugates at gradient dosages of each drug. After the undertaken of incubation in the dark at 37°C, the biofilms were irradiated at the Q-band (680 nm) of the PS, using Modulight laser lamp (irradiance: 524 mV/cm^2 and dose: 472 J/cm^2) for 15 min. In all methods, parallel experiments were done for the dark and the negative biofilms control group (without drugs) in triplicate.

2.5.3 Stability of biofilms

The optimal biofilm substrate for Raman spectroscopy, Scanning electron microscopy (SEM), electrochemical impedance spectroscopy (EIS), and cyclic voltammetry (CV), analysis, *S. aureus, S.pneumoniae* and *E. coli* biofilms were grown on indium-tin-oxide (ITO)-coated glass/aluminium slides (20 cm^2) with cells cultured in an extracellular matrix. The (ITO)-coated glass/aluminium slides were sterilised with ethanol and autoclaved before being placed in two separate sterile Petri dishes for each bacteria strain. In this thesis, Luria-Bertani (LB) broth was used to adjust the various bacteria to a concentration of 1×10^8 CFU/mL, and the medium was replaced every 24 h for 4 days. After this time, the prepared ITO-glass slides were gently washed with PBS (pH 7.2) to remove excess LB broth. The biofilms were then treated with 100 µL of Pcs alone and Pc conjugates using a predetermined concentration and irradiated at the Q-band (680 nm) of the photosensitisers, using Modulight laser lamp (irradiance: 524 mV/cm^2 and dose: 472 J/cm^2) for 15 min**.**

2.6 PDT activity studies

2.6.1 *In vitro* dark cytotoxicity studies

Before the in vitro photodynamic therapy studies of the drugs, in vitro cytotoxicity studies were done in the dark on human breast cancer cells (MCF–7 cells). The MCF–7 cells were grown in Dulbecco's modified Eagle's medium (DMEM), which had 4.5 g/L glucose, L-glutamine, and phenol red. It also had 10% (v/v) heat-inactivated foetal calf serum (FCS) and 100 units/mL penicillin, 100 g/mL streptomycin, and amphotericin B. The cells were grown in 75 cm^2 vented flasks (Porvair®) and kept in an incubator at 37 ^oC, 5% CO_2, and a humidified atmosphere with a humidified atmosphere. The cells were subcultured regularly by standard trypsinisation.

Trypan blue dye exclusion test (0.40% trypan blue solution) was used to count the live trypsinised cells with a hemocytometer. In 96-well tissue culture plates (Porvair®), the cells were planted at a rate of 10,000 cells per well in DMEM with phenol red added. The cells were then kept at 37°C and 5% CO_2 for 24 h to help the cells stick to the wells. The attached cells were rinsed with 100 µL of phosphate buffer saline (PBS) once, and then 100 µL of supplemented DMEM with increasing amounts of each drug was added. The stock drug amounts were made in DMSO or PBS and brought up to the right volume with DMEM that had been supplemented. The effect of DMSO or PBS on the cells was studied by putting them in 1.0% (v/v) DMSO or PBS in boosted DMEM for 24 h. This is the highest concentration of DMSO or PBS in the drug gradient solutions. Placebo cells were kept in DMEM with phenol red added to it with or without DMSO and PBS.

The cells and drugs were put in 96-well plates and kept at 37°C, 5% CO_2, and dark for 24 h. After 24 hours, the wells were rinsed with 100 µL of DPBS, DMEM with phenol red was added, and the plates were put back in the oven for another 24 h. The number of placebo cells (cells without drugs that had phenol red added to DMEM) that lived was used to measure cell survival. After 24 h of re-incubation with phenol red-supplemented DMEM, the number of surviving cells was measured with a cell proliferation neutral red reagent (WST–1 test).

2.6.2 *In vitro* photodynamic therapy studies

The photodynamic treatment studies were evaluated by incubating attached cells seeded as previously stated in section (**2.6.1**). Gradient dosages of each drug were given in a 96-well plate with attached cells at a density of 10,000 cells/well in supplemented DMEM (100 µL). After 24 h of incubation at 37 ^oC in 5% CO_2 in the dark, the plate was rinsed with 100 µL PBS and the supplemented phenol red DMEM was replaced with supplemented phenol red free

DMEM. Following that, the plates were irradiated with a set light dosimetry of 472 J cm^{-2}. The illumination source was a Modulight® ML7200 series Illumination setup or lamp. Following illumination, the supplemented phenol red free DMEM was changed with supplemented phenol red DMEM; each experiment was carried out in three independent triplicates (n=3). Cell survival was calculated as a percentage of placebo cells (cells that did not receive any medications). Surviving cells were counted after 24 h of re-incubation with culture media using the WST-1 assay.

2.6.3 WST–1 toxicity and cell proliferation

The WST-1 assay was used to determine the toxicity and cell proliferation in the monolayers of drug-treated and placebo-treated cells, respectively. This was done according to the manufacturer's instructions, and the stained live cells were quantified using a Synergy 2 multi-mode microplate reader (BioTek®). The absorbance at 540 nm was measured using a Molecular Devices Spectra Max M5 plate reader.

Equation **2.1** was used to calculate the % cell viability:

$$\%\ \text{cell viability} = \frac{\text{Absorbance sample at 540 nm}}{\text{Absorbance control at 540 nm}} \times 100 \qquad (\mathbf{2.2})$$

where the absorbance of sample is the cells containing drugs while absorbance of control is the placebo cells containing only supplemented DMEM with phenol red. The IC_{50} values of the complexes were from percentage cell viability vs concentration curve.

2.6.4 Cellular uptake

The MCF-7 cells (1 × 105 cells/well) were seeded in 24-well cell culture plates and incubated for 24 h. The cells were exposed to the Pc complexes (20 µg/mL) for 24 h in the dark. After the incubation time, the cells were washed three times with PBS, lysed with 30 µL of Triton-X 100 and internalised complex is solubilised in 70 µL of DMSO. The cellular uptake was measured by determining the Q-band absorbance of the complexes with an ELISA reader.

CHAPTER THREE

SYNTHESES & CHARACTERISATION

Publications

The findings that are discussed and illustrated in the ensuing chapters have been published in peer-reviewed journals.

1. **Aviwe Magadla**, Tebello Nyokong, Enhanced photodynamic antimicrobial activity of surface modified SiNPs doped with zinc (II) phthalocyanines: The effect of antimicrobial ampicillin and extra charges from a sultone, Photodiagnosis Photodyn. Ther., 32, 2020, 101996
2. **Aviwe Magadla**, Balaji Babu, Pinar Sen, Tebello Nyokong, The photophysicochemical properties and photodynamic therapy activity of Schiff base substituted phthalocyanines doped into silica nanoparticles and conjugated to folic acid, Polyhedron, 115227.
3. **Aviwe Magadla**, Balaji Babu, John Mack and Tebello Nyokong, positively charged styryl pyridine substituted Zn (II) phthalocyanines for photodynamic therapy and Photoantimicrobial chemotherapy: effect of the number of charges, Dalton Trans., 50, 2021, 9129-9136.
4. **Aviwe Magadla**, Yolande Ikala Openda, Tebello Nyokong, The implications of ortho-, meta-and para-directors on the in-vitro photodynamic antimicrobial chemotherapy activity of cationic pyridyl-dihydrothiazole phthalocyanines, Photodiagnosis Photodyn Ther. 39, 2022, 103029.
5. **Aviwe Magadla**, Yolande Ikala Openda, Lekhetho S. Mpeta, Tebello Nyokong, Evaluation of the antibacterial activity of gallic acid anchored phthalocyanine-doped silica nanoparticles towards Escherichia coli and Staphylococcus aureus biofilms and planktonic cells, Photodiagnosis Photodyn Ther., 42, 2023, 103520.

6. **Aviwe Magadla**, Lekhetho S. Mpeta, Jonathan Britton, Tebello Nyokong, Photodynamic Antimicrobial Chemotherapy activities of Phthalocyanine-Antibiotic Conjugates against Bacterial Biofilms and interactions with Extracellular Polymeric Substances, Photodiagnosis Photodyn Ther., 44, 2023, 103878.

3.1 Syntheses and characterisation of phthalocyanines (Pcs)

Complexes ***4***, ***9***, ***10***, and ***11*** were successfully synthesised, as reported in literature [96–99]. Complexes ***1***, ***1Q***, ***2–8***, ***8Q–11Q***, as well as ***12*** and ***13*** will all be thoroughly discussed in this chapter. These complexes are reported for the first time in this thesis, **Schemes 3.1–3.6**.

3.1.1 Synthesis

3.1.1.1 2,9,16, 23-*Tetrakis*(2-(piperidin-1-yl) ethoxy) zinc (II) (*1*) and *tetrakis* (ethane-2,1-diyl)) *tetrakis* (1-methylpiperidin-1-ium) phthalocyanine zinc (II) (*1Q*).

Scheme 3.1 shows the synthesis of symmetrically substituted phthalocyanine complexes ***1*** and its quaternised derivative complex ***1Q***. Characterisation of the Pc complexes was achieved using infrared, ultraviolet–visible, MALDI-TOF mass and ^{1}H NMR spectroscopies, and elemental analyses.

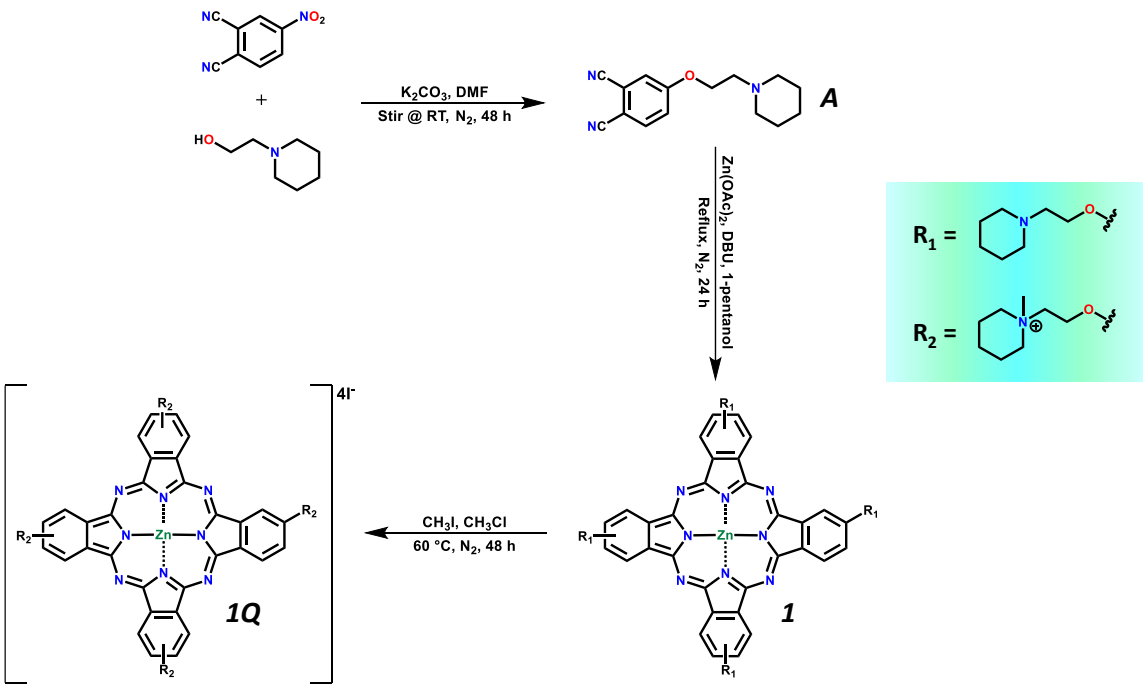

Scheme 3.1: Synthetic route for 4-(3-(piperidin-1-yl) ethanoxy) (A), complex *1* and *1Q*.

The ^{1}H NMR of 4-(3-(piperidin-1-yl) ethanoxy) phthalonitrile (***A***) has a total of 17 protons upon integration, 3 aromatic protons were observed between 7.29–8.64 ppm and 14 aliphatic protons were observed between 1.36–4.23 ppm. Upon cyclotetramerization of ***A*** to form ***1*** a total of 68 protons were obtained: 12 aromatic protons from 7.65 to 9.27 ppm which are attributed to the Pc macrocyclic ring. An addition of 56 protons was also observed between 1.48–4.61 ppm these protons are assigned to the aliphatic ligands of the Pc. The quaternised complex ***1Q*** had an additional sharp singlet upfield (δ =3.15 ppm) from the additional CH_3 protons. For ***1Q*** the 12 aromatic protons from the Pc macrocyclic ring appeared between 7.91 and 9.39 ppm. Aliphatic protons were observed between 1.69 and 4.15 ppm.

The Fourier transform infrared (FT-IR) spectroscopy was used to assess the functional groups present on the respective molecules. Upon cyclotetramization of ***A*** to form complex ***1*** the absence of the nitrile at 2212 cm^{-1} in ***1*** indicates the successful formation of complex, **Figure A1 (a)** (Appendix). Elemental analysis and mass spectra gave the expected values for both ***1*** and ***1Q***.

3.1.1.2 *Tetrakis N, N'* –Bis (4-(diethylamino) benzylidene) amino) propan-2-yl) oxy) phthalocyanine zinc (II) (*2*) and *tetrakis N, N'*–Bis (4-(diethylamino) benzylidene) amino) propan-2-yl) oxy) phthalocyanine zinc (II) (*3*).

Scheme 3.2 depicts the synthetic route for complex ***2***. Firstly, complex ***B*** was synthesised by Schiff base reaction of 4-(diethylamino) benzaldehyde with 1,3-diamino-2-propanol. Complex ***B*** was then reacted with 4-nitophthalonitrile via nucleophilic aromatic substitution to form the phthalonitrile ***C***, **Scheme 3.2**. Complex ***2*** was produced by cyclocondensation of ***C*** in the

presence of DBU, zinc metal salt and n-hexanol. Complex ***3*** was formed by reaction of formyl substituted phthalocyanine (***4***) with 4-(diethylamino) benzaldehyde, **Scheme 3.2**.

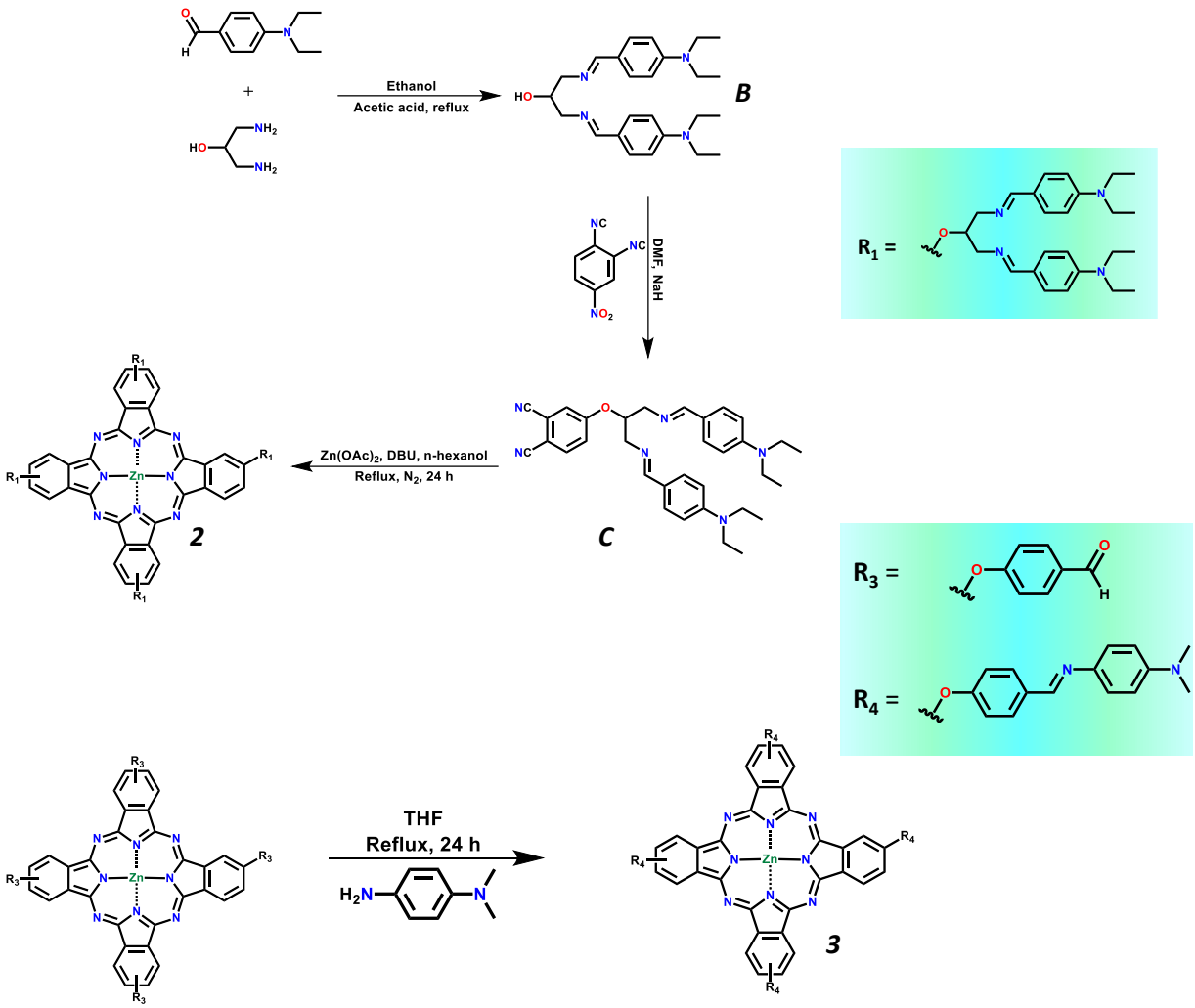

Scheme 3.2: Synthetic route of *N, N'*–bis (4-(diethylamino) benzylidene) amino) propan-2-ol (*A*), *N, N'*–bis (4-(diethylamino) benzylidene) amino) propan-2-yl) oxy) phthalonitrile (*C*), complex (*2***) and complex ***3*.**

The ^{1}H NMR spectra of *N, N'*–bis (4-(diethylamino) benzylidene) amino) propan-2-yl) oxy) phthalonitrile ***C*** depicted a multiple at 1.08–1.13 ppm which gave 12 protons upon integration which account for CH_3 groups. A quartet depicted at 3.45 ppm which was integrated to 8 protons corresponding to CH_2 groups was observed. An addition of 5 more protons corresponding to CH_2 of ***C*** were integrated as two triplets at 3.76 and 3.96 ppm and as a singlet at 5.14 ppm. Signals resonating from 6.64 to 8.11 ppm were integrated to a total of 11 protons that correspond to the aromatic ring of ***C***. A singlet at 9.62 ppm corresponding to the 2 alkene protons was observed further downfield bringing the total number of protons for ***C*** to 38.

The ^{1}H NMR spectra of complex ***2*** depicted a total of 152 protons. Two multiplets resonating at 0.97–1.00 ppm and 1.04–1.06 ppm was observed integrated to give 24 protons each, which are attributed to the CH_3 group of ***2***. A signal resonating as a singlet at 2.97 ppm was also integrated to a total of 16 protons which also correspond to CH_2 alkane chains of ***2***. The 4 aliphatic protons of the ether group of ***C*** appeared at 3.07 ppm as a singlet for ***2***. The 32 protons pertaining to the CH_2 dimethyl amino group were also observed between 3.36 and 3.38 ppm. The 32 aromatic protons pertaining to the aromatic rings of ***2*** were observed from 6.70 to 7.61 ppm. The aromatic protons (12) belonging to the Pc macrocyclic ring appeared between 8.28 and 8.64 ppm as singlet signals. The signal observed high upfield resonating as a singlet with 8 protons at 9.56 ppm pertains for the alkene groups of ***2***. The ^{1}H NMR spectra of complex ***3*** also gave the expected number of protons on integration appropriately. For complex ***2***, mass to charge ratio of 2201.17 m/z was calculated and 2202.13 m/z was obtained, while ***3*** had a calculated mass to charge ratio of 1528.52 and 1529.50 was obtained. The disappearance of the C≡N band at 2224 cm^{-1} in the FT-IR spectrum of ***C*** from that of ***2*** confirms formation of the latter, **Figure 3.1**.

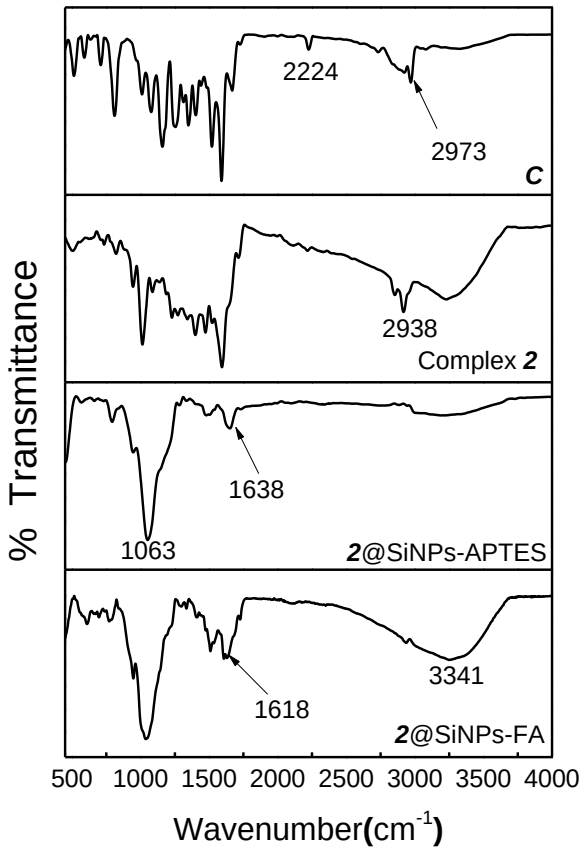

Figure 3.1: FT–IR spectra of B, *2*, *2*@SiNPs-APTES and *2*@SiNPs-FA.

Table 3.1. Q–band maxima (λ_{abs} (nm)) and Lipophilicity in 1%DMSO–H_2O (where applicable) of synthesised Pc complexes.

Complex	Media (λ_{abs})	Q–band λ_{abs} (nm)	Log $P_{O/W}$
1	DMSO	678	—
1Q	DMSO	684	—
2	DMSO	688	—
3	DMSO	684	—
4	DMSO	683	0.47
5	DMSO	683	–0.21
6	DMSO	684	–0.39
7	DMSO	679	—
8	DMSO	687	—
8Q	DMSO	683	—
9	DMSO	684	0.20
9Q	DMSO	683	–0.17
10	DMSO	679	0.19
10Q	DMSO	678	–0.18
11	DMSO	678	0.21
11Q	DMSO	682	–0.16
12	DMSO	690	–3.08
***12*-CIP**	DMSO	687	–0.33
13	DMSO	684	–3.87
***13*-CIP**	DMSO	684	0.33

3.1.1.3 *Tetrakis*(1-butyl-4-(4(tetraphenoxy)styryl) pyridin-1-ium) phthalocyanine (*5*) *and tetrakis*(4-(4-(tetraphenoxy) styryl)-1-(4-(triphenyl-phosphonio) butyl) pyridin-1-ium) phthalocyanine zinc (II) (*6*).

The synthesis of 1-butyl-4-methylpyridin-1-ium bromide (**PyB**) and butyl triphenylphosphine (**PyBP**), which are precursors to complexes *5* and *6* is shown in **Scheme 3.3**.

Scheme 3.3 shows the schematic route for the synthesis of complexes *5* and *6.* The complexes were synthesised by Knoevenagel condensation reaction of tetrakis (2-formylphenoxy) phthalocyanine zinc (II) (*4*) with 1-butyl-4-methylpyridin-1-ium bromide (**PyB**) and butyl triphenylphosphine (**PyBP**) to form *5* and *6*, respectively. The elemental analyses gave percentage carbon values that were within 1% for the studied complexes, which are within the justifiable range for Pc complexes. ^{1}H NMR was recorded in DMSO-d_6 for all the complexes and yielded the expected signals. Complex *5* showed aromatic protons between 8.70 and 7.10 ppm, CH protons at 3.65 ppm, CH_2 protons between 1.72 and 0.38 ppm and CH_3 protons at 0.02 ppm. Complex *6* showed similar signals to *5*. Aromatic protons were integrated between 8.73 and 6.91 ppm, the additional signal for *6* at 7.01–6.91 ppm indicates the structural variation between *5* and *6* with the latter consisting of the triphenylphosphine group. In the context of aliphatic protons, the CH peak was observed at 3.67 ppm, and the CH_2 peak lies between 1.76 and 0.69 ppm.

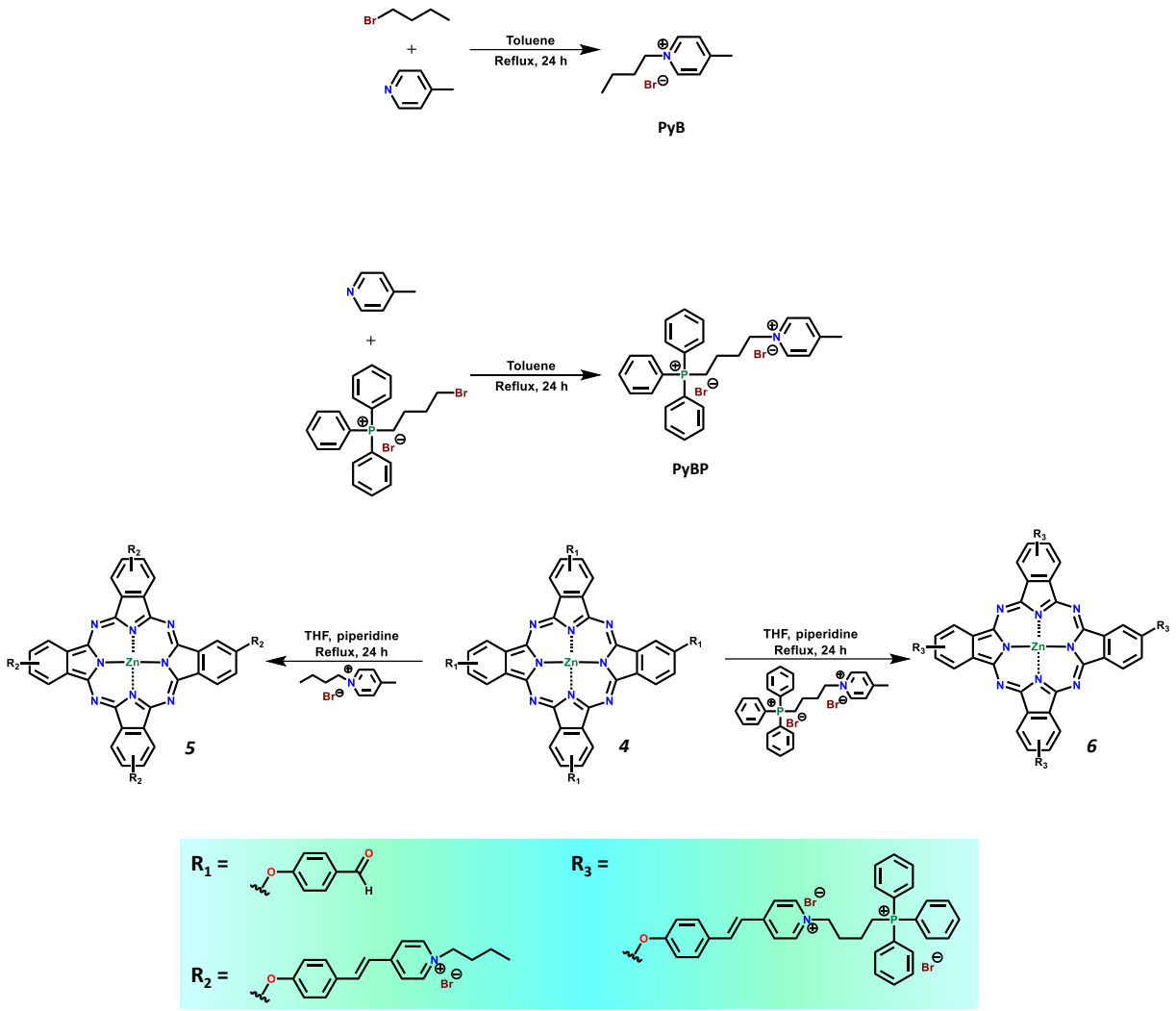

Scheme 3.3: Synthetic route of (PyB), (PyBP), and complexes *5* and *6*.

3.1.1.4 *Tetrakis* 4-(5-formylpyridin-2-yl) oxy) phthalocyanine zinc (II) (*7*), *tetrakis*-1-butyl-4-(2-(6-(tetra-phenoxy) pyridin-3-yl) vinyl) pyridin-1-ium phthalocyanine zinc (II) (*8*), and *tetrakis* 1-butyl-5-(2-(1-butylpyridin-1-ium-4-yl) vinyl)-2-(*tetra*-phenoxy) pyridin-1-ium phthalocyanine zinc (II) (*8Q*).

Scheme 3.4 shows the schematic route for 4-((5-formylpyridin-2-yl) oxy) phthalonitrile (***D***), complexes *7*, *8* and *8Q*. Complex *7* was synthesised by cyclotetramerization of ***D***. Knoevenagel condensation reaction of *7* with 1-butyl-4-methylpyridin-1-ium bromide yielded *8*. Further alkylation of complex *8* with 1-bromobutane afforded complex *8Q*, **Scheme 3.4**.

The ^{1}H NMR spectra of the complexes showed broad ^{1}HNMR signals in some instances. The broadness is assigned to both chemical exchanges as a consequence of aggregation–disaggregation equilibrium and the reality that symmetric Pc complexes exist as mixtures of four positional isomers. Phthalonitrile ***D*** showed an aldehydic proton at 8.25 ppm and aromatic protons between 7.90 and 7.13 ppm (**Figure A2)**. Complex *7* displayed aldehyde protons at 9.66 ppm and aromatic protons between 9.06 and 7.77 ppm. The aromatic protons and CH in Complex *8* were shown to be between 8.87 and 7.50 ppm, the CH_2 protons between 4.25 and 0.95 ppm, and the CH_3 protons between 0.71 and 0.60 ppm. Lastly, in similar fashion to *8*, complex *8Q* depicted a combination of aromatic and CH protons signals ranging between 9.03 and 7.02 ppm, CH_2 protons between 4.24 and 0.84 ppm and CH_3 protons at 0.67–0.52 ppm. Mass spectral data also confirmed the formation of the complexes. In the FT-IR spectrum of complex *7* the disappearance of the nitrile stretch of the phthalonitrile ***D*** at 2212 cm^{-1} confirms the successful synthesis of *7*, as shown above for complex *2*.

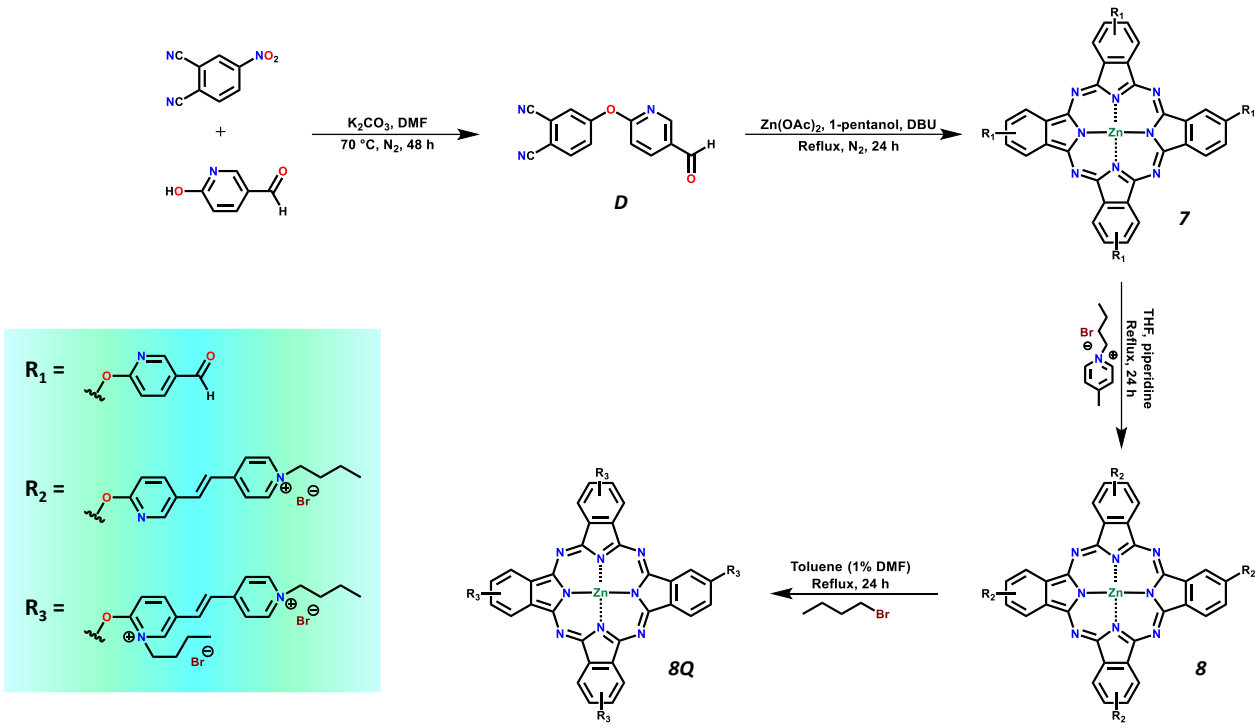

Scheme 3.4: schematic route for the synthesis of 4-((5-formylpyridin-2-yl) oxy) phthalonitrile, complexes *7*, *8* and *8Q*.

3.1.1.5 *Tetrakis* 3-(4-(4-pyridin-1-ium-1-yl) butyl)-2-mercapto-4,5-dihydrothiazol-3-ium phthalocyanine zinc (II) (*9Q*), *tetrakis* 3-(4-(3-pyridin-1-ium-1-yl) butyl)-2-mercapto-4,5-dihydrothiazol-3-ium phthalocyanine zinc (II) (*10Q*), and *tetrakis* 3-(4-(2-pyridin-1-ium-1-yl) butyl)-2-mercapto-4,5-dihydrothiazol-3-ium phthalocyanine zinc (II) (*11Q*).

The synthetic route for 3-(4-bromobutyl)-2-mercapto-4,5-dihydrothiazol-3-ium bromide **BMDBr** is shown in **Scheme 3.5**. Complexes *9Q*, *10Q*, and *11Q* were respectively synthesised by alkylation of Pc complexes *9*, *10*, and *11* with **BMDBr**. Complex *9Q*, *10Q*, and *11Q* depicted similar ^{1}H NMR spectra, some of which are broad due to previously mentioned factors. Complex *9Q* showed aromatic protons ranging from 8.76 to 6.37 ppm. CH_2 protons were observed between 3.19 and 1.60 ppm, and lastly SH at 1.41 ppm. Equally complex *10Q* displayed the same number of protons as *9Q*, with aromatic protons between 8.68 and 7.66 ppm. CH_2 protons occur between 3.16 and 1.40 ppm and SH at 0.96 ppm. Lastly, complex *11Q* likewise depicted aromatic protons between 8.77 and 6.57 ppm, CH_2 protons are between 3.90 and 1.44 ppm, and SH protons at 0.66 ppm.

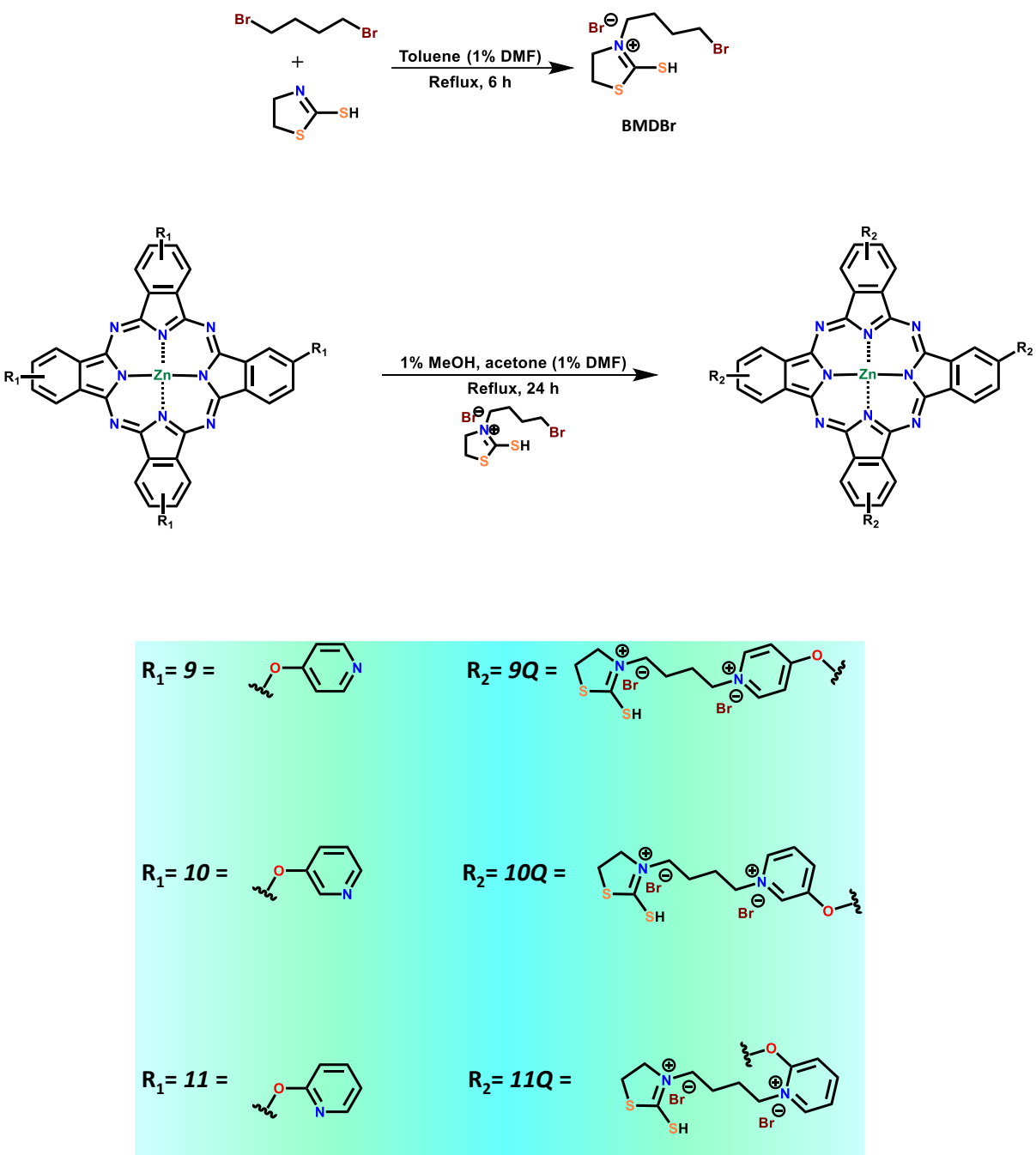

Scheme 3.5: Synthetic route for complexes *9Q*, *10Q*, and *11Q*.

3.1.1.6 Zinc (II) 3-(4-((3,17,23-tris(4-(Benzo(d)thiazol-2-yl] thiol) phthalocyanine-9-yl) oxy) phenyl) propanoic acid (*12*) and Zinc (II) 3-(4-(3,17,23-tris(3-(4-(triphenylphosphine) butyl) benzo[d]thiazol-3-ium bromide phthalocyanine-9-yl) oxy) phenyl) propanoic acid (*13*).

Scheme 3.6 illustrates the synthesis of the asymmetrical complex *12* and *13*. Complex *12* was synthesised using two dissimilar phthalonitriles in the presence of 1-hexanol, DBU and zinc acetate. DBU is used as a catalyst following literature methods, for the synthesis of phthalocyanines [160]. Possible products using this mixed condensation method include symmetric A_4 and B_4 compounds, asymmetric A_3B and A_2B_2, and the target AB_3 [160]. Complex *12* is linked to butyl triphenylphosphine (**PyBP**) to form *13*, **Scheme 3.6**.

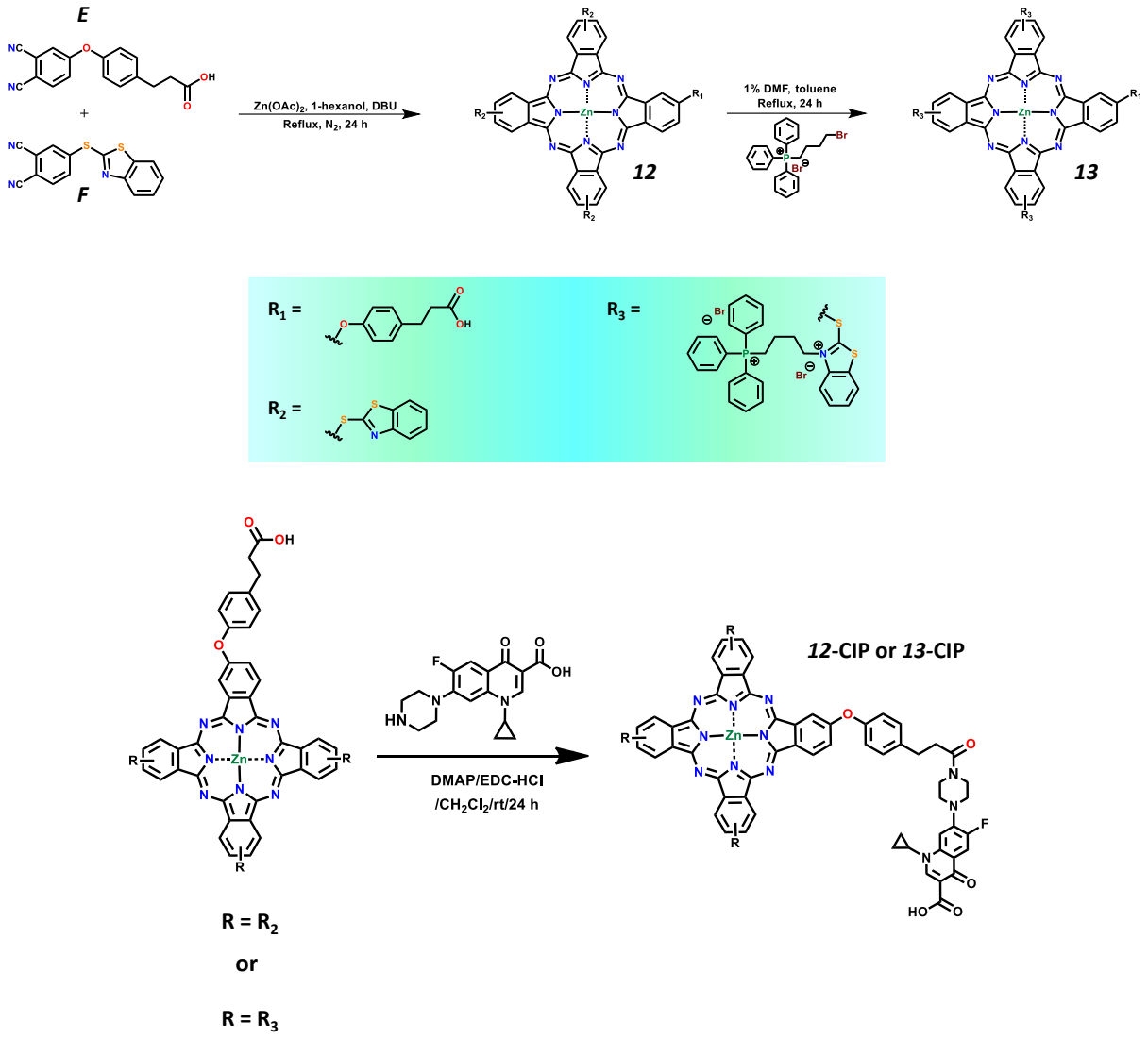

Scheme 3.6: Synthetic route for complexes *12*, *13*, *12*-CIP and *13*-CIP.

Both ***12*** and ***13*** are then linked to CIP to form ***12***-CIP and ***13***-CIP, respectively, **Scheme 3.6**. Due to instrument malfunction, the elemental composition of ***12***, ***13***, ***12***-CIP and ***13***-CIP could not be determined; instead, the complexes were characterised using ^{1}H NMR and mass spectroscopies. ^{1}H NMR spectroscopies were in accordance with the proposed ***12*** and ***13***. MALDI TOF mass spectra showed expected mass which considers the charge on the complex

for ***13***. The complexes showed good solubility in most organic solvents. Complex ***12*** gave aromatic protons in the ^{1}H NMR spectrum between 7.90–6.87 ppm and CH_2 protons were observed at 1.82 ppm. Due to reasons provided above, the ^{1}H NMR signals were broad. Complex ***13*** displayed aromatic protons signals between 7.10 to 6.93 ppm. Aliphatic CH_2 protons signals were integrated between 2.84 and 0.70 ppm. The Pc-CIP conjugates gave three aromatic and thirteen additional aliphatic protons. The aromatic protons range from 8.17-5.93 ppm and 8.17-6.90 ppm for ***12***-CIP and ***13***-CIP, respectively. The aliphatic protons were integrated at a range of 3.83-0.96 ppm (***12***-CIP) and 3.99-1.14 ppm (***13***-CIP). The carboxylic group proton from CIP were observed at 8.67 and 8.64 ppm for ***12***-CIP and ***13***-CIP, respectively.

The amide linkage between Pc complexes ***12*** and ***13*** to CIP was established using FT-IR, **Figure 3.2**. The bond was formed via the secondary amine of the piperazine ring of ciprofloxacin and the carboxylic functional group of the Pc complexes, as illustrated in **Scheme 3.6**. The amide vibrational bands were observed at 1624 and 1636 cm^{-1} for complexes ***12***-CIP and ***13***-CIP, respectively [167]. Characteristic aromatic C—H vibrational bands at 3056, 2924 cm^{-1}, aliphatic C—H vibration at 2849 cm^{-1}, C=O vibration at 1711 cm^{-1}, C=C vibrations at 1503, 1591 cm^{-1}, C–S–C vibrations at 1454, 1380 cm^{-1} and C–O–C 1223 cm^{-1} were shared amongst the complexes ***12*** and ***13***. The elemental composition of could not be obtained due to instrument breakdown only NMR and mass spectroscopies were used to characterise the complexes.

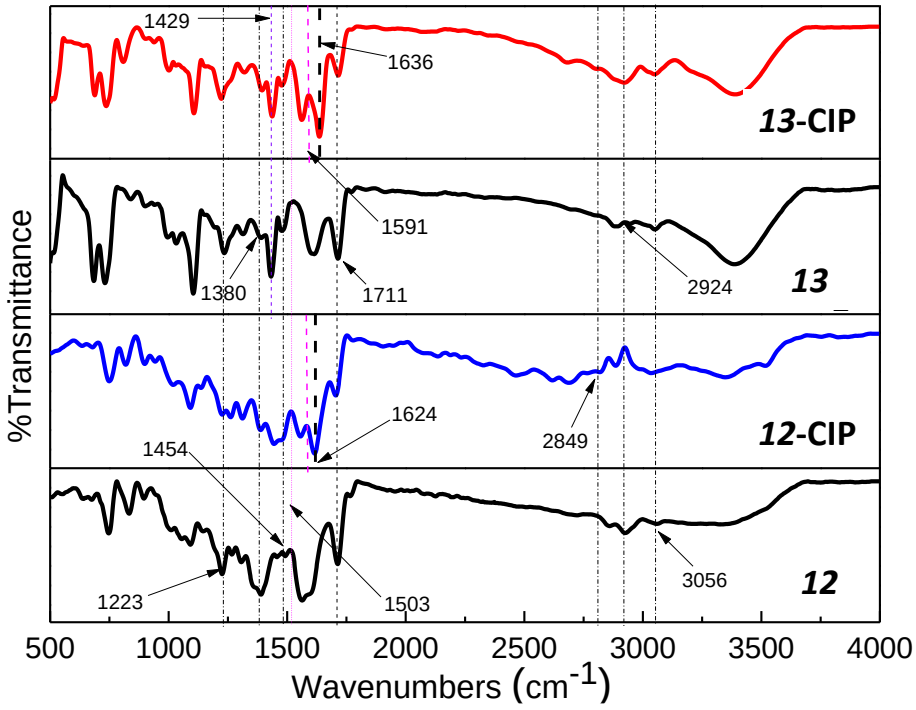

Figure 3.2: FT–IR spectra of *12*, *12*-CIP, *13*, and *13*-CIP.

3.1.2 Electronic absorption spectra of the studied Pcs

3.1.2.1 Symmetric Pcs

Figures 3.3—3.9 show the electronic absorption spectra of all of the studied Pcs and their respective conjugates in DMSO. The ground state electronic absorption spectra of the Pcs displayed characteristic monomeric behaviour in DMSO. The UV–vis spectra of complexes ***1*** and ***1Q*** showed no signs of band broadening due aggregation, typical of metalated Pc with degenerate D_{4h} symmetry, **Figure 3.3**. Complex ***1*** gave a Q band at 678 nm and ***1Q*** at 684 nm in DMSO, thus the latter is red shifted (**Table 3.1**).

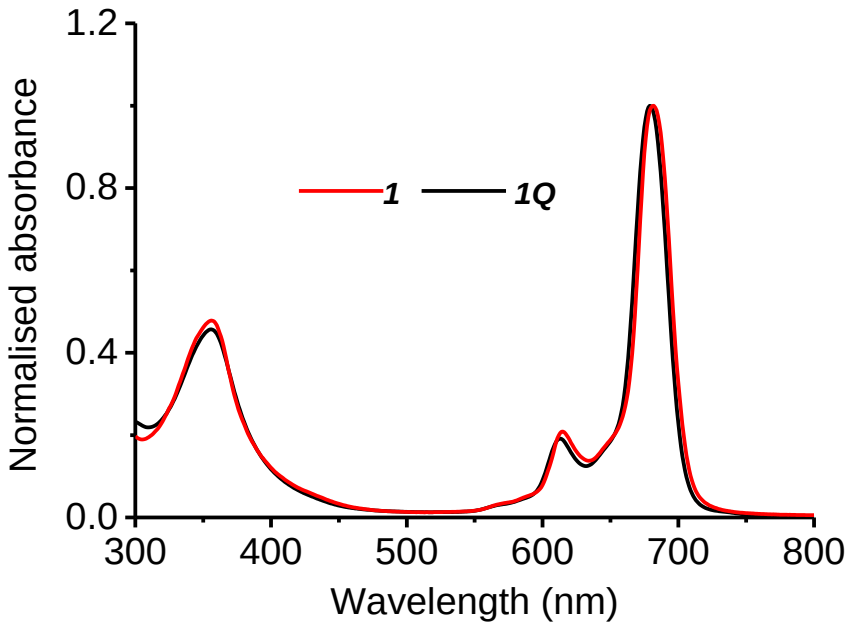

Figure 3.3: Absorption spectra of *1* and *1Q* in DMSO.

Complex ***3*** has a blue shifted Q–band compared to ***2*** (**Figure 3.4**). There is a blue shift for ***3*** is due to the reduction in the number of nitrogen groups in the former. Nitrogen containing groups are known to result in red shifting in Pc complexes [168].

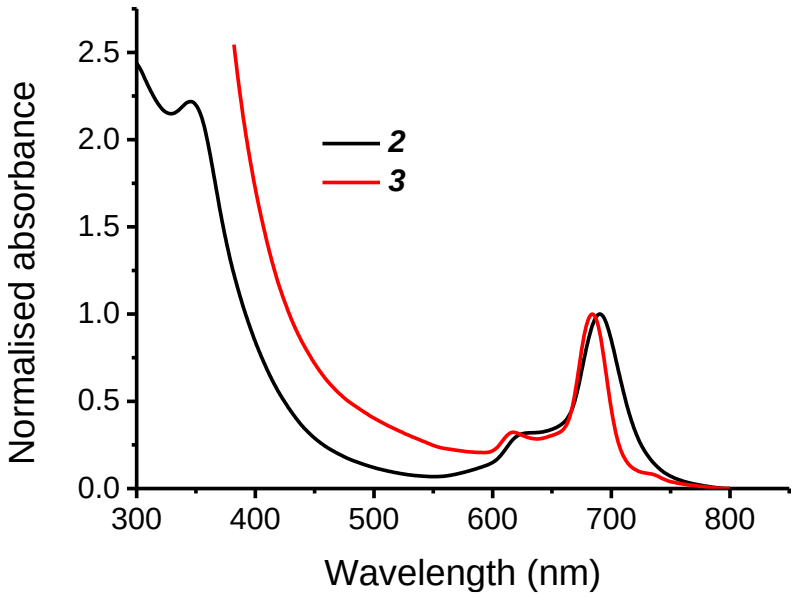

Figure 3.4: Absorption spectra of *2* and *3* in DMSO.

A typical monomeric behaviour was observed in DMSO for ***4***, ***5***, and ***6*** with a narrow Q band at 683/684 nm (**Table 3.1**) and a broad B band in the 300–350 nm region, **Figure 3.5**. A charge transfer band (CT) was observed in the 450–550 nm region in the spectra of ***5*** and ***6*** which is absent in that of the precursor complex ***4*** indicating the extension of ***4*** with 1-butyl-4-methylpyridin-1-ium and butyl triphenylphosphine groups to form ***5*** and ***6***, respectively. A narrow Q band was observed for ***7***, ***8***, and ***8Q*** at 679, 687, and 683 nm (**Table 3.1**) and a broad B band in the 300–350 nm region. Aggregation in Pcs is defined as the coplanar association of rings progressing from monomer to dimer and higher order complexes; it is influenced by various factors, including concentration, steric hindrance, temperature, and the nature of

substituent [169,170]. The pyridine ring on the substituents is aromatic hence will contribute to the π-π stacking. The Pc ring is closest to the pyridine in complex ***11Q***. Thus, aggregation is expected to be more enhanced in ***11Q*** (ortho-substituted) compared to ***10Q*** (meta-substituted) and ***9Q*** (para-substituted) [171]. The absorption spectra of all the Pc complexes exhibit split or broad Q-band in 1%DMSO/H_2O typical of aggregated Pcs [172], **Figure 3.5** and **3.6 (b)**.

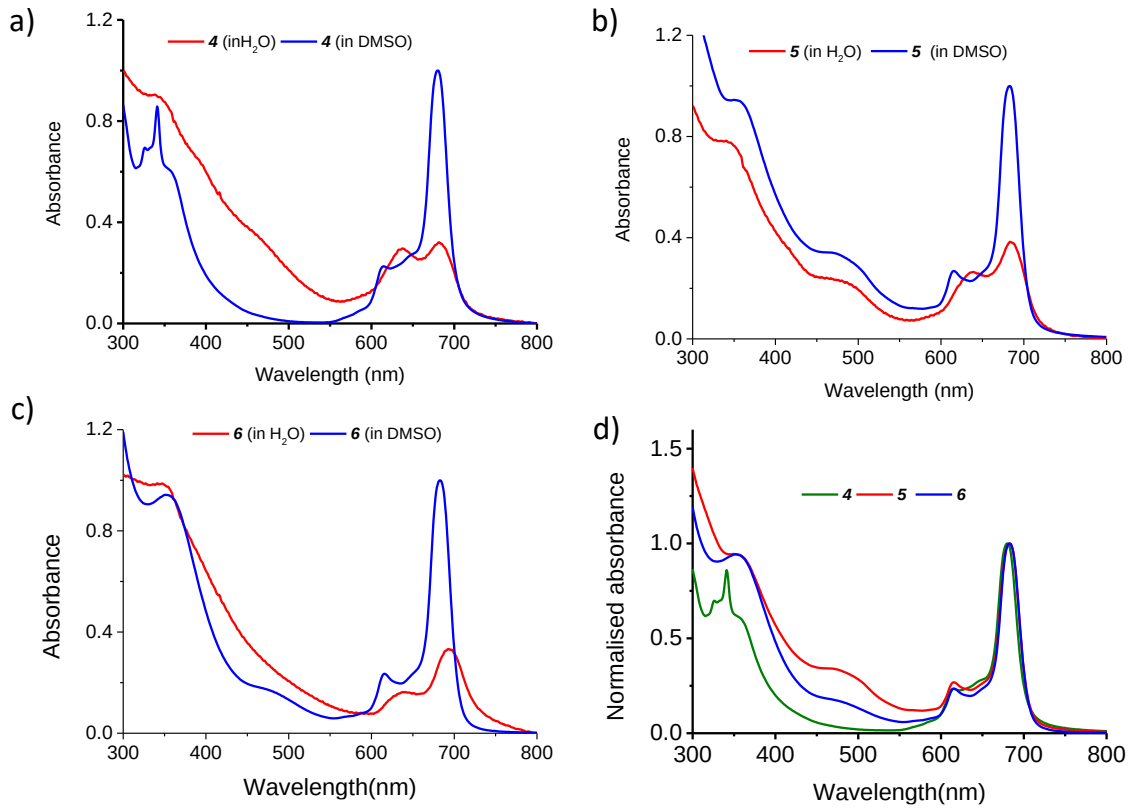

Figure 3.5: Absorption spectra of complexes *4* (a), *5* (b) and *6* (c) in DMSO and water/1% DMSO. (d) Overlay of the spectra of *4*, *5* and *6* in DMSO (concentration ~2.0 × 10^{-6} M).

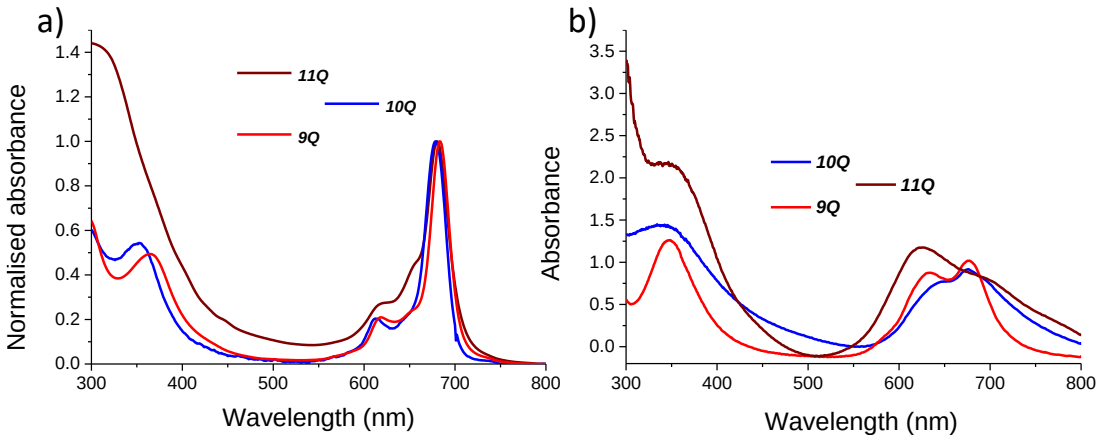

Figure 3.6: Absorption spectra of complexes *9Q*, *10Q*, and *11Q* (a) in DMSO (concentration ~2.0 × 10^{-6} M) and (b) in water/1% DMSO.

Optimised geometries were calculated for a zinc Pc model complex (ZnPc) and ***4–6*** by using the B3LYP functional of the Gaussian 09 software package with 6-31G basis sets. TD-DFT calculations were carried out in a similar manner with the CAM-B3LYP functional [173] since it contains a long-range correction. Optical spectra and TD-DFT calculations were carried out for complexes ***4***, ***5***, and ***6*** as examples. The electronic structures of Pcs can be readily understood with respect to a 16 atom 18 π-electron system corresponding to the inner ligand perimeter with a highest occupied molecular orbital (HOMO) and lowest unoccupied molecular orbital (LUMO) with M_L = ± 4 and ±5 properties [174,175], respectively. This results in B and Q bands of Gouterman's 4-orbital model [175] with ΔM_L = ± 1 and ±9 properties, respectively. Michl [174] introduced an **a**, **s**, -**a** and -**s** nomenclature for the four "Gouterman molecular orbitals, MOs" derived from the HOMO and LUMO of the parent perimeter depending on whether a nodal plane (**a**/-**a**) or MO coefficients (**s**/-**s**) are aligned with the *y*-axis, **Figure A3** (Appendix).

The MOs involving this additional transition for ***5*** and ***6*** is shown in **Figure A4** and **A5** (Appendix), with transitions shown in **Table A1** (Appendix). This is likely to primarily be responsible for the CT band that is observed in this spectral region (450–550 nm). In contrast with the Q and B band regions, very weak magnetic circular dichroism (MCD) intensity is observed in this spectral region, since the transitions involved lack the significant changes in orbital angular momentum properties with respect to the inner perimeter of the macrocyclic ring.

Magnetic circular dichroism (MCD), based on the analyses of the three Faraday terms, $\mathbf{A_1}$, $\mathbf{B_0}$ and $\mathbf{C_0}$ [176,177], can be used to identify the main electronic bands for ***4***, ***5*** and ***6*** since the intensity mechanism is related to changes in orbital angular momentum. Derivative-shaped pseudo-Faraday $\mathbf{A_1}$ term with crossover points between 600–750 nm (Q-band) and 300–400 nm (B-band) dominates the MCD spectra of ***5*** and ***6*** (**Figure 3.7**) due to the large orbital angular momentum changes associated with Q and B transitions, since the **-a** and **-s** MOs are near degenerate for symmetry reasons. Using the MCD spectroscopy of the complexes, the 683 and 354 nm and 682 and 355 nm wavelengths are assigned as pseudo-$\mathbf{A_1}$ terms to the Q and B transitions of ***5*** and ***6***, respectively (**Figure 3.7**).

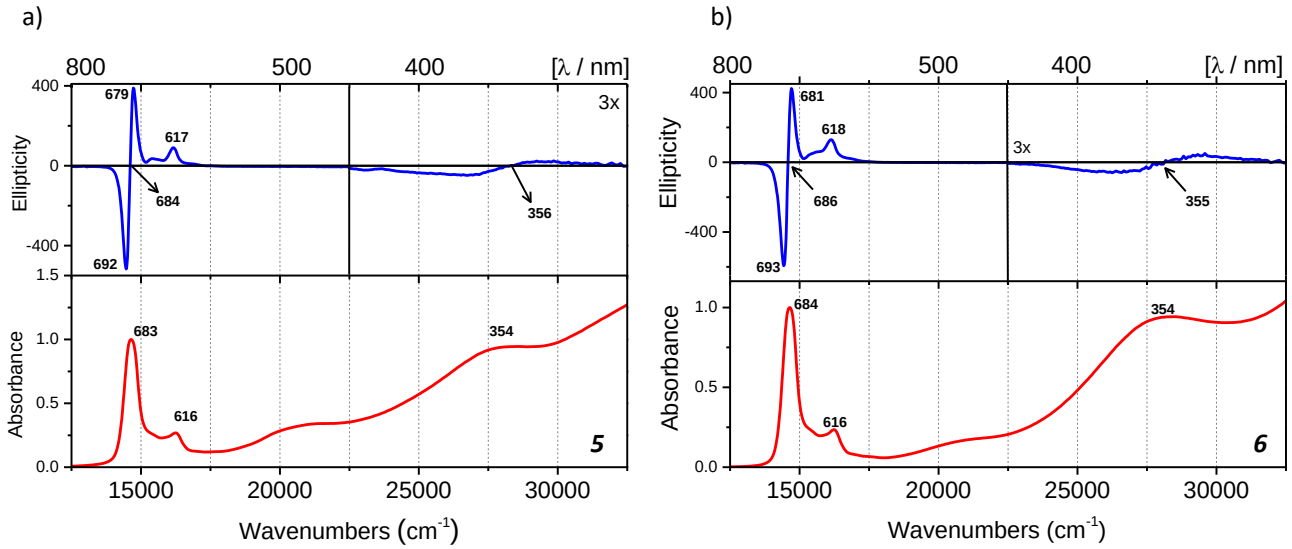

Figure 3.7: Absorption and MCD spectra of a) *5* and b) *6* in DMSO.

TD-DFT spectra (**Figure 3.8**) for ***4***, ***5*** and ***6*** were calculated using the Gaussian software package. Single intense bands arising from the Q and B transitions are predicted in the TD-DFT calculation. An intense band is predicted for a transition between MOs localised on the substituents of ***5*** and ***6*** in spectral region 450–550 nm, **Figure 3.8**.

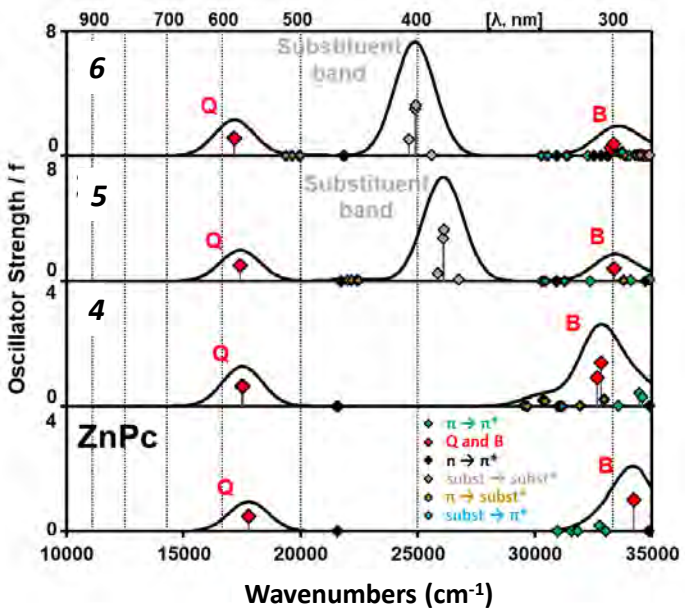

Figure 3.8: Calculated TD-DFT spectra of the ZnPc model complex and *4*–*6*. The predicted Q and B are highlighted with red diamonds. The Chemcraft program was used to simulate the calculated spectra using the fixed bandwidths of 1000 cm^{-1}.

3.1.2.2 Asymmetric Pcs

The ground state electronic absorption spectra for ***12***, ***12***-**CIP**, ***13***, and ***13***-**CIP** in DMSO, showed characteristic the Q and B bands, **Figure 3.9**. There was broadening of Q-bands due to aggregation. Complex ***12*** showed a more monomeric behaviour when compared to ***13***. This could be due to the fact that the latter contains triphenylphosphonio, which add additional π bonds, increasing aggregation. For complex ***12*** there is more aggregation in the presence of **CIP**, this could be due to more π bands in the latter. However, for complex ***13***, aggregation decreased in the presence of CIP for ***13***-**CIP**. The Q-band maximum for complex ***13*** is observed at 684 nm which is blue shifted compared to complex ***12*** at 690 nm, **Table 3.1**. The blue shift is due the fact that the mesomeric effect of the lone pair of the nitrogen atoms is removed following the linking of complex ***12*** to **PyBP** [178]. An enhancement in the absorption of the B bands in the 300–350 nm region for ***12***-**CIP** and ***13***-**CIP** is due to the absorption of CIP. There is no change in the Q band maxima for ***13*** following linking to CIP and a small blue shift for ***12***.

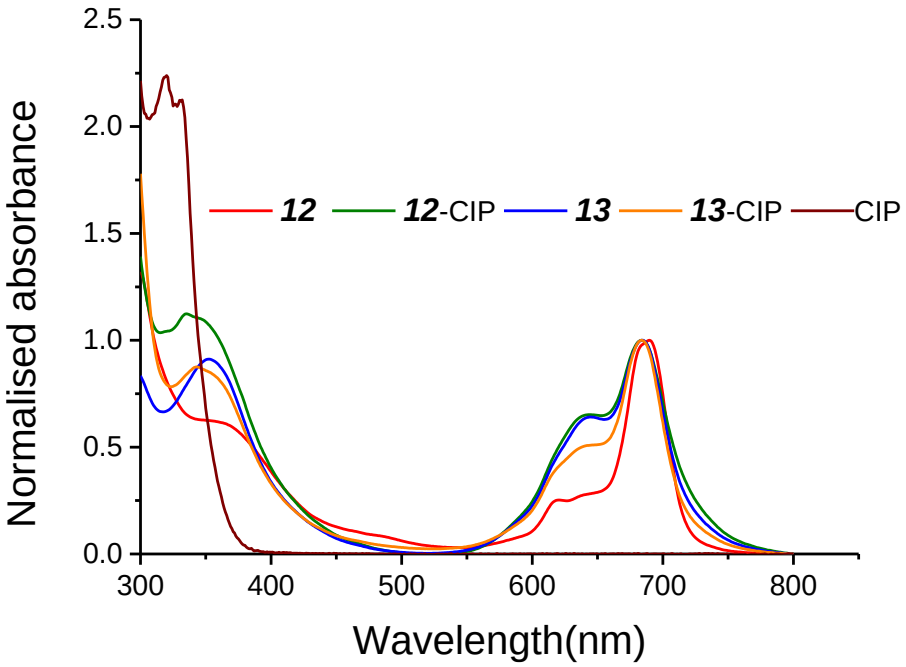

Figure 3.9: Overlay absorption spectra of CIP, *12*, *12*-CIP, *13*, and *13*-CIP in DMSO (Pc concentration ~ 2.0 x 10^{-6} M).

3.1.3 Lipophilicity measurement.

The lipophilicity (log $P_{octanol/water}$ ($P_{o/w}$)) measurements were determined to predict the ability of Pc complexes to diffuse to across a cell membrane. The log $P_{o/w}$ values were measured by the "shake-flask" method [179], and are presented as partition coefficients expressed in log $P_{o/w}$ for selected Pc complexes (**Table 3.1**). A negative log P_{oct} indicates hydrophilicity, whereas a positive value denotes a lipophilic nature. Bacteria membranes are characterised as lipids: hence the lipophilic complexes will diffuse most rapidly. The lipophilicity (log $P_{o/w}$) values of complexes ***4***-***6***, ***9***-***11***, ***9Q***-***11Q***, and ***12***-***13*** along with their corresponding conjugates ***12***-CIP and ***13***-CIP are determined as examples. The calculated log *P* values are ***4*** (0.47), ***5*** (−0.21) and ***6*** (−0.39). The value is positive for ***4*** indicating lipophilicity. Similarly, to complex ***4***, the calculated log $P_{o/w}$ values are positive for ***9***, ***10***, and ***11***, hence indicating lipophilicity.

The values are negative for ***5*** and ***6*** indicating hydrophilicity. Complex ***6*** gave a more negative value compared to ***5***, probably due to the two cationic charges present in ***6*** on each ring substituent as opposed to one charge for ***5***. For ***9Q*** (−0.17) > ***11Q*** (−0.16), > ***10Q*** (−0.18) the values are also negative indicating hydrophilicity. The values for the cationic ***9Q***, ***10Q***, and ***11Q*** are not too different. The same applies to ***9***, ***10***, and ***11***. Complexes ***12***, ***13*** along with their conjugates ***12***-CIP and ***13***-CIP gave log $P_{o/w}$ of –3.08, –3.87, –0.33, and 0.33, respectively. The higher lipophilic character of ***13***-CIP is attributed to the conformational composition of the complex and thus interacting more with the negatively charged cell wall [14], in addition to the introduction of the lipophilic CIP moiety [180] to the molecular structure of ***13***.

3.2 Nanoparticles (NPs) and composites

The reverse microemulsion synthetic route (**Scheme 3.7**) was used to encapsulate the Pc dye into SiNPs (**Pc**@SiNPs), this method encompasses, a solution of a Pc dye, water, and aqueous ammonia are combined with sufficient amounts of surfactant, cosurfactant, organic solvent, aqueous ammonia serves as both a catalyst (NH_3) and a reactant (H_2O) in the hydrolysis of TEOS. The surface of the **Pc**@SiNPs are further functionalised with an amino group for ease of surface modification, **Scheme 3.7**.

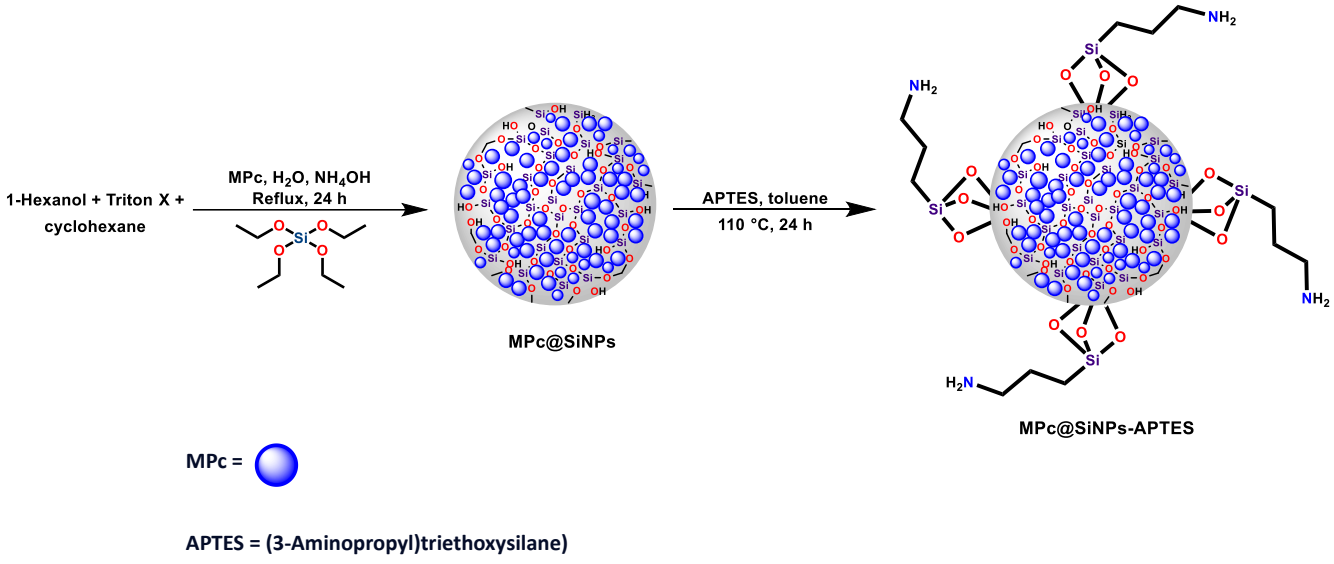

Scheme 3.7: Synthetic route for doping of Pc complexes (*1*, *1Q*, *2*, *3*, *7*, *8*, and *8Q*) into SiNPs and their amino functionalisation.

3.2.1 Pcs loading into SiNPs

The loading of Pc dye onto the SiNPs was assessed following literature methods [161], using UV-vis spectra. This involved comparing the Q-band absorbance intensity of the doped Pc conjugate with that of the Pc before conjugation. The loading values are shown in Table **3.2**. The loading is higher for PSn conjugates compared to AMP conjugates, this could be

attributed to the shorter reaction time, which could have resulted in less leaching of the Pc from silica matrix during the surface modification of **Pc**@SiNPs-APTES with PSn. The loading is higher for the cationic Pcs ***8*** and ***8Q***, compared to ***7***, this could be attributed to the greater binding between silica particles and cationic Pcs, which are negatively charged and positively charged [181], respectively. The difference in loading capacity of the Pcs is also attributed to the steric bulkiness of the Pc complexes.

3.2.2 Surface functionalisation of Pc@SiNPs-APTES and characterisation

For the surface functionalisation of the **Pc**@SiNPs-APTES, priority was given to ligands/molecules containing antimicrobial and anticancer properties with suitable linking moieties for ease of linkage to the surface Pc doped SiNPs-APTES, (**Figure 3.10; Scheme 3.8**).

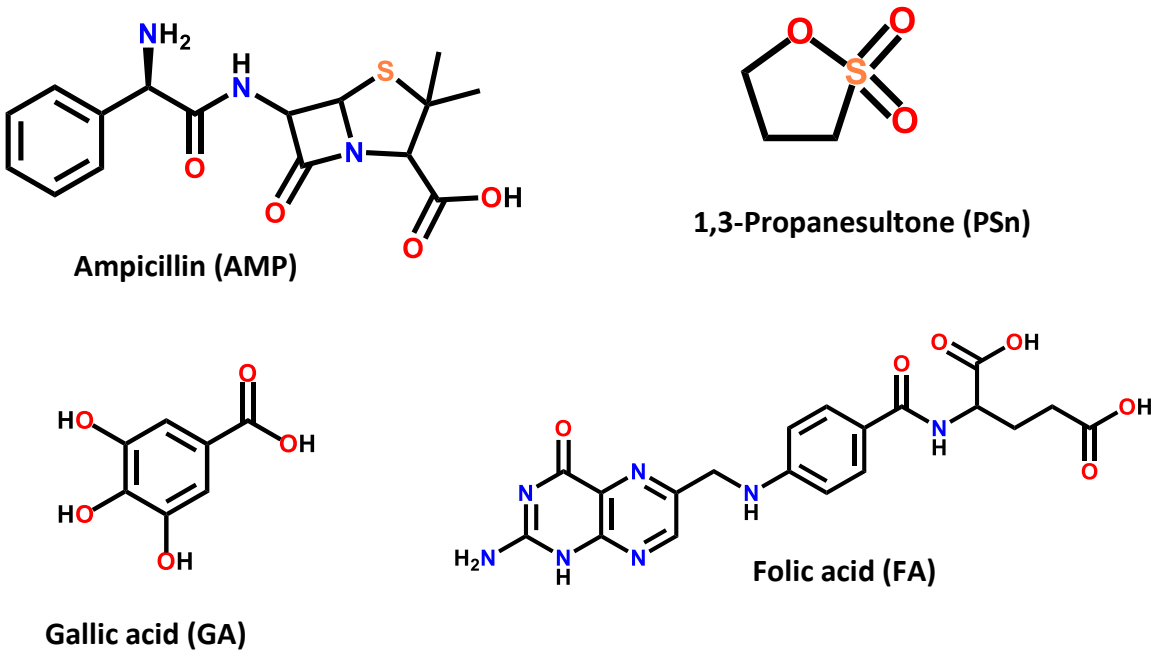

Figure 3.10: Representation of biomolecules used for surface functionalisation of Pc@SiNPs-APTES.

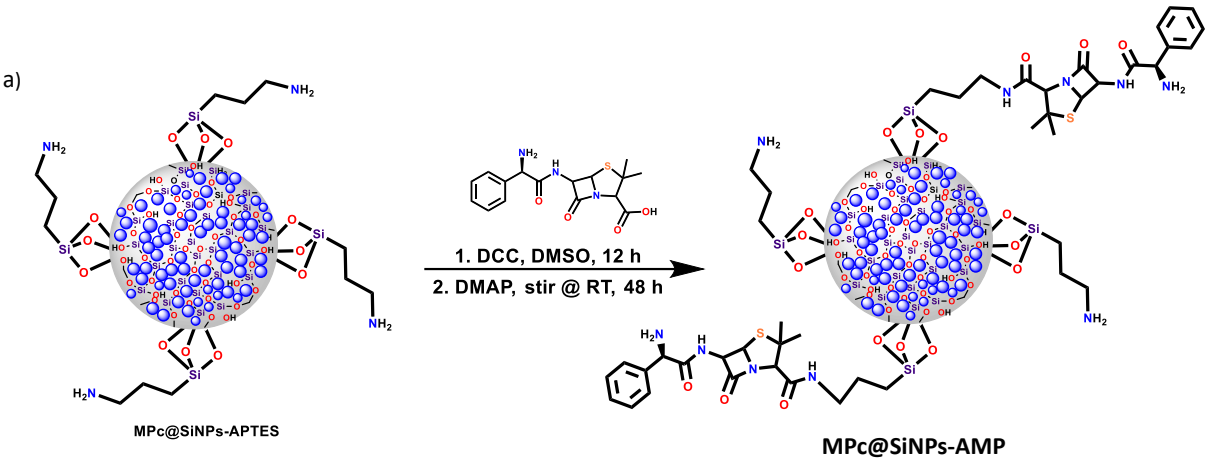
a)
MPc@SiNPs-APTES
1. DCC, DMSO, 12 h
2. DMAP, stir @ RT, 48 h
MPc@SiNPs-AMP

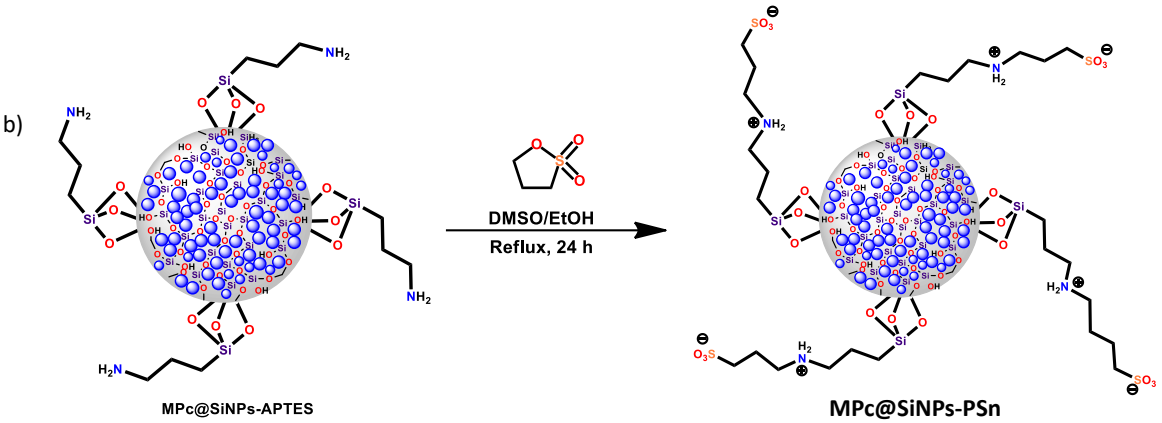
b)
MPc@SiNPs-APTES
DMSO/EtOH
Reflux, 24 h
MPc@SiNPs-PSn

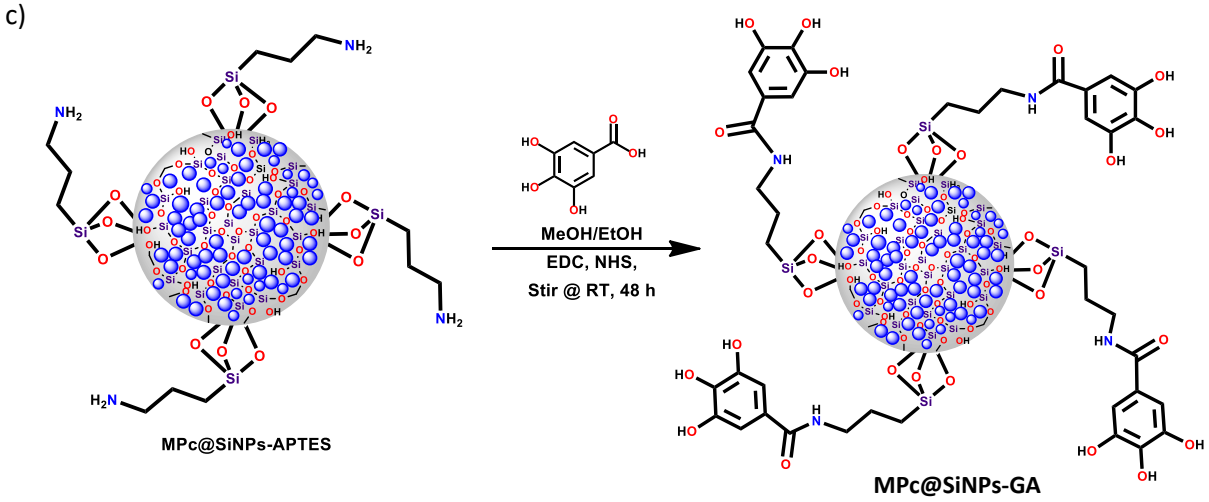
c)
MPc@SiNPs-APTES
MeOH/EtOH
EDC, NHS,
Stir @ RT, 48 h
MPc@SiNPs-GA

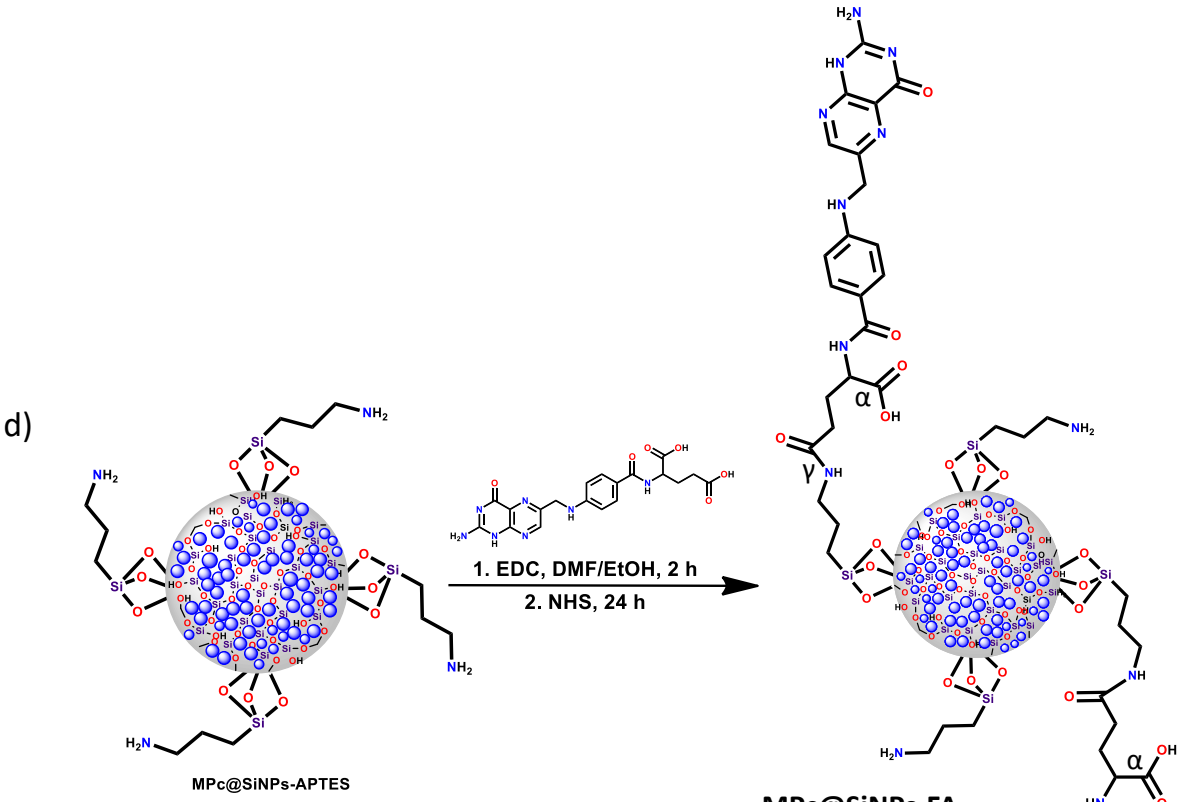

DMSO = Dimethylsulfoxide

DCC = *N, N'*-Dicyclohexylcarbodiimide

DMAP = 4-Dimethylaminopyridine

EtOH = Ethanol

EDC = 1-Ethyl-3-(3-dimethylaminopropyl) carbodiimide

NHS = N-Hydroxysuccinimide

MeOH = Methanol

Scheme 3.8: Synthetic route for surface functionalisation of Pc@SiNPs-APTES with a) ampicillin (AMP), b) 1,3-propanesultone (PSn), c) gallic acid (GA), and d) folic acid (FA).

Scheme **3.8** shows the surface fabrication of amino functionalised **Pc**@SiNPs-APTES with COOH group of gallic acid (GA), folic acid (FA), and ampicillin (AMP) via amide linkage. The protonation of **Pc**@SiNPs-APTES with 1.3-propanesultone (PSn) was also performed.

Table 3.2. DLS data, Loading and Q-band maxima (in DMSO) of the Pc@SiNPs conjugates synthesised.

Complex	DLS size (nm)[a]	Loading (µg Pc/mg SiNPs)	Q–band λ_{abs} (nm) of Pc@SiNPs-derivative	Q–band λ_{abs} (nm) of Pc alone
1@SiNPs-APTES	43.5 (40.2)	43	677	678
1@SiNPs-PSn	79.7	46	679	678
1@SiNPs-AMP	164.1	38	678	678
1Q@SiNPs-APTES	48.2	63	682	684
1Q@SiNPs-PSn	78.7	59	683	684
1Q@SiNPs-AMP	155.6	34	681	684
2@SiNPs-APTES	51.0	59	685	688
2@SiNPs-FA	58.3	48	685	688
3@SiNPs-APTES	53.2	43	685	684
3@SiNPs-FA	63.1	39	684	684
7@SiNPs-APTES	72	49	684	679
7@SiNPs-GA	126	43	689	679
8@SiNPs-APTES	44	77	691	687
8@SiNPs-GA	90	61	686	687
8Q@SiNPs-APTES	43	112	693	683
8Q@SiNPs-GA	79	98	689	683

[a]values in brackets are for SiNPs-APTES alone

3.2.2.1 FT-IR spectra and XPS

Figure 3.11 shows the FT-IR spectra of ***8Q***, ***8Q***@SiNPs-APTES, and ***8Q***@SiNPs-GA (as examples). A prominent siloxane band (Si—O—Si) at 1020–1166 cm^{-1} due to the presence of SiNPs. The absence of the primary amine from APTES vibrational band (at 1560 cm^{-1} in ***8Q***@SiNPs-APTES) along with the formation of a new vibrational band at 1647–1689 cm^{-1} (amide band O=C—NH) in (**Pc**@SiNPs-GA) indicate the formation of an amide bond [182].

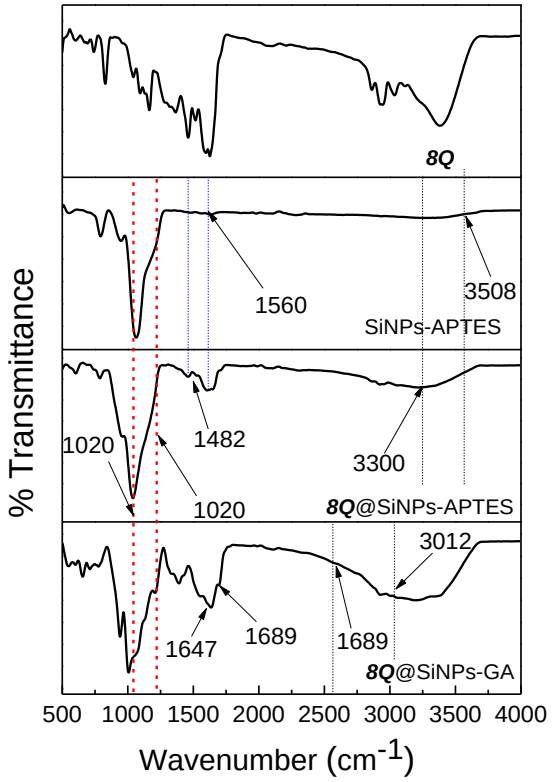

Figure 3.11: FT–IR spectra of complex *8Q* and its conjugates *8Q*@SiNPs-GA.

The protonation of ***1Q***@SiNPs-APTES to ***1Q***@SiNPs-PSn was confirmed by the shifts in the IR peak of siloxane band (Si—O—Si) from 1069 cm^{-1} in the former to 1128 cm^{-1} in the latter, and the introduction of the sulfonyl function band at 1021 cm^{-1}. **Figure A1 (b)** (Appendix) shows

covalent linkage of **Pc**@SiNPs-APTES to AMP to form **Pc**@SiNPs-AMP is proved by the shift in the position of the NH peak (3281 cm^{-1}) as well as the appearance of a peak at 1620 cm^{-1}.

FT-IR spectra was once more used to assess the linkage of FA to the surface of **Pc**@SiNPs-APTES. FA molecule possesses two carboxyl groups, termed α and γ, (Scheme **3.8**) which can act as handles for covalent attachment. Many folic acid conjugates form the covalent bond mainly through the γ carboxylic acid [183]. Thus, it is assumed in this work that coordination FA occurs mainly through the γ carboxylic acid. It has been reported that the α carboxylic acid moiety of FA disrupts folate receptor binding recognition more than the γ [184]. Following conjugation to FA the conjugates became partially water soluble.

The confirmation of an amide between FA and **Pc**@SiNPs-APTES is complicated by the fact that FA alone has amide bonds. Similarly, to ***8Q*** above, the encapsulation of the Pc complexes (using complex ***2*** as an example in this case) into SiNPs matrix is confirmed by the vibrational stretching of the siloxane band (Si—O—Si) in the 1063 cm^{-1}, **Fig 3.1**. The conjugation of folic acid to the surface of ***2***@SiNPs-APTES is confirmed by the shifts in the IR bands, as well as the vibrational stretching at 1618 cm^{-1}, **Fig 3.1** [183], in ***2***@SiNPs-FA and the slight broadening observed in the 3341 cm^{-1} regions. The latter vibration is due to the α or γ carboxylic OH group that did not take part in the amide bond formation, which provides evidence for the presence of folic acid on the surface **Pc**@SiNPs. For folic acid alone, the carbonyl peak shifts to 1698 cm^{-1} [182] when compared to ***2***@SiNPs-FA, indicating alterations.

The deconvoluted high resolution XPS N1s spectra of FA and ***2***@SiNPs-FA (as an example) are shown in **Figure 3.12**. The N 1s core level spectra for FA (**Figure 3.12**) could be fitted into three chemically distinct components with binding energies 397.2 eV, 397.8 eV and 399.5 eV due

to ($N_{in\ ring}$), (NH_2) and (CONH) bonds, respectively. The amide bond for FA (CONH) alone was observed 399.5 eV. This peak was still observed upon conjugation of FA to ***2***@SiNPs-APTES with an intensity of 3482 cps. A new peak (amide bond, N—H) at a binding energy 401.7 eV and an intensity 3702 cps was also observed confirming the interaction of ***2***@SiNPs-APTES with FA and the formation of ***2***@SiNPs-FA [185].

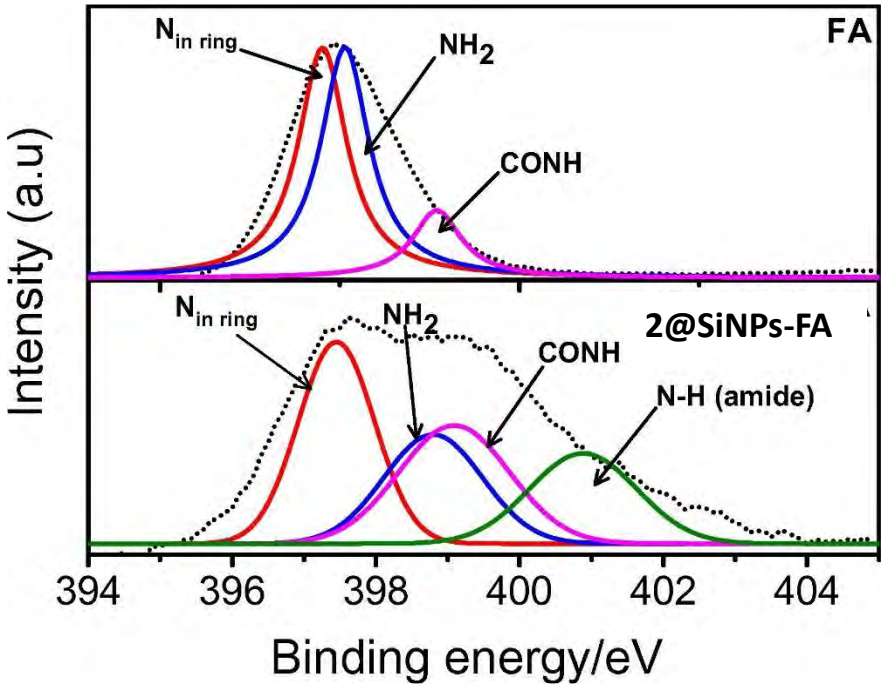

Figure 3.12: High resolution XPS N1s spectra of FA and *2*@SiNPs-FA.

3.2.2.2 Transmission electron microscope (TEM) and dynamic light scattering (DLS)

The morphology, dimensions and hydrodynamic diameter of synthesised **Pc**@SiNPs and the subsequent surface modified conjugates were measured using a transmission electron microscope (TEM) and dynamic light scattering (DLS). Using the Pc doped conjugates of complexes ***7***, ***8*** and ***8Q*** (as examples) **Figure 3.13**. TEM images show monodispersed particles for ***8Q***@SiNPs and ***8Q***@SiNPs-APTES but shows aggregation for ***8Q***@SiNPs-GA. Aggregation

in **Figure 3.13 (c)** for ***8Q***@SiNPs-GA as an illustration, may be due to possibility π-π stacking between the Pcs on adjacent NPs. Pcs are known for their π-π-stacking to form H aggregates [172]. All DLS plots (**Figure 3.14**) gave polydispersity index (PI) values between 0.10 -and 0.24. The size distributions of the analysed conjugate complexes are summarised on **Table 3.2**.

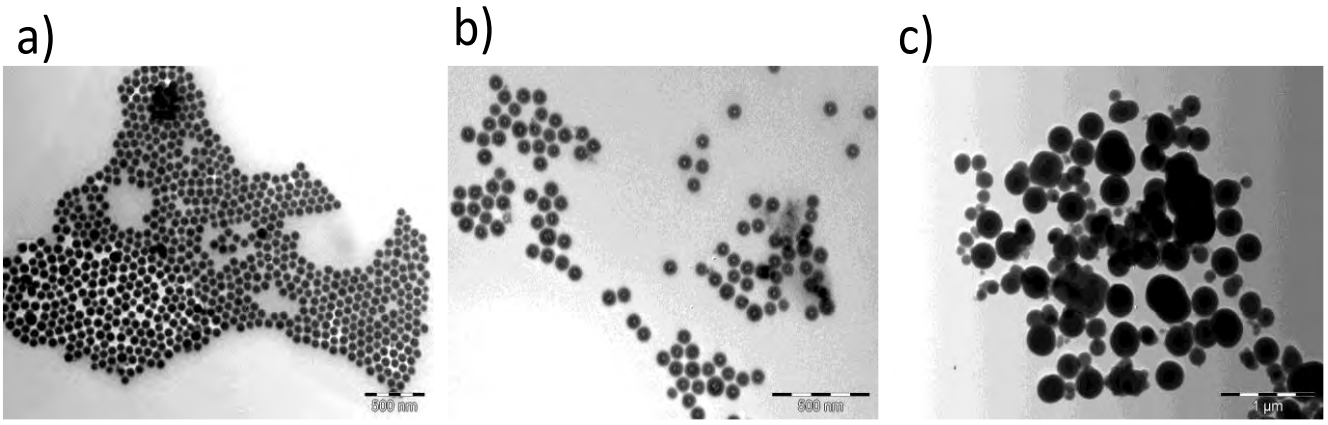

Figure 3.13: TEM images of synthesised Pc doped SiNPs for a) *8Q*@SiNPs, b) *8Q*@SiNPs-APTES and c) *8Q*@SiNPs-GA.

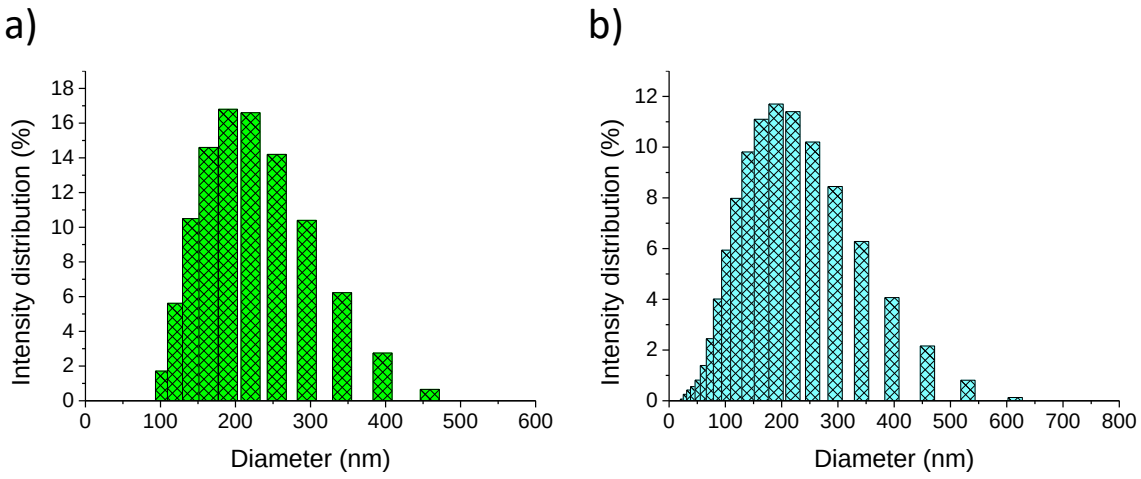

Figure 3.14: Dynamic light scattering of (a) *8Q*@SiNPs-APTES and (b) *8Q*@SiNPs-GA.

Using DLS, the average diameter of the surface modified **Pc**@SiNPs-APTES are measured to be around 72, 44 and 43 nm for complexes ***7***, ***8*** and ***8Q***, respectively, **Table 3.2**. Because of the GA linkage, the diameter of **Pc**@SiNPs-GA was slightly larger than that of APTES functionalised SiNPs, with average diameters of 126, 90, and 79 nm for ***7***@SiNPs-GA, ***8***@SiNPs-GA and ***8Q***@SiNPs-GA, respectively.

The electrostatic interactions play a pivotal role in PACT and drug delivery in general, as such, to validate the difference in the colloidal stability for the conjugates of Pc complexes ***7***, ***8*** and ***8Q*** specifically, surface zeta potential (ζ-potentials) was measured. The surface ζ-potentials for the Pc complexes alone are determined to be −12.03, 13.4, and 27.5 mV, for complexes ***7***, ***8*** and ***8Q***, respectively, **Table A2**. The values are negative for neutral ***7*** and positive for positively charged ***8*** and ***8Q***. ζ-potential value for GA alone of −10.5 mV was obtained, hence the values in the presence of GA are negative in **Table A2**. A high surface ζ-potentials (negative or positive) will confer stability, meaning the solution or dispersion will resist aggregation [186]. Low surface ζ-potentials values can undergo attractive forces that may exceed this repulsion resulting in aggregation.

3.2.2.3 UV–vis spectra

Upon encapsulation of complex ***1*** (as an example) into SiNPs in DMSO broadening of the Q band and enhancement of the B-band were observed in the absorption spectra of ***1***@SiNPs-APTES, ***1***@SiNPs-PSn and ***1***@SiNPs-AMP, **Figure 3.15 (a)**, this could be attributed to the enhanced absorption of AMP and PS around this region (**Figure 3.15 (b)**). Following the formation of ***1***@SiNPs-PSn, the UV–vis spectra of ***1***@SiNPs-PSn displayed a sharp peak at ~450 nm (**Figure 3.15 (a)**) which indicates the presence of a triazatetrabenzcorroles (TBC) complex [187,188], which are molecules resembling Pcs but lacking one of the nitrogen atoms

that bridges them. The TBC complexes are created when the Pc moiety in the MPc molecules is lost due to the elimination of the fourth azomethine nitrogen. This is attributed to the addition of PSn, which eliminates the Pc moiety's bridge nitrogen.

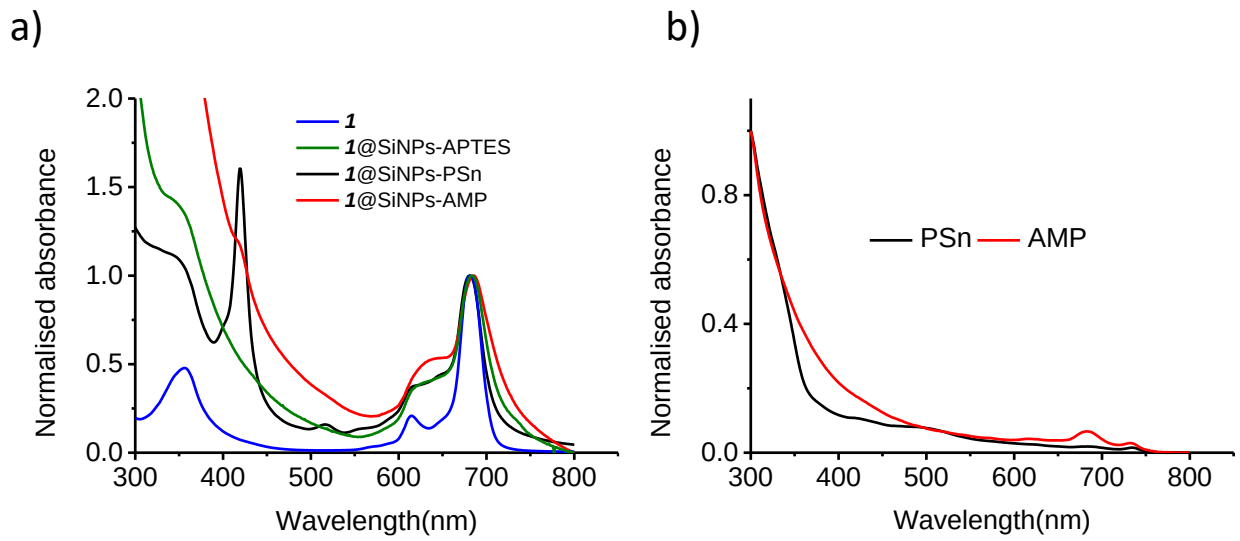

Figure 3.15: Absorption spectra of a) of *1*, *1*@SiNPs-APTES, *1*@SiNPs-PSn and *1*@SiNPs-AMP b) ampicillin (AMP) and 1.3-propanesultone (PSn) in DMSO.

The spectra of complexes ***1Q*** and its conjugates (***1Q***@SiNPs-APTES, ***1Q***@SiNPs-PSn and ***1Q***@SiNPs-AMP) in water show aggregation, **Figure 3.16.** Aggregation causes splitting and the broadening of the Q-band in Pcs due to the coplanar association of the Pc rings progressing from monomers leading to aggregates [172]. The absorption of SiNPs-APTES may also be a contributing cause to the enhanced absorption at 300 nm region (**Figure 3.16, insert**) in addition to the B-band enhancing contributions from PSn and AMP.

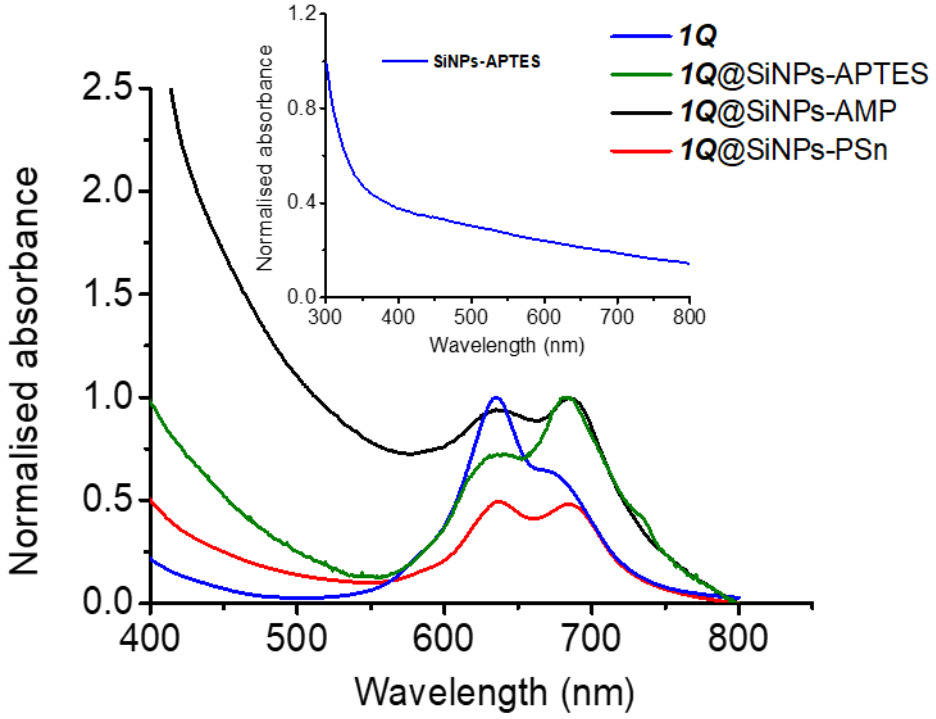

Figure 3.16: Absorption spectra of *1Q*, *1Q*@SiNPs-APTES, *1Q*@SiNPs-PS and *1Q*@SiNPs-AMP in water. Inset graph in shows SiNPs-APTES alone in DMSO.

In similar fashion to complexes ***1*** and ***1Q***, following the encapsulation of complexes ***7***, ***8*** and ***8Q*** (as examples) into SiNPs, a broadening of the Q band (due to aggregation) in spectra and enhancement of the B-band was observed, **Figure 3.17**. The broad B-band in the absorption spectra for ***7***@SiNPs-GA, ***8***@SiNPs-GA and ***8Q***@SiNPs-GA could be due to GA absorption, **Figure 3.17**. There is a red shift in the spectrum of ***8Q***@SiNPs-GA compared ***8Q***, but no significant shift ***8***@SiNPs-GA. Red shifts in the UV–vis spectra have been reported in distorted porphyrins [189].

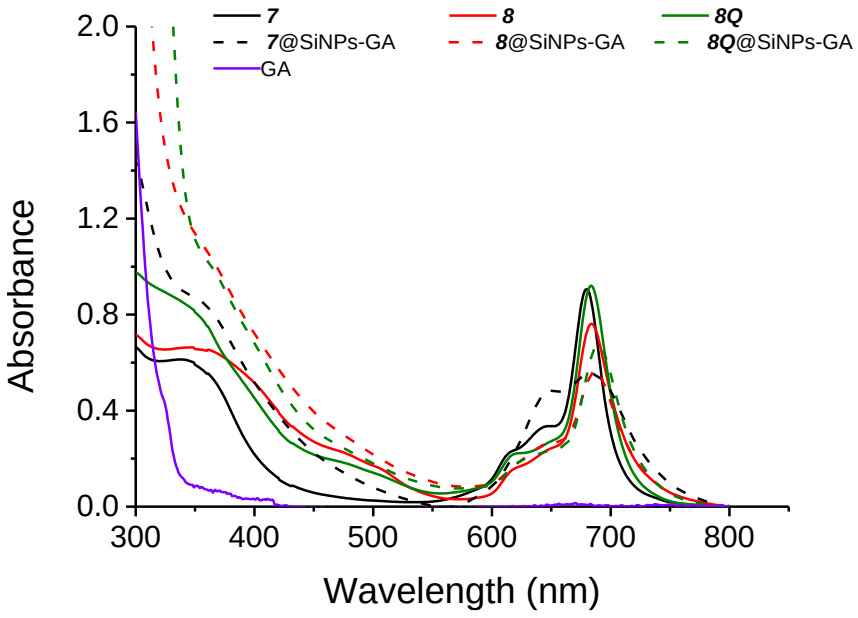

Figure 3.17: Overlay of absorption spectra of complexes *7*, *8* and *8Q* along with their conjugates *7*@SiNPs-GA, *8*@SiNPs-GA and *8Q*@SiNPs-GA and GA in DMSO, (concentration ~ 2.0 × 10^{-6} M).

3.2.2.4 Surface area and porosity using the Brunauer–Emmett–Teller (BET) technique

BET was performed to determine the N_2 adsorption/desorption isotherms, surface area, and pore size distribution of the Pc doped SiNPs material as shown in **Figure 3.18**, using conjugates of complex *8Q* as an illustration. The Pc doped SiNPs showed type IV isotherm for a) *8Q*@SiNPs, b) *8Q*@SiNPs-APTES, and c) *8Q*@SiNPs-GA which is typical of mesoporous material. The surface area for *8Q*@SiNPs was 10.99 m^2/g with a pore volume of 0.14 cm^3/g and pore size of 52.1 nm (**Table 3.3**).

Table 3.3. Porous textural parameters derived from the N_2 adsorption isotherms at -196 °C for ***8Q***@SiNPs, ***8Q***@SiNPs-APTES and ***8Q***@SiNPs-GA.

Sample	BET surface area (m^2/g)	Pore volume (cm^3/g	Pore size (nm)
8Q@SiNPs	10.99	0.14	52.1
8Q**@**SiNPs-APTES	6.37	0.045	28.34
8Q@SiNPs-GA	2.59	0.013	19.3

Upon functionalisation with APTES and GA a decrease in all parameters was observed as a consequence of the APTES and GA ligands inhabiting parts of the Pc doped SiNPs. It has been reported that rough surface increases surface area [190]. Thus, the decrease in surface area implies that the functionalization smoothens the surface of the doped SNPs resulting in blockage in porosity of certain parts of the SiNPs.

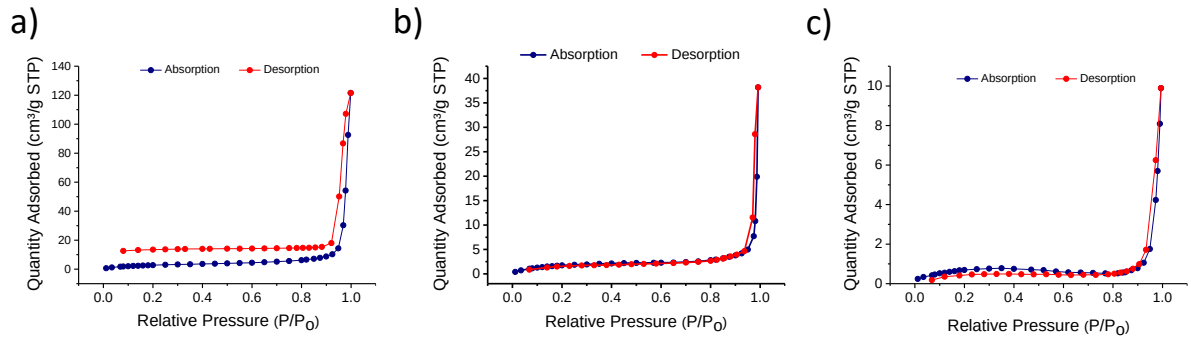

Figure 3.18: Nitrogen adsorption–desorption BET isotherms of a) *8Q*@SiNPs, b) *8Q*@SiNPs-APTES and c) *8Q*@SiNPs-GA.

3.3 Summary of chapter

This chapter makes explicit reference to the synthesis, characterisation, and surface functionalisation of phthalocyanine encapsulated silica nanoparticles. In DMSO, the Pcs' ground state electronic absorption spectra showed typical monomeric activity. For the synthesised Pc complexes, a narrow Q band was seen between 670 and 690 nm and a broad B band between 300 and 350 nm. A broadening in spectra and amplification of the B-band were seen when the Pc-SiNPs conjugates were enclosed and surface functionalised.

TEM micrographs of all the NPs demonstrated their spherical morphology and distributed particle sizes. When the Pc doped SiNPs' surface is functionalised with PSn, AMP, FA, and GA, significant aggregation is seen. Amide bonds were validated using FT-IR and XPS spectra, demonstrating that the conjugates were successfully synthesised.

CHAPTER FOUR
PHOTOPHYSICS AND PHOTOCHEMISTRY

Complexes ***1***, ***1Q***, ***2***-***11***, ***8Q***-***11Q***, as well as ***12*** and ***13***—and, if relevant, their corresponding conjugates—all underwent these studies. Long alkyl chain groups are known to lower fluorescence in Pcs and increase the rate of intersystem crossing [191], and the presence of a central zinc metal on the Pc macrocycle causes a significant increase in the spin-orbit coupling [192,193]. These factors, as well as the insertion of a functional group containing heteroatoms like the sulfur atoms, are discussed below. Rapid intersystem crossing rates have been observed in complexes with the phenyl bridge, which frequently explains the densely populated triplet state [194]**.** It is expected that Pcs containing these properties will show improved triplet state properties leading to effective singlet quantum yield generation.

4.1 Fluorescence (Φ_F) quantum yields and lifetimes (τ_F).

4.1.1 Pc and their Pc doped SiNPs conjugates

The Φ_F values of Pcs and their conjugates were determined as described in the literatures [142,143]. The fluorescence lifetime (τ_F) was determined using time correlated single photon counting set–up [141]. Since Φ_F and τ_F are complimentary processes, when one of them declines, the other will likewise increase.

Equation **1.1** was used to calculate the Φ_F of the Pcs and their conjugates, which is accomplished by exciting at a crossover wavelength between the sample and the standard. The Φ_F of the complexes is typical of zinc Pcs in DMSO. The Φ_F range from 0.08 to 0.18 for ***1*** and its doped conjugates, **Table 4.1**. Upon quaternisation there was a slight increase in Φ_F that ranged from 0.16 to 0.20. For ***1Q*** and its conjugates the τ_F were long where Φ_F were

high as expected. For ***1*** and its conjugates, there is no clear trend. Pc complexes ***2*** and ***3*** and their respective conjugates have relatively low Φ_F owing to electron-donating feature of Schiff groups. Complex ***2*** and its conjugates have lower Φ_F compared to ***3*** and its conjugates due to the four extra Schiff base groups on the structure of ***2***. The τ_F were all very low (<0.01 ns), **Table 4.1**.

For the Φ_F of complexes ***4***, ***5***, and ***6***, it was found that ***5*** and ***6*** had lower Φ_F values than ***4***, **Figure 4.1**. This shows that the substituents **PyB** and **PyBP** significantly quenched the excited singlet state of the complexes. Long alkyl chain groups are known to decrease Pcs fluorescence and increase the rate of intersystem crossing [191] which accounts for the drop in Φ_F for ***5*** and ***6***. As the Φ_F drops, the τ_F shortens.

Pc complexes ***7***, ***8*** and ***8Q*** as well as conjugates, showed negligible changes in Φ_F and τ_F, **Table 4.1**. Comparing complexes ***9***-***11*** and ***9Q***-***11Q***, which contain the same ring substituents but different nitrogen substitution locations, revealed similar results. Hence, the Pc complexes ***9Q***, ***10Q*** and ***11Q*** showed negligible changes in Φ_F in comparison to their respective precursor counterparts, ***9***, ***10*** and ***11***.

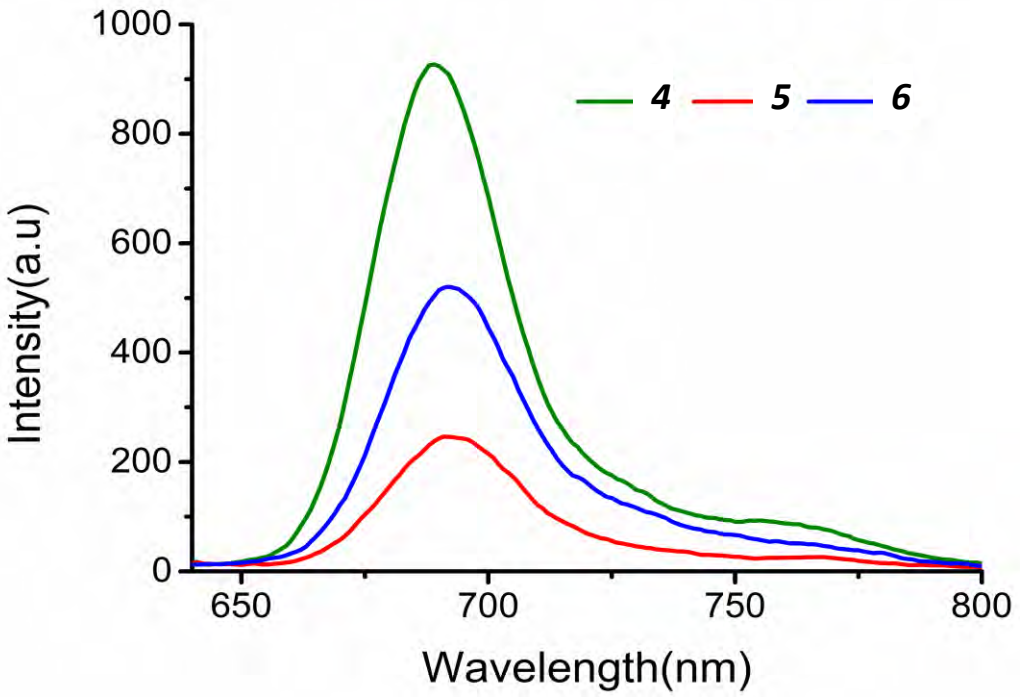

Figure 4.1: Emission spectra *4*, *5* and *6* in DMSO when excited at the respective Q-band (Absorbance of complexes were maintained ≤ 0.1).

4.1.2 Pc conjugates with CIP

The increase in the spin–orbit coupling [192,193], as a result of the sulfur atoms on complexes ***12*** and ***13***, is responsible for the low Φ_F values for Pc complexes ***12*** and ***13*** when alone, **Table 4.1**. There is a slight increase in Φ_F values in the presence of CIP. The increase could be due to the fact that CIP is also fluorescent [195].

Table 4.1: Fluorescence quantum yield and lifetime parameters of the Pcs and the respective conjugates, all studies were measure in DMSO.

Complex	Φ_F	τ_F (ns)
1	0.12	3.06
1@SiNPs-APTES	0.10	2.46
1@SiNPs-PSn	0.08	2.51
1@SiNPs-AMP	0.18	2.82
1Q	0.20	3.14
1Q@SiNPs-APTES	0.13	2.54
1Q@SiNPs-PSn	0.16	2.68
1Q@SiNPs-AMP	0.19	2.77
2	<0.01	<0.01
2@SiNPs-APTES	<0.01	<0.01
2@SiNPs-FA	<0.01	<0.01
3	0.18	<0.01
3@SiNPs-APTES	0.12	<0.01
3@SiNPs-FA	0.09	<0.01
4	0.12	2.89
5	0.03	2.84
6	0.06	1.08
7	0.05	2.32
7@SiNPs-APTES	0.03	1.75
7@SiNPs-GA	0.01	0.75
8	0.02	1.76
8@SiNPs-APTES	0.02	1.18

8@SiNPs-GA	0.01	1.00
8Q	0.02	1.19
8Q@SiNPs-APTES	0.03	1.02
8Q@SiNPs-GA	<0.01	1.17
9	0.17	2.02
9Q	0.15	1.92
10	0.24	2.39
10Q	0.23	1.97
11	0.03	2.32
11Q	0.02	0.89
12	0.025	1.39
12-CIP	0.031	2.14
13	0.044	2.20
13-CIP	0.058	3.02

4.2 Triplet (Φ_T) quantum yield and lifetime (τ_T)

An excited triplet state for Pcs is essential in evaluating the ability of Pcs to generate singlet oxygen which is critical for PS-related applications. The triplet state absorption measurements were conducted using the laser flash photolysis setup. The laser excitation wavelengths were at the crossover wavelengths. A UV-visible spectrophotometric cell with a 1 cm path length was filled with the solution, and purged with nitrogen for 20—40 min before measurements. Equation **1.2** was used to calculate the Φ_T of the Pcs and their conjugates. A time-evolved electronic absorption from the T_1–T_n state appeared after the solution was sealed and irradiated with the proper excitation laser source and detection wavelength. The triplet lifetimes (τ_T) were analysed from the triplet decay curve shown in **Figure 4.2** using ***4*** as an

example, and all the Pc complexes were found to follow second-order kinetics, which is representative of Pcs complexes at high concentration, owing to triplet–triplet recombination [196].

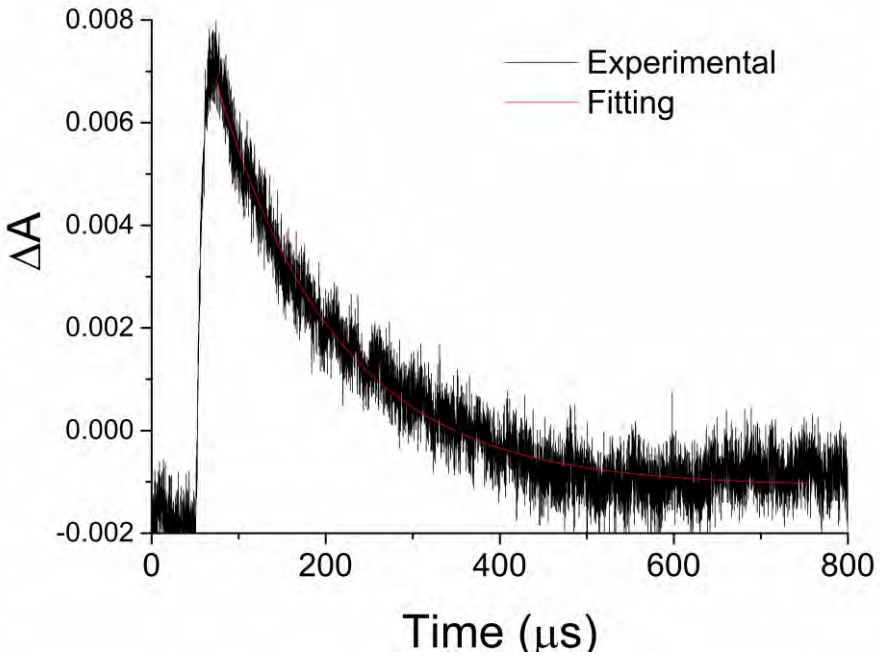

Figure 4.2: Excited triplet state absorption curve of complex *4* in DMSO.

4.2.1 Pc and their Pc doped SiNPs conjugates

The Φ_T and Φ_F values are competing processes; hence the former will be smaller where the latter is larger, as is the case in **Tables 4.1** and **4.2**. For ***1***, the Φ_T values for ***1***@SiNPs-PSn increase while that of ***1***@SiNPs-AMP drops compared to ***1***@SiNPs-APTES. In comparison to ***1Q*** alone, the Φ_T values for ***1Q***@SiNPs-PSn and ***1Q***@SiNPs-AMP drop (**Table 4.2**). Another explanation for the decline in Φ_T is non-radiative processes that take place when the Pc is trapped inside the matrix of the SiNPs [197]. Triplet lifetimes were shorter for ***1Q*** and longer

for ***1*** in the presence of SiNPs. The fact that SiNPs shield the Pcs from the outside environment may be the cause of an increase in τ_T.

When compared to their SiNPs-APTES doped equivalents in DMSO, the Pcs complexes alone, ***2*** and ***3*** exhibit larger Φ_T values as stated above. The energy lost when the Pcs are enclosed inside the silica matrix is the cause of the fall in Φ_T of the doped conjugates. It has been previously reported [198] that the presence of FA causes an increase in Φ_T. For ***2***@SiNPs-FA, τ_T lengthened as Φ_T increased compared to ***2*** alone or ***2***@SiNPs-APTES. The triplet-triplet annihilation effect [199] is attributed for the rise in Φ_T. According to expectations, for ***3***, Φ_T increases where τ_T decreases and vice versa [200]. The Φ_T values found for ***4***, ***5***, and ***6*** are 0.62, 0.71, and 0.69, respectively (**Table 4.2**). The intersystem crossing mentioned above is connected to the larger values for ***5*** and ***6*** [196].

Table 4.2 shows that for Pc complexes ***7***, ***8*** and ***8Q***, the doped conjugates had lower Φ_T values than their undoped counterparts. The decrease in Φ_T is again caused by non-radiative processes that occur when the Pc is trapped within the SiNPs matrix [197]. The τ_T was shortened in the presence of SiNPs and GA compared to Pcs alone, corresponding to the decrease in Φ_T, as seen in **Table 4.2**. However, when comparing Pc@SiNPs-APTES to Pc@SiNPs-GA, there is a reduction in τ_T where Φ_T increases for complexes ***7*** and ***8Q***.

Φ_T values for precursor complexes ***9***, ***10***, and ***11***, were 0.71, 0.76, and 0.80, respectively. Complex ***11*** (ortho) had a greater Φ_T value than complexes ***10*** (meta) and ***9*** (para). Φ_T values of 0.83, 0.81, and 0.84 were obtained for the cationic derivatives ***9Q***, ***10Q***, and ***11Q***, respectively. Thus, complexes ***9Q***, ***10Q***, and ***11Q***, had higher Φ_T values than their predecessor

complexes. The presence of heteroatoms like sulphur placed on the cationic Pc complexes ***9Q***, ***10Q***, and ***11Q*** increases spin-orbit coupling and, as a result, stimulates intersystem crossing to the triplet state [201]. Improved efficiency in spin-orbit coupling is known to shorten τ_T and increase Φ_T [200], as observed in **Table 4.2**.

4.2.2 Pc conjugates with CIP

The Φ_T values obtained for ***12***, ***12***-CIP, ***13*****,** and lastly ***13***-CIP are 0.78, 0.80, 0.71, and 0.84 (**Table 4.2**), respectively. The values slightly increase in the presence of CIP, yet there is also an increase in Φ_F. The increase in Φ_T in the presence of CIP could be due to the additional C=O groups which are known to enhance intersystem crossing [202]. A shortening in τ_T values upon linking CIP to the Pc complexes was observed, corresponding to increase in Φ_T. The large shortening of τ_T for complex ***12*** and ***13*** in the presence of CIP, could be due to aggregation, **Figure 3.9**. In addition, as stated above increases in the triplet state population is known to shorten the τ_T [200].

Table 4.2: Triplet quantum yield and lifetime parameters of the Pcs and the respective conjugates, all studies were measure in DMSO.

Complex	Φ_T	$\tau_{T(\mu s)}$
1	0.65	203
1@SiNPs-APTES	0.69	218
1@SiNPs-PSn	0.76	247
1@SiNPs-AMP	0.59	235
1Q	0.82	262
1Q@SiNPs-APTES	0.80	257
1Q@SiNPs-PSn	0.73	251
1Q@SiNPs-AMP	0.69	242
2	0.69	205
2@SiNPs-APTES	0.67	317
2@SiNPs-FA	0.71	284
3	0.63	303
3@SiNPs-APTES	0.52	342
3@SiNPs-FA	0.77	296
4	0.62	137
5	0.71	134
6	0.69	404
7	0.67	83
7@SiNPs-APTES	0.59	68
7@SiNPs-GA	0.61	53
8	0.77	56
8@SiNPs-APTES	0.71	23
8@SiNPs-GA	0.69	18

8Q	0.85	65
8Q@SiNPs-APTES	0.64	41
8Q@SiNPs-GA	0.81	23
9	0.71	187
9Q	0.83	156
10	0.76	170
10Q	0.81	152
11	0.80	322
11Q	0.84	251
12	0.78	359
12-CIP	0.80	32
13	0.71	208
13-CIP	0.84	22

4.3 Singlet quantum yield (Φ_Δ)

4.3.1 Pc and their Pc doped SiNPs conjugates

The singlet oxygen quantum yield (Φ_Δ) generation efficiencies of the Pc complexes were evaluated in DMSO by using 1,3-diphenylisobenzofuran (DPBF) and 9,10-antracenediyl-bis(methylene)dimalonoic acid (ADMA) in water as singlet oxygen scavengers. DPBF degradation was spectroscopically monitored at ~417 nm at predetermined time intervals. ADMA was used as a singlet oxygen quencher in water using AlPc–Smix containing a mixture of sulfonated derivatives (synthesised as reported in literature [156]), **Figure 4.3**. The Pcs and their conjugates Φ_Δ were calculated using Equation **1.4**. The Φ_Δ and Φ_T are

complimentary processes; a high number of triplet state molecules is expected to result in increased $\Phi_\Delta$values. Φ_Δ values are lower in water due to quenching of singlet oxygen [203], but they follow the same trend as observed in DMSO, **Table 4.3**.

In addition, oxygen has higher solubility in many organic solvents compared to water [204], which could be responsible for low singlet oxygen generation in water.

The increase in the Φ_Δ for ***1Q*** and its conjugates compared to ***1*** and its corresponding conjugates is attributed to the fact that the nitrogen groups quench the first excited singlet state through fast charge transfer, inhibiting the formation of its triplet state by intersystem crossing [205]. The lone pair of electrons are engaged following quaternization in ***1Q*** hence are not involved in quenching the first excited state as is the case with ***1***. The same applies to the conjugates containing PSn compared to APTES and AMP containing conjugates, where the PSn conjugates containing positively charged nitrogen groups have larger triplet and singlet oxygen quantum yields compared to the conjugates containing APTES and AMP, **Table 4.3**.

As previously stated, Φ_Δ and Φ_T are complementary processes, thus is expected to increase when Φ_T increases and vice versa. **Table 4.3** shows this tendency for complexes ***2***-***11***, ***8Q***, ***9Q***-***11Q***. However, as seen in **Table 4.3,** complexes ***11*** and ***11Q*** have a high Φ_T even though they showed aggregation but show low Φ_Δ. This could be due to the screening effect [206] of the aggregates in complex ***11***, which could limit access to the oxygen molecule and therefore reducing Φ_Δ. Similarly; in the presence of SiNPs, a decrease in Φ_Δ might also be due to the screening effect, in which SiNPs prevent oxygen molecules from engaging with excited triplet Pc [206].

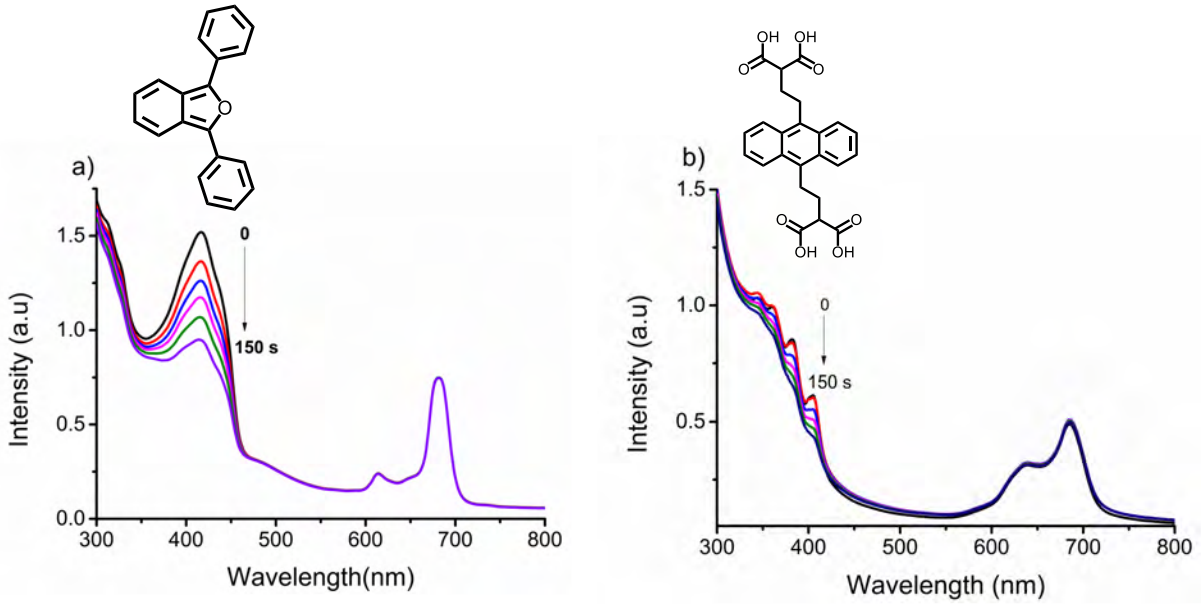

Figure 4.3: Photochemical degradation of 1, 3-diphenylisobenzofuran (DPBF) a) and 9,10-antracenediyl- bis(methylene)dimalonoic acid (ADMA) b) in the presence of *5* in DMSO and aqueous medium, respectively.

4.3.2 Pc conjugates with CIP

The measurements yielded Φ_{Δ} values of 0.45, 0.66, 0.54, and 0.61 for complexes ***12***, ***12***-CIP, ***13***, and ***13***-CIP, respectively. As stated above the efficiency of singlet oxygen generation is depended on the triplet state population. Thus, the Φ_{Δ} values are high where Φ_{T} values are high.

Table 4.3: Photophysicochemical parameters of the Pcs and their respective conjugates.

Complex	Media	Φ_T	Φ_Δ
1	DMSO	0.65	0.42
1@SiNPs-APTES	DMSO	0.69	0.44
1@SiNPs-PSn	DMSO	0.76	0.47
1@SiNPs-AMP	DMSO	0.59	0.38
1Q	DMSO	0.82	0.57
	1%DMSO–H_2O	—	0.15
1Q@SiNPs-APTES	DMSO	0.80	0.51
1Q@SiNPs-PSn	DMSO	0.73	0.54
	1%DMSO–H_2O	—	0.19
1Q@SiNPs-AMP	DMSO	0.69	0.46
	1%DMSO–H_2O	—	0.13
2	DMSO	0.69	0.39
2@SiNPs-APTES	DMSO	0.67	0.42
2@SiNPs-FA	DMSO	0.71	0.45
3	DMSO	0.63	0.41
3@SiNPs-APTES	DMSO	0.52	0.38
3@SiNPs-FA	DMSO	0.77	0.43
4	DMSO	0.62	0.44
5	DMSO	0.71	0.62
	1%DMSO–H_2O	—	0.32
6	DMSO	0.69	0.53
	1%DMSO–H_2O	—	0.46
7	DMSO	0.67	0.49

7@SiNPs-APTES	DMSO	0.59	0.44
7@SiNPs-GA	DMSO	0.61	0.39
8	DMSO	0.77	0.48
	1%DMSO–H_2O	—	0.13
8@SiNPs-APTES	DMSO	0.71	0.29
8@SiNPs-GA	DMSO	0.69	0.39
	1%DMSO–H_2O	—	0.03
8Q	DMSO	0.85	0.76
	1%DMSO–H_2O	—	0.18
8Q@SiNPs-APTES	DMSO	0.64	0.16
8Q@SiNPs-GA	DMSO	0.81	0.58
	1%DMSO–H_2O	—	0.07
9	DMSO	0.71	0.68
9Q	DMSO	0.83	0.79
	1%DMSO–H_2O	—	0.14
10	DMSO	0.76	0.70
10Q	DMSO	0.81	0.75
	1%DMSO–H_2O	—	0.10
11	DMSO	0.80	0.24
11Q	DMSO	0.84	0.27
	1%DMSO–H_2O	—	0.07
12	DMSO	0.78	0.45
	1%DMSO–H_2O	—	0.07
12-CIP	DMSO	0.80	0.66
	1%DMSO–H_2O	—	0.11
13	DMSO	0.71	0.54
	1%DMSO–H_2O	—	0.16

13-CIP	DMSO	0.84	0.61
	1%DMSO–H_2O	—	0.20

4.4 Summary of chapter

In solution, the photophysics and photochemistry of Pcs and their conjugates were investigated. All of the Pcs investigated demonstrated good photophysicochemical behaviour, with reasonably high triplet and singlet quantum yields. In comparison to neutral Pc macrocycles, Pc macrocycles with water solubilizing groups had higher triplet and singlet quantum yields. In compared to the Pcs alone, the Pc SiNPs doped conjugates demonstrated a decrease in triplet and singlet quantum yields.

Because of inefficient energy transfer, screening effects may have inhibited the interaction of the excited triplet state of the Pcs with the ground state molecular oxygen, resulting in reduced singlet oxygen quantum yield values. In other circumstances, the elongation of triplet lifetime could be attributed to the SiNPs' protection of the Pcs. In comparison to Pcs alone, the direct coupling of Pcs with CIP resulted in an increase in triplet and singlet oxygen quantum yield generation.

CHAPTER FIVE
IN-VITRO CELL STUDIES

5.1 Background on Photosensitizers used

For the photodynamic antimicrobial (PACT) studies complexes ***1***, ***1Q***, ***4-11***, ***8Q-11Q***, as well as ***12*** and ***13***—and, if relevant, their corresponding conjugates were considered for *In*-vitro analysis. Complexes ***2-6*** along with the doped conjugates of ***2*** and ***3*** are considered for application in photodynamic therapy (PDT).

The piperidine substituent on complexes ***1*** and ***1Q*** was chosen for quaternization but in addition, piperidine substituents have antimicrobial activity [207]. The bulky nature of piperidine will also help to prevent aggregation. Piperidine substituted Pcs containing a phenyl spacer has been reported for applications in DNA cleavage [208]. Complexes ***1*** and ***1Q*** are then loaded onto SiNPs and further linked to ampicillin (AMP) and 1, 3-propanesultone (PSn), these are expected to improve PACT activity by synergistic effect for the former and extra positive charges for the latter.

Complexes ***2*** and ***3*** with a Schiff base substitution are employed as PSs for PDT. For the investigations of photophysicochemical behaviour and for PACT, Schiff base Pcs have been described [209–212]. Given that both ZnPc derivatives and Schiff base compounds are anticancer-compounds, combining the two may enhance PDT through a synergistic effect. Complexes ***2*** and ***3*** are also encapsulated in SiNPs and folic acid (FA) is used to further modify the Pc doped SiNPs surface and studied for PDT activity using MCF-7 cell line.

For complexes ***4-8*** and ***8Q-11Q***, the impact of the number of cationic charges is examined. By utilising biological targeting agents, the cationic styryl pyridine triphenylphosphonium (**PyBP**)-based Pc complex ***6*** (with ***4*** and ***5*** serving as a reference Pc complexes) is utilised to increase specificity. It is well known that compounds that target the mitochondria are based on **PyBP**

type substituents, which have redox-signaling processes in cancer and neurological cells [213,214]. Additionally, precise mitochondrial targeting enhances the accuracy and potency of medications. Using *Escherichia coli* (*E. coli*) and MCF-7 breast cancer cells as the targeted biological agents, respectively, complexes ***4***, ***5*** and ***6*** are used in PACT and PDT.

Complexes ***7***, ***8***, and ***8Q*** are encapsulated into SiNPs with the surface additionally connected with gallic acid (GA) to advance the PACT activity against *S. aureus* and *E. coli*. To investigate the effects of group location and charge on complexes, positively charged thioazoline derivatised substituent, 3-(4-bromobutyl)-2-mercapto-4,5-dihydrothiazol-3-ium bromide **(BMDBr**) are added to the periphery of complexes ***9***, ***10*** and ***11*** to form ***9Q***, ***10Q***, and ***11Q***, respectively. Thioazoline derivatives are well-known antibacterial agents [215,216], hence it is anticipated that they will enhance Pc complexes' PACT activity. *E. coli* and *S. aureus* are used to test the PACT activity of complexes ***7***-***11*** and ***8Q***-***11Q*** on planktonic and biofilm forms of bacteria.

Asymmetrically substituted Pcs containing benzothiazole and carboxylic acid groups (***12***) is linked to **PyBP** to form ***13***. Both ***12*** and ***13*** are then linked to the antibiotic ciprofloxacin (CIP) via the secondary amine of the piperazine ring of the latter using an amide linkage to form ***12***-CIP and ***13***-CIP. This is the first time that Pcs have been covalently linked to CIP. ***13*** and ***13***-CIP contain cationic amphiphilic groups which enhance the electrostatic interactions to the biofilms [32]. The conjugates ***12***-CIP and ***13***-CIP are evaluated for the PACT activity using *E. coli* and *Streptococcus pneumoniae* (*S. pneumoniae*) and on planktonic and biofilm forms.

5.2. Photodynamic antimicrobial chemotherapy (PACT)

5.2.1 Planktonic antimicrobial activity of symmetric Pc and their Pc doped SiNPs conjugates (effect of the number of charges, position of nitrogen group, and effect of surfactant on SiNPs)

The plate count method [217] was used to examine the planktonic antimicrobial activity of the Pc complexes and composites studied for PACT. A significant decrease in cell viability after exposure to PS and laser radiation indicates substantial PACT activity, which can be further demonstrated by a high log reduction value of colony forming units per millilitre (log CFU/mL). The PACT activity of ***1Q*** and its conjugates ***1Q***@SiNPs-APTES, ***1Q***@SiNPs-AMP and ***1Q***@SiNPs-PSn was carried out towards *S. aureus* at a constant concentration of 45 mg/L at varied irradiation time in PBS, **Figure 5.1 (a)**. The concentration (45 mg/L) was used since it gave reasonable log reduction values and minimal dark toxicity (see **Figure A6**). Dark toxicity was very high beyond 45 mg/L. Complex ***1Q***, ***1Q***@SiNPs-APTES, ***1Q***@SiNPs-AMP and ***1Q***@SiNPs-PSn were also used for dark toxicity studies **Figure 5.1 (b)**, where bacteria viability above 85 % was obtained for all complexes. **Figure 5.1 (b)** shows that there is some dark toxicity in the presence of PSn and AMP this is due to the antimicrobial activity discussed in the introduction for AMP and PSn. Upon 60 min irradiation illumination with 680 nm light, log reduction values of 9.20, 9.30, 9.31 and 9.37 were obtained for complex ***1Q***, ***1Q***@SiNPs-APTES, ***1Q***@SiNPs-PS, and ***1Q***@SiNPs-AMP, respectively (**Table 5.1**).

The antimicrobial property of SiNPs-APTES, AMP and PSn were studied at different concentrations for both light and dark studies against the *S. aureus* (**Figure A7**). At high concentration doses (> 45 mg/L), AMP, SiNPs-ATES and PSn show high antimicrobial activity

both in light and dark studies, this is attributed to the known antibacterial properties of AMP and PSn. The higher PACT activity of ***1Q***@SiNPs-PSn compared to ***1Q*** alone is attributed to increased positive charges.

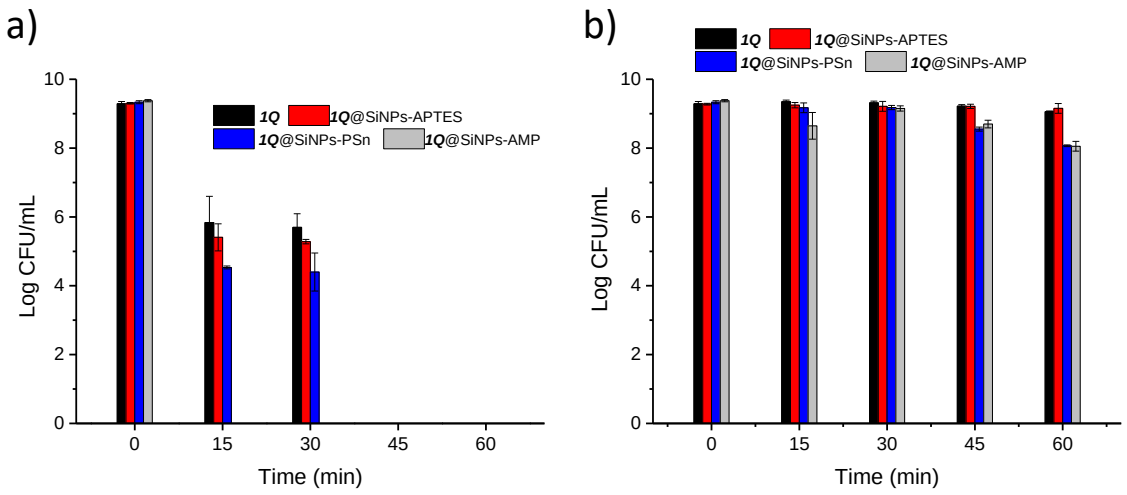

Figure 5.1: Survival graph of *S. aureus* following exposure to *1Q* and its doped conjugates in the presence of a) light and b) dark in PBS. Concentration = 45 mg/L.

For the studies concerning complexes ***4-8*** and ***8Q-11Q***, for continuity all planktonic based experiments were conducted at a constant concentration of 2.5 µM with varied irradiation intervals. A comparison study of the PACT activity of complexes ***4***, ***5*** and ***6*** towards *E. coli* was conducted. The concentration (2.5 µM) was used since it gave suitable log reduction values and minimal dark toxicity (see **Figure A8**). The Pc complex ***4*** was dissolved in 1% DMSO (diluted with PBS), and the cationic complexes ***5*** and ***6*** were dissolved in PBS only. A control consisting of 1% DMSO in the culture was assessed, and the organic solvent had negligible effects (**Figure 5.2 (a)**).

The calculated log reduction values were 0.2, 5.3 and 6.0 for ***4***, ***5*** and ***6***, respectively (**Table 5.1**). Cationic complexes ***5*** and ***6*** had the highest activity; hence they have higher log reduction values than ***4***. The low log reduction for ***4*** is due to the inability of ***4*** to penetrate or interact with cell wall since it not charged; this limits the singlet oxygen potential of the Pc complex to induce apoptosis. Complex ***6*** showed better antimicrobial activity compared to ***5***. This can be attributed to the increased number of positive charges in ***6***, which induce damage of the cell [164,218] and encourage superior penetration to the bacteria cell.

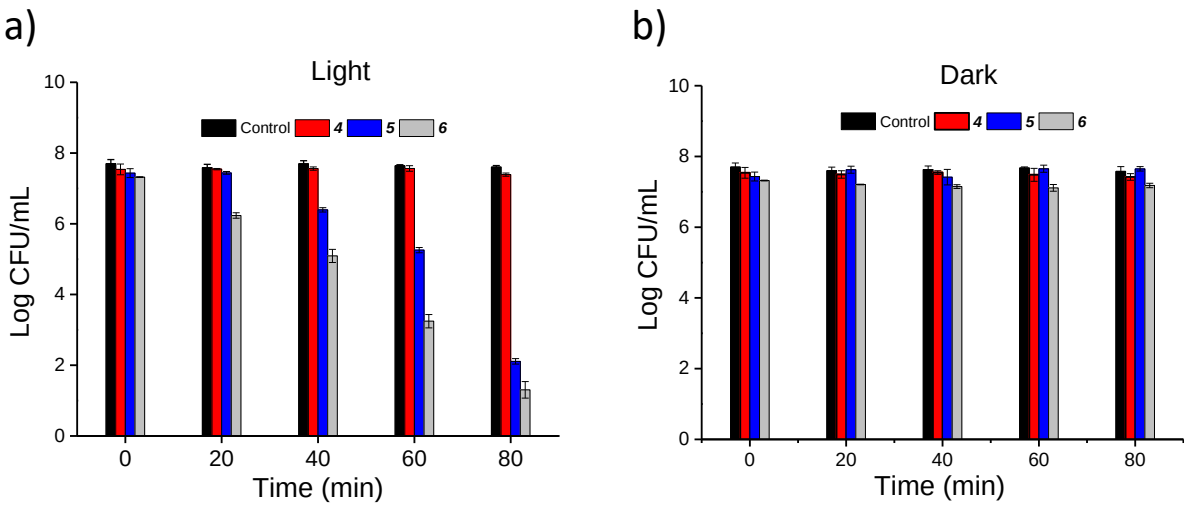

Figure 5.2: Survival graph of *E. coli* following exposure to ***4*, ***5*** and ***6*** in the presence of (a) light and (b) dark in %1 DMSO/PBS (***4***) and PBS (***5*** and ***6***). Concentration = 2.5 µM.**

Complexes ***7***, ***8***, ***8Q***, as well as their conjugates ***7***@SiNPs-GA, ***8***@SiNPs-GA, and ***8Q***@SiNPs-GA, were tested against *E. coli* and *S. aureus*. A control solution of *E. coli* and *S. aureus* without PS was studied with the same laser wavelength as the analysed samples. As presented in **Figure A9**, the Pcs and the conjugates displayed minimal or no apparent dark toxicity on planktonic *E. coli* and *S. aureus* at the Pcs concentrations studied. The studies were evaluated

at a constant concentration of 0.58 mg/L and 1.16 mg/L for *S. aureus* and *E. coli*, respectively. Cationic complexes ***8*** and ***8Q*** and their respective conjugates had the highest antibacterial activity toward *E. coli* with log CFU value of 8.55 compared to ***7*** and ***7***@SiNPs-GA, **Table 5.1**. Against *S. aureus*, ***7***@SiNPs-GA along with ***8***, ***8Q***, and their conjugates, displayed enhanced PACT activity with log CFU value 9.19, while complex ***7*** alone still displayed poor antibacterial activity (**Table 5.1**). The low log CFU for ***7*** alone is due to the lack of charge, leading to the insufficient ability to penetrate or interact with bacteria cell membrane; this limits the singlet oxygen potential of the Pc complex to induce apoptosis, especially towards gram-negative *E. coli*.

Pc complexes ***9Q***, ***10Q*** and ***11Q*** were dissolved in PBS only. The planktonic studies for *S. aureus* were evaluated at a constant concentration of 2.5 µM and 5 µM for *E. coli* with varying irradiation time intervals (see **Figure 5.3 (a)**). In an effort to improve the log CFU values, a higher concentration of 5 µM was used for planktonic studies for *E. coli* (**Figure 5.3 (b)**). The dark toxicity of the cationic Pc complexes was also evaluated at 2.5 µM and 5 µM for *S. aureus* and *E. coli*, respectively (see **Figure 5.4 (a)** and **(b)**). ***9Q***, ***10Q*** and ***11Q*** showed negligible dark toxicity. High PACT activities were obtained for complexes ***9Q***, ***10Q*** and ***11Q***, with high log reduction values of 9.29 for *S. aureus* (**Table 5.1**). For *E. coli*, complexes ***9Q*** and ***10Q*** showed a log reduction of 8.55. As stated above, complex ***11Q*** has a tendency to aggregate. It can be noted in **Figure 5.3** that complex ***11Q*** shows low activity for *E. coli*, corresponding to the low singlet oxygen quantum yield, **Table 5.1**. However, for *S. aureus*, complex ***11Q*** showed high activity. This could be due to the various concentrations used, where larger photosensitiser concentrations were used for *E. coli*, resulting in more aggregation, which could lower PACT activity.

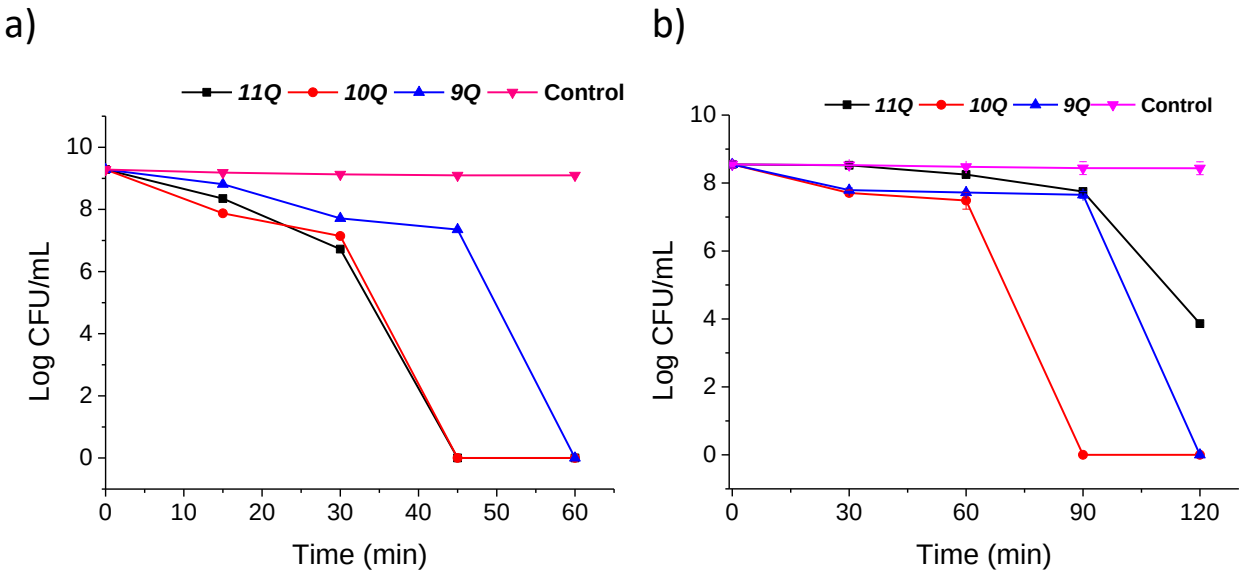

Figure 5.3: Survival curve of (a) *S. aureus* and (b) *E. coli* in PBS using to complexes *9Q*, *10Q*, and *11Q* in the presence of light in at Concentration = 2.5 µM (*S. aureus*) and 5 µM (*E. coli*).

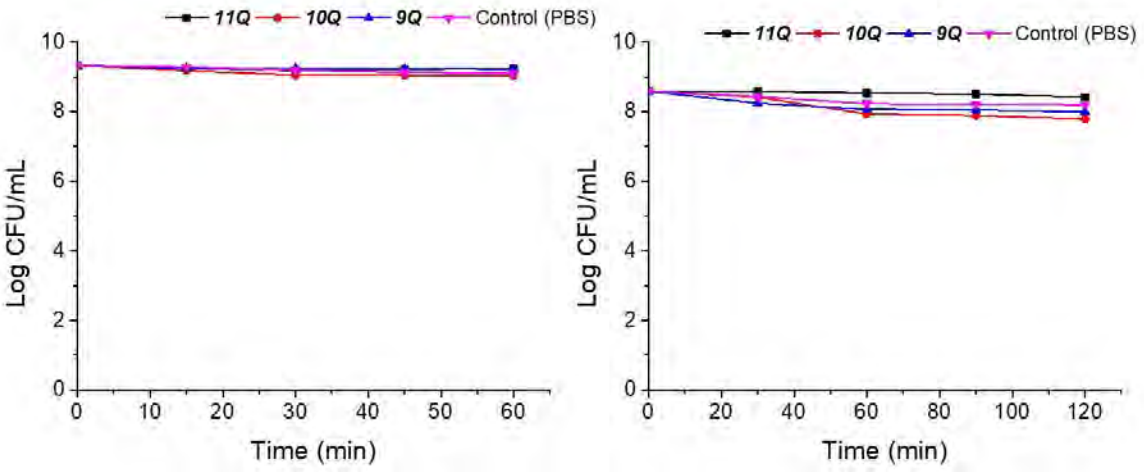

Figure 5.4: Survival curve of a) *S. aureus* and b) *E. coli* in PBS due to complexes *9Q*, *10Q*, and *11Q* in the dark in PBS at Concentration = 2.5 µM (*S. aureus)* and 5µM (*E. coli*)

Table 5.1: Log CFU values in the presence of light against *S. aureus* and *E. coli* planktonic cells after irradiation with 680 nm light (524 mW/cm^2).

Complex	media	Log CFU		Φ_Δ in DMSO
		E. coli	*S. aureus*	
1Q	PBS	—	9.20	0.57
1Q@SiNPs-APTES	PBS	—	9.30	0.51
1Q@SiNPs-PSn	PBS	—	9.31	0.54
1Q@SiNPs-AMP	PBS	—	9.37	0.46
4	1% DMSO/PBS	0.2	—	0.44
5	PBS	5.3	—	0.62
6	PBS	6.0	—	0.53
7	1% DMSO/PBS	0.61	0.98	0.49
7@SiNPs-GA	1% DMSO/PBS	1.26	9.19	0.39
8	PBS	8.55	9.19	0.48
8@SiNPs-GA	PBS	8.55	9.19	0.39
8Q	PBS	8.55	9.19	0.76
8Q@SiNPs-GA	PBS	8.55	9.19	0.58
9Q	PBS	8.55	9.29	0.79
10Q	PBS	8.55	9.29	0.75
11Q	PBS	4.69	9.29	0.27

5.2.2 Biofilm bacterial studies of symmetrical Pc and their Pc doped SiNPs conjugates (effect of the number of charges, position of nitrogen group, and effect of surfactant on SiNPs).

The literature [219] suggests that the difficulty in treating biofilms is due to the extracellular matrices' sticky and tenacious nature, which makes it difficult for antibacterial drugs to interact with bacterial biofilms. For this study, higher concentration doses of Pcs were used for biofilms. *S. aureus* and *E. coli* were selected for this study because of their propensity to form biofilms. For complexes ***7***, ***8***, and ***8Q*** studies were conducted at gradient concentrations of 1.45, 2.90, 5.80, 11.60, 23.20 mg/L, towards *S. aureus* and *E. coli* biofilms. As demonstrated in (**Figure 5.5 (a)** and **(b)**), the Pc complexes displayed some dark toxicity (but minimal) against *S. aureus* whereas no apparent dark toxicity was detected for *E. coli* at the studied concentrations. The high cell survival for the respective controls, untreated *E. coli* and *S. aureus*, were observed, indicating that (**Figure 5.5 (a)**, **(b)**) light irradiation alone would not kill the cells by heating (**Figure 5.6 (a)** and **(b)**, control). The bacterial biofilm cell viability (%) is defined by Eq. (**2.1**).

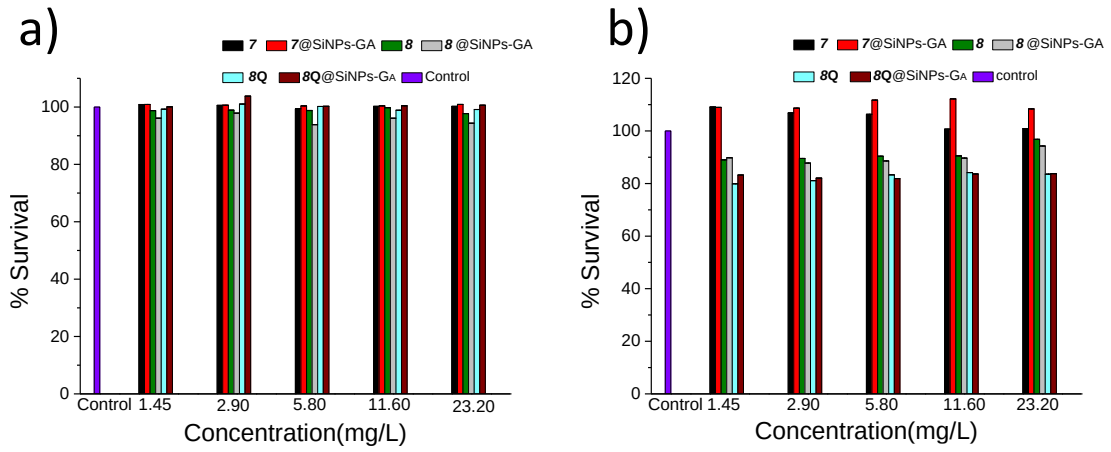

Figure 5.5: % **Survival graph for dark toxicity studies against *E. coli* (a) and *S. aureus* (b) biofilms after 15 min incubation at the indicated concentrations (concentration range studied: 1.45–23.20 mg/L).**

Figure 5.6 (a) and **(b)** depict the bactericidal activity of complexes ***7***, ***8***, and ***8Q*** as well as their doped conjugates in the presence of light. The light studies showed that the Pcs and their conjugates generally responded in a dose-dependent manner (**Figure 5.6**). When compared to complexes ***7*** and ***8*** alone, complex ***8Q*** displayed the most activity. When compared to the other conjugates, ***8Q***@SiNPs-GA demonstrated better antibacterial activity. For *E. coli*, cell survival, typically below 50%, was seen at a concentration of 1.45-23.20 mg/L for ***8Q*** and ***8Q***@SiNPs-GA (**Figure 5.6 (a)**). For *E. coli* complexes ***7***, ***8***, and ***8Q***, cell survival values of 39.57%, 29.38%, and 19.44%, respectively, were found at the highest concentration of 23.20 mg/L (**Table 5.2**). When compared to the Pc dyes alone, the doped counterparts demonstrated some improvement in antibacterial efficacy. For ***7***@SiNPs-GA, ***8***@SiNPs-GA, and ***8Q***@SiNPs-GA for *E. coli*, respectively, cell survival of 31.24%, 16.16%, and 13.15% were found.

Table 5.2: % Survival table in the presence of light against *E. coli* and *S. aureus* biofilms after irradiation at maximum studied concentration.

Complex	Concentration	% Survival of biofilms after irradiation with 680 nm light (524 mW/cm^{-2})	
		E. coli	*S. aureus*
7	23.20 mg/L	39.57	41.05
7@SiNPs-GA	23.20 mg/L	31.24	18.42
8	23.20 mg/L	29.38	26.72
8@SiNPs-GA	23.20 mg/L	16.16	15.57
8Q	23.20 mg/L	19.44	19.06
8Q@SiNPs-GA	23.20 mg/L	13.15	13.03
9	100 µM	39.27	25.03
9Q	100 µM	8.15	10.76
10	100 µM	31.20	24.91
10Q	100 µM	17.15	16.80
11	100 µM	27.22	26.41
11Q	100 µM	11.38	8.84

Cell survival of less than 50% for *S. aureus*, however, was only seen at higher concentrations of 11.60 and 23.20 mg/L, for ***8Q*** and ***8Q***@SiNPs-GA (**Figure 5.6 (b)**). For *S. aureus* cell survival values of 41.05 (***7***), 26.72 (***8***), and 19.06% (***8Q***). Cell survival values of 18.42%, 15.57%, and 13.03% for *S. aureus* biofilm utilising complexes ***7***@SiNPs-GA, ***8***@SiNPs-GA, and ***8Q***@SiNPs-GA, respectively, were found. Since the preceding studies showed that the effectiveness of

Pcs' intracellular absorption is strongly correlated with the number of positive ions present in their structures, ***8Q*** exhibits greater antibacterial action than ***8***, ***7***, and their doped conjugate equivalents. The Φ_{Δ} produced by the complexes is also reflected in the PACT activity (**Table 5.1**), more so for the Pc dyes alone.

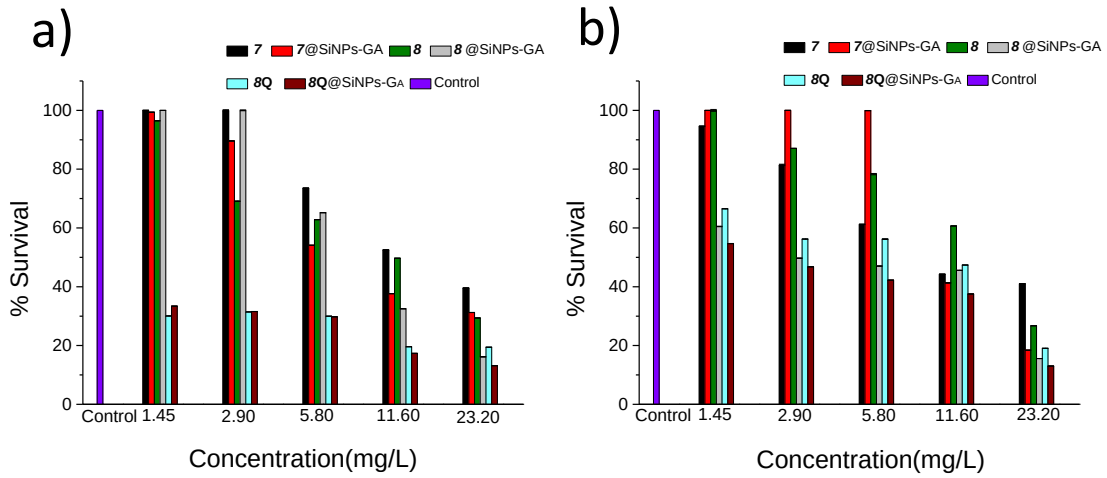

Figure 5.6: % Survival graph in the presence of light against *E. coli* (a) and *S. aureus* (b) biofilms after 30 min of irradiation at the indicated concentrations (concentration range studied: 1.45–23.20 mg/L).

The cell survival at 23.20 mg/L was considered to determine the log CFU value for the Pc complexes and their respective conjugates. This was carried out as follows, an aliquot of bacteria suspension was seeded, and upon irradiation, the suspensions were serially diluted ten-fold with PBS. 100 µL aliquots were spotted on agar plates for incubation. The bacteria colonies were counted at the end of the 18 h incubation period. The log CFU values for each of the Pc complexes and their doped conjugates are displayed in **Table 5.3.** The largest log

CFU reduction values were produced by ***8Q***@SiNPs-GA. For ***8Q*** and ***8Q***@SiNPs-GA, respectively, log CFU values of 4.81 and 8.60 were obtained towards *E. coli* biofilms. Log CFU values of 2.60 for ***8Q*** and 6.42 for ***8Q***@SiNPs-GA were confirmed for *S. aureus.* Since cationic substituted Pcs are known to be more efficient against gram (-) bacteria like *E. coli*, larger log CFU values for *E. coli* are obtained in **Table 5.3** than for *S. aureus.*

Table 5.3: Log CFU values in the presence of light against *S. aureus* and *E. coli* biofilms after irradiation with 680 nm light (524 mW/cm^2).

Complex	Media	Concentration	Φ_Δ in DMSO	Log CFU	
				E. coli	***S. aureus***
7	1% DMSO/PBS	23.20 mg/L	0.49	0.007	0.171
7@SiNPs-GA	1% DMSO/PBS	23.20 mg/L	0.39	0.025	0.111
8	PBS	23.20 mg/L	0.48	1.26	1.03
8@SiNPs-GA	PBS	23.20 mg/L	0.39	2.31	1.95
8Q	PBS	23.20 mg/L	0.76	4.81	2.60
8Q@SiNPs-GA	PBS	23.20 mg/L	0.58	8.60	6.42
9Q	PBS	100 µM	0.79	8.59	9.42
10Q	PBS	100 µM	0.75	2.44	9.42
11Q	PBS	100 µM	0.27	1.21	9.42

The dark (**Figure 5.7 (a)** and **(b)**) and PACT activity (**Figure 5.8 (a)** and **(b)**) of the Pc complexes (***9-11*** and ***9Q-11Q***) were performed at gradient concentrations of 6.25, 12.5, 25, 50, and 100 µM for both *S. aureus* and *E. coli* biofilms. The bacterial biofilm cell viability (%) is defined by Eq. (**2.1**).

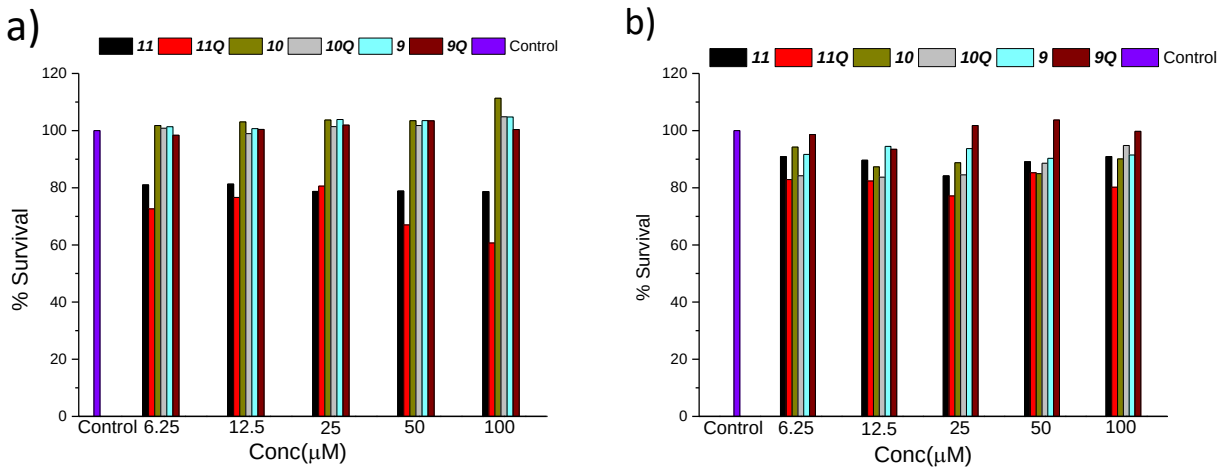

Figure 5.7: % Survival graph for dark toxicity studies against *S. aureus* (a) and *E. coli* (b) biofilms after 15 min at the indicated concentrations (Concentration range studied:6.25-100 µM).

The Pc complexes showed minimal antibacterial activity towards *S. aureus* and *E. coli* biofilms in the dark (**Figure 5.7 (a)** and **(b)**). The 96-well plates containing the corresponding biofilm strains in the presence of complexes ***9-11*** and ***9Q-11Q*** were exposed to Q-band 680 nm radiation in order to assess the antibacterial effect of complexes on *S. aureus* and *E. coli* biofilms. Cell viability below 50% was often seen for all complexes under study at concentrations of 100 µM (**Figure 5.8 (a)**, **(b)**). ***9Q*** demonstrated high antibacterial action, against *E. coli* biofilm with survival rate of 8.15% (**Table 5.2**), this is credited the high Φ_{Δ} for

9Q (**Table 5.3**). Since cationic Pcs are more efficient, cationic complexes ***9Q***, ***10Q***, and ***11Q*** exhibit greater PACT activity than neutral complexes ***9***, ***10***, and ***11***. The *S. aureus* biofilms displayed the highest log reduction value of 9.42 for complexes ***9Q***, ***10Q***, and ***11Q***, **Table 5.3**. For *E. coli* biofilms log reduction value of 8.59, 2.44, and 1.21 were obtained for complexes ***9Q***, ***10Q***, and ***11Q***, respectively (**Table 5.3**).

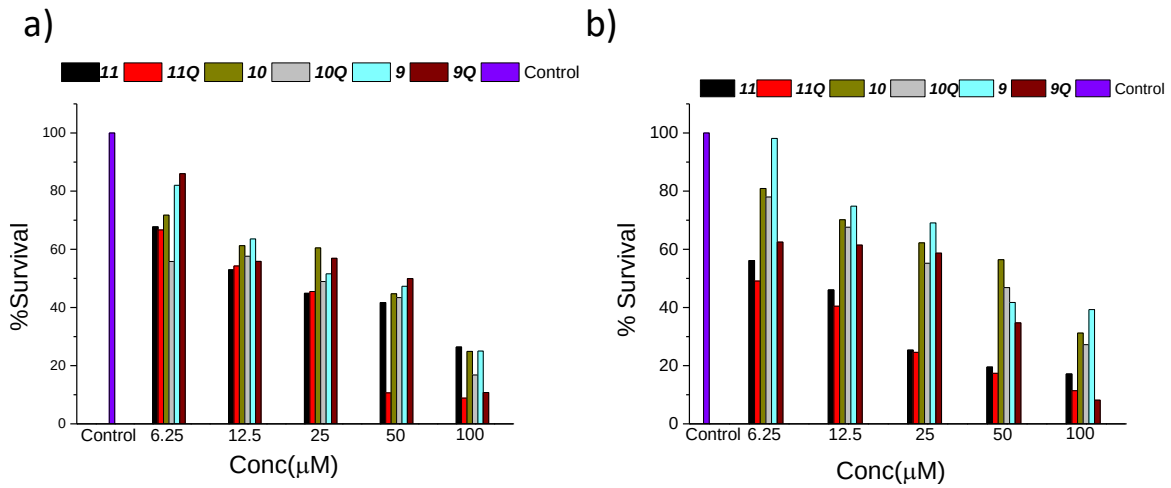

Figure 5.8: % Survival graph in the presence of light against *S. aureus* (a) and *E. coli* (b) biofilms after 15 min of irradiation at the indicated concentrations (Concentration range studied: 6.25–100 μM).

5.2.3 Biofilm antimicrobial activity of Pc conjugates with CIP (effect of symmetry, Pc-antibiotic synergistic effect)

5.2.3.1 Concentration optimisation

In order to establish optimum concentration of the Pcs to be used, their uptake (using electrochemical impedance spectroscopy (EIS)) by *S. pneumoniae* and *E. coli* bacteria at different concentrations of 4, 8, 16, and 32 µM (in 1% DMSO/PBS and using complex ***12***-CIP as an example) was studied, following 40 min incubation, **Figure 5.9**, **Figure A10**, and **Table A3** present the data in the form of Rct. Please note the incubation time of 40 min was employed for optimisation only. The optimal concentrations were 16 and 32 µM for *E. coli* and *S. pneumoniae* biofilm substrates, respectively, as judged by the highest conductivity (lowest Rct in **Tables A3**) in the presence of light. The Equivalent circuit adopted to fit the impedance data is outlined in **Figure A11.**

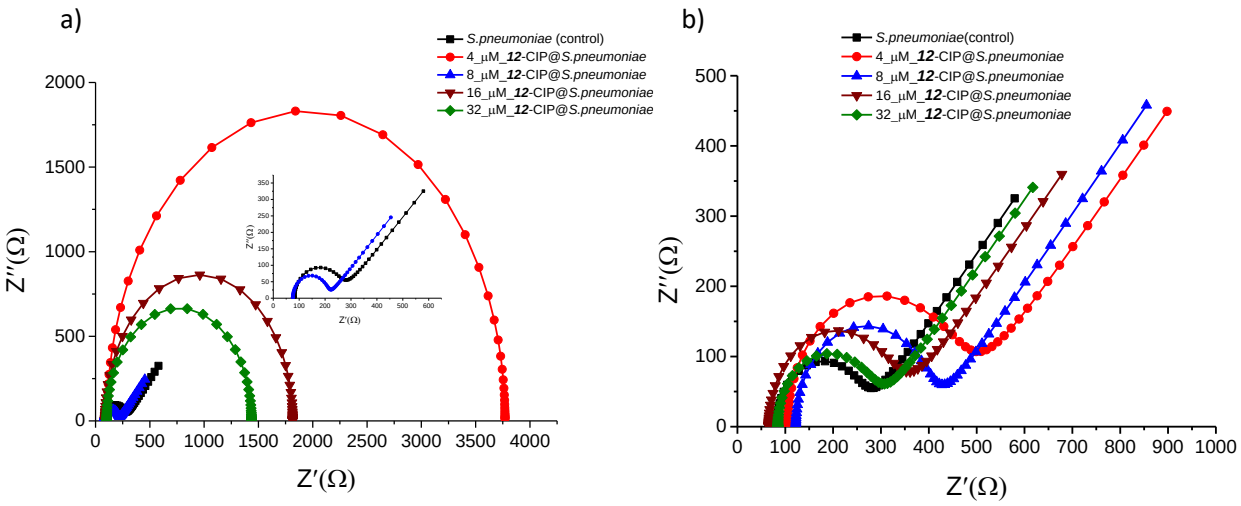

Figure 5.9: Nyquist plots of the impedance for *S. pneumoniae* biofilm on substrate on ITO-coated glass before a) and after b) 15 min illumination with laser light after treatment with *12*-CIP at 4-32µM concentration (1%DMSO/PBS, pH 7.4) in 0.1 M KCl containing 1 mM [Fe (CN)6]$^{3-/4-}$ solution. Inset graph in a) shows the expanded view of *S. pneumoniae* (control) and 8 µM *12*-CIP@*S. pneumoniae*.

5.2.3.2 Optimisation of incubation time using PS uptake

Square wave voltammetry (SWV) was used to ascertain the ideal drug uptake time; complex ***12***-CIP against *E. coli* is used as an example; **Figure 5.10 (i)** and **Figure 5.10 (ii) (a)** (for *E. coli*). Biofilms are known to be conductive hence SWV was employed [220]. ***12***-CIP@*Biofilm* substrates were incubated (for uptake) at 20 min intervals for 100 min. The SWV peak height is directly proportional to the concentration of the electroactive species (Pc-CIP) up-taken by biofilms. For *E. coli* (**Figure 5.10 (i)** and **Figure 5.10 (ii) (a)**), a rapid absorption of ***12***-CIP was observed from 20 to 80 min. After this period, the current showed a downward trend, probably because of saturation, hence 80 min incubation was employed for *E. coli* throughout the experiments. For S. *pneumoniae* (**Figure 5.10 (ii) (b)**), a high resistance for uptake is experienced by the drug up until 40 min. The highest studied time of 120 min for Pc-CIP uptake was used for *S. pneumoniae*. Gram-negative bacteria such as *E. coli* are surrounded by a thin peptidoglycan cell wall, which itself is surrounded by an outer membrane containing lipopolysaccharide. Gram-positive bacteria such as *S. pneumoniae* lack an outer membrane but are surrounded by layers of peptidoglycan many times thicker than is found in the Gram-negative bacteria [221], thus the differences in the uptake could be due to the differences in cell walls between the two types of bacteria. The data indicates that longer incubation periods of the biofilm in the presence of **Pc**-CIP generally leads to greater **Pc**-CIP uptake.

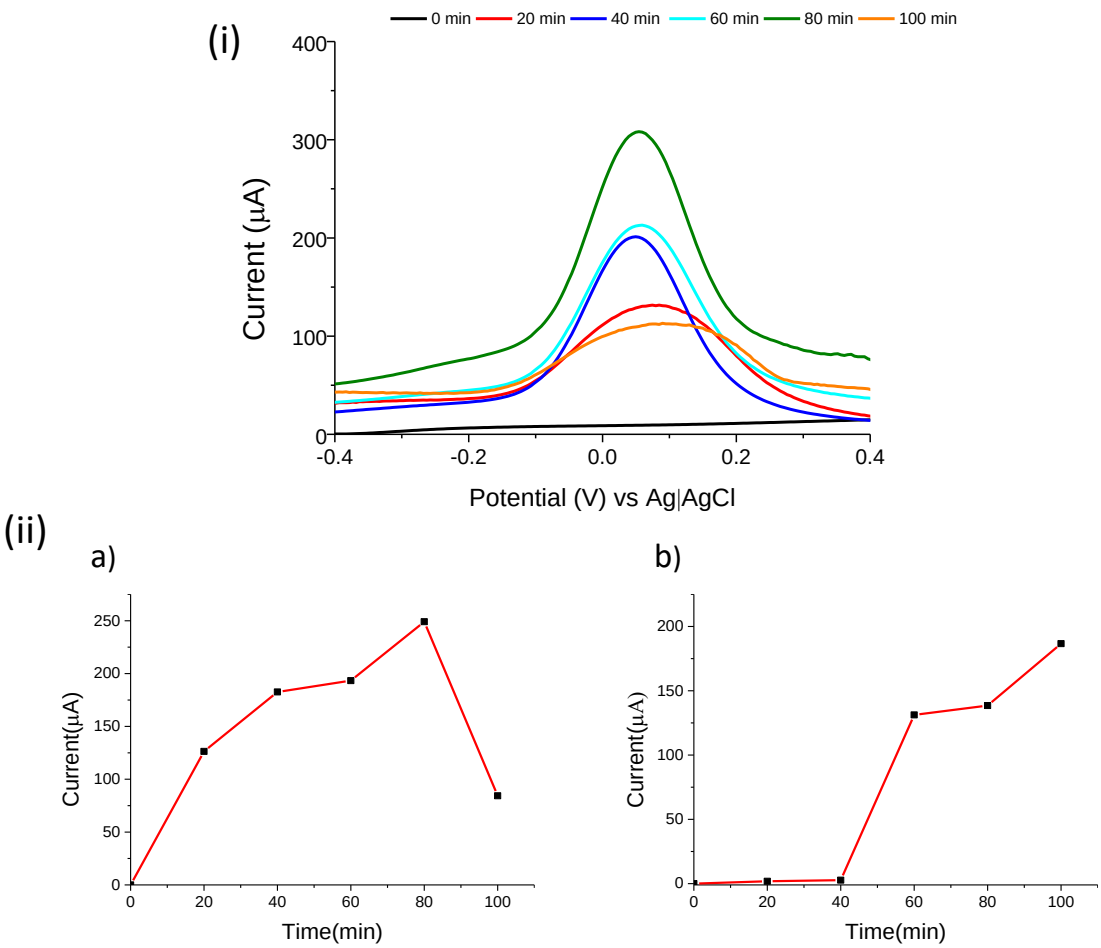

Figure 5.10: (i) Square wave voltammograms (SWV) illustrating the gradual uptake of *12*-CIP by *E. coli* on ITO-coated glass from 0 to 100 min and ii): peak current (from SWV) versus time for uptake of *12*-CIP by a) *E. coli* (16 µM) and b) *S. pneumoniae* (32 µM) both on ITO-coated glass. *12*-CIP in 1%DMSO/PBS (pH 7.4).

5.2.3.3 Cell viability and log reduction quantification.

The cell survival of ***12***-CIP and ***13***-CIP at concentrations of 16 µM (*E. coli*) and 32 µM (*S. pneumoniae*) were used to determine the log CFU value for the Pcs. This was carried out as follows; A test tube with 2 mL of PBS was added to the 96 h biofilm cell cultured ITO-glass slides of each strain of bacteria. The test tube was then placed in an oven with a shaker for 24 h at 37 °C in the dark. The bacteria culture was diluted to 1/1000 in PBS (working stock solution), corresponding to ~10^8 colony-forming units (CFU)/mL.

Against *E. coli*, complex ***12***-CIP displayed a cell viability value of 0.095% and a log reduction of 3.10 in the dark. After illumination, no viable cells were determined for *E. coli* using ***12***-CIP at 16 µM, with a log reduction value of 9.20 (**Table 5.4**, light). Cell viabilities of 0.089% (dark) and 0.025% (light) were determined for ***13***-CIP with corresponding log reduction values of 7.10 (dark) and 7.29 (light). Thus ***13***-CIP was toxic in the dark. The lower log reduction value for ***13***-CIP in the light is attributed to the more significant number of EPS entangled cells in the presence of ***13***-CIP as will be shown below using scanning electron microscopy (SEM). Most EPS are negatively charged, due to the dominance of carboxyl and hydroxyl functional groups, in different proportions depending on EPS composition, hence will interact strongly with the positively charged ***13***-CIP [222], making removing an established biofilm difficult by providing strong adhesion to a surface and acting as a barrier to diffusion of antimicrobial molecules [223]. *S. pneumoniae* strain displayed higher resistance towards the Pc-CIPs in the dark due to the high levels of EPS production for *S. pneumoniae* compared to *E. coli* [224]. Cell viability values of 8.25% and 30.35% with corresponding log reduction values of 0.91 and 0.37 were obtained for complexes ***12***-CIP and ***13***-CIP, respectively in the dark. Log CFU value of

7.23 with no viable cells was obtained after light exposure for ***12***-CIP and ***13***-CIP complexes (**Table 5.4**).

Table 5.4: Cell viability and log reduction values in the presence of dark and light against *E. coli* and *S. pneumoniae* biofilms after 80 min (*E. coli*) and 100 min (*S. pneumoniae*) uptake period of the Pc-CIP followed by 15 min illumination with laser probe at 16 and 32 µM concentration, correspondingly.

ITO-glass biofilm composition	**%Cell viability (Log reduction value)**	
	Dark toxicity	**Phototoxicity**
E. coli (control)	100	100
CIP@***E. coli***	0.27 (2.74)	-
12-CIP@***E.coli***	0.095 (3.10)	0.00 (9.20)
13-CIP@***E.coli***	0.089 (7.10)	0.025 (7.29)
S. pneumoniae (control)	100	100
CIP@ ***S. pneumoniae***	29.10 (0.38)	-
12-CIP@ ***S. pneumoniae***	8.25 (0.91)	0.00 (7.23)
13-CIP@ ***S. pneumoniae***	30.35 (0.37)	0.00 (7.23)

5.2.4 Characterisation of biofilm substrates and their stability in the presence of Pcs

E. coli, *S. pneumoniae*, and *S. aureus* biofilms were grown on indium-tin-oxide (ITO)-coated glass slides (20 cm^2) with cells cultured in an extracellular matrix in an effort to create the ideal biofilm substrate for Raman spectroscopy, cyclic voltammetry (CV) analysis, and electrochemical impedance spectroscopy (EIS). The ITO-glass slides were inserted in the sterile Petri plates for each bacterial strain after being ethanol sterilised and autoclaved. The different bacteria were brought to a concentration of 1×10^8 CFU/mL using Luria-Bertani (LB) broth, and the medium was changed every 24 h for four days. After this time, the prepared ITO-glass slides were gently washed with PBS (pH 7.2) to remove excess LB broth.

Only ***8Q*** and its conjugate, as well as ***12***-CIP and **13**-CIP, were used as examples. In order to prepare the biofilms (*E. coli* and *S. aureus*) for further examination, 100 µL of 23.20 mg/L of complex ***8Q*** and its conjugated ***8Q***@SiNPs-GA were added to the biofilm cultured slides. Similar treatment was done on complexes ***12***-CIP and ***13***-CIP at doses of 16 µM (*E. coli*) and 32 µM (*S. pneumoniae*).

5.2.4.1 Scanning electron microscopy (SEM) analysis

Complex ***8Q*** and its conjugated ***8Q***@SiNPs-GA were used to treat biofilm cells for SEM investigation. SEM analysis with ***8Q*** and its conjugated (***8Q***@SiNPs-GA), the biofilm substrate was cultured as described above, except aluminium slides (20 cm^2) were used. For all analysis, the biofilm covered ITO/aluminium slides were gently washed with PBS and fixed using 2.5% glutaraldehyde in 0.1 M PBS (pH 7.2) for 4 h at 4 °C. The fixed samples were subsequently dehydrated with ethanol in a gradual manner (30–100%) at 10 min intervals.

The effects of treatment using ***8Q*** and its conjugated (***8Q***@SiNPs-GA) on the structural stability of the bacterial biofilms were investigated using SEM after illumination with laser light. When light was present or absent, bacteria's biofilm morphology without Pc treatment showed colonies that resembled a compact structure. The control groups for *S. aureus,* as an example (**Figure 5.11 (a), (b)**) did not exhibit any signs of degradation in appearance. The bacteria displayed single colony distribution in **Figure 5.11 (c)** and **(d)** for *S. aureus* after PACT treatment using ***8Q*** and ***8Q***@SiNPs-GA. *S. aureus* exhibits minimal EPS production following light treatment with complexes ***8Q*** and ***8Q***@SiNPs-GA. EPS is judged by grouping of bacteria in the SEM image [225]. These findings imply that the examined Pc complexes can affect the structure of the biofilm and bacterial adherence.

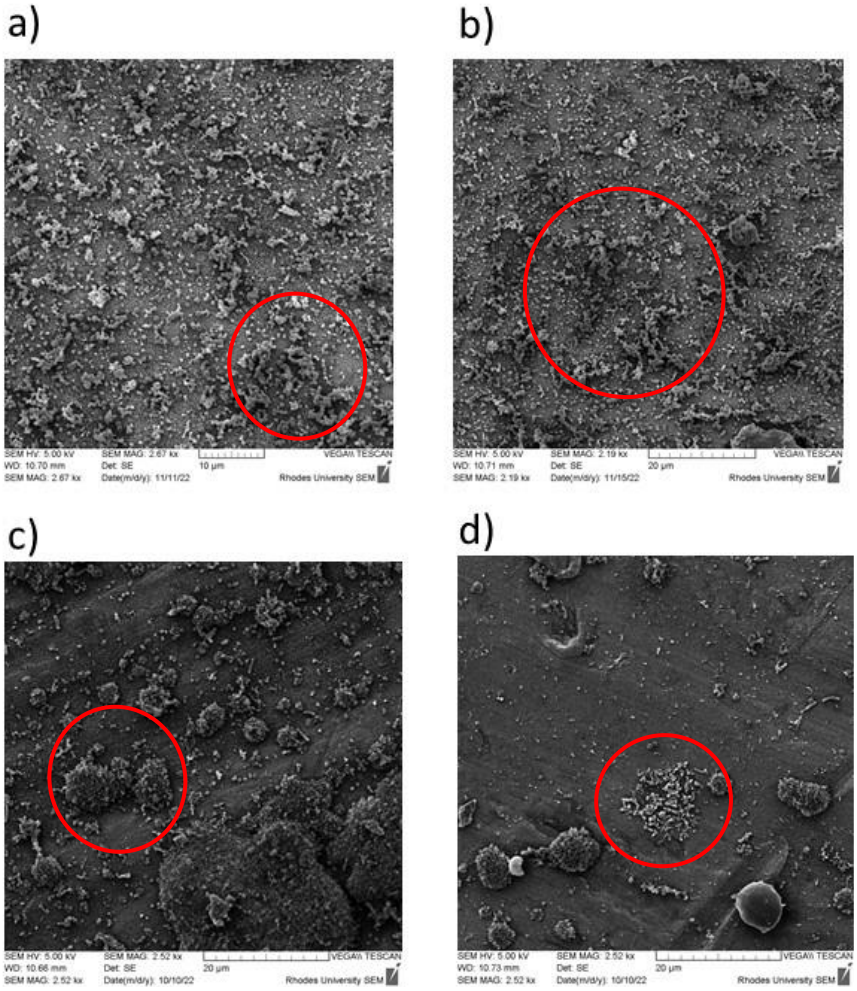

Figure 5.11: Scanning electron microscopy observations. Micrograph show representative images of *S. aureus* alone when untreated a) in the absence of light and b) in the presence of light. Pc-drug treated bacteria followed by irradiation with 680 nm light (524 mW/cm^2) at 23.20 mg/L concentration c) in the presence of *8Q* and d) in the presence of *8Q*@SiNPs-GA. The red circle indicates EPS-bound bacteria cells.

The representative photographs for the morphology of *E. coli* and *S. pneumoniae* obtained following treatment with ***12***-CIP and ***13***-CIP (as examples) are depicted in **Figure 5.12** and **Figure 5.13.** The surface of the ITO-glass covered with biofilm substrates was analysed before and after illumination with wavelength = 680 nm laser probe (524 mW/cm^2) following treatment with ***12***-CIP and ***13***-CIP. *E. coli* and *S. pneumoniae* SEM micrographs for controls were rod shaped (**Figure 5.12 (a)**, **(d) Figure 5.13 (a), (d)**, respectively).

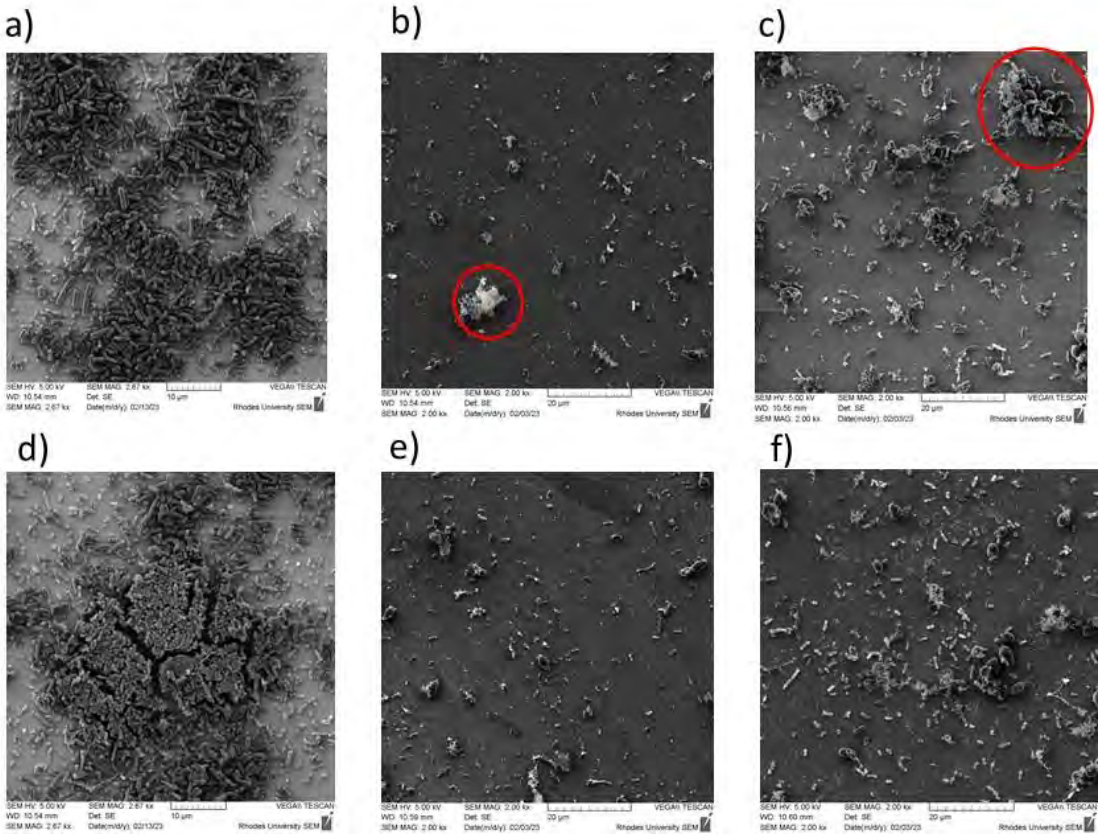

Figure 5.12: Scanning electron microscopy observations. Micrographs show representative images of *E. coli* when untreated a), after treatment with *12*-CIP b), and *13*-CIP c) without light. The bottom row illustrates *E. coli* when untreated d), *12*-CIP, e), and *13*-CIP f) following illumination with a 680 nm laser probe (524 mW/cm^2) for 15 min. *12*-CIP and *13*-CIP were studied at 16 µM concentration. The red circle indicates EPS-bound bacteria cells.

E. coli exhibits minimal EPS production in the dark and light (**Figure 5.12 b, e**) for ***12***-CIP. EPS is judged by grouping of bacteria in the SEM image [225] as stated above. When EPS-depleted bacteria cells are exposed to ***12***-CIP, proteins on the cell surface are easily inactivated even in the dark. The irregularity in structural confirmation is credited to cell degradation following light treatment with ***12***-CIP. A decline in relative efficacy observed following treatment of *E. coli* with ***13***-CIP maybe due to differences in cell wall structure as stated above.

The SEM micrographs of *S. pneumoniae* indicated higher levels of EPS secretion indicating degradation of the biofilm following treatment with **Pc**-CIP (**Figure 5.13**). Complexes ***12***-CIP and ***13***-CIP were able to disrupt and degrade a significant area of the bacterial colonies, with ***13***-CIP showing the highest antimicrobial activity with no EPS-bound cells in sight (**Figure 5.13 (f)**) after the illumination with the laser probe as judged by no groupings of bacteria.

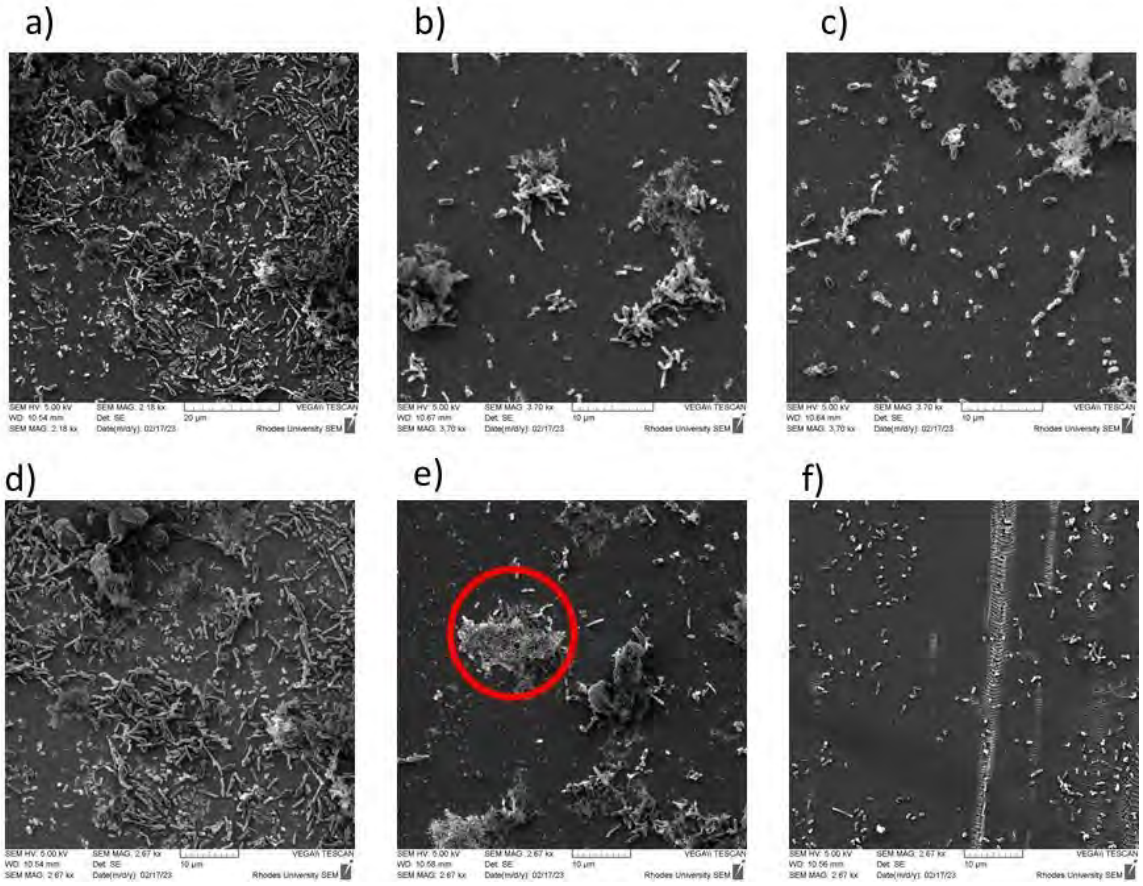

Figure 5.13: Scanning electron microscopy observations. Micrograph show representative images of *S. pneumoniae* when untreated a), *12*-CIP b), and *13*-CIP c) in the absence of light. The bottom row illustrates *S. pneumoniae* when untreated d), *12*-CIP e), and *13*-CIP f) following illumination with 680 nm laser probe (524 mW/cm^2) for 15 min. *12*-CIP and *13*-CIP were studied at 32 µM concentration. Red circle indicates EPS-bound bacteria cells.

5.2.4.2 Cyclic voltammetry (CV)

For complex ***8Q*** and its conjugated ***8Q***@SiNPs-GA, CV was used to determine charge transfer on the biofilm deposit on the ITO-glass surface prior to and after exposure to light irradiation, **Figure 5.14**. In the dark, a decrease in potential difference (ΔE) from 0.24 V, *E. coli* biofilm control was observed to (0.18 V) for *E. coli*/***8Q*** and (0.17 V) for *E. coli*/***8Q***@SiNPs-GA, **Figure 5.14 (b), Table 5.5**. The decrease is due to the enhanced electron transfer by incorporating the Pc complex and its doped conjugate on the biofilm composite; consequently, an increase in current in the cyclic voltammograms of the biofilm composites was evident (**Figure 5.14 (a)**).

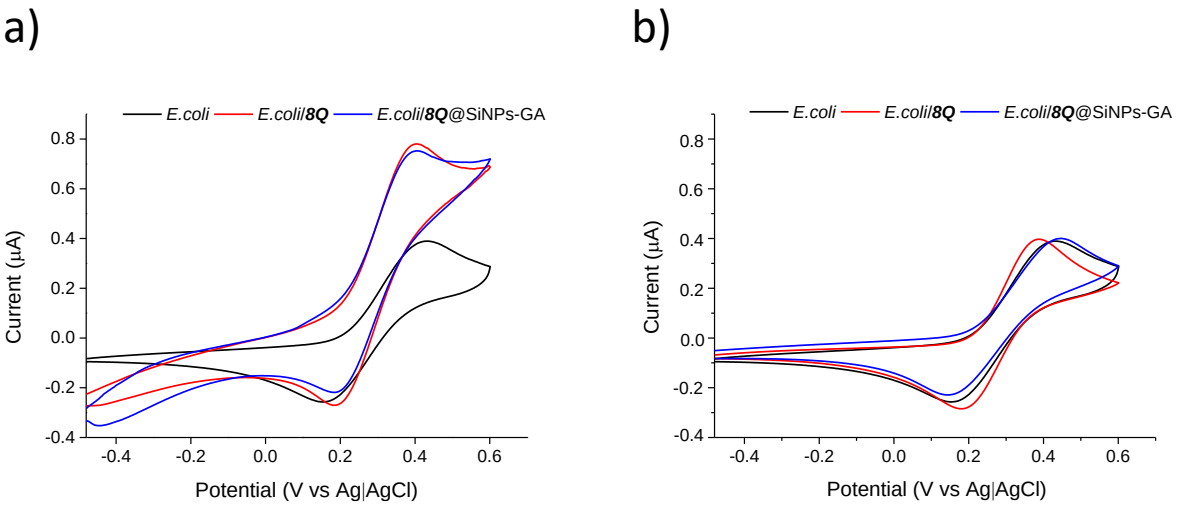

Figure 5.14: CV of ITO-glass biofilm substrates in the a) dark and b) light in 0.1 M KCl containing 1 mM $[Fe(CN)_6]^{3-/4-}$ solution. Scan rate=100 mV/s.

After illumination with 680 nm laser probe (524 mW/cm^2), a slight increase in ΔE to 0.26 V (**Table 5.5**) was indicated for *E. coli* biofilm (control). This indicates that light alone without the PS has no significant effect on the antibacterial activity in this study. An increase in ΔE value for *E. coli*/***8Q***@SiNPs-GA biofilms with potential values of 0.27 V (from 0.17 V) was observed. This implies an increase in charge transfer resistance that can be traced to enhanced blockage of the ITO-glass modified surface due to the breaking down of the structural composition of the biofilm; hence, a surface blockage results in lessening the conductive ability of the biofilms occurs [226]. Similar results were obtained for *S. aureus* bacteria composites (*S. aureus*/***8Q*** and *S. aureus*/***8Q*** @SiNPs-GA) (**Table 5.5**).

Table 5.5: Change in potential difference values (ΔE) in the presence of light and dark against *S. aureus* and *E. coli* biofilms after 30 min of irradiation at 23.20 mg/L concentration.

ITO-glass biofilm composition	**Change in potential difference values (ΔE)**	
	Dark toxicity	**Phototoxicity**
E. coli (control)	0.24	0.26
8Q*/*E. coli	0.18	0.19
8Q@SiNPs-GA/***E.coli***	0.17	0.27
S. aureus(control)	0.21	0.21
8Q*/*S. aureus	0.25	0.33
8Q@SiNPs-GA/***S. aureus***	0.18	0.20
0.1. M KCl containing 1 mM $[Fe(CN)_6]^{3-/4-}$ solution. Scan rate=100 mV/s.		

5.2.4.3 Electrochemical impedance spectroscopy (EIS)

Reduction in the stability of the EPS results in higher conductivity, hence lower charge transfer resistance (Rct) in EIS. For *E. coli*, the Rct numbers for ***12***-CIP and ***13***-CIP were lower than those for the control, **Table 5.6**. This means the conductivity is increased as a result of the less stable EPS meaning degraded products are more conductive. When ***12***-CIP and ***13***-CIP are present, both in the dark and in the light, the Rct values for *S. pneumoniae* are higher than for control. In the presence of ***13***-CIP, the conductivity of bacteria is lower than ***12***-CIP in the presence of light (hence more stability of EPS). The composition of EPS matrix molecules is not the same; it depends on the type of bacteria. There are differences in Pc-CIP uptake between the two strains because they do not have the same barrier; one is gram-negative (*E. coli*) and the other is gram-positive (*S. pneumoniae*).

.

Table 5.6: Rct values in the presence of dark and light against *E. coli* and *S. pneumoniae* biofilms after 120 min uptake followed by 15 min illumination with laser probe at 16 and 32 µM concentration, respectively.

ITO-glass biofilm composition	**Dark**	**Light**
	Rct(kΩ)	**Rct(kΩ)**
E. coli (control)	8.89	9.22
CIP@***E. coli***	7.49	-
12-CIP@***E. coli***	7.82	0.80
13-CIP@***E. coli***	8.46	0.31
S. pneumoniae (control)	0.76	0.79
CIP@ ***S. pneumoniae***	0.70	-
12-CIP@ ***S. pneumoniae***	1.67	1.74
13-CIP@ ***S. pneumoniae***	1.73	0.85

5.2.4.4 Raman Spectroscopy

Raman spectroscopy was used to investigate the identification, categorisation, and analysis of several substances found in the EPS of biofilm, including lipids, carbohydrates, proteins, nucleic acids, and polysaccharides, to name a few. High sensitivity, specificity, and accuracy are provided by Raman in the detection of biochemical degradation inside the matrix of the *S. aureus,* and *E. coli*, *S. pneumoniae* biofilms (**Figures 5.15—5.17**).

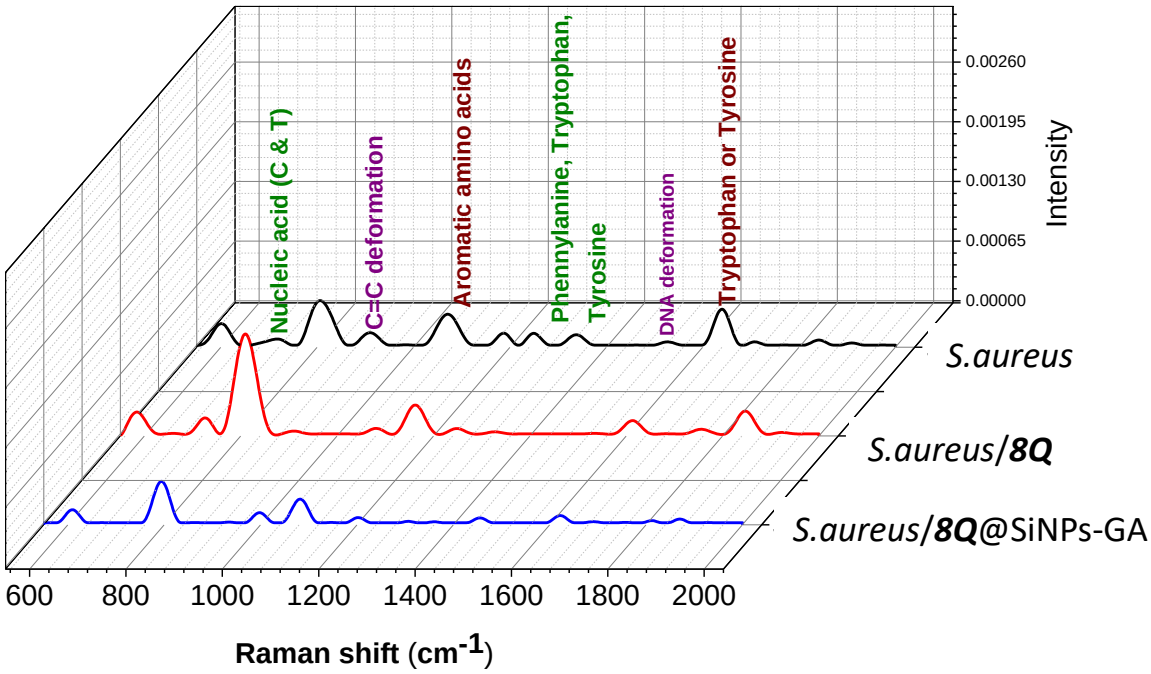

Figure 5.15: Raman spectra for S*. aureus* cells (biofilm) after illumination with 680 nm laser probe (524 mW/cm^2) for 15 min in the presence of *8Q* (*S. aureus*/*8Q*) and *8Q*@SiNPs-GA (*S. aureus*/*8Q*@SiNPs-GA) at concentration 23.20 mg/L.

Following administration of complex ***8Q*** and ***8Q***@SiNPs-GA (as an example) and irradiation for 15 min Raman spectral shifts and changes in peak heights were seen between the control (untreated *S. aureus* biofilms) and the Pc (and conjugates) treated *S. aureus* biofilms, as shown in **Figure 5.15**, which demonstrate the antibacterial activity of the towards *S. aureus* biofilm matrices. According to the literature [227–233], the breakdown of nucleic acid, DNA backbone, aromatic amino acids, phenylalanine, DNA deformation, tyrosine, and amide I causes a decrease in peak intensities when Pcs and conjugates are present. These changes in conformational integrity of *S.aureus* biofilm strains, imply cell death, as a result of singlet oxygen generated by the Pc complexes and conjugates [232,234].

The *E. coli* and *S. pneumoniae* were studied at 1 h and 24 h periods following treatment with ***12***-CIP and ***13***-CIP (as examples) and exposure to laser light, this was performed to evaluate the occurrence of cellular proliferation of the EPS-bound cells (**Figure 5.16 (a)**, (**b)**, and **Figure 5.17 (a)**, **(b)**). EPS enhances cell division of the bacterial colonies within biofilms [235]. The P=O bonds that emerge are a consequence of oxidation and are known to be fingerprints of cell death [236,237]. The changes in the Raman peak intensities in the presence of Pcs corresponds to the breaking down of nucleic acid, DNA backbone, aromatic amino acids, phenylalanine, DNA deformation, tyrosine, and amide I as outlined in literature [232,233]. The spectral differences between the 1h and 24 h control samples for *E. coli* (**Figure 5.16 (a), (b)**) and *S. pneumonie* (**Figure 5.17 (a), (b)**) did not show signs of nutrient/molecular degradation, but the Pc-CIP treated samples did show signs of DNA deformation, protein, and amino acid breakdown as judged by the of the P=O bond and degradation various proteins. The changes were most noticeable 24 h following therapy. Following 24 h of sample incubation, further cell degradation signals were measured for the treatment of *S.*

pneumoniae in the presence of ***12***-CIP. In contrast, no significant changes were detected in the treatment with ***13***-CIP. The treated samples spectrum change in Raman intensity and shape irregularities in comparison to the control samples are known to be the outcome of redox stress-related events [238]. These alterations indicate cell death.

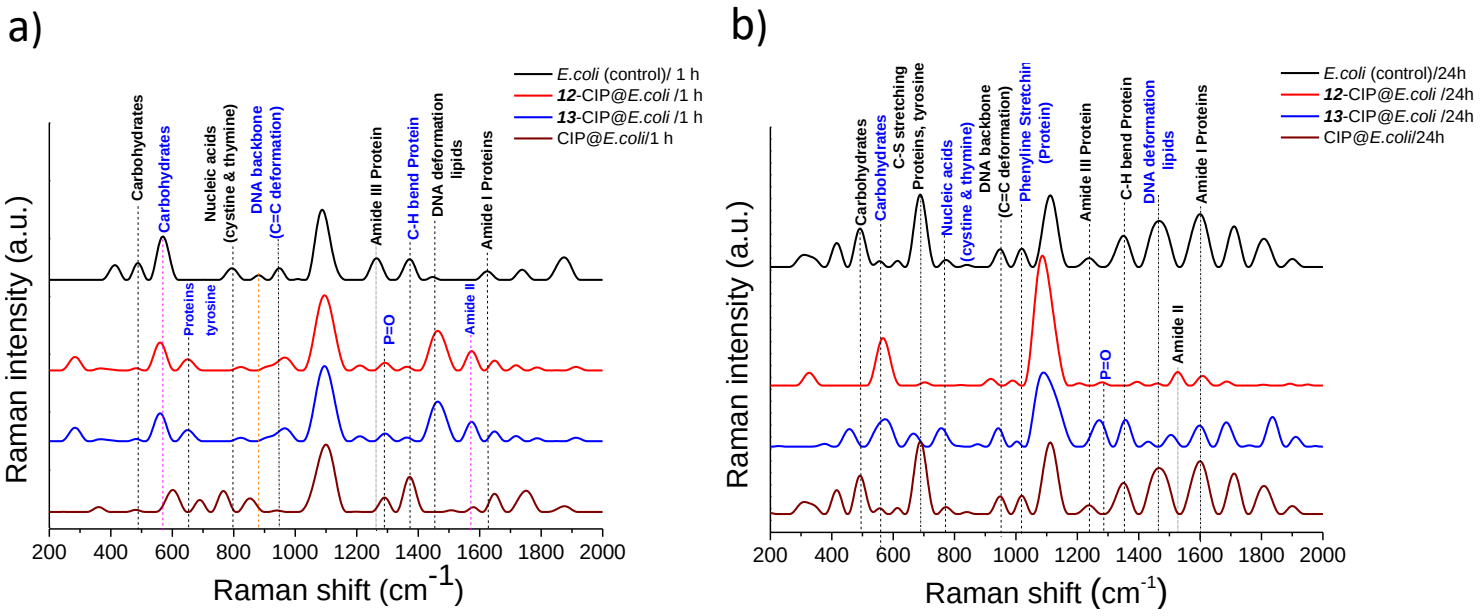

Figure 5.16: Raman spectra of *E. coli* strains a) at 1 h and b) 24 h after illumination with 680 nm laser probe (524 mW/cm^2) for 15 min in the presence of ***12*-CIP and ***13***-CIP (at 16 µM concentration) along with reference sample CIP alone (8 µg/mL).**

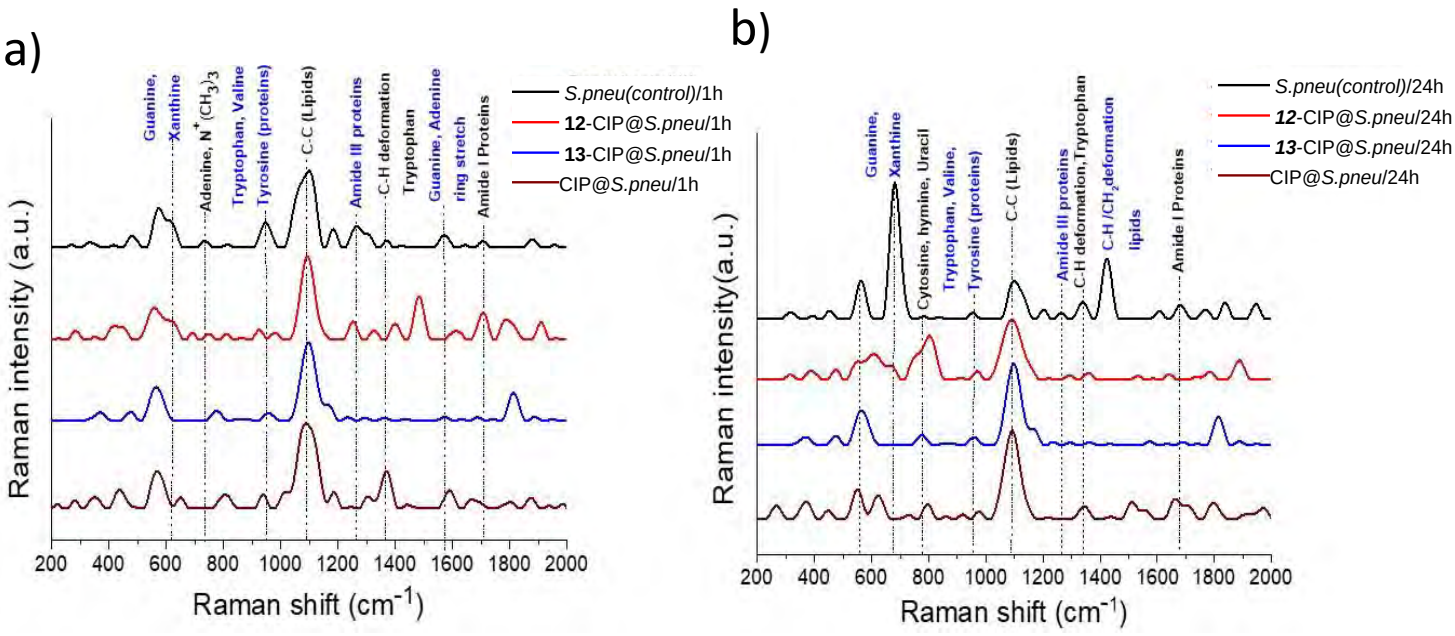

Figure 5.17: Raman spectra of *S. pneumoniae* strains a) at 1 h and b) 24 h after illumination with 680 nm laser probe (524 mW/cm^2) for 15 min in the presence of *12*-CIP and *13*-CIP (at 16 µM concentration) along with reference sample CIP alone (8 µg/mL).

5.2.4.5 Time of flight–secondary ion mass spectrometry (TOF-SIMS)

A supplemental experiment to determine the distribution Pc-CIP across the *E. coli* membrane was conducted using TOF-SIMS, **Figure 5.18 (I)**. TOF-SIMS was used to image individual molecular compounds in order to investigate the uptake of Pc-CIP uptake by EPS. Bacteria have a regulatory mechanism termed quorum sensing (QS) that enables them to monitor their population density [239]. Secondary ion mass spectrometry reveals signal m/z: 244 corresponding to 2-heptyl-4-quinolone (HHQ), key quorum-sensing quinolone which is also involved in biofilm sensing [240]. Additional signals at m/z: 115 and m/z: 79.0 belong to DNA fragments, specifically phylogenetic group markers phylogroup A and phylogroup D, respectively, were detected [241].

A significantly lower cell density was observed after treatment with ***12***-CIP and ***13***-CIP compared to the untreated *E. coli* substrate suggesting that the Pc-CIP complexes have disrupted the biofilm. 3D depth profiling experiments for the distribution of HHQ in the presence of complexes ***12***-CIP and ***13***-CIP across the membranes (**Figure 5.18 (II)**) suggested reduced accumulation of the quorum-sensing quinolone, meaning that cell-cell signalling is compromised. The infrequent distribution of HHQ in **Figure 5.18 (II)** ***12***-CIP and **(c)** ***13***-CIP mark oxidation stress reactions, which can lead to bacteria death; this indicates that the Pc-CIP complexes were able to diffuse the *E. coli* EPS-barrier effectively [240]. The intense red colour in control **(a)** is lowered in the presence of ***12***-CIP and ***13***-CIP. This change is attributed to the preferential binding of the complexes to the *E. coli* biofilm.

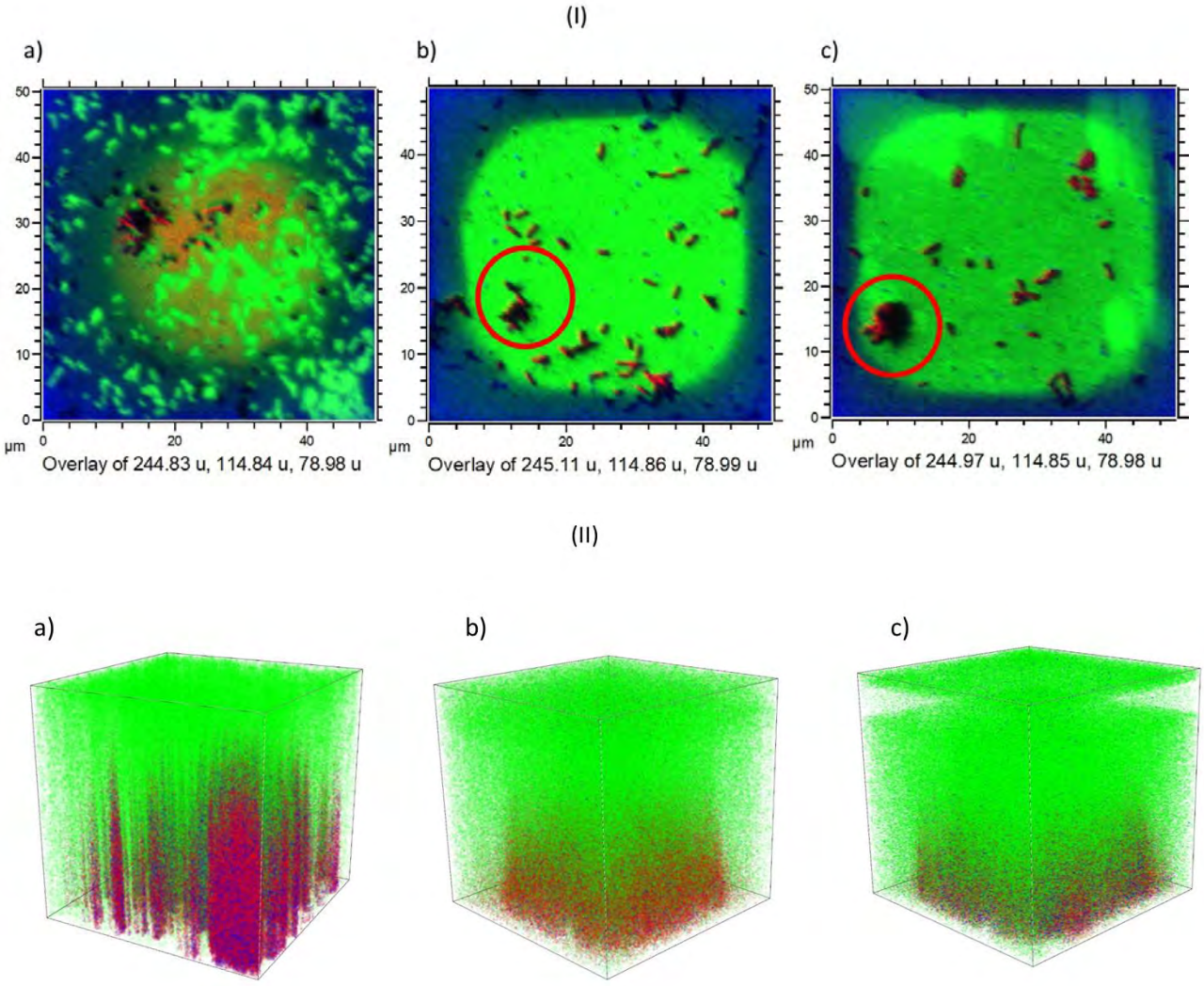

Figure 5.18: ToF–SIMS images showing (I) frozen hydrated *E. coli* biofilm a) without the Pcs (control), following 80 min uptake of b) *12*-CIP, and c) *13*-CIP, (II) Distribution of HHQ across *E. coli* biofilm grown on an ITO-coated glass substrate a) in the absence of Pcs (control), and in the presence of b) *12*-CIP, and c) *13*-CIP. "Live" (red) and "inactive" (green) cells.

5.3 Photodynamic therapy (PDT)

5.3.1 Cellular uptake

The cellular uptake plays an important role in the PDT activity of the photosensitiser. The cellular uptake of the Pc complexes was determined by measuring the absorbance of internalised Pc drug after incubating with MCF-7 cells for 24 h. **Figure 5.19** shows that folic acid coated conjugates (***2***@SiNPs-FA, ***3***@SiNPs-FA) shows better cellular uptake than ***2*** and ***3***, respectively. This difference in the cellular uptake is due to folic acid which is known to target the highly expressed folate receptors on cancer cells [242,243]. Complex ***3*** showed slightly better cellular uptake than ***2***.

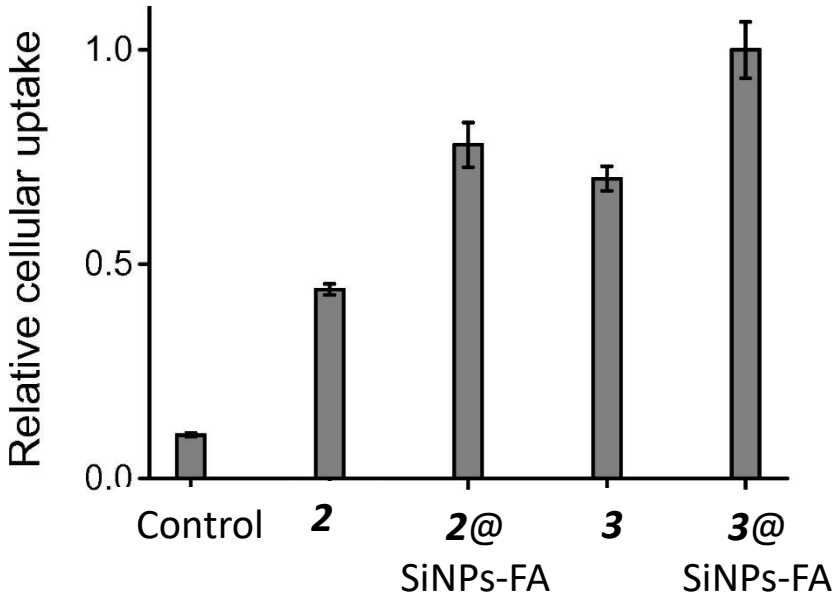

Figure 5.19: Relative cellular uptake plot for complexes *2*, *2*@SiNPs-FA, *3* and *3*@SiNPs-FA, at 10 µg/mL concentration in 1% DMSO. Control 1% DMSO.

Cationic PS are known to bind the anionic cell membrane through electrostatic interactions and facilitate the transfer of PS to the cell [244–246]. Cationic complexes ***5*** and ***6*** have higher cellular uptakes in comparison to the neutral complex ***4*** (**Figure 5.20**), furthermore ***6*** has a superior cellular uptake in comparison to ***5*** this is attributed to the higher number of cationic charges in ***6***.

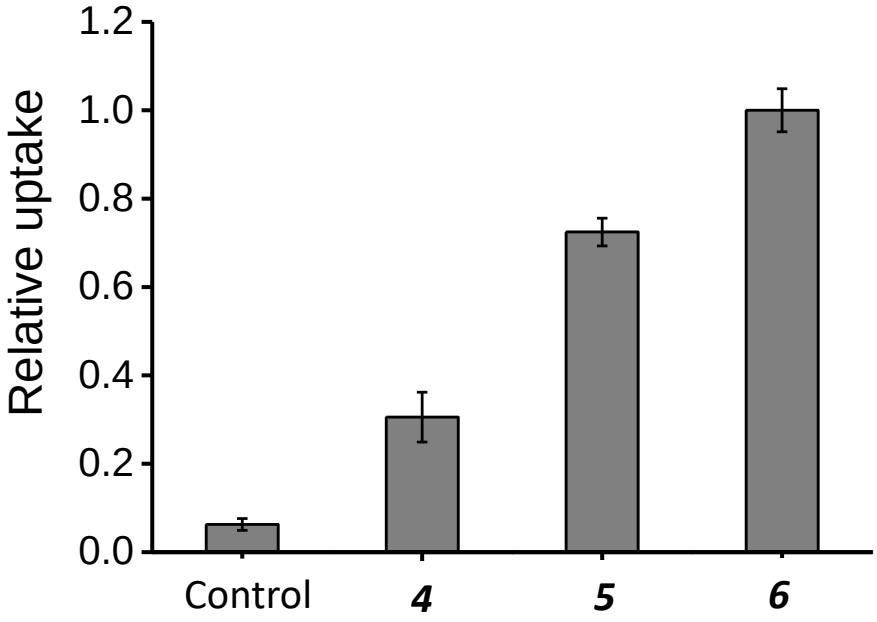

Figure 5.20: Relative cellular uptake plot for *4*, *5* and *6* at 10 µM concentration by measuring the absorbance 680 nm with a multi-plate reader.

5.3.2. Photocytotoxicity studies in MCF-7 cells

The cytotoxicity of Pcs and their folic acid conjugates on MCF-7 cancer cells in both the dark and upon irradiation at 680 nm with a 524 mW/cm^2 was assessed by MTT assay [247]. MCF-7 cells were incubated with different concentrations (0.8–50 µg/mL) of Pcs and conjugates for 24 h. Cells were irradiated with a 680 nm Modulight for 15 min. A separate set of treated cells were studied in parallel in the absence of light irradiation. **Figure 5.21** shows the concentration dependent percentage cell viability plot in light and dark respectively. The half maximal Inhibitory concentration (IC_{50}), the drug concentration required for 50% inhibition of cell growth was calculated (**Table 5.7**). All the conjugates show negligible dark toxicity at the tested concentrations with IC_{50} values > 50 µg/mL (**Table 5.7**, **Figure 5.21** dark). Irradiation of MCF-7 cells pre-treated with conjugates results in significant inhibition of cell growth. Complex ***3*** with IC_{50} value of 18.6 µg/mL showed better phototoxicity compared to ***2*** of IC_{50} value 21.9 µg/mL. On encapsulation to SiNPs-FA the complexes ***2*** and ***3*** showed enhanced PDT activity with IC_{50} values 19.2 µg/mL and 10.8 µg/mL respectively (**Table 5.7**). The PDT activity of the complexes follows the order: ***3***@SiNPs-FA (10.8 µg/mL) < ***3*** (18.6 µg/mL) < ***2***@SiNPs-FA (19.2 µg/mL) < ***2*** (21.9 µg/mL). The observed trend in phototoxicity is consistent with the cellular uptake.

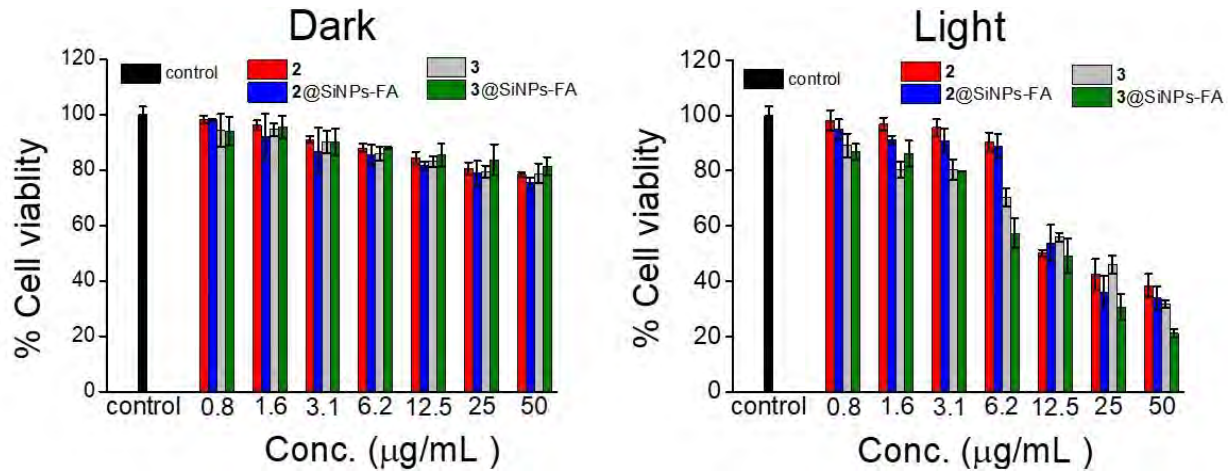

Figure 5.21 :(Dark) and (Light) PDT plots for complexes *2*, *2*@SiNPs-FA, *3* and *3*@SiNPs-FA, at indicated concentrations in 1% DMSO. Dark toxicity plots for complexes *2*, *2*@SiNPs-FA, *3* and *3*@SiNPs-FA at indicated concentrations in 1% DMSO. Control = DMSO (1%).

The dark toxicity and PDT activity studies for ***4***, ***5***, and ***6*** were carried out using MCF-7 breast cancer cells. The dark toxicity and PDT activity of the Pcs were performed at gradient concentrations of 1.6, 3.1, 6.3, 12.5, 25, 50 and 100 μM (**Figure 5.22**). ***4***, ***5***, and ***6*** showed negligible dark toxicity with IC_{50} value > 75 μM (**Table 5.7**, **Figure 5.22 (b)**).

Table 5.7: IC_{50} values of Pc complexes against MCF-7 cells.

Complex	IC_{50} (µg/mL)	
	Dark[a]	Light[b]
2	> 50	21.9 (± 1.2)
2@SiNPs-FA	> 50	19.2 (± 1.1)
3	> 50	18.6 (± 1.0)
3@SiNPs-FA	> 50	10.8 (± 0.7)
4	> 75	15.1 (± 1.1)
5	> 75	8.2 (± 1.0)
6	> 75	4.9 (± 1.3)

[a]24 h incubation in the dark. [b]24 h incubation in the dark followed by exposure to a 680 nm Modulight medical laser (524 mW/cm^2) for 15 min. Error bars represent standard deviation (n = 3).

The PDT activity experiments (**Figure 5.22 (a)**) for the complexes involved the addition of ***4***, ***5***, and ***6*** in a 96-well tissue culture plate containing MCF-7 cells. Illumination for PDT studies was obtained with a 680 nm laser probe Modulight medical laser for 15 min (524 mW/cm^2). The IC_{50} values follow the order: ***6*** (4.9 µM) < ***5*** (8.2 µM) < ***4*** (15.1 µM), **Table 5.7**. These values are in accordance with the cellular uptake trend.

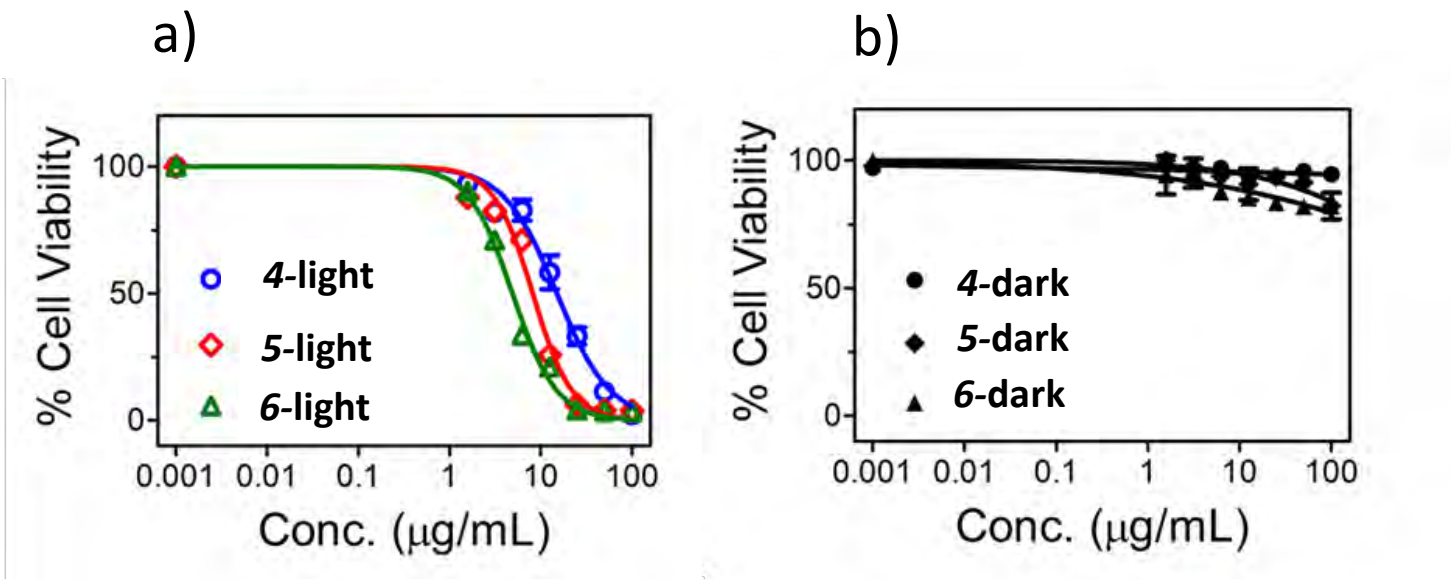

Figure 5.22: Cytotoxicity plots for *4*, *5*, and *6* in the (a) light and (b) dark at the indicated concentrations (Concentration range studied: 100–1.6 µM) Incubation time: 24 h.

5.5 Summary of chapter

Phthalocyanines and their conjugates were tested against *Escherichia coli* (*E. coli*), *Staphylococcus aureus* (*S. aureus*), *Streptococcus pneumoniae* (*S. pneumoniae*), and human breast adenocarcinoma cells (MCF-7 cells) for in vitro dark cytotoxicity, photodynamic antimicrobial chemotherapy (PACT), and photodynamic therapy (PDT), respectively. While the *in-vitro* PDT investigations were carried out at various concentration doses and fixed illumination dosimetry, the *in vitro* dark viability studies were carried out at a physiological temperature and variable concentration doses with no light treatment.

When the Pc complexes are present alone or enclosed in surface-modified silica nanoparticles, the influence of varied numbers of charges on photodynamic (PACT) is examined towards *E. coli*, *S. aureus*, and *S. pneumoniae* in both planktonic and biofilm forms. The cationic complexes displayed the highest activity with log CFU (colony forming units). The viability of in vitro biofilms of *E. coli*, *S. aureus*, and *S. pneumoniae* was significantly reduced by the cationic complexes as well.

MCF-7 cells are used to test the complexes and their doped equivalents for PDT activity. Every complex displayed dark toxicity of greater than 50%. When exposed to laser light, the folic acid conjugates **Pc**@SiNPs-FA displayed higher phototoxicity towards MCF-7 cells. The IC_{50} values for the cationic Pcs, ***5***, and ***6***, are 8.2 and 4.9 µM for good cellular absorption and PDT action against MCF-7 cells, respectively.

6.1 General conclusion

A variety of analytical spectroscopic techniques were used to successfully synthesise and characterise symmetrical and asymmetrical phthalocyanines (Pcs). With the aid of MALDI-TOF MS, UV-vis spectroscopy, and elemental analysis, the complexes' purity was verified. The complexes that were synthesised gave results that matched the predicted structures. The complexes' typical absorption bands demonstrated that they were soluble in the majority of solvents.

Some of the symmetrical Pcs are encapsulated into silica nanoparticles (SINPs). Covalently attaching biomolecules including AMP, FA, PSn, and GA to the surface of the amino Pc@SiNPs-NH_2 allows for the diversification of the Pc doped silica (Pc@SiNPs). CIP is conjugated to the asymmetric Pcs using the secondary amine on ciprofloxacin. Transmission electron microscopy and dynamic light scattering were used to evaluate the morphologies and size of the Pc doped conjugates. The Pcs and SiNPs conjugates' successful amide bond formation was verified using FT-IR and X-ray photoelectron spectra.

The Pcs' photochemistry and photophysics were evaluated both on their own and in SiNPs conjugates form. It is important to note that the nature of substituent also very important for the Pcs' fluorescence feature. Φ_F and τ_F have a straight proportional relationship, thus the decrease in Φ_F is complemented by the shortening in τ_F. Pcs and their conjugates showed insignificant changes in Φ_F. Low Φ_F and high Φ_T were in line with the trend in the Φ_F and Φ_T measurements. Due to inconsistency between the Φ_T and Φ_Δ of the **Pc**@SiNPs conjugates, the obtained Φ_Δ values of several conjugates did not follow the anticipated patterns. In several instances, low Φ_Δ was noticed in the Pc conjugates.

The ineffective energy transfer between the excited triplet state photosensitiser and ground state molecular oxygen could be the cause of the low Φ_Δ.

The Pcs and their conjugates' where applicable, in-*vitro* cytotoxicity demonstrated relative dark toxicity at very high concentrations. Significant activity was seen in the PDT experiments of the Pcs and their conjugates at the tested concentrations. In both PDT and PACT, the cationic Pcs outperformed the neutral Pc in terms of biological activity. When used against MCF-7 cells, cationic Pc dyes (***5*** and ***6***) exhibit noticeably improved cellular absorption and PDT activity. Additionally, the PACT activity of the cationic Pcs is higher than that of the neutral Pcs. The quick, label-free, quantitative, non-invasive, and effective detection of biochemical changes in *E. coli*, *S. aureus*, and *S. pneumoniae* biofilm was made possible with the help of Raman spectroscopy. The findings of this study suggest that both PDT and PACT are significantly influenced by the nature of substituent, Pc delivery system (NPs), and Φ_Δ.

6.2 FUTURE PROSPECTS

It is critical to screen and identify microbes that can efficiently degrade pollutants and generate bio-electrical energy, as well as investigate the potential mechanisms of cooperation between different microorganisms for bio-electrical energy development. As a result, efforts will be made to combine phthalocyanines, various nanomaterial and biofilm-based biocatalysts, and their electron transfer mechanisms and pollutant degradation capabilities activity will be evaluated in photoelectroactive microbial fuel cell. Photosensitisers with optimal PDT and PACT activity will be evaluated further.

[1]. "New report calls for urgent action to avert antimicrobial resistance crisis," https://www.who.int/news/item/29-04-2019-new-report-calls-for-urgent-action-to-avert-antimicrobial-resistance-crisis (Accessed on June 6, 2023).

[2]. D. Sharma, L. Misba, A. U. Khan, *Antimicrob. Resist. Infect. Control.* **2019**, *8* (*1*), 76. DOI: https://doi.org/10.1186/s13756-019-0533-3.

[3]. H. Ceri, M. E. Olson, C. Stremick, R. R. Read, D. Morck, A. Buret, *J. Clin. Microbiol.* **1999**, *37* (*6*), 177. DOI: https://doi.org/10.1128/JCM.37.6.1771-1776.1999.

[4]. R. Mirzaei, R. Mohammadzadeh, M. Y. Alikhani, M. Shokri Moghadam, S. Karampoor, S. Kazemi, A. Barfipoursalar, R. Yousefimashouf, *IUBMB (Int. Union Biochem. Mol. Biol)*. **2020**, *72* (*7*), 1271. DOI: https://doi.org/10.1002/iub.2266.

[5]. P. S. Stewart, *Microbiol. Spectr.* **2015**, *3*, 7. DOI: https://doi.org/10.1128/microbiolspec.MB-0010-2014.

[6]. Global Burden of Disease 2019 Cancer risk collaborators (J. J. Lang, K. Compton, R. Xu, A. R. Acheson, H. J. Henrikson, J. M. Kocarnik, L. Penberthy, A. Aali, Q. Abbas, B. Abbasi, et al.), *Lancet*. **2022**, *400* (*10352*), 563. DOI: https://doi.org/10.1016/S0140-6736(22)01438-6.

[7]. Adolescent Young Adult Cancer Collaborators (L.M. Force, R. Xu, K. Compton, D. Lu, H. J. Henrikson, J.M. Kocarnik, J.D. Harvey, A. Pennini, F.E. Dean, et al), *Lancet Oncol.* **2022**, *23*, 27, doi:10.1016/S1470-2045(21)00581-7.

[8]. Global Burden of Disease 2019 Cancer Collaboration (J. M. Kocarnik, K. Compton, F. E. Dean, W. Fu, B. L. Gaw, J. D. Harvey, H. J. Henrikson, D. Lu, A. Pennini, et al.), *J. Am. Chem. Ass. Oncol.* **2022**, *8* (*3*), 420. DOI: https://doi.org/10.1001/jamaoncol.2021.6987.

[9]. D. van Elsland, J. Neefjes, *Eu. Mol. Bio Org. Rep.* **2018**, *19* (*11*), e46632. DOI: https://doi.org/10.15252/embr.201846632.

[10]. L. Dalton-Griffin, P. Kellam, *J. Biol.* **2009**, *8* (*7*), 67. DOI: https://doi.org/10.1186/jbiol168

[11]. X. Hu, Y.-Y. Huang, Y. Wang, X. Wang, M. R. Hamblin, *Front. Microbiol.* **2018**, *9*, 1299. DOI: https://doi.org/10.3389/fmicb.2018.01299.

[12]. M. Klausen, M. Ucuncu, M. Bradley, *Molecules*. **2020**, *25* (*22*), 5239. DOI: https://doi.org/10.3390/molecules25225239.

[13]. E. Polat, K. Kang, *Biomedicines*. **2021**, *9* (*6*), 584. DOI: https://doi.org/10.3390/biomedicines9060584.

[14]. J. Ghorbani, D. Rahban, S. Aghamiri, A. Teymouri, A. Bahador, *Laser Ther.* **2018**, *27*, 293, doi:10.5978/islsm.27_18-RA-01.

[15]. P. Agostinis, K. Berg, K. A. Cengel, T. H. Foster, A. W. Girotti, S. O. Gollnick, S. M. Hahn, M. R. Hamblin, A. Juzeniene, D. Kessel, *CA Cancer J. Clin.* **2011**, *61* (*4*), 250. DOI: https://doi.org/10.3322/caac.20114.

[16]. M. Kolarikova, B. Hosikova, H. Dilenko, K. Barton-Tomankova, L. Valkova, R. Bajgar, L. Malina, H. Kolarova, *Med. Res. Rev*. **2023**, 717. DOI: https://doi.org/10.1002/med.21935.

[17]. T. Dai, B. B. Fuchs, J. J. Coleman, R. A. Prates, C. Astrakas, T. G. St. Denis, M. S. Ribeiro, E. Mylonakis, M. R. Hamblin, G. P. Tegos, *Front. Microbiol*. **2012**, *3*, 120. DOI: https://doi.org/10.3389/fmicb.2012.00120.

[18]. S. Callaghan, M. O. Senge, *Photochem. Photobiol. Sci.* **2018**, *17* (*11*), 1490. DOI: https://doi.org/10.1039/c8pp00008e.

[19]. E. Alves, M. A. Faustino, M. G. Neves, A. Cunha, J. Tome, A. Almeida, *Future Med. Chem.* **2014**, *6* (*2*), 141. DOI: https://doi.org/10.4155/fmc.13.211.

[20]. B. Ezraty, A. Gennaris, F. Barras, J.-F. Collet, *Nat. Rev. Microbiol.* **2017**, *15* (*7*), 385. DOI: https://doi.org/10.1038/nrmicro.2017.26.

[21]. A. Galstyan, U. Dobrindt, *J. Mater. Chem. B*. **2018**, *6* (*28*), 4630. DOI: https://doi.org/10.1039/C8TB01357H.

[22]. R. Youf, M. Müller, A. Balasini, F. Thétiot, M. Müller, A. Hascoët, U. Jonas, H. Schönherr, G. Lemercier, T. Montier, *Pharmaceutics*. **2021**, *13* (*12*), 1995. DOI: https://doi.org/10.3390/pharmaceutics13121995.

[23]. M. R. Hamblin, H. Abrahamse, *Antibiotics*. **2020**, *9* (*2*), 53. DOI: https://doi.org/10.3390/antibiotics9020053.

[24]. Y. Tian, D. Yin, L. Yan, *Wiley Interdiscip. Rev. Nanomed. Nanobiotechnol.* **2023**, *15* (*1*), e1831. DOI: https://doi.org/10.1002/wnan.1831.

[25]. O. Sizar, S. W. Leslie, C. G. Unakal, in *StatPearls* (Eds: E. Hughes, G. Rubio), Stat Pearls Publishing, Treasure Island (FL) **2023**.

[26]. S. Morris, E. Cerceo, *J. Antibiot.* **2020**, *9* (*4*), 196. DOI: https://doi.org/10.3390/antibiotics9040196.

[27]. R.F. Maldonado, I. Sá-Correia, M.A. Valvano, *FEMS Microbiol. Rev.* **2016**, *40*, 480, doi:10.1093/femsre/fuw007.

[28]. K. H. Jacobson, I. L. Gunsolus, T. R. Kuech, J. M. Troiano, E. S. Melby, S. E. Lohse, D. Hu, W. B. Chrisler, C. J. Murphy, G. Orr, *Environ. Sci. Technol.* **2015**, *49* (*17*), 10642. DOI: https://doi.org/10.1021/acs.est.5b01841.

[29]. A. Mobed, M. Hasanzadeh, *RSC Adv.* **2022**, *12* (*16*), 9704. DOI: https://doi.org/10.1039/D1RA09393B.

[30]. A. Sułek, B. Pucelik, M. Kobielusz, A. Barzowska, J. M. Dąbrowski, *Int. J. Mol. Sci.* **2020**, *21* (*22*), 8716. DOI: https://doi.org/10.3390/ijms21228716.

[31]. E. Alves, L. Costa, C. M. Carvalho, J. P. Tomé, M. A. Faustino, M. G. Neves, A. C. Tomé, J. A. Cavaleiro, Â. Cunha, A. Almeida, *BMC Microbiol.* **2009**, *9* (*1*), 70. DOI: https://doi.org/10.1186/1471-2180-9-70.

[32]. A. Galstyan, *Chem. Eur. J.* **2021**, *27* (*6*), 1903. DOI: https://doi.org/10.1002/chem.202002703.

[33]. M. Rohde, *Microbiol. Spectr.* **2019**, *7* (*3*), 10. DOI: https://doi.org/10.1128/microbiolspec.GPP3-0044-2018.

[34]. S. Brown, J. P. Santa Maria, S. Walker, *Annu. Rev. Microbiol.* **2013**, *67* (*1*), 313. DOI: https://doi.org/10.1146/annurev-micro-092412-155620.

[35]. Z. Malik, *J. Biophotonics*. **2020**, *2*, 5. DOI: https://doi.org/10.1002/tbio.201900030.

[36]. F. Sperandio, Y.-Y. Huang, M. Hamblin, *Recent Pat Anti infect Drug Discov.* **2013**, *8* (*2*), 108. DOI: https://doi.org/10.2174/1574891X113089990012.

[37]. R. M. Reddinger, N. R. Luke-Marshall, S. L. Sauberan, A. P. Hakansson, A. A. Campagnari, *mBio (Mast. Biosc)*. **2018**, *9* (*1*), e02089-17. DOI: https://doi.org/10.1128/mBio.02089-17.

[38]. N. Nair, R. Biswas, F. Götz, L. Biswas, *Infect. Immun.* **2014**, *82* (*6*), 2162. DOI: https://doi.org/10.1128/IAI.00059-14.

[39]. P. Choudhary, S. Singh, V. Agarwal, in *Bacterial Biofilms* (Eds: S. Dincer, M. Sümengen Özdenefe, A. Arkut), IntechOpen, Northen Cyprus, Turkey **2020**.

[40]. R. M. Donlan, *Emerg. Infect. Dis.* **2002**, *8* (*9*), 881. DOI: https://doi.org/10.3201/eid0809.020063.

[41]. F. Song, H. Koo, D. Ren, *J. Dent. Res.* **2015**, *94* (*8*), 1027. DOI: https://doi.org/10.1177/0022034515587690.

[42]. R. Srinivasan, S. Santhakumari, P. Poonguzhali, M. Geetha, M. Dyavaiah, L. Xiangmin, *Front. Microbiol.* **2021**, *12*, 676458, doi:10.3389/fmicb.2021.676458.

[43]. T. Kushibiki, T. Hirasawa, S. Okawa, M. Ishihara, *J. Healthc. Eng.* **2013**, *4* (*1*), 87. DOI: https://doi.org/10.1260/2040-2295.4.1.87.

[44]. G. Gunaydin, M. E. Gedik, S. Ayan, *Front. Chem.* **2021**, *9*, 686303. DOI: https://doi.org/10.3389/fchem.2021.686303.

[45]. J. R. Sounik, B. D. Rihter, W. E. Ford, M. A. J. Rodgers, M. E. Kenney, in (Ed: T. J. Dougherty), Los Angeles, CA **1991**.

[46]. D. E. J. G. J. Dolmans, D. Fukumura, R. K. Jain, *Nat. Rev. Cancer.* **2003**, *3* (*5*), 380. DOI: https://doi.org/10.1038/nrc1071.

[47]. L. V. Uspenskiĭ, L. V. Chistov, E. A. Kogan, V. B. Loshchenov, I. A. Ablitsov, V. K. Rybin, V. I. Zavodnov, D. I. Shiktorov, N. F. Serbinenko, I. G. Semenova, *Khirurgiia (Mosk)*. **2000**, (*2*), 38.

[48]. E. F. Stranadko, M. I. Garbuzov, V. G. Zenger, A. N. Nasedkin, N. A. Markichev, M. V. Riabov, I. V. Leskov, *Vestn. Otorinolaringol.* **2001**, (*3*), 36.

[49]. E. V. Filonenko, V. V. Sokolov, V. I. Chissov, E. A. Lukyanets, G. N. Vorozhtsov, *Photodiagnosis Photodyn. Ther.* **2008**, *5* (*3*), 187. DOI: https://doi.org/10.1016/j.pdpdt.2008.06.001.

[50]. J. Miller, E. Baron, H. Scull, A. Hsia, J. Berlin, T. Mccormick, V. Colussi, M. Kenney, K. Cooper, N. Oleinick, *Toxicol. Appl. Pharmacol.* **2007**, *224* (*3*), 290. DOI: https://doi.org/10.1016/j.taap.2007.01.025.

[51]. Z. Huang, *Photodiagnosis Photodyn. Ther.* **2008**, *5* (*4*), 285. DOI: https://doi.org/10.1016/j.pdpdt.2009.01.005.

[52]. E. Ben-Hur, R. Kol, R. Marko, E. Riklis, I. Rosenthal, *Int. J. Radiat. Biol.* **1988**, *54* (*1*), 21. DOI: https://doi.org/10.1080/09553008814551471.

[53]. A.-G. Niculescu, A. M. Grumezescu, *Appl. Sci.* **2021**, *11* (*8*), 3626. DOI: https://doi.org/10.3390/app11083626.

[54]. A. Escudero, C. Carrillo-Carrión, M. C. Castillejos, E. Romero-Ben, C. Rosales-Barrios, N. Khiar, *Mater. Chem. Front.* **2021**, *5* (*10*), 3788. DOI: https://doi.org/10.1039/D0QM00922A.

[55]. C. Vannostrum, *Adv. Drug Deliv. Rev.* **2004**, *56* (*1*), 9. DOI: https://doi.org/10.1016/j.addr.2003.07.013.

[56]. Y. Nakamura, A. Mochida, P. L. Choyke, H. Kobayashi, *Bioconjug. Chem.* **2016**, *27* (*10*), 2225. DOI: https://doi.org/10.1021/acs.bioconjchem.6b00437.37.

[57]. A. K. Iyer, G. Khaled, J. Fang, H. Maeda, *Drug Discov. Today*. **2006**, *11* (*17–18*), 812. DOI: https://doi.org/10.1016/j.drudis.2006.07.005.

[58]. C. A. Kulkarni, B. D. Fink, B. E. Gibbs, P. R. Chheda, M. Wu, W. I. Sivitz, R. J. Kerns, *J. Med. Chem.* **2021**, *64* (*1*), 662. DOI: https://doi.org/10.1021/acs.jmedchem.0c01671.

[59]. Y. Wang, W. Wang, R. Gu, J. Chen, Q. Chen, T. Lin, J. Wu, Y. Hu, A. Yuan, *Adv. Sci.* **2023**, 2300286. DOI: https://doi.org/10.1002/advs.202300286.

[60]. Q. Zhou, Z.-F. Liu, T. J. Marks, P. Darancet, *J. Phys. Chem. A*. **2021**, *125* (*19*), 4055. DOI: https://doi.org/10.1021/acs.jpca.0c10766.

[61]. D. Gounden, M. N. Pillay, T. Raab, N. Nombona, L. Schmidt-Mende, W. E. Van Zyl, *Mater. Adv.* **2020**, *1* (*8*), 3058. DOI: https://doi.org/10.1039/D0MA00725K.

[62]. A. Atsay, A. Gül, M. Burkut Koçak, *Dyes Pigm.* **2014**, *100*, 177. DOI: https://doi.org/10.1016/j.dyepig.2013.09.012.

[63]. M. Machacek, A. Cidlina, V. Novakova, J. Svec, E. Rudolf, M. Miletin, R. Kučera, T. Simunek, P. Zimcik, *J. Med. Chem.* **2015**, *58* (*4*), 1736. DOI: https://doi.org/10.1021/jm5014852.

[64]. H. Pekbelgin Karaoğlu, A. Kalkan Burat, *Molecules*. **2020**, *25* (*2*), 363. DOI: https://doi.org/10.3390/molecules25020363.

[65]. A. T. Bilgicli, Y. Tekin, E. H. Alici, M. N. Yaraşir, G. Arabaci, M. Kandaz, *J. Coord.* **2015**, *68* (*22*), 4102. DOI: https://doi.org/10.1080/00958972.2015.1080361.

[66]. L. Martín-Gomis, F. Fernández-Lázaro, Á. Sastre-Santos, *J. Mater. Chem. A*. **2014**, *2* (*38*), 15672. DOI: https://doi.org/10.1039/C4TA01894J.

[67]. K. P. C. H. Puttaningaiah, S. Aralekallu, A. Chikkabasur Kumbara, L. K. Sannegowda, *ACS Appl. Nano Mater.* **2023**, *6* (*10*), 8880. DOI: https://doi.org/10.1021/acsanm.3c01328.

[68]. L. Ma, Y. Zhang, P. Yuan, *Opt. Express*. **2010**, *18* (*17*), 17666. DOI: https://doi.org/10.1364/OE.18.017666.

[69]. M. Li, B. Mai, A. Wang, Y. Gao, X. Wang, X. Liu, S. Song, Q. Liu, S. Wei, P. Wang, *RSC Adv.* **2017**, *7* (*65*), 40734. DOI: https://doi.org/10.1039/C7RA06073D.

[70]. P.-C. Lo, M. S. Rodríguez-Morgade, R. K. Pandey, D. K. P. Ng, T. Torres, F. Dumoulin, *Chem. Soc. Rev.* **2020**, *49* (*4*), 1041. DOI: https://doi.org/10.1039/C9CS00129H.

[71]. K. M. Alam, P. Kumar, S. Gusarov, A. E. Kobryn, A. P. Kalra, S. Zeng, A. Goswami, T. Thundat, K. Shankar, *ACS Appl. Mater. Interfaces*. **2020**, *12* (*39*), 43992. DOI: https://doi.org/10.1021/acsami.0c07179.

[72]. Z. Kanat, H. Dinçer, *Dalton Trans.* **2014**, *43* (*23*), 8654. DOI: https://doi.org/10.1039/C4DT00238E.

[73]. N. B. McKeown, I. Chambrier, M. J. Cook, *J. Chem. Soc., Perkin trans. 1.* **1990**, (*4*), 1169. DOI: https://doi.org/10.1039/P19900001169.

[74]. B. I. Kharisov, U. Ortiz Méndez, J. L. Almaraz Garza, J. R. Almaguer Rodríguez, *New J. Chem.* **2005**, *29* (*5*), 686. DOI: https://doi.org/10.1039/b415712p.

[75]. B. I. Kharisov, L. M. Blanco, L. M. Torres-Martinez, A. García-Luna, *Ind. Eng. Chem. Res.* **1999**, *38* (*8*), 2880. DOI: https://doi.org/10.1021/ie9806545.

[76]. M. N. Kopylovich, V. Yu. Kukushkin, M. Haukka, K. V. Luzyanin, A. J. L. Pombeiro, *J. Am. Chem. Soc.* **2004**, *126* (*46*), 15040. DOI: https://doi.org/10.1021/ja046759i.

[77]. V. N. Nemykin, E. A. Lukyanets, *Arkivoc*. **2010**, *2010* (*1*), 136. DOI: https://doi.org/10.3998/ark.5550190.0011.104.

[78]. M. S. Rodríguez-Morgade, G. De la Torre, T. Torres, in *The Porphyrin Handbook* (Eds: K. M. Kadish, K. M. Smith, R. Guilard), Academic Press, Amsterdam **2003**.

[79]. Y. Liu, D. Zhu, T. Wada, A. Yamada, H. Sasabe, *J. Heterocycl. Chem.* **1994**, *31* (*4*), 1017. DOI: https://doi.org/10.1002/jhet.5570310453.

[80]. X.-F. Zhang, Q. Xi, J. Zhao, *J. Mater. Chem.* **2010**, *20*, 6726. DOI: https://doi.org/10.1039/c0jm00695e.

[81]. M. Bayda, F. Dumoulin, G. L. Hug, J. Koput, R. Gorniak, A. Wojcik, *Dalton Trans.* **2017**, *46* (*6*), 1914. DOI: https://doi.org/10.1039/C6DT02651F.

[82]. M. Kasha, H. R. Rawls, M. Ashraf El-Bayoumi, *Pure Appl. Chem*. **1965**, *11* (*3–4*), 371. DOI: https://doi.org/10.1351/pac196511030371.

[83]. O. E. Sielcken, M. M. Van Tilborg, M. F. M. Roks, R. Hendriks, W. Drenth, R. J. M. Nolte, *J. Am. Chem. Soc.* **1987**, *109* (*14*), 4261. DOI: https://doi.org/10.1021/ja00248a021.

[84]. W. J. Schutte, M. Sluyters-Rehbach, J. H. Sluyters, *J. Phys. Chem.* **1993**, *97* (*22*), 6069. DOI: https://doi.org/10.1021/j100124a047.

[85]. X. Li, X.-H. Peng, B.-D. Zheng, J. Tang, Y. Zhao, B.-Y. Zheng, M.-R. Ke, J.-D. Huang, *Chem. Sci.* **2018**, *9* (*8*), 2098. DOI: https://doi.org/10.1039/C7SC05115H.

[86]. M. Kostka, P. Zimcik, M. Miletin, P. Klemera, K. Kopecky, Z. Musil, *J. Photochem. Photobiol. A: Chem.* **2006**, *178* (*1*), 16. DOI: https://doi.org/10.1016/j.jphotochem.2005.06.014.

[87]. D. Wöhrle, G. Schnurpfeil, S. G. Makarov, A. Kazarin, O. N. Suvorova, *Macroheterocycles*. **2012**, *5* (*3*), 191. DOI: https://doi.org/10.6060/mhc2012.120990w.

[88]. F. Bächle, C. Maichle-Mössmer, T. Ziegler, *ChemPlusChem*. **2019**, *84* (*8*), 1081. DOI: https://doi.org/10.1002/cplu.201900381.

[89]. Y. Bian, J. Chen, S. Xu, Y. Zhou, L. Zhu, Y. Xiang, D. Xia, *New J. Chem.* **2015**, *39* (*7*), 5750. DOI: https://doi.org/10.1039/C5NJ00494B

[90]. J. Chen, T. Zhang, S. Wang, R. Hu, S. Li, J. S. Ma, G. Yang, *Spectrochim. Acta A Mol. Biomol. Spectrosc.* **2015**, *149*, 426. DOI: https://doi.org/10.1016/j.saa.2015.04.093.

[91]. M. Halaskova, A. Rahali, V. Almeida-Marrero, M. Machacek, R. Kucera, B. Jamoussi, T. Torres, V. Novakova, A. De La Escosura, P. Zimcik, *ACS Med. Chem. Lett.* **2021**, *12* (*3*), 502. DOI: https://doi.org/10.1021/acsmedchemlett.1c00045.

[92]. C. Jing, R. Wang, H. Ou, A. Li, Y. An, S. Guo, L. Shi, *Chem. Comm.* **2018**, *54* (*32*), 3985. DOI: https://doi.org/10.1039/C7CC09954A.

[93]. H. Yalazan, K. Tekintas, V. Serdaroğlu, E. Tugba Saka, N. Kahriman, H. Kantekin, *Inorg. Chem. Commun.* **2020**, *118*, 107998. DOI: https://doi.org/10.1016/j.inoche.2020.107998.

[94]. H. Zhu, D. Zhang, E. Feng, X. Sheng, *Phys. Chem.* **2023**, *25* (*15*), 10278. DOI: https://doi.org/10.1039/D2CP04372F.

[95]. F. Cieplik, L. Tabenski, W. Buchalla, T. Maisch, *Front. Microbiol.* **2014**, *5*, 15. DOI: https://doi.org/doi.org/10.3389/fmicb.2014.00405.

[96]. P. Sen, N. Dege, S. Z. Yildiz, *J. Coord. Chem.* **2017**, *70* (*16*), 2751. DOI: https://doi.org/10.1080/00958972.2017.1360490

[97]. I. Scalise, E. N. Durantini, *Bioorg. Med. Chem*. **2005**, *13* (*8*), 3037. DOI: https://doi.org/10.1016/j.bmc.2005.01.063.

[98]. W. Chidawanyika, A. Ogunsipe, T. Nyokong, *New J. Chem.* **2007**, *31* (*3*), 377. DOI: https://doi.org/10.1039/b615663k.

[99]. D. Wöhrle, N. Iskander, G. Graschew, H. Sinn, E. A. Friedrich, W. Maier-Borst, J. Stern, P. Schlag, *Photochem. Photobiol.* **1990**, *51* (*3*), 351. DOI: https://doi.org/10.1111/j.1751-1097.1990.tb01721.x.

[100]. J. M. M. Rodrigues, A. S. F. Farinha, Z. Lin, J. A. S. Cavaleiro, A. C. Tome, J. P. C. Tome, *Sensors*. **2021**, *21* (*5*), 1632. DOI: https://doi.org/10.3390/s21051632.

[101]. A. Fashina, E. Antunes, T. Nyokong, *Polyhedron*. **2013**, *53*, 278. DOI: https://doi.org/10.1016/j.poly.2013.01.037.

[102]. R. C. H. Wong, D. K. P. Ng, W.-P. Fong, P.-C. Lo, *Chem. Eur. J.* **2017**, *23* (*65*), 16505. DOI: https://doi.org/10.1002/chem.201703188.

[103]. E. Dube, R. Soy, M. Shumba, T. Nyokong, *J. Lumin*. **2021**, *234*, 117939. DOI: https://doi.org/10.1016/j.jlumin.2021.117939.

[104]. G. Singh, P. K. Khatri, S. K. Ganguly, S. L. Jain, *RSC Adv.* **2014**, *4* (*55*), 29124. DOI: https://doi.org/10.1039/C4RA02355B.

[105]. J. Vivero-Escoto, M. Elnagheeb, *Nanomaterials*. **2015**, *5* (*4*), 2302. DOI: https://doi.org/10.3390/nano5042302.

[106]. Z. Chen, X. Wang, W. Lang, D. Qi, *RSC Adv.* **2019**, *9* (*56*), 32490. DOI: https://doi.org/10.1039/C9RA06455A.

[107]. R. Lin, L. Zhou, Y. Lin, A. Wang, J. H. Zhou, S. H. Wei, *Spectroscopy*. **2011**, *26* (*3*), 179. DOI: https://doi.org/10.1155/2011/591813.

[108]. P. I. Rafailidis, E. N. Ioannidou, M. E. Falagas, *Drugs*. **2007**, *67* (*13*), 1829. DOI: https://doi.org/10.2165/00003495-200767130-00003.

[109]. K. Rajamanickam, J. Yang, M.K. Sakharkar, *Front. Pharmacol.* **2018**, *9*, doi:10.3389/fphar.2018.01486.

[110]. A. Borges, C. Ferreira, M. J. Saavedra, M. Simões, *Microb. Drug Resist.* **2013**, *19* (*4*), 256. DOI: https://doi.org/10.1089/mdr.2012.0244.

[111]. K. Nakamura, Y. Yamada, H. Ikai, T. Kanno, K. Sasaki, Y. Niwano, *J. Agric. Food Chem.* **2012**, *60* (*40*), 10048. DOI: https://doi.org/10.1021/jf303177p.

[112]. T. A. Vico, V. B. Arce, M. F. Fangio, L. B. Gende, C. A. Bertran, D. O. Mártire, M. S. Churio, *J. Nanopart. Res.* **2016**, *18* (*11*), 348. DOI: https://doi.org/10.1007/s11051-016-3652-2.

[113]. E. Domínguez, M. P. Moliné, M. S. Churio, V. B. Arce, D. O. Mártire, S. N. Mendiara, B. S. Álvarez, L. B. Gende, N. Damiani, *Apidologie*. **2019**, *50* (*5*), 616. DOI: https://doi.org/10.1007/s13592-019-00675-y.

[114]. L. T. Senbanjo, M. A. Chellaiah, *Front. Cell Dev. Biol.* **2017**, *5,* 18. DOI: https://doi.org/10.3389/fcell.2017.00018.

[115]. X. Wang, X. Sun, J. Lao, H. He, T. Cheng, M. Wang, S. Wang, F. Huang, *Colloids Surf. B*. **2014**, *122*, 638. DOI: https://doi.org/10.1016/j.colsurfb.2014.07.043.

[116]. N. Nwahara, G. Abrahams, E. Prinsloo, T. Nyokong, *Photodiagnosis Photodyn. Ther.* **2021**, *36*, 102527. DOI: https://doi.org/10.1016/j.pdpdt.2021.102527.

[117]. B. S. Wang, J. Wang, J.-Y. Chen, *J. Mater. Chem. B*. **2014**, *2* (*11*), 1594. DOI: https://doi.org/10.1039/C3TB21620A.

[118]. J. T. Ferreira, J. Pina, C. A. F. Ribeiro, R. Fernandes, J. P. C. Tomé, T. Torres, M. S. Rodríguez-Morgade, *J. Porphyr. Phthalocyanines*. **2021**, *25*, 1193. DOI: https://doi.org/10.1142/S108842462150122.

[119]. K. Abou Aitah, A. Swiderska-Sroda, A. A. Farghali, J. Wojnarowicz, A. Stefanek, S. Gierlotka, A. Opalinska, A. K. Allayeh, T. Ciach, W. Lojkowski, *Oncotarget*. **2018**, *9* (*41*), 26466. DOI: https://doi.org/10.18632/oncotarget.25470.

[120]. Z. Sun, C. Shi, X. Wang, Q. Fang, J. Huang, *Carbohydr. Polym.* **2017**, *155*, 321. DOI: https://doi.org/10.1016/j.carbpol.2016.08.069.

[121]. F. Luan, L. Wei, J. Zhang, Y. Mi, F. Dong, Q. Li, Z. Guo, *Polymers (Basel)*. **2018**, *10* (*4*), 395. DOI: https://doi.org/10.3390/polym10040395.

[122]. P. C. Balaure, A. M. Grumezescu, *Nanomaterials*. **2020**, *10* (*8*), 1527. DOI: https://doi.org/10.3390/nano10081527.

[123]. Z. Lin, Z. Lin, Y. Guo, H. Wu, J. Song, Y. Zhang, W. Zhang, H. Li, D. Hou, R. Huang, *Nanomaterials*. **2023**, *13* (*7*), 1228. DOI: https://doi.org/10.3390/nano13071228.

[124]. K. C. Majhi, M. Yadav, in *Green Sustainable Process for Chemical and Environmental Engineering and Science* (Eds: Inamuddin, R. Boddula, M. I. Ahamed, A. M. Asiri), Elsevier, Jharkhand, India **2021**.

[125]. M. Tintoré, S. Mazzini, L. Polito, M. Marelli, A. Latorre, Á. Somoza, A. Aviñó, C. Fàbrega, R. Eritja, *Int. J. Mol. Sci.* **2015**, *16* (*11*), 27625. DOI: https://doi.org/10.3390/ijms161126046.

[126]. M. Sajid, *Curr. Opin. Environ. Sci. Health.* **2022**, *25*, 100319. DOI: https://doi.org/10.1016/j.coesh.2021.100319.

[127]. M. Colilla, M. Vallet-Regí, *Int. J. Mol. Sci.* **2020**, *21* (*22*), 8605. DOI: https://doi.org/10.3390/ijms21228605.

[128]. H. Bronner, F. Brunswig, D. Pluta, Y. Krysiak, N. Bigall, O. Plettenburg, S. Polarz, *ACS Appl. Mater. Interfaces*. **2023**, 15 (*11*), 14067. DOI: https://doi.org/10.1021/acsami.3c00210.

[129]. Y.-C. Yeh, T.-H. Huang, S.-C. Yang, C.-C. Chen, J.-Y. Fang, *Front. Chem.* **2020**, *8*, 286. DOI: https://doi.org/10.3389/fchem.2020.00286.

[130]. Z. Li, Y. Mu, C. Peng, M. F. Lavin, H. Shao, Z. Du, *Wiley Interdiscip Rev Nanomed Nanobiotechnol*. **2021**, *13* (*1*), e1658. DOI: https://doi.org/10.1002/wnan.1658

[131]. A. A. Nayl, A. I. Abd-Elhamid, A. A. Aly, S. Bräse, *RSC Adv.* **2022**, *12* (*22*), 13706. DOI: https://doi.org/10.1039/D2RA01587K.

[132]. J.Y. Liu, C. M. Sayes, *Toxicol. Res.* **2022**, *11* (*4*), 565. DOI: https://doi.org/10.1093/toxres/tfac038

[133]. C. W. Ang, L. Tan, Z. Qu, N. P. West, M. A. Cooper, A. Popat, M. A. T. Blaskovich, *ACS Biomater. Sci. Eng.* **2022**, *8* (*10*), 4196. DOI: https://doi.org/10.1021/acsbiomaterials.1c00807.

[134]. S. Santra, K. Wang, R. Tapec, W. Tan, *J. Biomed. Opt.* **2001**, *6* (*2*), 160. DOI: https://doi.org/10.1117/1.1353590.

[135]. W. L. Vos, R. Sprik, A. Van Blaaderen, A. Imhof, A. Lagendijk, G. H. Wegdam, *Phys. Rev. B*. **1996**, *53* (*24*), 16231. DOI: https://doi.org/10.1103/PhysRevB.53.16231.

[136]. M. Brunel, F. Le Luyer, M. Canva, A. Brun, F. Chaput, L. Malier, J.-P. Boilot, *Appl. Phys. B*. **1994**, *58* (*6*), 443. DOI: https://doi.org/10.1007/BF01081074.

[137]. X. Zhao, R. Tapec-Dytioco, K. Wang, W. Tan, *Anal. Chem.* **2003**, *75* (*14*), 3476. DOI: https://doi.org/10.1021/ac034330o.

[138]. D. Desai, M. Åkerfelt, N. Prabhakar, M. Toriseva, T. Näreoja, J. Zhang, M. Nees, J. M. Rosenholm, *Pharmaceutics*. **2018**, *10* (*4*), 237. DOI: https://doi.org/10.3390/pharmaceutics10040237.

[139]. I. Slowing, J. Viveroescoto, C. Wu, V. Lin, *Adv. Drug Deliv. Rev.* **2008**, *60* (*11*), 1278. DOI: https://doi.org/10.1016/j.addr.2008.03.012.

[140]. M. Montalti, L. Prodi, E. Rampazzo, N. Zaccheroni, *Chem. Soc. Rev.* **2014**, *43* (*12*), 4243. DOI: https://doi.org/10.1039/C3CS60433K.

[141]. J. R. Lakowicz, *Principles of Fluorescence Spectroscopy*, Springer US, Boston, MA **2006**.

[142]. S. Fery-Forgues, F. Al-Ali, *J. Photochem. Photobiol. C*. **2004**, *5* (*2*), 139. DOI: https://doi.org/10.1016/j.jphotochemrev.2004.07.001.

[143]. A. Ogunsipe, J.-Y. Chen, T. Nyokong, *New J. Chem.* **2004**, *28* (*7*), 822. DOI: https://doi.org/10.1039/B315319C.

[144]. A. Vlahovici, I. Druţă, M. Andrei, M. Cotlet, R. Dinică, *J. Lumin.* **1999**, *82* (*2*), 155. DOI: https://doi.org/10.1016/S0022-2313(99)00027-7.

[145]. D. C. Hone, P. I. Walker, R. Evans-Gowing, S. FitzGerald, A. Beeby, I. Chambrier, M. J. Cook, D. A. Russell, *Langmuir*. **2002**, *18* (*8*), 2985. DOI: https://doi.org/10.1021/la0256230.

[146]. M. Wahl, *PicoQuant*. **2014**, 14.htt://www.picoquant

[147]. N. M. Dimitrijevic, P. V. Kamat, *J. Phys. Chem.* **1992**, *96* (*12*), 4811. DOI: https://doi.org/10.1021/j100191a017.

[148]. T. Nyokong, *Pure Appl. Chem.* **2011**, *83* (*9*), 1763. DOI: https://doi.org/10.1351/PAC-CON-10-11-22.

[149]. T. H. Tran Thi, C. Desforge, C. Thiec, S. Gaspard, *J. Phys. Chem.* **1989**, *93* (*4*), 1226. DOI: https://doi.org/10.1021/j100341a013.

[150]. T. Liu, X. Zhang, H. Zhang, H. Zhao, Z. Zhang, Y. Tian, *Opt. Express*. **2020**, *28* (*18*), 25757. DOI: https://doi.org/10.1364/OE.401423.

[151]. M. Durmuş, V. Ahsen, T. Nyokong, *J. Photochem. Photobiol. A*. **2007**, *186* (*2–3*), 323. DOI: https://doi.org/10.1016/j.jphotochem.2006.08.025.

[152]. S. Gördük, *J. Turk. Chem. Soc. A: Chem.* **2021**, *8* (*1*), 279. DOI: https://doi.org/10.18596/jotcsa.812081.

[153]. N. A. Kuznetsova, N. S. Gretsova, O. A. Yuzhakova, V. M. Negrimovskii, O. L. Kaliya, E. A. Luk'yanets, *Russ. J. Gen. Chem.* **2001**, *71* (*1*), 36. DOI: https://doi.org/10.1023/A:1012369120376.

[154]. J. R. Harjani, R. D. Singer, M. T. Garcia, P. J. Scammells, Green Chem. 2009, 11, 83, doi:10.1039/B811814K.

[155]. W. Yang, P. S. Chan, M. S. Chan, K. F. Li, P. K. Lo, N. K. Mak, K. W. Cheah, M. S. Wong, Chem. Commun. 2013, 49, 3428, doi:10.1039/C3CC41240G.

[156]. M. Ambroz, A. Beeby, A. J. MacRobert, M. S. C. Simpson, R. K. Svensen, D. Phillips, *J. Photochem. Photobiol. B, Biol.* **1991***, 9 (1),* 87. DOI: https://doi.org/10.1016/1011-1344(91)80006-4.

[157]. M. Göksel, Z. Biyiklioglu, M. Durmuş, *J. Biol. Inorg. Chem.* **2017**, *22*, 953, doi:10.1007/s00775-017-1473-0.

[158]. E. Dube, N. Nwaji, D. O. Oluwole, J. Mack, T. Nyokong, *J. Photochem. Photobiol. A* **2017**, *349*, 148, doi: 10.1016/j.jphotochem.2017.09.020.

[159]. N. Jia, C. He, S. Wang, W. Song, Z. Chen, Y. Zu, Y. Gao, Y. Dong, *Opt. Mater.* **2018**, *76*, 81, doi: 10.1016/j.optmat.2017.12.012.

[160]. V. Nemykin, S. Dudkin, F. Dumoulin, C. Hirel, A. Gurek, V. Ahsen, *ARKIVOC* **2014**, 142, doi:10.3998/ark. 5550190.p008.412.

[161]. R. P. Bagwe, C. Yang, L. R. Hilliard, W. Tan, *Langmuir* **2004**, *20*, 8336, doi:10.1021/la049137j.

[162]. S. H. Hussein-Al-Ali, M. E. El Zowalaty, M. Z. Hussein, B. M. Geilich, T. J. Webster, *Int. J. Nanomedicine* **2014**, *9*, 3801, doi:10.2147/IJN.S61143.

[163]. S. Çolak, M. Durmuş, S. Zeki Yıldız, *Dalton Trans.* **2016**, *45*, 10402, doi:10.1039/C6DT01084A.

[164]. O. L. Osifeko, M. Durmuş, T. Nyokong, *J. Photochem. Photobiol.* **2015**, *301*, 47, doi: 10.1016/j.jphotochem.2014.12.011.

[165]. J. Tan, Z. Liu, Y. Sun, L. Yang, L. Gao, *Mycopathologia* **2019**, *184*, 525, doi:10.1007/s11046-019-00352-9.

[166]. L. J. Tavares, E. D. de Avila, M. I. Klein, B. H. D. Panariello, D. M. P. Spolidório, *J. Photochem. Photobiol. B, Biol.* **2018**, *188*, 135, doi: 10.1016/j.jphotobiol.2018.09.010.

[167]. A. D. Verderosa, C. de la Fuente-Núñez, S. C. Mansour, J. Cao, T. K. Lu, R. E. W. Hancock, K. E. Fairfull-Smith, *Eur. J. Med. Chem.* **2017**, *138*, 590, doi: 10.1016/j.ejmech.2017.06.058.

[168]. T. Nyokong, in *Functional Phthalocyanine Molecular Materials* (Ed: J. Jiang), Springer, Berlin, Heidelberg **2010**.

[169]. K. Palewska, J. Sworakowski, J. Lipiński, *Opt. Mater.* **2012**, *34*, 1717, doi: 10.1016/j.optmat.2012.02.009.

[170]. H. Engelkamp, R. J. M. Nolte, *J. Porphyr. Phthalocy.* **2000**, *4*, 454, doi:10.1002/1099-1409(200008)4:5<454::AID-JPP261>3.0.CO;2-D.

[171]. K. Leduskrasts, E. Suna, *RSC Advances* **2019**, *9*, 460, doi:10.1039/C8RA08771G.

[172]. M.J. Stillman, T. Nyokong, in Phthalocyanine-properties and Applications, (Ed: C. C. Leznoff and B. Lever), VCH, New York 1, (**1989**) 133–290.

[173]. M. J. Frisch, *et al.*, *Gaussian 09* (see Appendix for full reference and a detail description of the computational methods as ref [A_1])

[174]. J. Michl, *Tetrahedron* **1984**, *40*, 3845, doi:10.1016/S0040-4020(01)99999-5.

[175]. M. Gouterman, Optical spectra and electronic structure of porphyrins and related rings, in *The Porphyrins*, ed. D. Dolphin, Academic Press, New York, 1978, vol. III, pp. 1–165 Part A.

[176]. N. Kobayashi, A. Muranaka, *Circular Dichroism and Magnetic Circular Dichroism Spectroscopy for Organic Chemists*, Royal Society of Chemistry, London **2011**.

[177]. J. Mack, Y. Asano, N. Kobayashi, M. J. Stillman, *J. Am. Chem. Soc.* **2005***, 127* (*50*)*,* 17697. DOI: https://doi.org/10.1021/ja0540728.

[178]. M. Durmuş, A. Erdoğmuş, A. Ogunsipe, T. Nyokong, *Dyes Pigm.* **2009**, *82*, 244, doi: 10.1016/j.dyepig.2009.01.008.

[179]. B. Babu, R. C. Soy, J. Mack, T. Nyokong, *New J. Chem.* **2020**, *44*, 11006, doi:10.1039/D0NJ01564D.

[180]. S. V. Blokhina, A. V. Sharapova, M. V. Ol'khovich, T. V. Volkova, G. L. Perlovich, *Eur. J. Pharm. Sci.* **2016**, *93*, 29, doi: 10.1016/j.ejps.2016.07.016.

[181]. D. Dutta, D. Thakur, D. Bahadur, *J. Chem. Eng.* **2015**, *281*, 482, doi: 10.1016/j.cej.2015.06.110.

[182]. B. C. Smith, *Infrared Spectral Interpretation: A Systematic Approach*, CRC Press, New York, 1998 **2018**.

[183]. R. Schneider, F. Schmitt, C. Frochot, Y. Fort, N. Lourette, F. Guillemin, J.-F. Müller, M. Barberi-Heyob, *Bioorg. Med. Chem.* **2005**, *13*, 2799, doi: 10.1016/j.bmc.2005.02.025.

[184]. A. R. Vortherms, R. P. Doyle, D. Gao, O. Debrah, P. J. Sinko, *Nucleos. Nucleot. Nucleic Acids* **2008**, *27*, 173, doi:10.1080/15257770701795946.

[185]. M. F. Cipreste, I. Gonzalez, T. Maria da Mata Martins, A. M. Goes, W. Augusto de Almeida Macedo, E. M. Barros de Sousa, *RSC Adv.* **2016**, *6*, 76390, doi:10.1039/C6RA14068H.

[186]. M. A. Mikolajczyk, A. Gajewicz, B. Rasulev, N. Schaeublin, E. Maurer-Gardner, S. Hussain, J. Leszczynski, T. Puzyn, *Chem. Mater.* **2015**, *27*, 2400, doi:10.1021/cm504406a.

[187]. Z. Song, F. Zhang, X. Li, S. -K. Chan, F. Zhao, Y. Tang, *J. Porphyr. Phthalocyanines* **2002**, *06*, 484, doi:10.1142/S1088424602000609.

[188]. J.P. Fox, D.P. Goldberg, *Inorg. Chem.* **2003**, *42*, 8181, doi:10.1021/ic034792k.

[189]. S. J. Takayama, G. Ukpabi, M. E. P. Murphy, A. G. Mauk, *PNAS* **2011**, *108*, 13071, doi:10.1073/pnas.1101459108.

[190]. S. Xu, S. Hartvickson, J. X. Zhao, *ACS Appl. Mater. Interfaces* **2011**, *3*, 1865, doi:10.1021/am200052a.

[191]. L. H. Zucolotto Cocca, M. M. Ayhan, A. G. Gürek, V. Ahsen, Y. Bretonnière, J. De Paula Siqueira, F. Gotardo, C. R. Mendonça, C. Hirel, L. De Boni, *Molecules* **2016**, *21*, 635, doi:10.3390/molecules21050635.

[192]. C. M. Marian, *WIREs Comput. Mol. Sci.* **2012**, *2*, 187, doi:10.1002/wcms.83.

[193]. A. J. Tilley, R. D. Pensack, T. S. Lee, B. Djukic, G. D. Scholes, D. S. Seferos, *J. Phys. Chem. C* **2014**, *118*, 9996, doi:10.1021/jp503708d.

[194]. M.T. Colvin, A.B. Ricks, A.M. Scott, D.T. Co, M.R. Wasielewski, *J. Phys. Chem. A* **2012**, *116*, 1923, doi:10.1021/jp212546w.

[195]. S. Xie, S. Manuguri, G. Proietti, J. Romson, Y. Fu, A. K. Inge, B. Wu, Y. Zhang, D. Häll, O. Ramström, *Proc. Natl. Acad. Sci. U.S.A.* **2017**, *114*, 8464, doi:10.1073/pnas.1708556114.

[196]. M. G. Debacker, O. Deleplanque, B. Van Vlierberge, F. X. Sauvage, *Laser Chem.* **1900**, *8*, 497437, doi:10.1155/LC.8.1.

[197]. H. S. Muddana, T. T. Morgan, J. H. Adair, P. J. Butler, *Nano Lett.* **2009**, *9*, 1559, doi:10.1021/nl803658w.

[198]. N. Nwahara, J. Britton, T. Nyokong, *J. Coord. Chem.* **2017**, *70*, 1601, doi:10.1080/00958972.2017.1313975.

[199]. C. Zhang, J. Zhao, S. Wu, Z. Wang, W. Wu, J. Ma, S. Guo, L. Huang, *J. Am. Chem. Soc.* **2013**, *135*, 10566, doi:10.1021/ja405170j.

[200]. J. R. Darwent, P. Douglas, A. Harriman, G. Porter, M.-C. Richoux, *Coord. Chem. Rev.* **1982**, *44*, 83, doi:10.1016/S0010-8545(00)80518-4.

[201]. A. Saha, M. Chen, M. Lederer, A. Kahnt, X. Lu, D. M. Guldi, *Chem. Sci.* **2017**, *8*, 1360, doi:10.1039/C6SC03207A.

[202]. K. N. Bardakova, Y. V. Faletrov, E. O. Epifanov, N. V. Minaev, V. S. Kaplin, Y. A. Piskun, P. I. Koteneva, V. M. Shkumatov, N. A. Aksenova, A. I. Shpichka, *Polymers* **2021**, *13*, 3385, doi:10.3390/polym13193385.

[203]. M. Kaneko, H. Ueno, S. Masuda, K. Suzuki, H. Okimi, M. Hoshino, L. Lapok, D. Wöhrle, *J. Porphyr. Phthalocyanines* **2005**, *09*, 667, doi:10.1142/S1088424605000782.

[204]. H. Ramesh, T. Mayr, M. Hobisch, S. Borisov, I. Klimant, U. Krühne, J. M. Woodley, *J. Chem. Technol. Biotechnol.* **2016**, *91*, 832, doi:10.1002/jctb.4862.

[205]. X.-F. Zhang, X. Li, L. Niu, L. Sun, L. Liu, *J. Fluoresc.* **2009**, *19*, 947, doi:10.1007/s10895-009-0494-7.

[206]. E. I. Sagun, E. I. Zenkevich, V. N. Knyukshto, A. M. Shulga, D. A. Starukhin, C. von Borczyskowski, *Chem. Phys.* **2002**, *275*, 211, doi:10.1016/S0301-0104(01)00517-1.

[207]. H.-N. Shin, S. H. Seo, H. Choo, G. Kuem, K. I. Choi, G. Nam, *Bioorganic Med. Chem. Lett.* **2013**, *23*, 1193, doi: 10.1016/j.bmcl.2013.01.033.

[208]. A. Özel, Ü. Demirbaş, B. Barut, H. Kantekin, *J. Mol. Struct.* **2019**, *1186*, 325, doi: 10.1016/j.molstruc.2019.03.047.

[209]. M. Pişkin, E. Canpolat, Ö. F. Öztürk, *J. Mol. Struct.* **2020**, *1202*, 127181, doi: 10.1016/j.molstruc.2019.127181.

[210]. H. Şahal, M. Pişkin, G. A. Organ, Ö. F. Öztürk, M. Kaya, E. Canpolat, *J. Coord. Chem.* **2018**, *71*, 3763, doi:10.1080/00958972.2018.1524140.

[211]. K. Serbest, İ. Değirmencioğlu, Y. Ünver, M. Er, C. Kantar, K. Sancak, *J. Organomet. Chem.* **2007**, *692*, 5646, doi: 10.1016/j.jorganchem.2007.09.026.

[212]. P. Sen, T. Nyokong, *Polyhedron* **2019**, *173*, 114135, doi: 10.1016/j.poly.2019.114135.

[213]. D. G. Villanueva, *Pharm. Pharm. Sci.* **2015**, *2*, 9, doi:10.15226/2374-6866/2/1/00121.

[214]. J. Zielonka, J. Joseph, A. Sikora, M. Hardy, O. Ouari, J. Vasquez-Vivar, G. Cheng, M. Lopez, B. Kalyanaraman, *Chem. Rev.* **2017**, *117*, 10043, doi: 10.1021/acs.chemrev.7b00042.

[215]. K. M. S. Herrera, L. S. Ferreira, A. V. Braga, J. P. Souza, J. T. Andrade, A. C. Soares, L. F. Soares, R. C. R. Chagas, J. M. S. Ferreira, *An. Acad. Bras. Ciênc.* **2019**, *91*, e20181077, doi:10.1590/0001-376520181077.

[216]. K. G. Ali, I. H. Bukhari, S. Ali, S. Shahzadi, *J. Chem. Soc. Pak.* **2018**, *40*, 213.

[217]. P. Dalgaard, T. Ross, L. Kamperman, K. Neumeyer, T. A. McMeekin, *Int. J. Food Microbiol.* **1994**, *23*, 391, doi:10.1016/0168-1605(94)90165-1.

[218]. A. Sindelo, O. L. Osifeko, T. Nyokong, Synthesis, *Inorg. Chim. Acta* **2018**, *476*, 68, doi: 10.1016/j.ica.2018.02.020.

[219]. Q. Deng, P. Sun, L. Zhang, Z. Liu, H. Wang, J. Ren, X. Qu, *Adv. Funct. Mater* **2019**, *29*, 1903018, doi:10.1002/adfm.201903018.

[220]. H. Richter, K. P. Nevin, H. Jia, D. A. Lowy, D. R. Lovley, L. M. Tender, *Energy Environ. Sci.* **2009**, *2*, 506, doi:10.1039/b816647a.

[221]. T. J. Silhavy, D. Kahne, S. Walker, *Cold Spring Harb. Perspect. Biol.* **2010**, *2*, a000414, doi:10.1101/cshperspect.a000414.

[222]. P. Ding, W. Song, Z. Yang, J. Jian, *Bioprocess Biosyst. Eng.* **2018**, *41*, 781, doi:10.1007/s00449-018-1911-6.

[223]. H.-C. Flemming, J. Wingender, *Nat. Rev. Microbiol.* **2010**, *8*, 623, doi:10.1038/nrmicro2415.

[224]. D. H. Limoli, C. J. Jones, D. J. Wozniak, *Microbiol. Spectr.* **2015**, *3*, 223. doi:10.1128/microbiolspec. MB-0011-2014.

[225]. C. Zhang, F. Gao, W. Wu, W.-X. Qiu, L. Zhang, R. Li, Z.-N. Zhuang, W. Yu, H. Cheng, X.-Z. Zhang, *ACS Nano* **2019**, *13*, 11249, doi:10.1021/acsnano.9b04315.

[226]. F. Harnisch, S. Freguia, *Chem. Asian J.* **2012**, *7*, 466, doi:10.1002/asia.201100740.

[227]. X. X. Han, H. Y. Jia, Y. F. Wang, Z. C. Lu, C. X. Wang, W. Q. Xu, B. Zhao, Y. Ozaki, *Anal. Chem.* **2008**, *80*, 2799, doi:10.1021/ac702390u.

[228]. M. Kögler, J. Itkonen, T. Viitala, M. G. Casteleijn, *Sci. Rep.* **2020**, *10*, 2472, doi:10.1038/s41598-020-59091-3.

[229]. J.-W. Tang, Q.-H. Liu, X.-C. Yin, Y.-C. Pan, P.-B. Wen, X. Liu, X.-X. Kang, B. Gu, Z.-B. Zhu, L. Wang, *Front. Microbiol.* **2021**, *12*, 14. doi.org/10.3389/fmicb.2021.696921

[230]. Z. Pilát, S. Bernatová, J. Ježek, J. Kirchhoff, A. Tannert, U. Neugebauer, O. Samek, P. Zemánek, *Sensors* **2018**, *18*, 1623, doi:10.3390/s18051623.

[231]. J. W. Chan, H. Winhold, M. H. Corzett, J. M. Ulloa, M. Cosman, R. Balhorn, T. Huser, *Cytom. Part A* **2007**, *71A*, 468, doi:10.1002/cyto.a.20407.

[232]. I. Notingher, *Sensors* **2007**, *7*, 1343, doi:10.3390/s7081343.

[233]. A. Rygula, K. Majzner, K. M. Marzec, A. Kaczor, M. Pilarczyk, M. Baranska, *J. Raman Spectrosc.* **2013**, *44*, 1061, doi:10.1002/jrs.4335.

[234]. G. B. Jung, Y. J. Lee, G. Lee, H.-K. Park, *Biomed. Opt. Express, BOE* **2013**, *4*, 2673, doi:10.1364/BOE.4.002673.

[235]. H.-C. Flemming, T. R. Neu, D. J. Wozniak, *J Bacteriol.* **2007**, *189*, 7945, doi:10.1128/jb.00858-07.

[236]. P. Bazylewski, R. Divigalpitiya, G. Fanchini, *RSC Adv.* **2017**, *7*, 2964, doi:10.1039/C6RA25879D.

[237]. S. Verrier, I. Notingher, J. M. Polak, L. L. Hench, *Biopolymers* **2004**, *74*, 157, doi:10.1002/bip.20063.

[238]. P. Bhosale, *Appl. Microbiol. Biotechnol.* **2004**, *63*, 351, doi:10.1007/s00253-003-1441-1.

[239]. S. Heeb, M. P. Fletcher, S. R. Chhabra, S. P. Diggle, P. Williams, M. Cámara, *FEMS Microbiol. Rev.* **2011**, *35*, 247, doi:10.1111/j.1574-6976.2010.00247. x.

[240]. R. Chug, B. Khosla, M. Singh, *Int. J. Curr. Microbiol. App. Sci* **2015**, *4*, 884.

[241]. M. Sauget, M.-H. Nicolas-Chanoine, N. Cabrolier, X. Bertrand, D. Hocquet, *Int. J. Med. Microbiol.* **2014**, *304*, 977, doi: 10.1016/j.ijmm.2014.06.004.

[242]. B. Frigerio, C. Bizzoni, G. Jansen, C. P. Leamon, G. J. Peters, P. S. Low, L. H. Matherly, M. Figini, *J. Exp. Clin. Cancer Res.* **2019**, *38*, 125, doi:10.1186/s13046-019-1123-1.

[243]. G. L. Zwicke, G. Ali Mansoori, C. J. Jeffery, *Nano Rev.* **2012**, *3*, 18496, doi:10.3402/nano.v3i0.18496.

[244]. S. Pisarek, K. Maximova, D. Gryko, *Tetrahedron* **2014**, *70*, 6685, doi: 10.1016/j.tet.2014.05.090.

[245]. J. Kollar, M. Machacek, M. Halaskova, J. Lenco, R. Kucera, J. Demuth, M. Rohlickova, K. Hasonova, M. Miletin, V. Novakova, *J. Med. Chem.* **2020**, *63*, 7616, doi: 10.1021/acs.jmedchem.0c00481.

[246]. Y. Chin, S. H. Lim, Y. Zorlu, V. Ahsen, L. V. Kiew, L. Y. Chung, F. Dumoulin, H. B. Lee, *PLOS ONE* **2014**, *9*, e97894, doi: 10.1371/journal.pone.0097894.

[247]. M. V. Berridge, P. M. Herst, A. S. Tan, *Biotechnol. Annu. Rev* **2005**, *11*, 127, doi:10.1016/S1387-2656(05)11004-7.

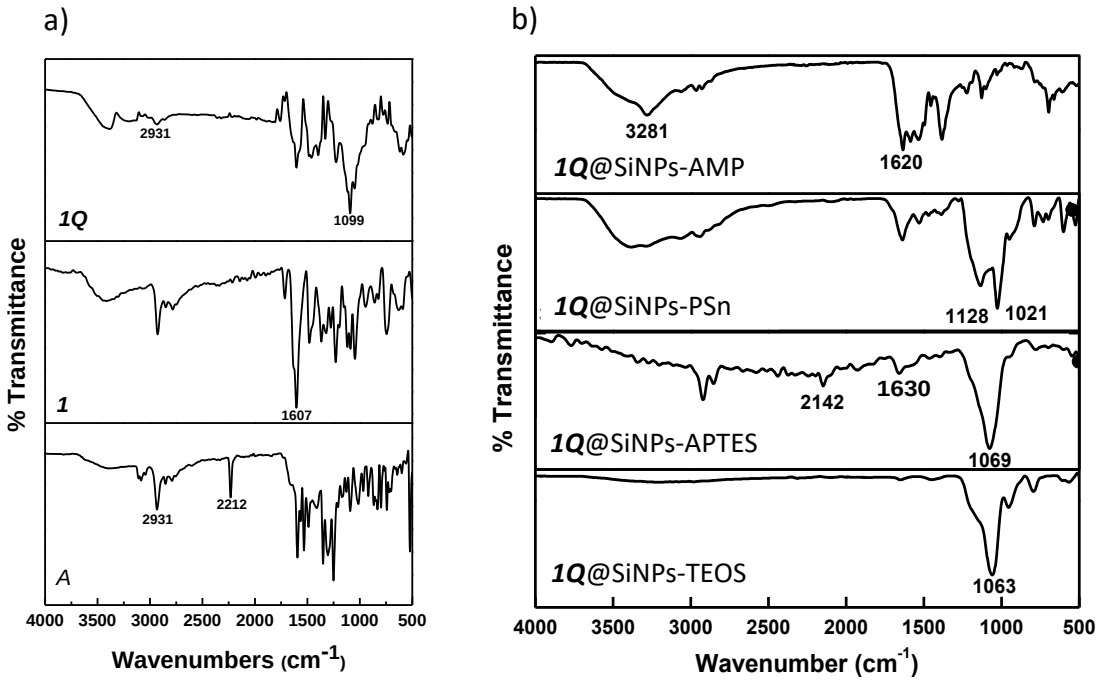

Figure A1: FT–IR spectra of a) phthalonitrile *A*, *1, and 1Q* b) *1Q*@SiNPs-TEOS, *1Q*@SiNPs-APTES, *1Q*@SiNPs-PS and *1Q*@SiNPs-AMP.

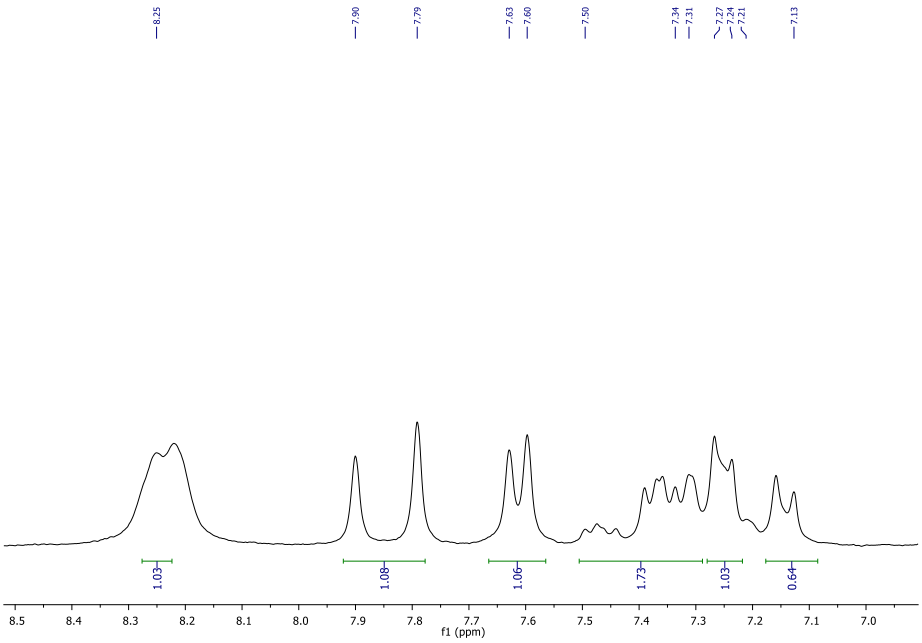

Figure A2: ^{1}H-NMR spectrum of ***D*** at 80MHz in DMSO-d_6.

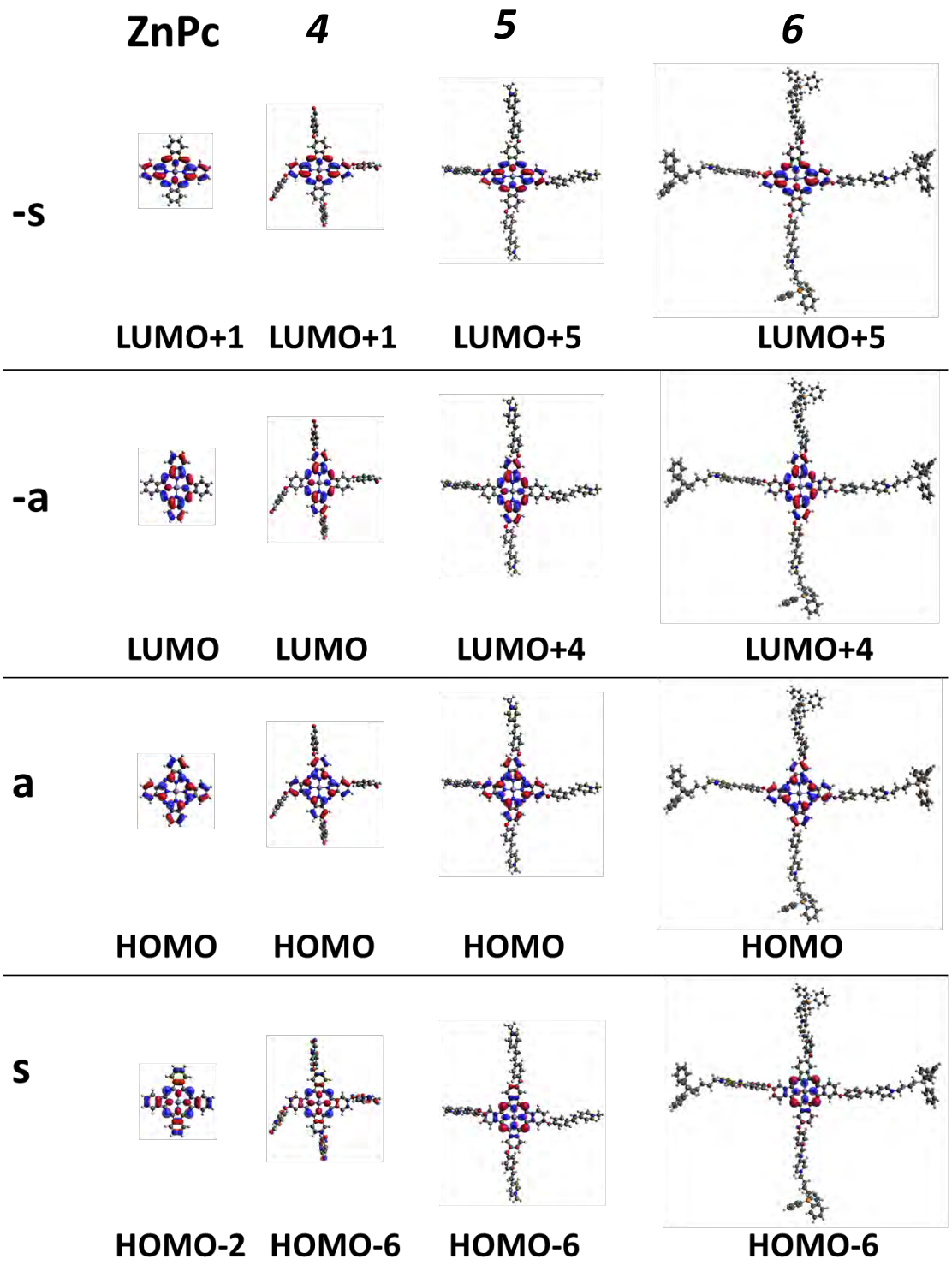

Figure A3: The angular nodal patterns of the frontier orbitals of *4*-*6* and the unsubstituted parent ZnPc model complex that are associated with the Q and B transitions at an isosurface of 0.2 a.u.

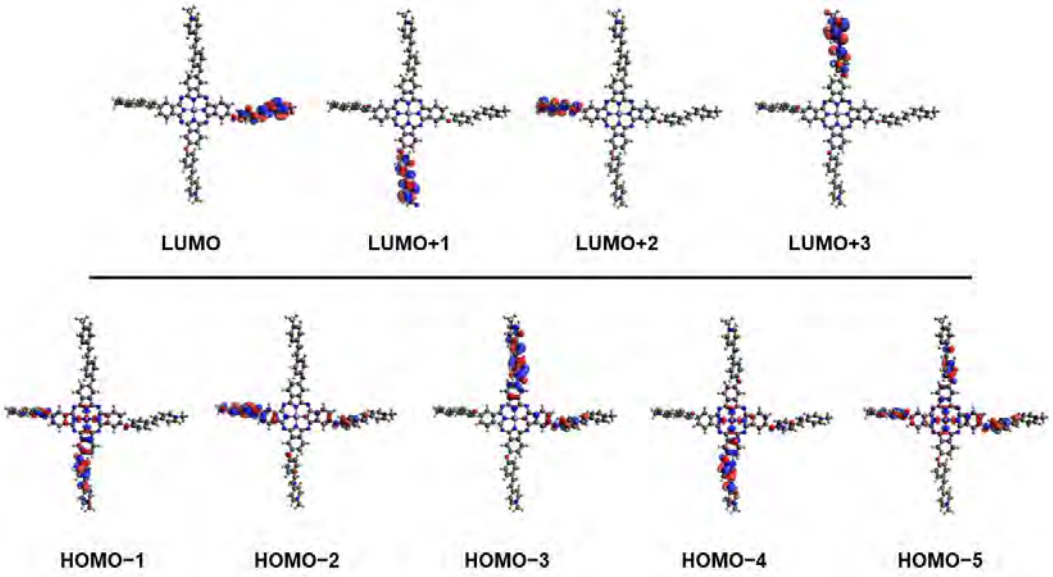

Figure A4: The angular nodal patterns of the frontier orbitals of *5* that are associated with the CT band at an isosurface of 0.2 a.u.

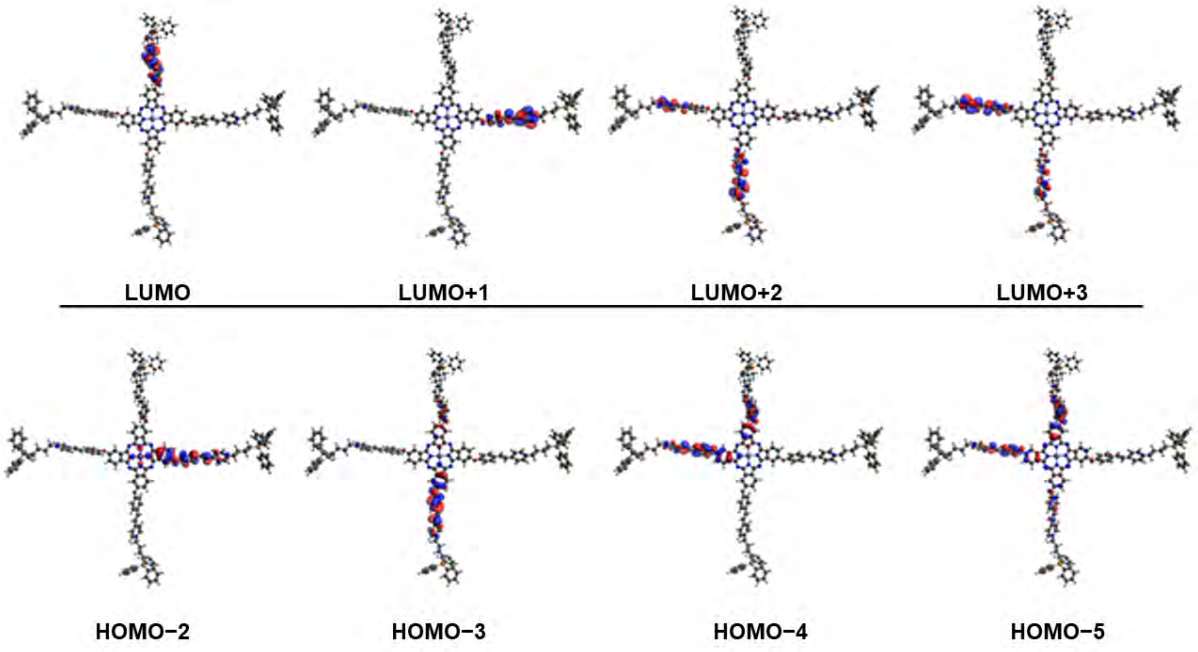

Figure A5: The angular nodal patterns of the frontier orbitals of *6* that are associated with the CT band at an isosurface of 0.2 a.u.

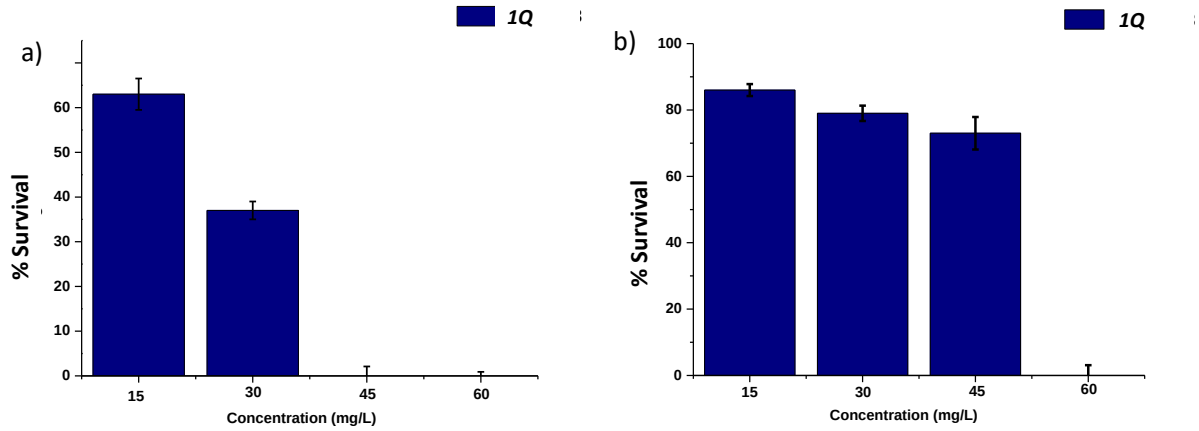

Figure A6: Survival graph of *S. aureus* following exposure to *1Q* presence of (a) light and (b) dark in PBS. Concentration = 15, 30 ,45 and 60 mg/L

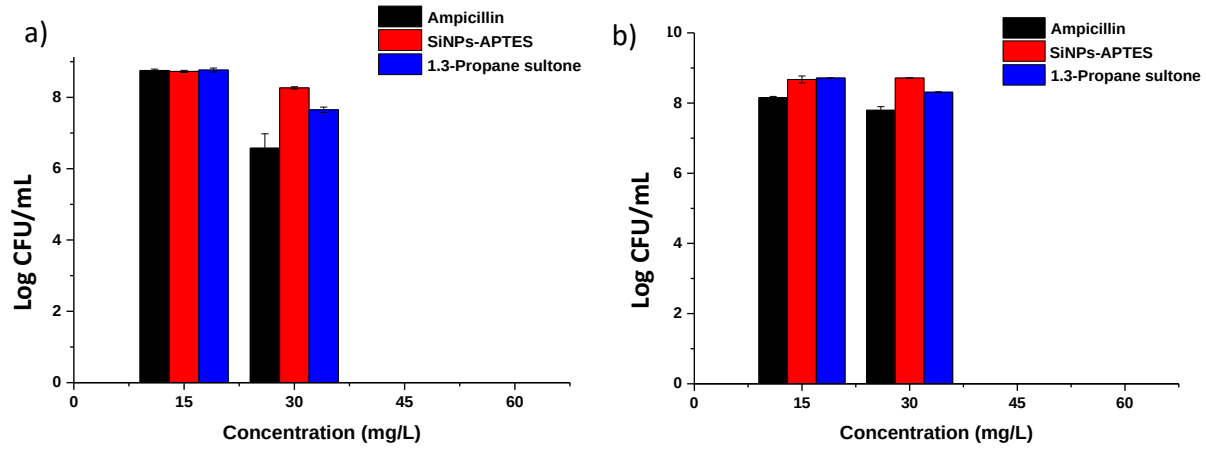

Figure A7: Log CFU/mL due to Ampicillin, SiNPs-APTES and 1.3-Propane sultone of (a) light and (b) dark against *S. aureus* in PBS. Concentration = 15, 30 ,45 and 60 mg/L.

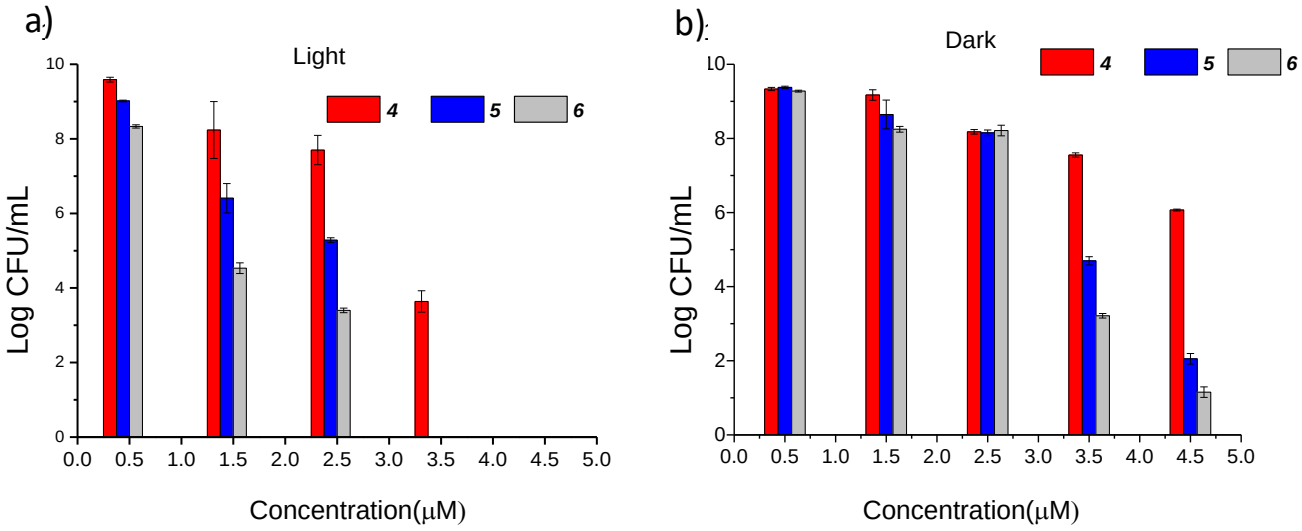

Figure A8: Survival graph of *E. coli* following treatment with *4*, *5*, and *6* in the presence of a) light and b) dark in PBS. Concentration = 0.5, 1.5, 2.5, 3.5 and 4.5 µM.

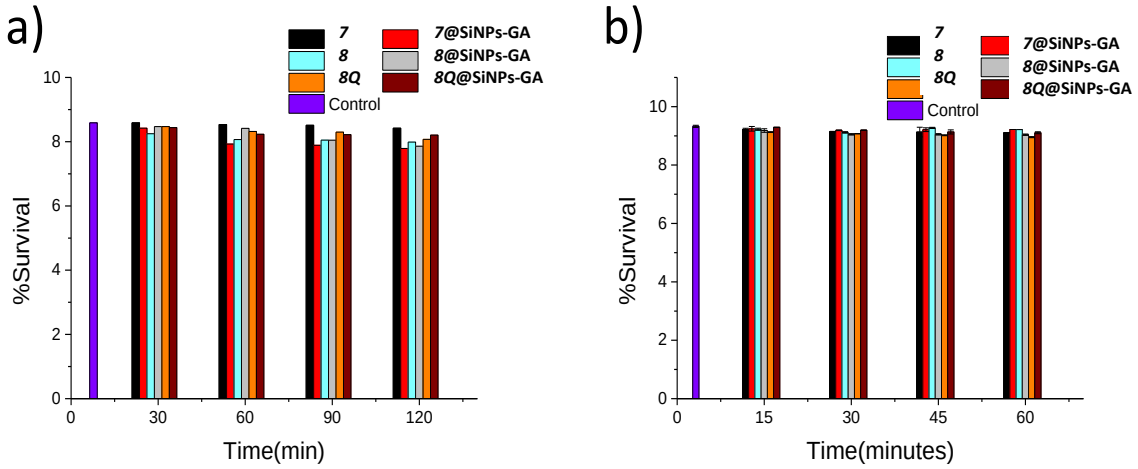

Figure A9: Survival graph of a) *E. coli* and b) *S. aureus* (planktonic) *in* PBS due to complexes *7*, *8*, *8Q*, and their doped Pc conjugates in the dark at concentration = 0.58 (*S. aureus*) and 1.16 mg/L (*E. coli*).

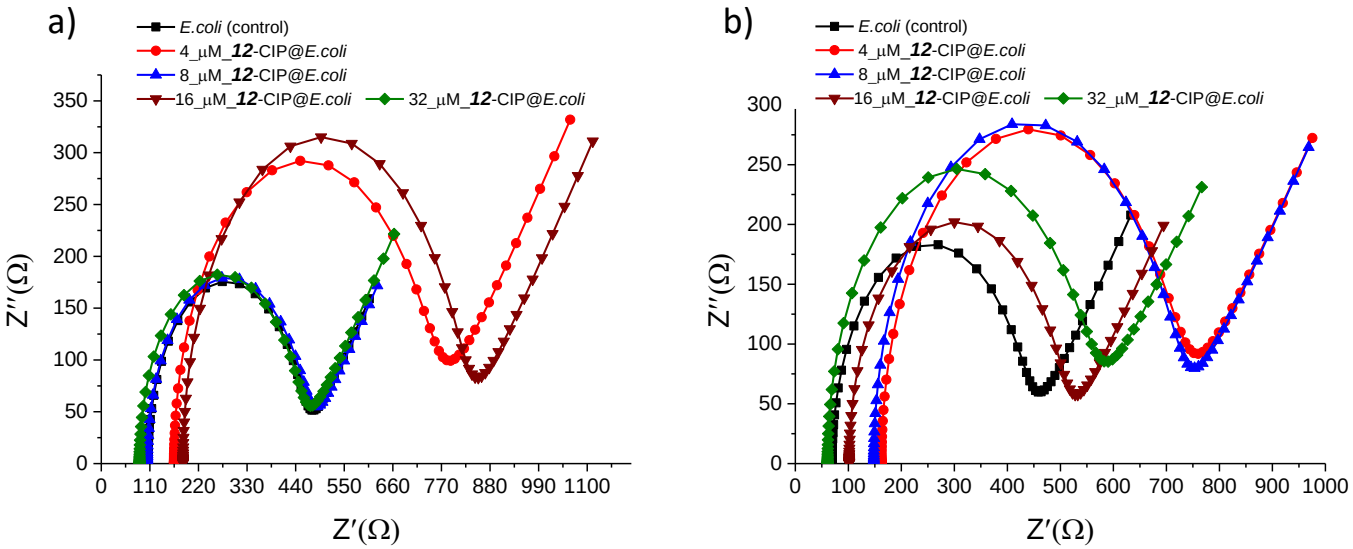

Figure A10: Nyquist plots of the impedance for *E. coli* biofilm substrate before a) and after b) illumination with laser light after treatment with *12*-CIP at 4-32µM concentration (1%DMSO/PBS, pH 7.4) in 0.1 M KCl containing 1 mM $[Fe(CN)_6]^{3-/4-}$ solution.

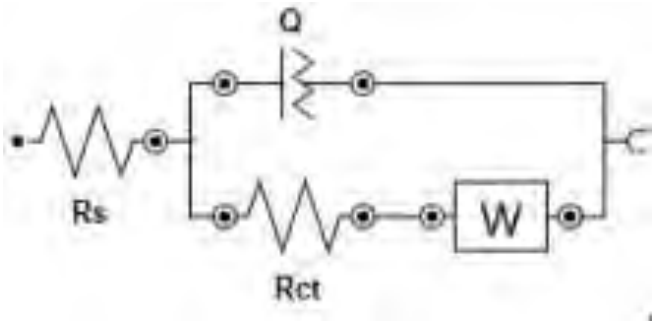

Figure A11: Equivalent circuit adopted to fit the impedance data where Rs is the ohmic resistance of the electrolyte solution, Q the phase constant element, W the Warburg impedance, and R_{ct} the electron-transfer resistance.

Table A1. TD-DFT spectra of the B3LYP optimised geometries for ***4*** – ***6*** and ZnPc calculated with the CAM-B3LYP functional and 6-31G(d,p) basis sets [A_1].

4					
Band	**#[a]**	**λ_{calc} [b]**	***f*** **[c]**	**λ_{exp} [d]**	**Wave Function[e] =**
Q	1	572	0.63	683	**96% a → -a/-s**; …
	2	570	0.64		**96% a → -a/-s**; …
B	16	306	0.91	353	41% H−4^{S} → -a/-s; **18% s → -a/-s;** 16% 1b1g^{N} → -a; …
	17	305	1.39		-40% H−4^{S} → -a/-s; **26% s → -a/-s;** …
5					
Band	**#[a]**	**λ_{calc} [b]**	***f*** **[c]**	**λ_{exp} [d]**	**Wave Function[e] =**
Q	1	574	0.99	683	**87% a → -a/-s; 6% s → -a/-s;** …
	2	575	0.98		**88% a → -a/-s; 6% s → -a/-s;** …
CT	9	387	0.52	472	15% H−4^{S} → L+2^{S}; 12% H−1^{S,N} → L+1^{S}; …
	10	384	2.75		30% H−2^{S} → L+2^{S}; 13% H−5^{S,N} → L^{S}; 11% H−3^{S} → L^{S}; …
	11	383	3.30		35% H−3^{S} → L+2^{S}; 17% H−4^{S,N} → L+1^{S}; 12% H−1^{S,N} → L+1^{S}; …
	12	374	0.11		19% H−3^{S} → L+2^{S}; 15% H−2^{S} → L+2^{S}; 10% H−4^{S,N} → L+1^{S}; …
B	20	300	0.78	356	**39% s → -a/-s;** 21% H−4^{S,N} → -a/-s; 17% H−5^{S,N} → -a/-s; …
	21	300	0.81		**42% s → -a/-s;** 24% H−5^{S,N} → -a/-s; 10% H−4^{S,N} → -a/-s; …
6					
Band	**#[a]**	**λ_{calc} [b]**	***f*** **[c]**	**λ_{exp} [d]**	**Wave Function[e] =**
Q	1	583	1.17	684	**80% a → -a/-s;** 7% a → L+1^{S}; **5% s → -a/-s;** …
	2	582	1.12		**82% a → -a/-s;** 6% a → L^{S}; **5% s → -a/-s;** …
CT	9	406	1.03	476	30% H−2^{S} → L+1^{S}; 10% H−5^{S} → L^{S}; …
	10	402	2.99		14% H−2^{S} → L+1^{S}; 13% H−5^{S} → L^{S}; 10% H−3^{S} → L+2; 10% H−4^{S} → L^{S}; …
	11	401	3.27		19% H−3^{S} → L+2^{S}; 16% H−4^{S} → L+3^{S}; 10% H−3^{S} → L+3; 10% H−5^{S} → L+2^{S}; …
	12	390	0.07		18% H−3^{S} → L+2^{S}; 13% H−5^{S} → L+3^{S}; 12% H−2^{S} → L+1^{S}; 11% H−4^{S} → L+3^{S}; …
B	24	301	0.51	355	25% H−5^{S} → -a/-s; **23% s → -s;** 11% H−2^{S} → a; 10% H−2^{S} → L^{S}; …
	25	300	0.74		**36% s → -a/-s;** 34% H−5^{S} → -s; **7% s → -a/-s;** …
ZnPc					
Band	**#[a]**	**λ_{calc} [b]**	***f*** **[c]**	**λ_{exp} [d]**	**Wave Function[e] =**
Q	1	563	0.47	672	**100% a → -a;** …
	2	562	0.47		**100% a → -s;** …
B	12	292	1.00	344	**73% s → -a/-s;** 15% 1b$_{2u}$ → -a/-s; **7% s → -a/-s;** …
	13	292	1.00		**73% s → -a/-s;** 15% 1b$_{2u}$ → -a/-s; **7% s → -a/-s;** …

Table A2: Zeta potential measurements for Pc@SiNPs-/APTES/GA.
(Pc=***7***, ***8*** or ***8Q***).

Sample	Zeta potential
7@SiNPs-APTES	-32.7 ± 1.33 (-12.03)
7@SiNPs-GA	-5.1 ± 0.461 (-12.03)
8@SiNPs-APTES	21.8 ± 2.26 (13.4)
8@SiNPs-GA	-5.2 ± 1.24 (13.4)
8Q@SiNPs-APTES	24.2 ± 2.07 (27.5)
8Q@SiNPs-GA	-7.03 ± 1.24 (27.5)

Values for the Pcs' measurements alone are indicated in brackets.

Table A3: Rct values in the dark and light against E. coli biofilms after 40 min uptake of *12*-CIP (added concentrations of 4 to 32 µM) followed by 15 min illumination with laser probe.

Concentration of ***12***-CIP@biofilm ITO-glass composite	***E. coli***		***S. pneumoniae***	
	Rct(Ω)		**Rct(Ω)**	
	Dark	**Light**	**Dark**	**Light**
Control	344	480	158	175
4 µM	569	545	3670	351
8 µM	351	559	133	277
16 µM	619	358	1730	257
32 µM	357	396	1330	134
Rct values of bare ITO-glass = 866 Ω in 0.1 M KCl containing 1 mM $[Fe(CN)6]^{3-/4-}$ solution.				

[A_1]. Gaussian 09, Revision A.02, M. J. Frisch, G. W. Trucks, H. B. Schlegel, G. E. Scuseria, M. A. Robb, J. R. Cheeseman, G. Scalmani, V. Barone, G. A. Petersson, H. Nakatsuji, X. Li, M. Caricato, A. Marenich, J. Bloino, B. G. Janesko, R. Gomperts, B. Mennucci, H. P. Hratchian, J. V. Ortiz, A. F. Izmaylov, J. L. Sonnenberg, D. Williams-Young, F. Ding, F. Lipparini, F. Egidi, J. Goings, B. Peng, A. Petrone, T. Henderson, D. Ranasinghe, V. G. Zakrzewski, J. Gao, N. Rega, G. Zheng, W. Liang, M. Hada, M. Ehara, K. Toyota, R. Fukuda, J. Hasegawa, M. Ishida, T. Nakajima, Y. Honda, O. Kitao, H. Nakai, T. Vreven, K. Throssell, J. A. Montgomery, Jr., J. E. Peralta, F. Ogliaro, M. Bearpark, J. J. Heyd, E. Brothers, K. N. Kudin, V. N. Staroverov, T. Keith, R. Kobayashi, J. Normand, K. Raghavachari, A. Rendell, J. C. Burant, S. S. Iyengar, J. Tomasi, M. Cossi, J. M. Millam, M. Klene, C. Adamo, R. Cammi, J. W. Ochterski, R. L. Martin, K. Morokuma, O. Farkas, J. B. Foresman, and D. J. Fox, Gaussian, Inc., Wallingford CT, 2016.